UNITED STATES AIR FORCE

SUMMER RESEARCH PROGRAM -- 1992

SUMMER RESEARCH EXTENSION PROGRAM
FINAL REPORTS

VOLUME 5

AIR FORCE CIVIL ENGINEERING LABORATORY
ARNOLD ENGINEERING DEVELOPMENT CENTER
FRANK J. SEILER RESEARCH LABORATORY
WILFORD HALL MEDICAL CENTER

RESEARCH & DEVELOPMENT LABORATORIES
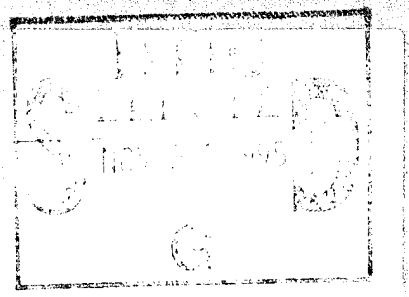
5800 UPLANDER WAY

CULVER CITY, CA 90230-6608

SUBMITTED TO:

LT. COL. CLAUDE CAVENDER
PROGRAM MANAGER

AIR FORCE OFFICE OF SCIENTIFIC RESEARCH

BOLLING AIR FORCE BASE

WASHINGTON, D.C.

MAY 1993

19951124 041

REPORT DOCUMENTATION PAGE

1. AGENCY USE ONLY (leave blank)	2. REPORT DATE 28 Dec 92	3. REPORT TYPE AND DATES COVERED Annual 1 Sep 91 – 31 Aug 92

4. TITLE AND SUBTITLE

1992 Summer Faculty Research Program (SFRP)
Volume 5 (SREP)

5. FUNDING NUMBERS

F49620-90-C-0076

6. AUTHOR(S)

Mr Gary Moore

7. PERFORMING ORGANIZATION NAME(S) AND ADDRESS(ES)

Research & Development Laboratoreis (RDL)
5800 Uplander Way
Culver City CA 90230-6600

8. PERFORMING ORGANIZATION REPORT NUMBER

AFOSR-TR-95

0726

9. SPONSORING/MONITORING AGENCY NAME(S) AND ADDRESS(ES)

AFOSR/NI
110 Duncan Ave., Suite B115
Bldg 410
Bolling AFB DC 20332-0001
Lt Col Claude Cavender

DTIC
SELECTED
NOV 2 8 1995
G

11. SUPPLEMENTARY NOTES

12a. DISTRIBUTION/AVAILABILITY STATEMENT

UNLIMITED

12b. DISTRIBUTION CODE

13. ABSTRACT (Maximum 200 words)

The purpose of this program is to develop the basis for cintinuing research of interest to the Air Force at the institution of the faculty member; to stiumlate continuing relations among faculty members and professional peers in the Air Force to enhance the research interests and capabilities of scientific and engineering educators; and to provide follow-on funding for research of particular promise that was started at an Air Force laboratory under the Summer Faculty Research Program.

During the summer of 1992 185 university faculty conducted research at Air Force laboratories for a period of 10 weeks. Each participant provided a report of their research, and these reports are consolidated into this annual report.

14. SUBJECT TERMS

15. NUMBER OF PAGES

16. PRICE CODE

17. SECURITY CLASSIFICATION OF REPORT	18. SECURITY CLASSIFICATION OF THIS PAGE	19. SECURITY CLASSIFICATION OF ABSTRACT	20. LIMITATION OF ABSTRACT
UNCLASSIFIED	UNCLASSIFIED	UNCLASSIFIED	UL

UNITED STATES AIR FORCE

SUMMER RESEARCH PROGRAM -- 1992

SUMMER RESEARCH EXTENSION PROGRAM FINAL REPORTS

VOLUME 5

AIR FORCE CIVIL ENGINEERING LABORATORY
ARNOLD ENGINEERING DEVELOPMENT CENTER
FRANK J. SEILER RESEARCH LABORATORY
WILFORD HALL MEDICAL CENTER

RESEARCH & DEVELOPMENT LABORATORIES

5800 Uplander Way

Culver City, CA 90230-6608

Program Director, RDL
Gary Moore

Program Manager, AFOSR
Lt. Col. Claude Cavender

Program Manager, RDL
Scott Licoscos

Program Administrator, RDL
Gwendolyn Smith

Submitted to:

AIR FORCE OFFICE OF SCIENTIFIC RESEARCH

Bolling Air Force Base

Washington, D.C.

May 1993

PREFACE

This volume is part of a five-volume set that summarizes the research of participants in the 1992 AFOSR Summer Research Extension Program (SREP). The current volume, Volume 5 of 5, presents the final reports of SREP participants at Air Force Civil Engineering Laboratory (AFCEL), Arnold Engineering Development Center (AEDC), Frank J. Seiler Resaerch Laboratory (FJSRL), and Wilford Hall Medical Center (WHMC).

Reports presented in this volume are arranged alphabetically by author and are numbered consecutively -- e.g., 1-1, 1-2, 1-3; 2-1, 2-2, 2-3, with each series of reports preceded by a 22-page management summary. Reports in the five-volume set are organized as follows:

VOLUME	TITLE
1A	Armstrong Laboratory (part one)
1B	Armstrong Laboratory (part two)
2	Phillips Laboratory
3	Rome Laboratory
4A	Wright Laboratory (part one)
4B	Wright Laboratory (part two)
5	Air Force Civil Engineering Laboratory, Arnold Engineering Development Center, Frank J. Seiler Research Laboratory, Wilford Hall Medical Center

Accesion For		
NTIS CRA&I	☑	
DTIC TAB	☐	
Unannounced	☐	
Justification		
By		
Dist.ibution /		
Availability Codes		
Dist	Avail and / or Special	
A-1		

1992 SUMMER RESEARCH EXTENSION PROGRAM FINAL REPORTS

Air Force Civil Engineering Laboratory
Arnold Engineering Development Center
Frank J. Seiler Research Laboratory
Wilford Hall Medical Center

1992 SUMMER RESEARCH EXTENSION PROGRAM (SREP) MANAGEMENT REPORT

1.0 BACKGROUND

Under the provisions of Air Force Office of Scientific Research (AFOSR) contract F49620-90-C-0076, September 1990, Research & Development Laboratories (RDL), an 8(a) contractor in Culver City, CA, manages AFOSR's Summer Research Program. This report is issued in partial fulfillment of that contract (CLIN 0003AC).

The name of this program was changed during this year's period of performance. For that reason, participants' cover sheets are captioned "Research Initiation Program" (RIP), while the covers of the comprehensive volumes are titled "Summer Research Extension Program" (SREP). The program's sponsor, the Air Force Office of Scientific Research (AFOSR), changed the name to differentiate this program from another which also bore its original name.

Apart from this name change, however, the program remained as it has been since its initiation as the Mini-Grant Program in 1983. The SREP is one of four programs AFOSR manages under the Summer Research Program. The Summer Faculty Research Program (SFRP) and the Graduate Student Research Program (GSRP) place college-level research associates in Air Force research laboratories around the United States for 8 to 12 weeks of research with Air Force scientists. The High School Apprenticeship Program (HSAP) is the fourth element of the Summer Research Program, allowing promising mathematics and science students to spend two months of their summer vacations at Air Force laboratories within commuting distance from their homes.

SFRP associates and exceptional GSRP associates are encouraged, at the end of their summer tours, to write proposals to extend their summer research during the following calendar year at their home institutions. AFOSR provides funds adequate to pay for 75 SREP subcontracts. In addition, AFOSR has traditionally provided further funding, when available, to pay for additional SREP proposals, including those submitted by associates from Historically Black Colleges and Universities (HBCUs) and Minority Institutions (MIs). Finally, laboratories may transfer internal funds to AFOSR to fund additional SREPs. Ultimately the laboratories inform RDL of their SREP choices, RDL gets AFOSR approval, and RDL forwards a subcontract to the institution where the SREP associate is employed. The subcontract (see Attachment 1 for a sample) cites the SREP associate as the principal investigator and requires submission of a report at the end of the subcontract period.

Institutions are encouraged to share costs of the SREP research, and many do so. The most common cost-sharing arrangement is reduction in the overhead, fringes, or administrative changes institutions would normally add on to the principal investigator's or research associate's labor. Some institutions also provide other support (e.g., computer run time, administrative assistance, facilities and equipment or research assistants) at reduced or no cost.

When RDL receives the signed subcontract, we fund the effort initially by providing 90% of the subcontract amount to the institution (normally $18,000 for a $20,000 SREP). When we receive the end-of-research report, we evaluate it administratively and send a copy to the laboratory for a technical evaluation. When the laboratory notifies us the SREP report is acceptable, we release the remaining funds to the institution.

2.0 THE 1992 SREP PROGRAM

SELECTION DATA: In the summer of 1991, 170 faculty members (SFRP associates) and 142 graduate students (GSRP associates) participated in the summer program. Of those, 147 SFRPs and 10 GSRPs submitted SREP proposals; 88 SFRP SREPs and 7 GSRP SREPs were selected for funding (total: 95).

	Summer 1991 Participants	Submitted SREP Proposals	SREPs Funded
SFRP	170	147	88
GSRP	142	10	7

The funding was provided as follows:

Contractual slots funded by AFOSR	75
Laboratory-funded	13
Additional funding from AFOSR	7
Total	95

Seven HBCU/MI associates from the 1991 summer program submitted SREP proposals; five were selected (one was lab-funded; four were funded by additional AFOSR funds).

By laboratory, the applications submitted and selected show in the following table:

	Applied	Selected
Air Force Civil Engineering Laboratory	6	4
Armstrong Laboratory	34	20
Arnold Engineering Development Center	12	2
Frank J. Seiler Research Laboratory	5	3
Phillips Laboratory	30	18
Rome Laboratory	16	11
Wilford Hall Medical Center	1	1
Wright Laboratory	53	36
TOTAL	157	95

Note: Phillips Laboratory funded 2 SREPs; Wright Laboratory funded 11; and AFOSR funded 7 beyond its contractual 75.

ADMINISTRATIVE EVALUATION: The administrative quality of the SREP associates' final reports was satisfactory. Most complied with the formatting and other instructions RDL provided to them. In the final days of December 1992 and in the first two months of 1993, several associates called and requested no-cost extensions of up to six months. After consultation with our AFOSR Contracting Officer's Representative, RDL approved the requests but asked that all such associates provide an interim report to be included in this volume. That caused an AFOSR-approved delay beyond the 1 April 1993 submission of this report. The subcontracts were funded by $1,893,616 of Air Force money. Institutions' cost sharing amounted to $948,686.

TECHNICAL EVALUATION: The form we used to gather data for technical evaluation and the technical evaluations of the SREP reports are provided as Attachment 2. This summary evaluation is shown by SREP number. The average rating range was from 3.1 to 5.0. The overall average for those evaluated was 4.6 out of 5.00. The three rating factors with the highest average scores were:

o   The USAF should continue to pursue the research in this RIP report.
o   The money spent on this RIP report was well worth it.
o   I'll be eager to be a focal point for summer and RIP associates in the future.

Thus it is clear that the laboratories place a high value on AFOSR's Summer Research Program: SFRP, GSRP, and SREP.

3.0 SUBCONTRACTS SUMMARY

Table 1 lists contractually required information on each SREP subcontract. The individual reports are published in volumes as follows:

Laboratory	Volume
Air Force Civil Engineering Laboratory	5
Armstrong Laboratory	1
Arnold Engineering Development Center	5
Frank J. Seiler Research Laboratory	5
Phillips Laboratory	2
Rome Laboratory	3
Wilford Hall Medical Center	5
Wright Laboratory	4

Researcher's name Institution Location	Highest Degree	Subcontract Number Department	Duration Sharing
Abbott, Ben A Vanderbilt University Nashville, TN 37235	MS	135 Dept of Electrical Engineering 19966.00	01/01/92-12/31/92 0.00
Acharya, Raj State University of New York, Buffalo Buffalo, NY 14260	PhD	151 Dept of Electrical & Comp Engrg 20000.00	01/01/92-12/31/92 0.00
Adams, Christopher M Oklahoma State University Stillwater, OK 74078	PhD	68 Dept of Chemistry 20000.00	01/01/92-12/31/92 0.00
Anderson, Richard A University of Missouri, Rolla Rolla, MO 65401	PhD	50 Dept of Physics 20000.00	01/01/92-12/31/92 5000.00
Arora, Vijay K Wilkes University Wilkes-Barre, PA 18766	PhD	3 Dept of Electrical & Comp Engrg 19996.00	10/01/91-09/30/92 36208.00
Ball, William P Duke University Durham, NC 27706	PhD	71 Dept of Civil & Environmental Eng 20000.00	01/01/92-12/31/92 26747.00
Battles, Frank P Massachusetts Maritime Academy Buzzard's Bay, MA 025321803	PhD	152 Dept of Basic Sciences 20000.00	01/01/92-12/31/92 22000.00
Bieniek, Ronald J University of Missouri, Rolla Rolla, MO 65401	PhD	147 Dept of Physics 19945.00	01/01/92-12/31/92 4000.00
Blystone, Robert V Trinity University San Antonio, TX 78212	PhD	127 Dept of Biology 20000.00	01/01/92-12/31/92 14783.00
Cha, Soyoung S University of Illinois, Chicago Chicago, IL 60680	PhD	011 Dept of Mechanical Engineering 20000.00	01/01/92-12/31/92 38 2.00
Chandra, D. V. Satish Kansas State University Manhattan, KS 66506	PhD	89 Dept of Electrical Engineering 20000.00	01/1 '92-10/17/92 11170
Chenette, Eugene R University of Florida Gainesville, FL 32611	PhD	106 Dept of Electrical Engineering 20000.00	01/01/ -12/31/92 C 0
Christensen, Douglas A University of Utah Salt Lake City, UT 84112	PhD	83 Dept of Electrical Engineering 19999.00	01/01/92-12/31/92 5000.00

Chubb, Gerald P Ohio State University Columbus, OH 43235	PhD 26 Dept of Aviation 20000.00	01/01/92-12/31/92 7600.00
Courter, Robert W Louisiana State University Baton Rouge, LA 70803	PhD 8 Dept of Mechanical Engineering 20000.00	10/01/91-09/30/92 445.00
Dey, Pradip P Hampton University Hampton, VA 23668	PhD 120 Computer Science Department 19921.00	01/01/92-12/31/92 0.00
Draut, Arthur W Embry Riddle Aeronautical University Prescott, AZ 86301	PhD 133 Computer Science Dept 19431.00	01/06/92-05/08/92 0.00
Dreisbach, Joseph University of Scranton Scranton, PA 185104626	PhD 108 Dept of Chemistry 20000.00	12/01/91-12/01/92 4000.00
Dror, Itiel Harvard University Cambridge, MA 02138	BS 76 Dept of Psychology 20000.00	01/01/92-12/31/92 0.00
Drost-Hansen, W. University of Miami Coral Gables, FL 33124	PhD 124 Dept of Chemistry 20000.00	12/01/91-12/01/92 12000.00
Dunleavy, Lawrence P University of South Florida Tampa, FL 33620	PhD 41 Dept of Electrical Engineering 20000.00	01/01/92-12/31/92 6463.00
Evans, Joseph B University of Kansas Lawrence, KS 66045	PhD 96 Dept of Electrical & Comp Engrg 20000.00	01/01/92-12/31/92 0.00
Flowers, George T Auburn University Auburn, AL 368495341	PhD 73 Dept of Mechanical Engineering 19986.00	01/01/92-12/30/92 12121.00
Gantenbein, Rex E University of Wyoming Laramie, WY 82071	PhD 22 Dept of Computer Science 20000.00	01/01/91-12/31/92 26643.00
Garcia, Ephrarim Vanderbilt University Nashville, TN 37235	PhD 32 Dept of Mechanical Engineering 20000.00	12/01/91-11/30/92 9659.00
German, Fred J Auburn University Auburn University, AL 36830	PhD 49 Dept of Electrical Engineering 20000.00	01/01/92-12/31/92 0.00
Gould, Richard D North Carolina State University Raleigh, NC 276957910	PhD 87 Dept of Mech and Aerospace Engrg 20000.00	01/01/92-12/31/92 14424.00
Gove, Randy L University of Alabama, Huntsville Huntsville, AL 35899	MS 122 Dept of Physics 20000.00	01/01/92-12/31/92 3469.00
Grabowski, Marek University of Colorado, Colorado Springs Colorado Springs, CO 809337150	PhD 92 Dept of Physics 19700.00	01/01/92-12/31/92 0.00

Gunaratne, Manjriker University of South Florida Tampa, FL 33620	PhD 90 Dept of Civil Engrg & Mechanics 19994.00	01/01/92-12/31/92 10062.00	
Hall, Ernest L University of Cincinnati Cincinnati, OH 452210072	PhD 134 Dept of Robotics Research 19975.00	01/01/92-12/31/92 0.00	
Hamilton, William L Salem State College Salem, MA 01970	PhD 47 Dept of Geography 20000.00	01/01/92-12/31/92 32000.00	
Hamilton, Kirk L Xavier University of Louisiana New Orleans, LA 70125	PhD 57 Dept of Biology 20000.00	01/01/92-12/31/92 16100.00	
Harris, Harold H University of Missouri, St.Louis St. Louis, MO 63121	PhD 94 Dept of Chemistry 19300.00	01/01/92-12/31/92 8600.00	
Hartung, George H University of Hawaii Honolulu, HI 96822	PhD 46 Dept of Physiology 20000.00	01/01/92-12/31/92 7530.00	
Hatfield, Steven L University of Kentucky Lexington, KY 40506	BS 23 Dept of Materials Science & Engrg 20000.00	01/01/92-12/31/92 28625.00	
Hedman, Paul O'Dell Brigham Young University Provo, UT 84602	PhD 17 Dept of Chemical Engineering 19999.00	01/01/92-12/31/92 6928.00	
Heister, Stephen D Purdue University West Lafayette, IN 47907	PhD 5 School of Aero & Astronautics 20000.00	01/01/92-12/31/92 4419.00	
Hess, David J University of Texas, Austin Austin, TX 78713	BA 149 Dept of Psychology 19914.00	01/01/92-12/31/92 8784.00	
Hoffman, R. W Case Western Reserve University Cleveland, OH 44106	PhD 99 Dept of Physics 19770.00	01/01/92-12/31/92 0.00	
Huerta, Manuel A University of Miami Coral Gables, FL 33124	PhD 62 Dept of Physics 20000.00	01/01/92-12/31/92 1207.00	
Hui, David University of New Orleans New Orleans, LA 70148	PhD 116 Dept of Mechanical Engineering 20000.00	01/01/92-12/31/92 .00	
Iyer, Ashok University of Nevada, Las Vegas Las Vegas, NV 89154	PhD 74 Dept of Electrical & Comp Engrg 20000.00	01/01/92-12/31/92 18549.00	
Khonsari, Michael M University of Pittsburgh Pittsburgh, PA 15260	PhD 53 Dept of Mechanical Engineering 20000.00	01/01/92-12/31/92 32956.00	
Kibert, Charles J University of Florida Gainesville, FL 32611	PhD 2 Dept of Fire Testing & Research 20000.00	01/01/92-12/31/92 6928.00	

Klarup, Douglas G University of Montana Missoula, MT 59812	PhD 84 Dept of Chemistry 20000.00	01/01/92-12/31/92 0.00
Koblasz, Arthur J Georgia Institute of Technology Atlanta, GA 30332	PhD 145 Dept of Civil Engineering 19956.00	01/01/92-09/30/92 0.00
Kornreich, Philipp Syracuse University Syracuse, NY 13244	PhD 35 Dept of Electrical & Comp Engrg 20000.00	10/01/91-09/30/92 0.00
Kuo, Spencer P Polytechnic University Farmingdale, NY 11735	PhD 59 Dept of Electrical Engineering 20000.00	01/01/92-12/31/92 9916.00
Langhoff, Peter W Indiana University Bloomington, IN 47402	PhD 115 Dept of Chemistry 20000.00	01/01/92-12/31/92 35407.00
Lee, Byung-Lip Pennsylvania State University University Park, PA 16802	PhD 93 Dept of Engrg Science & Mechanics 20000.00	01/01/92-12/31/92 8173.00
Leigh, Wallace B Alfred University Alfred, NY 14802	PhD 118 Dept of Electrical Engineering 19767.00	01/01/92-12/31/92 18770.00
Liddy, Elizabeth Syracuse University Syracuse, NY 132444100	PhD 104 Dept of Information Studies 20000.00	01/01/92-12/31/92 0.00
Liu, Cheng University of North Carolina, Charlotte Charlotte, NC 28270	PhD 6 Dept of Engineering Technology 20000.00	11/01/99-12/31/92 0.00
Main, Robert G California State University, Chico Chico, CA 959290504	PhD 28 Dept of Communication Design 20000.00	01/01/92-06/30/92 7672.00
Mains, Gilbert J Oklahoma State University Stillwater, OK 74078	PhD 52 Dept of Chemistry 19071.00	01/01/92-12/31/92 8746.00
Marathay, Arvind S University of Arizona Tucson, AZ 85721	PhD 51 Dept of Optical Sciences 20000.00	01/01/92-12/31/92 0.00
Martin, Charlesworth R Norfolk State University Norfolk, VA 23504	PhD 125 Dept of Physics & Engineering 20000.00	01/01/92-12/31/92 0.00
Mayes, Jessica L University of Kentucky Lexington, KY 405034203	BS 16 Dept of Material Science & Engrng 20000.00	01/01/92-12/31/92 28625.00
Mulligan, Benjamin E University of Georgia Athens, GA 30602	PhD 54 Dept of Psychology 19895.00	01/01/92-12/31/92 13677.00
Munday, Edgar G University of North Carolina, Charlotte Charlotte, NC 28223	PhD 38 Dept of Mechanical Engineering 20000.00	10/01/91-10/30/92 11638.00

Name / Institution	Degree	No.	Period	Dept	Amount 1	Amount 2
Nurre, Joseph H Ohio University Athens, OH 45701	PhD	56	01/01/92-12/31/92	Dept of Electrical & Comp Engrg	19842.00	15135.00
Orkwis, Paul D University of Cincinnati Cincinnati, OH 452210070	PhD	14	10/01/91-10/30/92	Dept of Engineering Mechanics	19966.00	23017.00
Patra, Amit L University of Puerto Rico Mayaquez, PR 00681	PhD	69	01/01/92-12/31/92	Dept of General Engineering	20000.00	2750.00
Peters II, Richard A Vanderbilt University Nashville, TN 37235	PhD	160	01/01/92-12/31/92	Dept of Electrical Engineering	20000.00	0.00
Pollack, Steven K University of Cincinnati Cincinnati, OH 452200012	PhD	31	01/01/92-12/31/92	Dept of Materials Sci & Engrg	20000.00	14877.00
Prescott, Glenn E University of Kansas Lawrence, KS 66045	PhD	72	01/01/92-12/31/92	Dept of Electrical Engineering	20000.00	8000.00
Price, James L University of Iowa Iowa City, IA 52242	PhD	48	01/01/92-12/30/92	Dept of Sociology	20000.00	8600.00
Qazi, Salahuddin SUNY, Utica Utica, NY 13504	PhD	129	01/01/92-12/31/92	Dept of Electrical Engineering	20000.00	25000.00
Rappaport, Carey M Northeastern University Boston, MA 02115	PhD	58	01/01/92-06/30/92	Dept of Electrical & Comp Engrng	19999.00	0.00
Rawson, Jenny L North Dakota State University Fargo, ND 58105	PhD	144	01/01/92-12/31/92	Dept of Electrical Engineering	19997.00	19826.00
Riccio, Gary E University of Illinois, Urbana Urbana, IL 61821	PhD	80	01/01/92-12/31/92	Dept of Human Perception	20000.00	0.00
Rotz, Christopher A Brigham Young University Provo, UT 84602	PhD	136	12/01/91-12/31/92	Dept of Manufacturing Engineering	20000.00	11814.00
Schwartz, Martin University of North Texas Denton, TX 762035068	PhD	55	01/01/92-12/31/92	Dept of Chemistry	20000.00	18918.00
Senseman, David M University of Texas, San Antonio San Antonio, TX 78285	PhD	77	12/01/91-11/30/92	Dept of Information	20000.00	19935.00
Sensiper, Martin University of Central Florida Orlando, FL 32816	BS	15	11/01/91-05/31/92	Dept of Electrical Engineering	20000.00	0.00
Shamma, Jeff S University of Texas, Austin Austin, TX 78713	PhD	70	01/01/92-12/31/92	Dept of Electrical Engineering	20000.00	0.00

Name / Institution	Degree	No.	Period	Amount	Dept	Amount 2
Shively, Jon H California State University, Northridge Northridge, CA 91330	PhD	140	01/01/92-12/31/92	20000.00	Dept of CIAM	14553.00
Singh, Sahjendra N University of Nevada, Las Vegas Las Vegas, NV 89014	PhD	79	01/01/92-12/31/92	20000.00	Dept of Electrical Engineering	20595.00
Smith, Gerald A Pennsylvania State University University Park, PA 16802	PhD	63	07/01/92-07/01/93	20000.00	Dept of Physics	0.00
Stephens, Benjamin R Clemson University Clemson, SC 29634	PhD	114	01/01/92-12/31/92	19988.00	Dept of Psycology	4250.00
Sudkamp, Thomas Wright State University Dayton, OH 45435	PhD	97	01/01/92-08/31/92	20000.00	Dept of Computer Science	18739.00
Sydor, Michael University of Minnesota, Duluth Duluth, MN 55804	PhD	11	01/01/92-12/31/92	20000.00	Dept of Physics	0.00
Tankin, Richard S Northwestern University Evanston, IL 60208	PhD	44	01/01/92-12/31/92	20000.00	Dept of Mechanical Engineering	29103.00
Taylor, Michael D University of Central Florida Orlando, FL 32816	PhD	141	05/01/92-07/31/92	20000.00	Dept of Mathematics	1587.00
Teegarden, Kenneth J University of Rochester Rochester, NY 14627	PhD	98	01/01/92-12/31/92	20250.00	Dept of Optics	60600.00
Tew, Jeffrey D Virginia Polytech Instit and State Univ Blacksburg, VA 24061	PhD	137	03/01/92-09/30/92	17008.00	Dept of Industrial Engineering	4564.00
Tipping, Richard H University of Alabama Tuscaloosa, AL 35487	PhD	81	01/01/92-05/31/92	20000.00	Dept of Physics & Astronomy	15000.00
Tripathi, Ram C University of Texas, San Antonio San Antonio, TX 78249	PhD	105	01/01/92-12/31/92	20000.00	Dept of Mathematics	2274.00
Wells, Fred V Idaho State University Pocatello, ID 83209	PhD	155	01/01/92-12/31/92	20000.00	Dept of Chemistry	8000.00
Whitefield, Phillip D University of Missouri, Rolla Rolla, MO 65401	PhD	25	01/01/92-12/31/92	19991.00	Dept of Chemistry	25448.00
Wolfenstine, Jeffrey B University California, Irvine Irvine, CA 92717	PhD	18	01/01/92-12/31/92	20000.00	Dept of Mechanical Engineering	11485.00
Wolper, James S Idaho State University Pocatello, ID 83209	PhD	138	01/15/92-09/30/92	20000.00	Dept of Mathematics	4828.00

Zavodney, Lawrence D
Ohio State University
Columbus, OH 43210

PhD   148   01/01/92-12/31/92
Dept of Engineering Mechanics
20000.00   0.00

Zimmerman, Wayne J
Texas Women University
Denton, TX 76204

PhD   111   01/01/92-12/31/92
Dept of Mathematics
19990.00   8900.00

ATTACHMENT 1:

SAMPLE SREP SUBCONTRACT

AIR FORCE OFFICE OF SCIENTIFIC RESEARCH
1993 SUMMER RESEARCH EXTENSION PROGRAM SUBCONTRACT 93-36

BETWEEN

Research & Development Laboratories
5800 Uplander Way
Culver City, CA 90230-6608

AND

University of Delaware
Sponsored Programs Admin.
Newark, DE 19716

REFERENCE: Summer Research Extension Program Proposal 93-36
Start Date: 01/01/93   End Date: 12/31/93
Proposal amount: $20000.00

(1) PRINCIPAL INVESTIGATOR: Dr. Ian W. Hall
Materials Science
University of Delaware
Newark, DE 19716

(2) UNITED STATES AFOSR CONTRACT NUMBER: F49620-90-C-09076

(3) CATALOG OF FEDERAL DOMESTIC ASSISTANCE NUMBER (CFDA): 12.800
PROJECT TITLE: AIR FORCE DEFENSE RESEARCH SOURCES PROGRAM

(4) ATTACHMENTS 1 AND 2: SREP REPORT INSTRUCTIONS

*** SIGN SREP SUBCONTRACT AND RETURN TO RDL ***

1. <u>BACKGROUND:</u> Research & Development Laboratories (RDL) is under contract (F49620-90-C-0076) to the United States Air Force to administer the Summer Research Programs (SRP), sponsored by the Air Force Office of Scientific Research (AFOSR), Bolling Air Force Base, D.C. Under the SRP, a selected number of college faculty members and graduate students spend part of the summer conducting research in Air Force laboratories. After completion of the summer tour participants may submit, through their home institutions, proposals for follow-on research. The follow-on research is known as the Research Initiation Program (RIP). Approximately 75 RIP proposals annually will be selected by the Air Force for funding of up to $20,000; shared funding by the academic institution is encouraged. RIP efforts selected for funding are administered by RDL through subcontracts with the institutions. This subcontract represents such an agreement between RDL and the institution designated in Section 5 below.

2. <u>RDL PAYMENTS:</u> RDL will provide the following payments to RIP institutions:

- 90 percent of the negotiated RIP dollar amount at the start of the RIP Research period.
- the remainder of the funds within 30 days after receipt at RDL of the acceptable written final report for the RIP research.

3. <u>INSTITUTION'S RESPONSIBILITIES:</u> As a subcontractor to RDL, the institution designated on the title page will:

   a. Assure that the research performed and the resources utilized adhere to those defined in the RIP proposal.

   b. Provide the level and amounts of institutional support specified in the RIP proposal.

   c. Notify RDL as soon as possible, but not later than 30 days, of any changes in 3a or 3b above, or any change to the assignment or amount of participation of the Principal Investigator designated on the title page.

   d. Assure that the research is completed and the final report is delivered to RDL not later than twelve months from the effective date of this subcontract. The effective date of the subcontract is one week after the date that the institution's contracting representative signs this subcontract, but no later than January 15, 1992.

   e. Assure that the final report is submitted in the format shown in Attachment 1.

2

f.   Agree that any release of information relating to this subcontract (news releases, articles, manuscripts, brochures, advertisements, still and motion pictures, speeches, trade association meetings, symposia, etc.) will include a statement that the project or effort depicted was or is sponsored by: Air Force Office of Scientific Research, Bolling AFB, D.C.

g.   Notify RDL of inventions or patents claimed as the result of this research in a format specified in Attachment 1.

h.   RDL is required by the prime contract to flow down patent rights and technical data requirements in this subcontract. Attachment 2 to this subcontract contains a list of contract clauses incorporated by reference in the prime contract.

4.   All notices to RDL shall be addressed to:

RDL Summer Research Program Office
5800 Uplander Way
Culver City, CA 90230-6608

5.   By their signatures below, the parties agree to the provisions of this subcontract.

Abe S. Sopher
RDL Contracts Manager

Signature of Institution Contracting Official

Typed/Printed Name

Date

Title

Institution

Date/Phone

3

Attachment 1
Final Report Format

1.   All RIP Principal Investigators will submit a final report of the research conducted.

2.   One copy of the report is due to RDL no later than twelve months after the effective date of the RIP subcontract. At the same time, submit one copy to the Air Force laboratory focal point.

3.   The title page should contain the title of the research, the Principal Investigator and or other co-investigators, the month and year of issue, the university with department and address, and acknowledgement of sponsorship by AFOSR (see clause 3f of this subcontract).

4.   For text, use a font that is 12 characters per inch (elite) and as close to letter quality as possible. Start with the title in all caps one and one-half inches from the top of the first page; if the title requires two or more lines, single space it. Double space below the title, and then center and type the researcher's title and name. Then space twice and begin the double-spaced text.

Use a one-and-one-half-inch left margin and a one-inch right margin for the body of the text. Center page numbers at the foot of each page, one inch from the bottom. Each page should have a one-inch margin at the top. The format should be that of a standard research paper: it should begin with a one-paragraph abstract (on its own page) summarizing your work and should be followed by an introduction, a discussion of the problem, a results section, and a conclusion. Since multiple copies of your report may be required, assure that all pages can be readily copied to a black-and-white 8 1/2" by 11" page. (No colors, such as blue or green, that don't photocopy well, and no foldouts, please.)

5.   The report must be accompanied by a separate statement on whether or not any inventions or patents have resulted from this research. If yes, use a DD Form 882 (supplied by RDL on request) to indicate the patent filing date, serial number, title, and a copy of the patent application, and patent number and issue date for any subject invention in any country in which the subcontractor has applied for patents.

4

Contract Clauses

This contract incorporates by reference the following clauses of the Federal Acquisition Regulations (FAR), with the same force and effect as if they were given in full text. Upon request, the Contracting Officer or RDL will make their full text available (FAR 52.252-2).

FAR CLAUSES	TITLE AND DATE
52.202-1	DEFINITIONS (APR 1984)
52.203-1	OFFICIALS NOT TO BENEFIT (APR 1984)
52.203-3	GRATUITIES (APR 1984)
52.203-5	COVENANT AGAINST CONTINGENT FEES (APR 1984)
52.304-6	RESTRICTIONS ON SUBCONTRACTOR SALES TO THE GOVERNMENT (JUL 1985)
52.203-7	ANTI-KICKBACK PROCEDURES (OCT 1988)
52.203-12	LIMITATION ON PAYMENTS TO INFLUENCE CERTAIN FEDERAL TRANSACTIONS (JAN 1990)
52.204-2	SECURITY REQUIREMENTS (APR 1984)
52.209-6	PROTECTING THE GOVERNMENT'S INTEREST WHEN SUBCONTRACTING WITH CONTRACTORS DEBARRED, SUSPENDED, OR PROPOSED FOR DEBARMENT (MAY 1989)
52.212-8	DEFENSE PRIORITY AND ALLOCATION REQUIREMENTS (MAY 1986)
52.215-1	EXAMINATION OF RECORDS BY COMPTROLLER GENERAL (APR 1984)
52.215-2	AUDIT - NEGOTIATION (DEC 1989)
52.222-26	EQUAL OPPORTUNITY (APR 1984)
52.222-28	EQUAL OPPORTUNITY PREAWARD CLEARANCE OF BCON ACTS (APR 1984)
52.222-35	AFFIRMATIVE ACTION FOR SPECIAL DISABLED AND VIETN M ERA VETERANS (APR 1984)
52.222-36	AFFIRMATIVE ACTION FOR HANDICAPPED WORKERS (APR 1984)

52.222-37	EMPLOYMENT REPORTS ON SPECIAL DISABLED VETERANS AND VETERANS OF THE VIETNAM ERA (JAN 1988)
52.223-2	CLEAN AIR AND WATER (APR 1984)
52.232-6	DRUG-FREE WORKPLACE (MAR 1989)
52.224-1	PRIVACY ACT NOTIFICATION (APR 1984)
52.224-2	PRIVACY ACT (APR 1984)
52.225-13	RESTRICTIONS ON CONTRACTING WITH SANCTIONED PERSONS (MAY 1989)
52.227-1	AUTHORIZATION AND CONSENT (APR 1984)
52.227-2	NOTICE AND ASSISTANCE REGARDING PATENT AND COPYRIGHT INFRINGEMENT (APR 1984)
52.227-10	FILING OF PATENT APPLICATIONS - CLASSIFIED SUBJECT MATTER (APR 1984)
52.227-11	PATENT RIGHTS - RETENTION BY THE CONTRACTOR (SHORT FORM) (JUN 1989)
52.228-6	INSURANCE - IMMUNITY FROM TORT LIABILITY (APR 1984)
52.228-7	INSURANCE - LIABILITY TO THIRD PERSONS (APR 1984)
52.230-5	DISCLOSURE AND CONSISTENCY OF COST ACCOUNTING PRACTICES (SEP 1987)
52.232-23	ASSIGNMENT OF CLAIMS (JAN 1986)
52.237-3	CONTINUITY OF SERVICES (APR 1984)
52.246-25	LIMITATION OF LIABILITY - SERVICES (APR 1984)
52.249-6	TERMINATION (COST-REIMBURSEMENT) (MAY 1986)
52.249-14	EXCUSABLE DELAYS (APR 1984)
52.251-1	GOVERNMENT SUPPLY SOURCES (APR 1984)

DoD FAR CLAUSES	TITLE AND DATE
252.203-7001	SPECIAL PROHIBITION ON EMPLOYMENT (MAR 1989)
252.203-7002	STATUTORY COMPENSATION PROHIBITIONS AND REPORTING REQUIREMENTS RELATING TO CERTAIN FORMER DEPARTMENT OF DEFENSE (DoD) EMPLOYEES (APR 1988)
252.223-7500	DRUG-FREE WORK FORCE (SEP 1988)
252.225-7001	BUY AMERICAN ACT AND BALANCE OF PAYMENTS PROGRAM (APR 1985)
252-225-7023	RESTRICTION ON ACQUISITION OF FOREIGN MACHINE TOOLS (JAN 1989)
252.227-7013	RIGHTS IN TECHNICAL DATA AND COMPUTER SOFTWARE (OCT 1988)
252.227-7018	RESTRICTIVE MARKINGS ON TECHNICAL DATA (OCT 1988)
252.227-7029	IDENTIFICATION OF TECHNICAL DATA (APR 1988)
252.227-7034	PATENTS - SUBCONTRACTS (APR 1984)
252.227-7037	VALIDATION OF RESTRICTIVE MARKINGS ON TECHNICAL DATA (APR 1988)
252.231-7000	SUPPLEMENTAL COST PRINCIPLES (APR 1984)
252.231-7001	PENALTIES FOR UNALLOWABLE COSTS (APR 1988)
252.231-7003	CERTIFICATION OF INDIRECT COSTS (APR 1986)
252.251-7000	ORDERING FROM GOVERNMENT SUPPLY SOURCES (APR 1984)
252.271-7001	RECOVERY OF NONRECURRING COSTS ON COMMERCIAL SALES OF DEFENSE PRODUCTS AND TECHNOLOGY AND OF ROYALTY FEES FOR USE OF DoD TECHNICAL DATA (FEB 1989)

7 November 1991

AFOSR/PKO
Bldg. 410, Room C-124
Bolling AFB, DC 20332-6448

Attn: Ms. Kathleen Wetherell

Dear Ms. Wetherell:

Enclosed for your approval is the model subcontract for the Research Initiation Program under the Summer Research Programs (Contract F9620-90-C-0076). The blanks will be filled by merging information from our dBase IV database.

Sincerely,

Abe S. Sopher
Contracts Manager

cc: AFOSR/NI (Lt. Col. Cavendar)

ATTACHMENT 2:

SAMPLE TECHNICAL EVALUATION FORM AND TECHNICAL

EVALUATION SUMMARY

1992 RESEARCH INITIATION PROGRAM TECHNICAL EVALUATION

RIP NO: 92-2
RIP ASSOCIATE: Dr. Charles Kibert

Provided are several evaluation statements followed by ratings of (1) through (5). A rating of (1) is the lowest and (5) is the highest. Circle the rating level number you best feel rates the statement. Document additional comments on the back of this evaluation form.

Mail or fax the completed form to:

RDL
Attn: 1992 RIP TECH EVALS
5800 Uplander Way
Culver City, CA 90230-6608
(Fax: 310 216-5940)

1. This RIP report has a high level of technical merit   1 2 3 4 5

2. The RIP program is important to accomplishing the lab's   1 2 3 4 5
    mission

3. This RIP report accomplished what the associate's proposal   1 2 3 4 5
    promised

4. This RIP report addresses area(s) important to the USAF   1 2 3 4 5

5. The USAF should continue to pursue the research in this   1 2 3 4 5
    RIP report

6. The USAF should maintain research relationships with this   1 2 3 4 5
    RIP associate

7. The money spent on this RIP effort was well worth it   1 2 3 4 5

8. This RIP report is well organized and well written   1 2 3 4 5

9. I'll be eager to be a focal point for summer and RIP   1 2 3 4 5
    associates in the future

10. The one-year period for complete RIP research is about   1 2 3 4 5
    right

****USE THE BACK OF THIS FORM FOR ADDITIONAL COMMENTS****

LAB FOCAL POINT'S NAME (PRINT): _____

OFFICE SYMBOL: _____   PHONE: _____

Technical Evaluation Questionnaire Rating Factors

Subcontract no.	1	2	3	4	5	6	7	8	9	10	Average
135	5	4	5	4	4	4	4	4	5	5	4.4
50	4	4	5	4	4	4	4	3	5	5	4.2
3	4	3	3	3	3	3	3	3	3	4	3.2
71	4	4	4	4	3	5	5	4	5	5	4.3
152	3	4	3	4	4	3	4	3	4	5	3.7
147	5	5	5	5	5	5	5	5	5	4	4.9
011	4	4	5	4	5	5	5	4	5	4	4.5
106	5	5	4	5	5	5	5	5	5	5	4.9
83	5	4	5	5	5	5	5	5	5	4	4.8
26	5	4	4	5	5	5	5	5	4	4	4.6
8	5	3	4	4	5	5	5	3	5	5	4.4
120	1	5	2	4	5	3	2	1	4	4	3.1
133	3	2	4	5	5	4	3	4	3	5	3.8
108	5	4	4	5	5	5	5	5	5	5	4.8
76	5	5	5	5	5	5	5	5	5	3	4.8
122	5	5	5	5	5	4	5	5	5	5	4.9
92	4	5	5	5	5	5	5	5	5	5	4.9
47	5	5	5	5	5	4	4	5	5	5	4.8
57	4	4	4	5	5	4	4	4	4	2	4.0
17	5	5	5	5	5	5	5	5	5	5	5.0
5	5	3	4	4	4	5	5	5	4	3	4.2
62	5	4	5	4	4	5	5	5	5	5	4.7
74	4	3	4	4	4	4	5	4	4	5	4.1
53	4	3	4	4	3	4	3	5	3	4	3.7
84	5	4	4	5	5	5	5	5	5	4	4.7
145	4	4	5	4	5	5	5	5	5	4	4.6
35	5	5	5	5	5	5	5	5	5	5	5.0

Technical Evaluation Questionnaire Rating Factors

Subcontract no.	1	2	3	4	5	6	7	8	9	10	Average
59	5	4	5	5	5	5	5	5	5	5	4.9
115	5	5	5	5	5	5	5	5	5	5	5.0
118	4	5	5	5	5	5	5	4	5	4	4.7
104	5	3	4	3	5	4	5	5	4	5	4.3
6	3	5	5	5	3	5	5	4	5	3	4.3
28	5	4	5	5	5	4	5	4	4	4	4.5
51	5	5	4	5	5	5	5	5	5	4	4.8
16	5	5	5	5	5	4	5	5	5	5	4.9
54	5	4	5	4	5	4	5	5	5	5	4.7
56	3	3	5	4	5	3	4	5	5	5	4.2
69	4	5	4	5	5	4	5	5	5	5	4.7
72	5	5	5	5	5	5	5	5	5	5	5.0
129	5	5	5	5	5	5	5	5	5	5	5.0
58	3	4	5	4	3	4	5	4	4	4	4.0
144	5	5	5	5	5	5	5	5	5	5	5.0
80	5	5	5	5	5	5	5	5	4	4	4.8
136	5	4	5	5	5	5	5	5	5	4	4.8
55	5	5	5	5	5	5	5	5	5	4	4.9
77	5	4	3	4	3	4	4	4	5	4	4.0
15	5	4	5	5	5	5	5	4	5	5	4.8
70	5	4	4	5	5	5	5	5	5	4	4.7
140	5	5	5	5	5	5	5	5	5	5	5.0
79	4	3	5	4	5	4	5	5	4	5	4.4
63	5	5	5	5	5	5	5	5	5	5	5.0
97	5	4	4	5	5	5	5	5	5	5	4.8
11	5	4	4	4	4	5	4	4	5	3	4.2
44	5	5	5	5	5	5	5	5	5	5	5.0
141	5	4	5	4	4	5	5	5	5	4	4.6
98	5	5	5	5	5	5	5	5	5	5	5.0

Technical Evaluation Questionnaire Rating Factors

Subcontract no.	1	2	3	4	5	6	7	8	9	10	Average
81	4	4	3	4	4	4	4	5	5	4	4.1
105	5	5	5	5	5	5	5	5	5	5	5.0
25	4	4	4	5	5	5	4	5	4	2	4.2
18	5	3	5	5	5	3	5	5	5	4	4.5
138	5	4.	5	5	5	5	5	3	5	3	4.5
111	5	5	5	5	5	5	5	5	5	5	5.0
Avg by factor:	4.5	4.2	4.5	4.6	4.7	4.6	4.7	4.6	4.7	4.4	4.6

AIR FORCE CIVIL ENGINEERING LABORATORY

ESTIMATION OF CONTAMINANT TRANSPORT PARAMETERS FROM LABORATORY STUDIES: BATCH AND COLUMN TECHNIQUES

William P. Ball, Assistant Professor
and
Dirk F. Young, Graduate Student
Department of Geography and Environmental Engineering

The Johns Hopkins University
Baltimore, MD 21218

December, 1992

Estimation of Contaminant Transport Parameters from
Laboratory Studies: Batch and Column Techniques

William P. Ball, Assistant Professor, and Dirk F. Young, Graduate Student
Department of Geography and Environmental Engineering,
The Johns Hopkins University, Baltimore, MD 21218

Abstract

This research emphasizes improvement in laboratory methods and data interpretation techniques, as applied to the estimation of subsurface transport parameters related to organic chemical sorption and desorption by aquifer solids. In particular, we have refined a laboratory column technique for the study of sorption equilibrium and rate for volatile organic chemicals and have explored the accuracy of parameter estimation with regard to (1) agreement of column results with predictions based on *a priori* estimation of parameters using accurate (but arduous) batch methods, and (2) the "inverse problem" of estimating transport parameters directly from column experiments.

Part 1 of the report deals with predicting the breakthrough of tetrachloroethene through packed columns of aquifer material. Predictions were based on measured physical parameters of the system (*e.g.*, particle size, intra- and inter-particle porosity, column velocity and length) as well as sorption parameters determined by extensive batch study, both from prior research and from additional equilibrium batch study as part of this project. The transport model used for the prediction accounted for rate-limited sorption by an intraparticle diffusion mechanism. Model predictions showed excellent agreement with column breakthrough data, and supported a hypothesis of intraparticle pore diffusion as the causative mechanism of slow sorption in this material.

Part 2 of the report describes the estimation of transport parameters using only the column breakthrough data. The methods used to determine these parameters included least squares analysis applied to the intraparticle pore diffusion model as well as a model that approximates diffusion with a first-order mass transfer coefficient. In addition, we explored the applicability and potential errors asscociated with using the method of moments to determine the retardation factor. The various methods of parameter estimation produced a wide range of values and offered valuable insight into the column conditions and data interpretation techniques which are most appropriate for accurate parameter estimation.

Estimation of Contaminant Transport Parameters from
Laboratory Studies: Batch and Column Techniques

William P. Ball, Assistant Professor, and Dirk F. Young, Graduate Student
Department of Geography and Environmental Engineering,
The Johns Hopkins University, Baltimore, MD 21218

INTRODUCTION

This research aimed to develop and evaluate laboratory-based methods for the estimation of sorption equilibrium and rate parameters important to the understanding and simulation of organic chemical transport in the subsurface. Over the course of this project, we have established a column capability in our laboratory that supplements a highly sensitive and precise batch methodology for estimating sorption equilibrium and rate parameters, and we have examined, in some detail, the relative accuracy and applicability of the column technique. In particular, we have conducted a detailed evaluation of (1) the extent to which batch-derived parameters can be used to predict behavior in a flowing column and (2) the extent to which the column experiments alone can be used to estimate transport parameters. The latter evaluation included analysis of parameter estimation by two methods: (1) least-squares fitting of numerical transport models to experimental data, and (2) evaluation of data in terms of temporal moments of the breakthrough curve, including evaluation of the effect of experimental conditions, duration and sensitivity (detection level) on the accuracy of the results.

For the purposes of this report, our discussion has been divided into two parts. Part 1 deals with predicting the breakthrough of tetrachloroethene through packed columns of aquifer material, and Part 2 deals with the inverse problem of estimating simulation parameters from column data alone. The accurate prediction of solute transport through groundwater is an important goal of contaminant hydrologists and can greatly benefit in locating and cleaning up contaminated areas. The success of a prediction, however, can only be evaluated by observations of contaminant transport. In Part 1 of this paper, we test our conceptual understanding of a model system through a priori simulation of column transport. In Part 2, we assume good conceptual understanding and explore issues of accuracy in parameter estimation between different laboratory methods.

PART 1: PREDICTIONS

BACKGROUND

Investigators modeling contaminant transport through porous media often assume that equilibrium exists between the sorbed and aqueous phases. Recent work, however, has indicated that

sorption and desorption processes in groundwater can be quite slow, and this may have important implications on the fate and transport of synthetic organic chemicals in the subsurface (Valocchi, 1985; Goltz and Roberts, 1986; Nkedi-Kizza et al., 1989). Intrasorbent diffusion has often been cited as the causative mechanism for slow sorption and desorption at the particle scale, either as diffusion through intraparticle pores (e.g., Ball and Roberts, 1991b; Wu and Gshwend, 1986) or slow diffusion through organic matter (e.g., Bouchard et al. 1988; Brusseau and Rao, 1989; Pignatello, 1989).

In the present work, we further evaluate a previously proposed intraparticle diffusion model (Ball and Roberts, 1991b) using batch and column experiments with a sorbate and a sorbent which were the subject of extensive prior batch study and sorbent characterization (Ball, 1989; Ball and Roberts, 1991a,b; Ball et al., 1990). The goal of the current work was to re-evaluate the batch-estimated sorption capacity of the same sorbate/sorbent systems studied by Ball and Roberts and to test the application of the previously applied diffusion model to column transport.

As discussed subsequently, the sorbent/solute system exhibited a nonlinear sorption isotherm, although isotherms were observed to be reasonably linear in the concentration range most relevant to the column work. Ball and Roberts also assumed isotherm linearity in their original estimates of pore diffusion coefficients with this same sorbate/sorbent system (Ball, 1989; Ball and Roberts, 1991b). However, these two sets of experiments (the present work and that of Ball, 1989) were conducted at sufficiently different final aqueous concentration that they gave notably different sorption capacities when interpreted with a linear model. Nonetheless, if retarded diffusion through intraparticle pores causes the rate limitation, then the same pore diffusion coefficient should characterize uptake irrespective of concentration. In this way, the transport experiment reported here provided an opportunity to further test the applicability of the pore-diffusion mechanism for this material.

Intraparticle Diffusion. Diffusion-limited sorption at the grain scale may be conceptualized as either diffusion through fluid-filled intragranular pores accompanied by intraparticle sorption and partitioning, sometimes referred to as retarded pore diffusion (Wu and Gshwend, 1986; Ball and Roberts 1991b,c) or simply as intrasorbent diffusion (Miller and Weber, 1986; Brusseau et al., 1991; Ball and Roberts, 1991b,c; Miller and Pedit, 1992). Evidence for decreasing rates of uptake with increasing sorption has been shown by many researchers (Karickhoff, 1984; Brusseau and Rao, 1989; Ball and Roberts, 1991b) and suggests some form of internal retardation mechanism. Ball and Roberts (1991b) have suggested that a retarded pore-diffusion model may be applicable to the uptake of halogenated organic chemicals by sand-sized aquifer solids from a Borden, Ontario field site (the material used in the current study).

The simplest intraparticle-diffusion model represents sorbent grains as uniformly porous spheres with homogeneously distributed sorption capacity. Such a model has been described in great

detail elsewhere (e.g. Wu and Gshwend, 1986; Ball and Roberts 1991b,c), and is briefly summarized here.

By combining Fick's law with a mass balance over a volume element of the sorbent, intrasorbent diffusion can be represented as follows:

$$\epsilon_i \frac{\partial C_{im}}{\partial t} + \rho_a \frac{\partial q}{\partial t} = \epsilon_i D_p \nabla^2 (C) + \rho_a D_s \nabla^2 (q) \tag{1}$$

where C_{im} = intrasorbent (or immobile) fluid concentration [mass of solute in intraparticle water at time t and at radius r / volume of intraparticle water],

q = solid-phase concentration [mass solute sorbed to intraparticle solid at time t and radius r/ mass sorbent],

ϵ_i = intraparticle porosity [intraparticle pore volume/total particle volume],

ρ_a = apparent density [mass of particle / volume of particle],

D_p = effective pore diffusion coefficient [L^2/T],

D_s = effective sorbed-phase diffusion [L^2/T],

∇^2 = the Laplacian operator.

Additionally, if sorption is reversible and is described by a linear isotherm, then

$$q = K_d C_{im} \tag{2}$$

where K_d = the equilibrium linear partitioning constant [M/L^3].

Under these conditions, an apparent diffusion coefficient can be defined as follows:

$$\frac{\partial C_{im}}{\partial t} = D_a \nabla^2 C_{im} \tag{3}$$

and

$$D_a = \frac{\epsilon_i D_p}{(\epsilon_i + \rho_a K_d)} + \frac{\rho_a K_d D_s}{(\epsilon_i + \rho_a K_d)}, \tag{4}$$

where D_a = the apparent diffusion coefficient [L^2/T].

1-5

If the sorbent grains are assumed to be spherical, then Equation 3 can be rewritten as

$$\frac{\partial C_{im}}{\partial t} = \frac{D_a}{r^2} \frac{\partial}{\partial r}\left[r^2 \frac{\partial C_{im}}{\partial r}\right],\tag{5}$$

where r = the radial coordinate within the sphere [L].

A further simplification can be made if diffusion of the sorbed species is not believed to occur. For this case, the solute diffuses only through the fluid-filled pores, and Equation 4 simplifies to

$$D_a = \frac{D_p}{(1+\rho_a K_d/\epsilon_i)}\tag{6}$$

If this assumption is correct (that diffusion is driven only by an aqueous-phase concentration gradient), then from Equation 6, it is apparent that D_a is a function of the sorption capacity (K_d). In other words, a highly sorbing solute should require longer to reach equilibrium than a solute that sorbs less, and this would be reflected in its lower D_a value. Since D_p is only a function of bulk molecular diffusivity and pore geometry, D_p should be constant for a given solute and sorbent. By the above reasoning, the same pore diffusion coefficient that characterizes a system at low concentration would be expected to characterize the system at high concentrations as well, as long as the effect of concentration on extent of partitioning is considered. Under conditions of a nonlinear isotherm, proper modeling over the full concentration range requires consideration of the complete (nonlinear) isotherm. For example, for a Freundlich isotherm,

$$q = K_f C^{1/n}\tag{7}$$

where K_f = Freundlich coefficient [L^3/M]

$1/n$ = Freundlich exponent [-].

In Equations (4) and (6), the K_d term arises as the partial derivative of q with respect to C, due to application of the chain rule to the $\partial q/\partial t$ term in Equation (1). With a Freundlich isotherm, we can see that the effective K_d in Equations (4) and (6) is a function of concentration; i.e.,

$$K_d = \frac{\partial q}{\partial C} = \frac{1}{n} K_f C^{\frac{1}{n}-1} \tag{8}$$

Alternatively, if we estimate K_d simply as the ratio of q to C at any given concentration, then we have

$$K_d = K_f C^{\frac{1}{n}-1} \tag{9}$$

which differs from Equation (8) by a factor of $1/n$. If the isotherm is observed to be very close to linear over the vast majority of the concentration range covered by the experiment, application of the simple averaged K_d ($=q/C$) may be an appropriate means of estimating $\partial q/\partial C$. For the sake of simplicity, and because the Freundlich isotherm is mechanistically no more justifiable than the assumed linear relationship, the latter approach is taken here. We emphasize that the application of this approach hinges on approximate linearity over a broad range of concentrations important to much of the column experiment. As noted subsequently, we expect (and observed) deviations of this model from the column results at very low concentrations where the effective distribution coefficient is much higher.

Transport Modeling. For an intrasorbent diffusion model, such as that represented by Equations 1 through 6, to be useful in interpreting or predicting solute movement, it must be coupled to a transport model. Many of the rate-limited-sorption transport models which are currently applied to solute movement through groundwater or laboratory columns are based on the simplifying assumption that the porous medium may be divided into mobile and immobile regions. For the simple case of intraparticle diffusion into single aggregated particles or grains, the immobile region is defined as the intraparticle pore volume and its associated sorption capacity, while the mobile region is defined as the interparticle pore volume and its associated sorption capacity. With the assumptions in this model, advection and hydrodynamic dispersion can occur only in the mobile region, and solute can enter the immobile region only by diffusion, as described above. Conceptually, sorption capacity associated with the mobile region implies that some fraction of the sorbent is subject to instantaneous sorption and desorption. In reality, this fraction need only be fast relative to advective transport and might be characterized as being the result of either (a) sorption sites located on the exterior of the particle or (b) sorption which is associated with very small particles and thus subject to fast rates of diffusive uptake. In one-dimensional form, the two-region transport model can be expressed as follows (Parker and Van Genuchten, 1984):

$$(\theta_m + f\rho_b K_d)\frac{\partial C_m}{\partial t} + [\theta_{im} + (1-f)\rho_b K_d]\frac{\partial \overline{C_{im}}}{\partial t} = \theta_m D_H \frac{\partial^2 C_m}{\partial x^2} - v_m \theta_m \frac{\partial C_m}{\partial x} \qquad (10)$$

where $\overline{C_{im}}$ = average concentration in the mobile region [M/L³],

θ_m = mobile region porosity [—]; Note: $\theta = \theta_m + \theta_{im}$

θ_{im} = immobile region porosity [—],

θ = total porosity [—],

f = fraction of sorption that is instantaneous [—],

ρ_b = bulk density [M/L³],

v_m = mobile region velocity [L/T].

In Equation 10, the term, $\partial \overline{C_{im}}/\partial T$, represents the diffusion-limited uptake into the immobile zone. The spherical diffusion model can be coupled to the two-region transport model through this term as follows (Nkedi Kizza et al., 1982):

$$\frac{\partial C_{im}}{\partial t} = \frac{D_p}{1 + (1-f)\rho_b K_d/\theta_{im}}\left[\frac{1}{r^2}\frac{\partial}{\partial r}\left(r^2 \frac{\partial C_{im}}{\partial r}\right)\right] \qquad (11)$$

The average concentration for use in Equation 10 is found by integrating the concentration distribution over the sphere radius,

$$\overline{C_{im}} = 3\int_0^a C_{im} r^2 dr \qquad (12)$$

where a = the sphere (grain) radius [L].

Equations 10, 11, and 12 thus form the two-region solute transport model with rate-limited sorption due to spherical diffusion.

MATERIALS AND METHODS

Sorbent and Solute. The aquifer material used in this work came from the Borden aquifer (Borden, Ontario) and was sieved to obtain sand-sized grains of uniform size (40-60 mesh or roughly 0.25 to 0.42 mm in diameter). The material had been studied extensively in prior work (three years before the present study) by Ball and co-workers (Ball, 1989; Ball et al. 1990; Ball and Roberts 1990 a,b) and was shown to have a high carbonate content and measurable intragranular porosity (see Physical Parameter Determination below). The air-dried material had been stored in the dark at room

temperature in polyethylene bags (Whirl-Pak, Nasco, Fort Atkinson, WI) since the time that the aquifer material was collected in 1983 (Curtis et al. 1986).

The ^{14}C-labeled tetrachloroethene (PCE) used in these experiments was from Dupont Biomedical Products (Boston, MA), and unlabeled PCE was from Alpha Products (Danvers, MA). Both were used as received. The ^{14}C-labeled PCE used in batch experiments was of a different lot than that used in column experiments; ^{14}C purity was determined for both lots as described subsequently.

Physical Parameter Determination. The physical properties of the sorbent material as well as the parameters relevant to Equation 10 are summarized in Table 1. The bulk density (ρ_b) of the packed column was determined by dividing the mass of the sand within the column by the internal column volume, where the latter was estimated by weight difference of the empty and water-filled column. The total porosity of the column (θ) was then calculated by the following equation:

$$\theta = 1 - \frac{M_s}{V_c \rho_s} \qquad (13)$$

where M_s = mass of sand within the column [M],

V_c = volume of column [L^3],

ρ_s = solid density [mass of solid/volume of solid].

The solid density (ρ_s) in the above equation was determined by weighing a 1-liter flask partially filled with dehydrated sand (dried overnight at 104°C and cooled in a vacuum desiccator). The sand-filled flask was then purged with dry CO_2 for several hours to ensure complete saturation of all pore spaces with CO_2. The flask was then filled with degassed DI water (see Column Methods for degassing) and allowed to equilibrate until the CO_2 dissolved. The flask was topped off to the 1-liter mark and the volume of sand was determined by weight difference. The apparent density (ρ_a) was then calculated as follows:

$$\rho_a = \rho_s (1 - \epsilon_i) \qquad (14)$$

The immobile porosity (θ_{im}) was determined by the following relationship:

$$\theta_{im} = \frac{\epsilon_i}{1 - \epsilon_i} (1 - \theta) \qquad (15)$$

where the internal porosity (ϵ_i) in the above equation was directly measured by mercury porosimetry in prior work (Ball et al., 1990). The mobile porosity was then determined by difference between total column porosity and the calculated intraparticle porosity: $\theta_m = \theta - \theta_{im}$.

Table 1. Summary of Model Parameters and Sorbent Characteristics.

a	particle radius	0.16 mm	Ball and Roberts, 1991b
ρ_b	bulk density	1.708 g/mL	this work
ρ_a	apparent density	2.620 g/mL	this work
ρ_s	solid density	2.674 g/mL	this work
θ	total porosity	0.362	this work
θ_{im}	immobile porosity	0.0118	this work
θ_m	mobile porosity	0.350	this work
ε_i	intraparticle porosity	0.0181	Ball et al., 1990
D_p	PCE pore diffusivity[*]	$7.93 \times 10^{-9} cm^2/s$	Ball and Roberts, 1991b
f	instantaneous sorbing fraction	0.04	Ball and Roberts, 1991b
K_d	partitioning coefficient (1992)	0.35 mL/g	this work
K_d	partitioning coefficient (1989)	1.2 mL/g	Ball and Roberts, 1991a
f_{oc}	percent of organic carbon	0.02%	Ball et al, 1990; this work

[*]Based on measured D_a value of $4.10 \times 10^{-11} cm^2/s$ and independent estimate of internal retardation (Ball and Roberts, 1991b).

Surface area was measured by BET N_2 adsorption and found to be 0.23 m^2/g (Ball et al., 1990). This value indicates that a typical grain has a BET surface area that is 33 times higher than the external area of a sphere of equal size. Ball et al. (1990) also noted that there was only a minor change in surface area with pulverization. This, together with the high BET surface area, was taken as evidence that the particles have significant internal surface area and porosity.

Organic carbon content had been measured in prior work (Ball et al., 1990) and was remeasured for the current work by an outside laboratory (Desert Analytics, Tuscon, AZ). Both measurements gave similar results with an organic carbon content of approximately 0.02 percent.

Batch Methods. The equilibrium partitioning coefficient (K_d) was determined by a batch isotherm method, which was essentially identical to the methods previously applied by Ball and Roberts (1991a). Batch studies were prepared at four concentration levels each with five replicates. Preliminary isotherm work allowed estimation of the initial concentration such that the final concentrations would be approximately 30, 100, 300, and 1000 µg/L. The mass of aquifer material was determined gravimetrically after adding to 10-ml, funnel-top, flame-sealable ampules (Wheaton, Millville, NJ). A solution comprising de-ionized water, 0.005 M $CaSO_4$, and 0.02% NaN_3 was added to the ampules. The ampules were allowed to stand for several hours with occasional gentle shaking until gas bubbles were removed. The ampules were then filled to a level so as to minimize headspace; the exact amount of solution was determined gravimetrically. Ampules were then spiked with radio-labeled PCE and immediately flame sealed. Sealed ampules were rotated at 5 rpm in a temperature-controlled chamber (20°C). After an equilibration time of 28 days, the ampules were centrifuged, and a 1-mL aqueous sample was taken for use in scintillation counting.

To account for losses to headspace, 23 blanks (ampules without solids) were used across the concentration range. Headspaces were measured after sampling by filling the inverted cracked ampule top and the ampule body with water using a precision digital titrating pipette (Ranin, Emeryville CA). Losses to the headspace were determined by the difference between the mass added to the ampules and the mass in the aqueous phase. This value was divided by the headspace volume and related to the final aqueous concentration by a linear least squares fit ($R^2 = 0.99$). Headspace losses were equal to about 10 percent of the final aqueous mass. Losses in the sorption experiment ampules were assumed to follow the same proportionality to headspace volume and concentration as that determined from the linear regression analysis of the blanks.

Sorbed mass was determined by subtracting the aqueous-phase mass and the losses from the initial mass. Batch data was fit with both linear and Freundlich isotherm models using linear regression and averaging techniques as subsequently described.

1-11

Apparent diffusivity and the associated pore diffusivity were taken from previous work (Ball and Roberts, 1991b), as obtained from batch rate experiments with this same material. In particular, the fraction of instantaneous uptake (f) and the apparent diffusion coefficient (D_a) were previously estimated by means of a least squares fit to uptake data, using batch methods similar to those described above, except with ampules analyzed over a range of times. This diffusion model fit of the data by Ball (1989) is reproduced here in Figure 1. In this figure, Ball (1989) presents the uptake in terms of a ratio of apparent K_d to an ultimate K_d, where the ultimate K_d is 1.2 mL/g, and the apparent K_d is the calculated sorption capacity prior to equilibrium.

The pore diffusivity (D_p) shown in Table 1 was calculated by Ball and Roberts (1991b) from the fitted D_a value in accordance with Equation 6 and using independent estimates of ρ_a, ε_i, and K_d (=1.2 mL/g; Ball and Roberts, 1991a). As shown in Figure 1 and in Table 1, this size fraction of material showed little instantaneous sorption (f = 0.04), such that the vast majority of the sorption capacity was diffusion limited. For the purposes of modeling in this work, as in the work of Ball and Roberts (1991b), the particle radius (a) was taken as the geometric mean of the sieve sizes.

In addition to the batch sorption experiments with the 40-60 mesh material, batch equilibrium experiments were performed on pulverized material as well. Ball and Roberts (1992a,b) showed that, with this material, pulverization speeds up the equilibration process but does not alter the ultimate sorption capacity. Pulverization was accomplished by crushing the material with a mortar and pestle until the material would pass through a 200-mesh sieve. Batch experiments with the pulverized material were performed in the same manner as for the unaltered material except that the equilibration time was 6 days and the final concentrations spanned a much greater range (from 18 to 52,000 µg/L).

As a note, the batch work by Ball and Roberts (1991a,b) was carried out under somewhat different conditions than the current study. In their work, the aquifer material was autoclaved and filter-sterilized $CaCO_3$-saturated water was used as the aqueous media. In order to check for possible effects of the differences in synthetic groundwater, four samples of pulverized material were run in parallel--two using the $CaSO_4$/NaN_3 method and two using the $CaCO_3$/autoclave method. Only a slight difference was observed between the two methods in terms of the measured sorption capacity, with K_d values found to be 0.23/0.24 mL/g and 0.20/0.21 mL/g, respectively for these two sets of samples. For this subset of results, final aqueous concentrations ranged from 2000 to 2100 µg/L.

Column Methods. The aquifer material was carefully packed into a low-dead-volume 25-cm long, stainless-steel column (2.1 cm ID; Waters, Milford, MA) by tamping the sand every 1 cm the column was filled. To ensure complete saturation of both intragranular and intergranular pore the packed column was purged with bone-dry CO_2 and slowly filled with the working solution (same as in batch experiments) that had been degassed. Degassing was accomplished by ultrasonication under

vacuum until bubbling stopped and then purging the solution with helium. The column was fed with degassed solution until the column weight stabilized to the nearest 0.001 g (about 3 days).

The column experimental procedure was carried out in a manner similar to that described by MacIntyre et al. (1991). The setup is shown in Figure 2. Two syringe pumps (Isco LC 5000, Lincoln, NE) were connected with low-volume tubing (0.023 mm ID, Waters, Milford MA) to the column through a 6-port switching valve (Valco, Houston, TX). These syringe pumps were selected because they provide high-precision, pulse-free flow and maintain the PCE solution under headspace-free conditions in a tightly sealed stainless-steel environment. One syringe pump contained the clean, PCE-free solution, and one pump contained ^{14}C-labeled PCE at 630 µg/L (activity = 20,000 DPM/mL) as well as tritiated water (28,000 DPM/mL) which was used as a nonsorbing tracer. An input pulse (square wave) was created by switching between the two pumps. Sample fractions were collected by direct discharge under the surface of the scintillation fluid in vials (no exposure to headspace) by means of a robotic fraction collector (Gilson 212B, Middleton, WI). ^{14}C and ^{3}H were analyzed by a dual-channel scintillation counter (Beckman LS 9800, Irvine, CA).

Column experiments were run at two flow rates differing by an order of magnitude, with the conditions as shown in Table 2. The hydrodynamic dispersion coefficient (D_H) was determined by applying the two-region diffusion model (without sorption) to the tritiated water data. A least-squares fitting routine (CXTFIT, Parker and van Genuchten, 1984) was applied to the data with D_H as the only fitted parameter. The fitted tritium breakthrough curves are shown in Figures 3a and 3b. These figures demonstrate the comparative unimportance of hydrodynamic dispersion to solute spreading in this system. These figures also demonstrate that, in the absence of sorption and associated intragranular solute capacity, the effect of intraparticle diffusion is imperceptible.

Purity Check. Purity checks were performed on the ^{14}C-labeled PCE using HPLC (HP Series 1050 HPLC pump and Alltech Econosphere C18 5µm in 4.6-mm I.D by 250-mm long column) at an elution flow rate of 1 mL/min. The elution fluid consisted of 100 percent water for the first 5 minutes. Thereafter, methanol was introduced linearly over time until, at 25 minutes, the eluting fluid consisted of 100 percent methanol. One-minute samples were taken consecutively for 40 minutes, and analyzed by scintillation counting.

Column Simulation Model. For this work, a computer program incorporating Crank-Nicholson finite-difference solutions to Equations 10 through 12 was used to simulate the column breakthrough. The FORTRAN program was developed by Goltz after the model equations of Nkeddi-Kizza et al. (1982) and has been previously applied to simulations of this type (Goltz and Roberts, 1986). The values of all input parameters were determined independently, as previously described. No parameter adjustments were made except in the context of the sensitivity analyses described later.

1-13
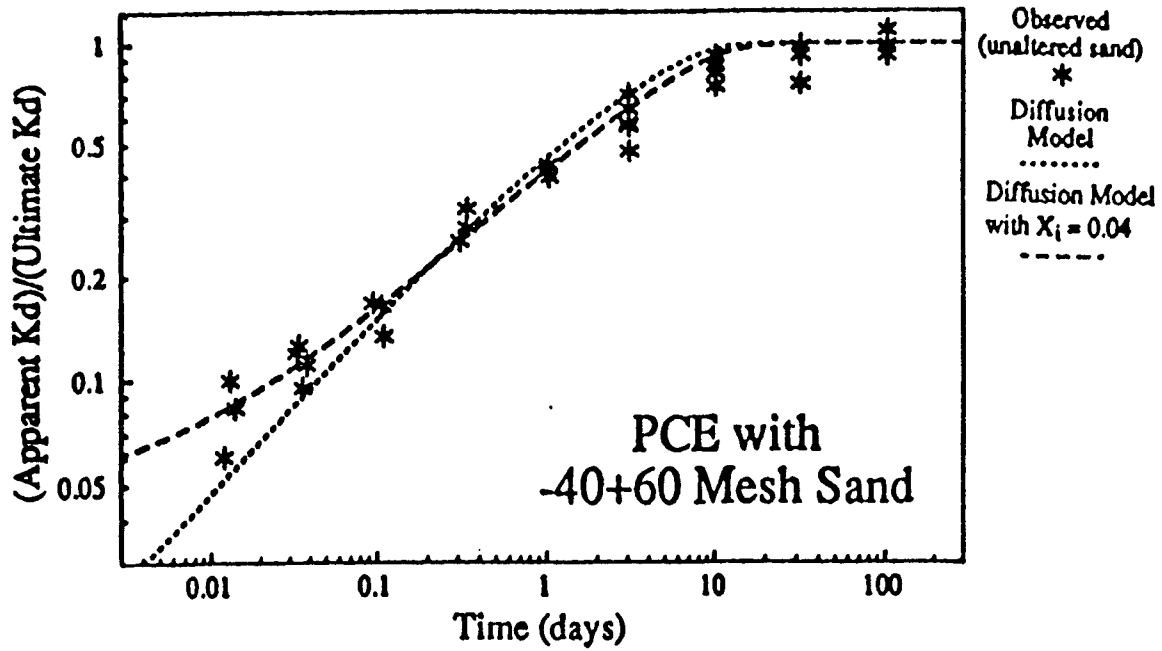
Figure 1. Fitting of D_a and f (called X_i here by Ball) to batch uptake data for PCE and Borden 40-60 sand (dashed line). Also shown is a 1-parameter diffusion model fit in which f = 0 (dotted line). (from Ball, 1989)
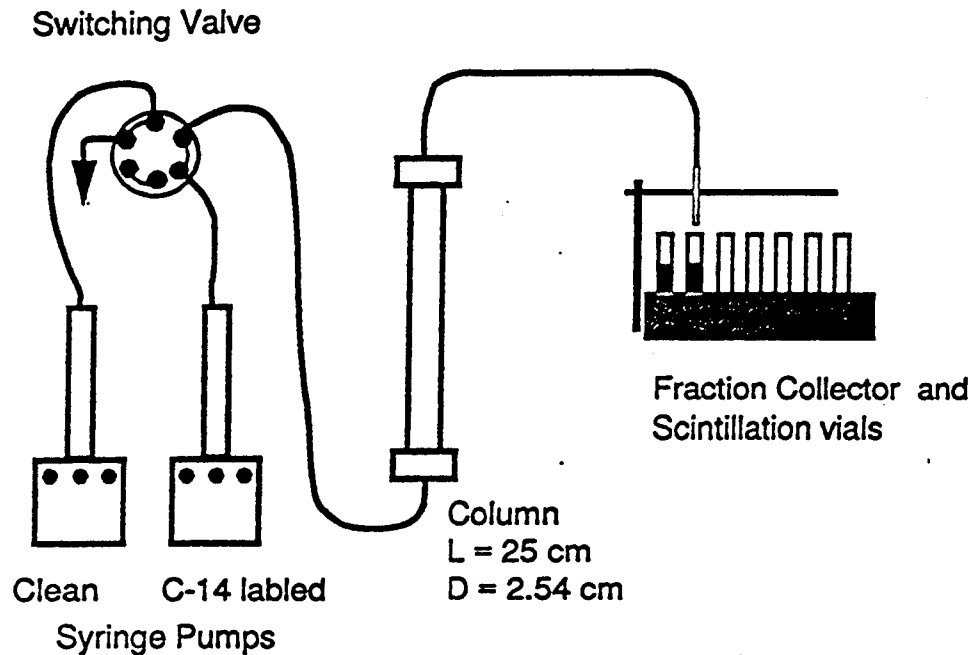
Figure 2. Schematic of setup for column experiments.

Table 2. Summary of column experiment conditions

Column Run	Flow Rate (ml/hr)	Velocity[a] (cm/hr)	Pulse Duration (days)	D_H[b] (cm²/hr)	Run Duration (pore volumes)	(days)
fast	40	30.9	0.25	0.0324	65	2.2
slow	3.9	2.98	2.5	0.00265	30	10.6

[a]Calculated as $v = QL/\theta V$, where Q = flow rate, V = empty column volume, θ = porosity, L = column length.
[b]Hydrodynamic dispersion coefficient as obtained from fitting two-region advective/dispersion model (without sorption) to tritium breakthrough data (see text).

Table 3. Summary of isotherm analysis.

Material (n = number of data points)	Concentration Range (µg/L)	K_d by Regression Through Zero (mL/g)	R²	Average K_d (mL/g)	Standard Deviation (mL/g)	Freundlich Fit K_f (µg/kg))(µg/L)$^{1/n}$	1/n
This work							
Unaltered (n = 21)	36 - 795	0.32	0.97	0.35	0.049	0.48	0.94
Pulverized (n = 16)	18 - 418	0.35	0.98	0.41	0.099	0.75	0.86
Pulverized (n = 14)	1680 - 52,000	0.21	0.98	0.23	0.13	0.43	0.92
Ball, (1989)[a]:							
Unaltered (n = 11)	2.9 - 19	N/A[b]	N/A[b]	1.19	0.13	N/A[b]	N/A[b]
Pulverized (n = 7)	4.0 - 4.3	N/A[b]	N/A[b]	1.08	0.068	N/A[b]	N/A[b]
All Data (n = 69)	2.9 - 52,000	0.21	0.99	0.56	0.39	1.21	0.79

[a]Ball reported an average K_d of 1.2 mL/g based on the combined results of unaltered samples with an equilibration time greater than 100 days and pulverized samples. The above values for unaltered material were determined using all samples with an equilibration time of greater than 10 days; see Figure 1.

[b]Full isotherm was not developed by Ball for this size fraction.
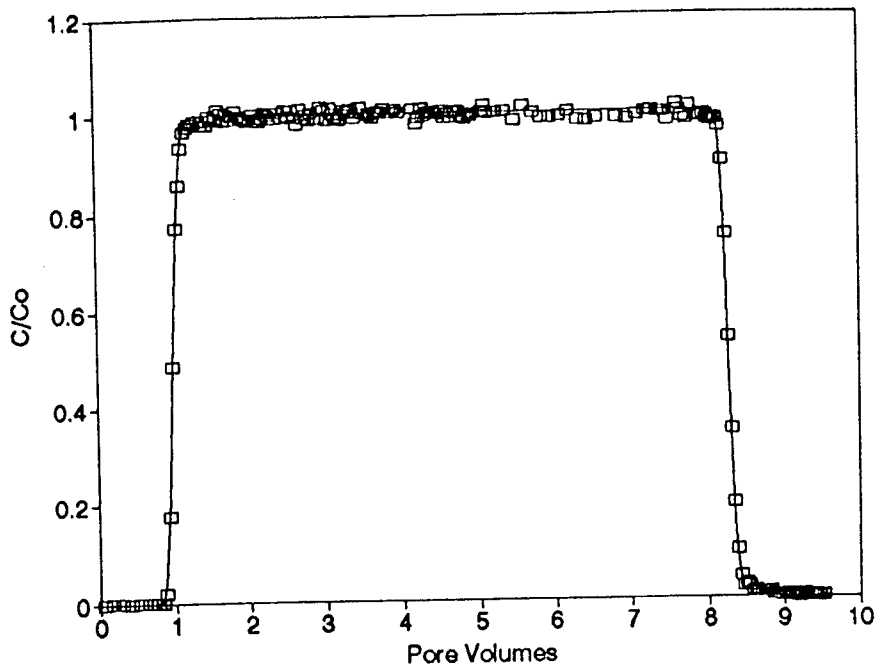
Figure 3a. Breakthrough data and the fitted model for the nonsorbing tritiated water tracer from which the hydrodynamic dispersion coefficient was obtained for the low-flow column.
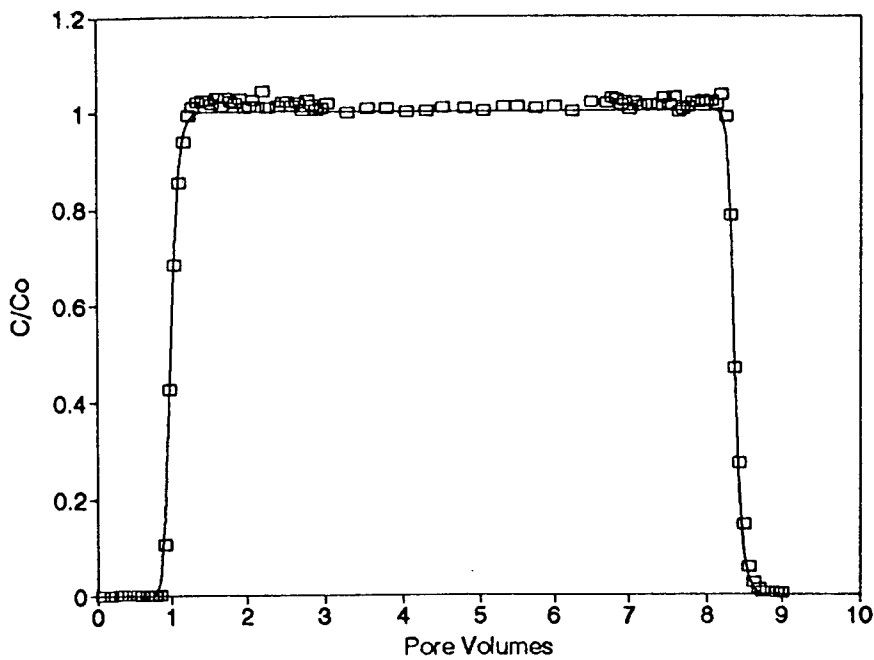
Figure 3b. Breakthrough data and the fitted model for the nonsorbing tritiated water tracer from which the hydrodynamic dispersion coefficient was obtained for the high-flow column.

RESULTS AND DISCUSSION

Isotherm. Figure 4a shows the batch-derived isotherm results of the current work for the pulverized and unaltered material. Also appearing on this figure are the data from the past work of Ball (1989) for this same solute/sorbent system. An examination of the combined data set, which encompasses five orders of magnitude in concentration, revealed that the isotherm was nonlinear, and that the following Freundlich isotherm model fit the data:

$$q = 1.21 C^{0.79} \tag{16}$$

The level of nonlinearity is virtually identical to that observed by Ball (Ball, 1989; Ball and Roberts, 1989a) in studies with bulk borden material and covering a similarly broad range of concentrations. The nonlinearity suggests that the previously described models, which were based on a linear isotherm assumption, may not be fully appropriate for this system. Over smaller concentration ranges the data may be approximately linear and reasonably well characterized by an apparently constant K_d. Such was the case with PCE isotherms and bulk Borden material (Ball and Roberts, 1991a). Other researchers (e.g. Lee et al., 1988; Bouchard et al., 1988; Larsen et al. 1992) have also worked with linear isotherms derived from batch experiments encompassing a single order of magnitude in concentration, and have shown good agreement with column-derived results. Still others (e.g. van Genuchten et al., 1977) have linearized batch-derived nonlinear isotherms and successfully applied the results to column work.

For the purposes of *a priori* column predictions in this work, we applied column transport models that relied upon the linear isotherm assumption, and we used the K_d measurement that was made in the same concentration range over which the bulk of the column data were collected. K_d was thus taken as the average K_d of all 21 recent samples with unaltered material, for which the final aqueous concentrations ranged from 36 to 795 µg/L (roughly the concentration range of the column experiment). For this data set, an almost linear isotherm fit was obtained (Freundlich $1/n = 0.94$; see Table 3), with a suggested K_d value of 0.35 mL/g. Comparison of this value with the value of 1.2 mL/g reported by Ball and Roberts (1991a) for a much lower concentration range (2.9 to 4.3 µg/L) reveals the potentially significant effects of nonlinearity. Figure 4b presents a plot of these two linear isotherm models and clearly shows the limited range of their usefulness.

A summary of the various isotherm fits through various concentration ranges and with pulverized, unaltered, and combined material is presented in Table 3. For the purposes of comparison, K_d was determined by both regressing a line through the origin and by taking an average K_d of the samples. Though in most cases the two values do not significantly differ, Ball and Roberts (1991a) discuss the appropriateness of taking the average K_d (rather than a linear regression of the
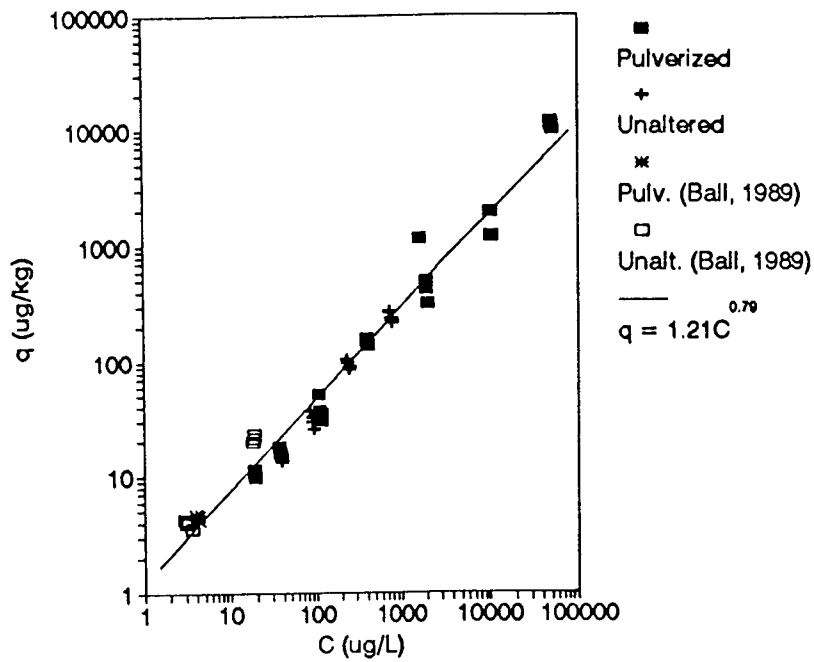
Figure 4a. Isotherm for Borden 40-60 sand and PCE incorporating data from the present work as well as data from Ball (1989). The data indicate nonlinearity that is modeled here as a Freundlich isotherm.
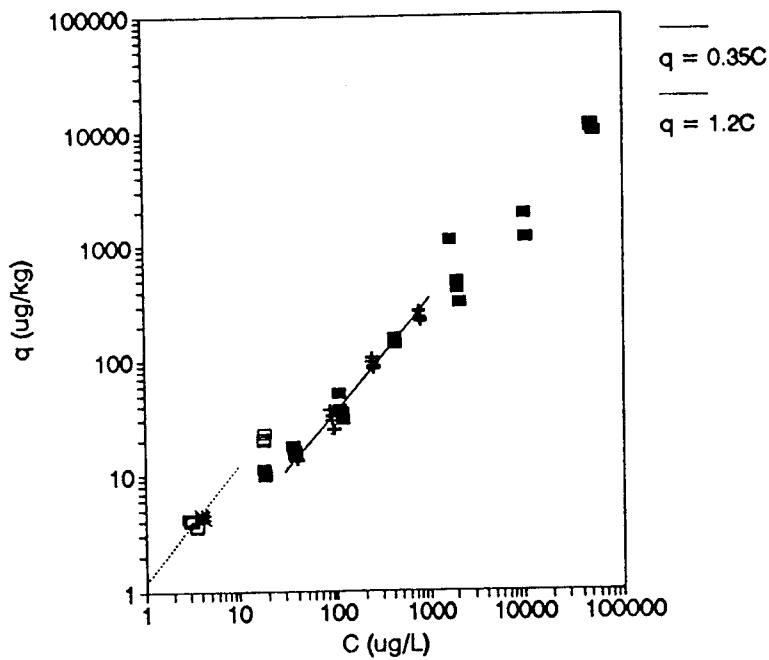
Figure 4b. Isotherm showing the linear model assumed by Ball and Roberts (1991a,b) where $K_d = 1.2$ mL/g and the linear model used in the present work where $K_d = 0.35$ mL/g.

isotherm plot) for cases of constant relative error in aqueous measurements (as with scintillation counting). For this case, the standard error of sorbed-phase concentration measurement varies directly with aqueous concentration, and the average K_d approach is recommended.

Rows 1 and 2 of Table 3 show a comparison between the unaltered and pulverized material over similar concentration ranges. It appears, from the closeness of the K_d values for these two materials, that pulverization does not greatly affect the sorption capacity of this material. Ball and Roberts (1991a) found similar results with pulverized material and numerous size fractions.

[14]C-Labeled PCE Purity. The purity results are given in Figure 5, which shows the HPLC-elution results for the different standard solutions of PCE which were used for column and batch experiments. The data suggest that ^{14}C-labeled PCE accounts for roughly 85 percent of total activity, with all potential impurities eluting earlier than the PCE. Early elutions imply that the impurities had less of an affinity for organic phases than PCE. Such impurities would tend to decrease the batch-measured equilibrium distribution coefficient (K_d).

The effect of impurities on batch experiments can be investigated by assuming a worst-case scenario, that is, that all contaminants are completely nonsorbing. For this case, the relationship between the actual equilibrium coefficient and the measured equilibrium coefficient follows:

$$\frac{K_d^a}{K_d^m} = \frac{1}{1 - X\left[\frac{K_d^m M_s}{V_w} + 1\right]} \tag{17}$$

where K_d^a = actual K_d (mL/g)

$\quad K_d^m$ = measured K_d (mL/g)

$\quad X$ = fraction of impurities

$\quad M_s$ = mass of solids (g)

$\quad V_w$ = volume of water (mL)

In our case, the mass of sand was typically 10 g and the volume of water was typically 9 mL. Under these conditions, if all contaminants are assumed to remain in the aqueous phase, then the maximum possible K_d for PCE is calculated to be 0.44 mL/g. In our case, the actual error would be much lower since most of the contamination did sorb to some extent in the HPLC column and might be presumed to sorb to the aquifer material as well (although not as strongly as PCE).

To further confirm the accuracy of our measured equilibrium coefficient and also to rule out interference from colloids, Hemry (1992) performed sorption experiments (with PCE and the same aquifer material) using a headspace analysis technique developed by Garbarini and Lion (1985). In his
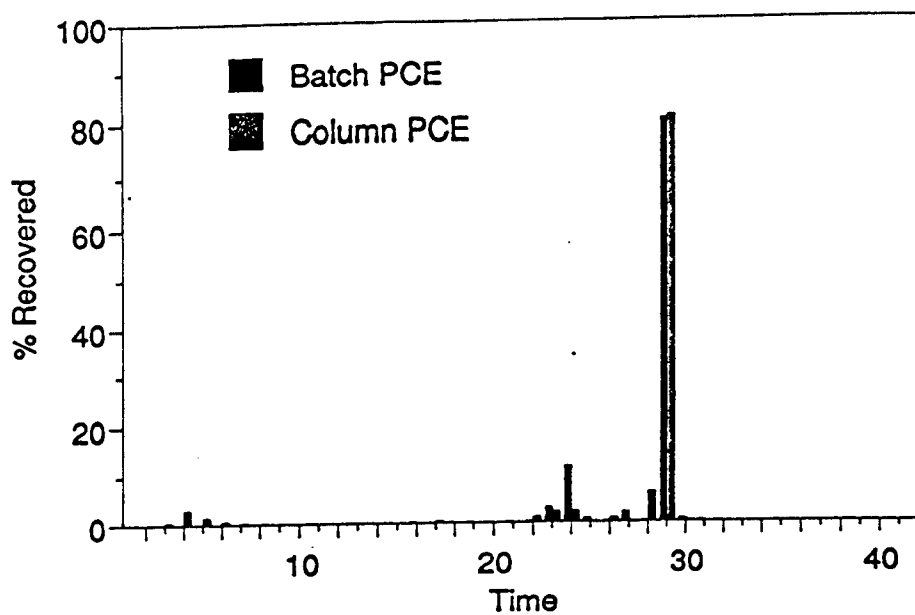
Figure 5. Purity check for ^{14}C-labeled PCE by trapping HPLC eluent. Batch and column PCE were from different lots.

studies, Hemry also found a K_d value of 0.35 mL/g (± 0.03, n = 7) for PCE with the 40-60 mesh Borden material.

Predictions. Column breakthrough data and *a priori* model predictions for the slow column are shown in Figure 6. These predictions are made using the parameters given in Tables 1 and 2, all of which were obtained by means completely independent of the PCE breakthrough results. Two predictions are shown — one using the partitioning coefficient of Ball and Roberts (1991a), and one using the more recently determined partitioning coefficient. The prediction using the K_d determined from the present batch experiments (K_d = 0.35 mL/g) shows very close agreement with the data, whereas the prediction based on the K_d that was determined by Ball and Roberts (1991a) at lower concentrations (K_d = 1.2 mL/g) shows an obvious deviation, and further justifies our choice of K_d. The same predictions are made for the fast column and are shown in Figure 7. This figure shows that there is still fairly good agreement of the prediction with the data, as long as the lower K_d value is used. An apparent inadequacy of the prediction is observed, however, in its failure to capture the data at the curve's frontal and distal knees. The prediction also indicates a slightly earlier breakthrough than the data. These apparent inadequacies of the model may reflect some combination of (1) additional rate mechanisms not accounted for by the estimated diffusion rate and which were not significant for the lower velocity column, and/or (2) omission of nonlinear sorption from the model.

As Figure 7 also shows, at the higher velocity, there is less of an obvious deviation between the two model predictions (K_d = 0.35 or 1.2 mL/g), indicating that at high flows the experiment becomes less sensitive to the equilibrium sorption coefficient (K_d). Such an effect is indicative of extreme nonequilibrium in which very little solute has time to sorb and thus flows through the column with the mobile-phase advection regardless of the potential extent of sorption in the immobile region. Similar effects are apparent in the work of other researchers (Brusseau et al. 1989; Brusseau and Rao, 1989). Since the breakthrough curve is close to exhibiting plug flow characteristics (i.e., an almost vertical front at dimensionless time of one pore volume), curve shape becomes insensitive to any further increases in velocity. Insensitivity of this type may also help explain the observation by Brusseau (1992) that breakthrough curves did not exhibit a leftward shift with increasing velocity.

Pore vs. Sorbed-Phase Diffusion. The predictions of Figures 6 and 7 were based on the concept that retarded diffusion through fluid-filled, intragranular pores is the mechanism for rate-limited uptake. If, on the other hand, diffusion in the sorbed phase is believed to dominate the rate of uptake, then D_a would be determined by the second term on the right-hand side of Equation 4. Under these conditions, one might assume that the term D_s should remain constant, and that D_a will therefore remain constant irrespective of changes in K_d ($\rho_a K_d \gg \varepsilon_i$). (In terms of the pore diffusion model and a
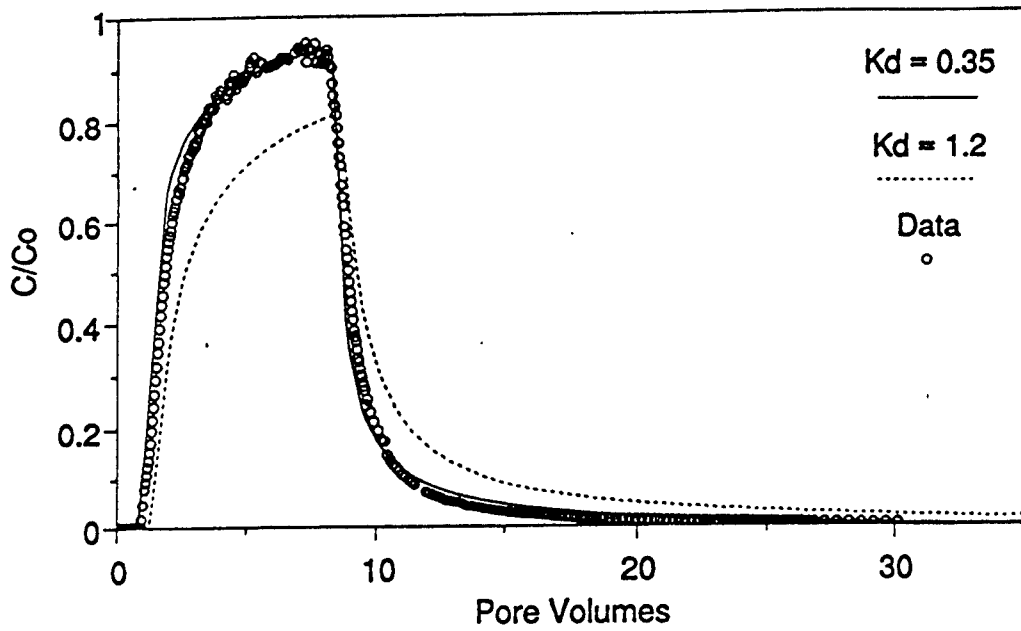
Figure 6. Breakthrough data and pore diffusion model prediction for the slow column. Model parameters as given in Tables 1 and 2.
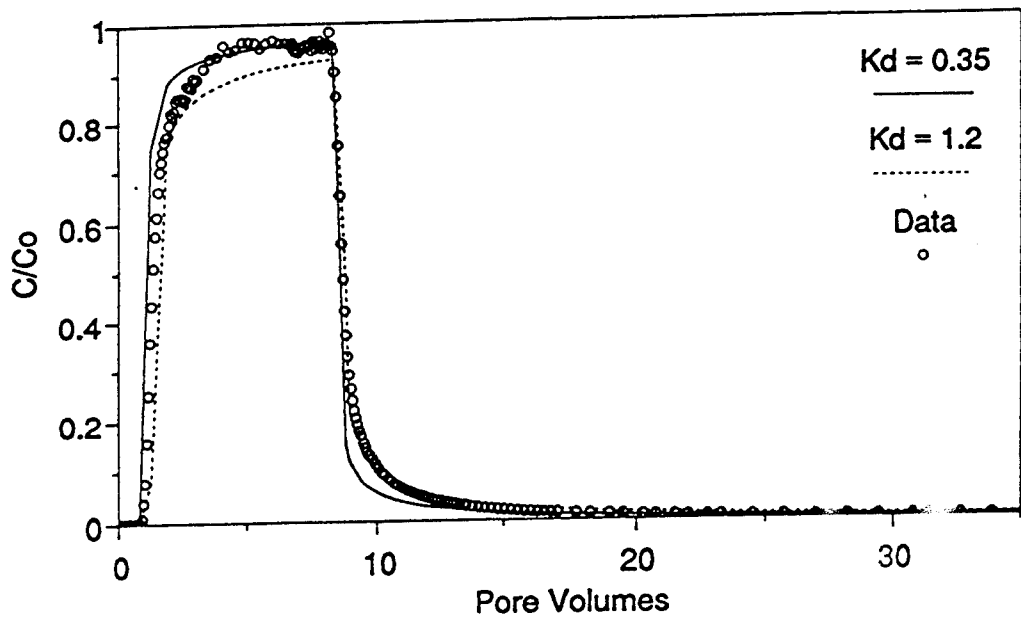

Figure 7. Breakthrough data and pore diffusion model prediction for the ' umn. odel parameters as given in Tables 1 and 2.

linear isotherm, this would be equivalent to having a pore diffusion coefficient at the lower K_d which is 0.27 times lower than the previous batch-determined estimate.) The predictions comparing the assumption of a constant D_p and a constant D_a are shown in Figures 8 and 9 for the slow and fast columns, respectively. These figures clearly show that the assumption of constant pore diffusivity is more appropriate than one of constant sorbed-phase diffusivity. Sorbed-phase diffusion could still conceivably be the responsible rate-limiting mechanism, but only if the sorbed-phase diffusivity increased for the conditions of the column experiment (i.e., at the higher aqueous concentration and lower effective K_d)

Sensitivity to D_p. To further investigate the proposed rate model, a sensitivity analysis was performed. Figure 10 shows the baseline prediction ($D_p = 7.93 \times 10^{-9}$ cm^2/s) for the low-velocity column, as well as two other predictions which were generated for rate limitations 5 times and 0.5 times the predicted mass-transfer rate. This figure shows that the model is fairly sensitive to mass-transfer limitations, and that the data fall reasonably well within these limits. The sensitivity of D_p for the high-velocity column is shown in Figure 11. As shown, the prediction is much less sensitive to D_p at the higher velocity. Again, the data fall reasonably well within the bounds of $0.5D_p$ and $5D_p$.

The sensitivity issue is further scrutinized in Figures 12 and 13, which are magnifications of the tail section of Figures 10 and 11, respectively. For the tail of the slow column (Figure 12), for which data are lacking, the best fit is much less obvious than for the full curve, although the $5D_p$ curve is clearly inappropriate. For the higher flow column (Figure 13), for which the tail was measured for more pore volumes than the slow column, the predicted D_p fits the data quite well. We believe that, in general, longer column runs should be conducted so that more emphasis can be placed on the tail sections of breakthrough curves and thus allow a more sensitive investigation of rate limitations in this region, which can be critical to subsurface remediation. In addition, the elution tails will be quite sensitive to the effects of nonlinear isotherms, as noted below.

Effect of Incorporating Nonlinearity. Incorporating the effects of isotherm nonlinearity with a "favorable" sorption isotherm (i.e., Freundlich $1/n < 1$) is expected to have the effect of sharpening the breakthrough front while prolonging the elution tail. The latter effect is the result of enhanced solute retention (both in intraparticle and interparticle regions) at lower aqueous concentrations. Isotherm nonlinearity has been previously applied to diffusion-limited column transport (e.g. Crittenden et al., 1986) and has also been used in describing diffusion-limited sorption and desorption in batch work (Miller and Pedit, 1992). While it is unclear as to whether the predictions of this work would be improved if isotherm nonlinearity were incorporated into the model, Figures 12 and 13 do illustrate that at the very low concentrations associated with long-term elution, the tailing may be more severe than the model suggests, indicating slower release in this concentration range. Application of an
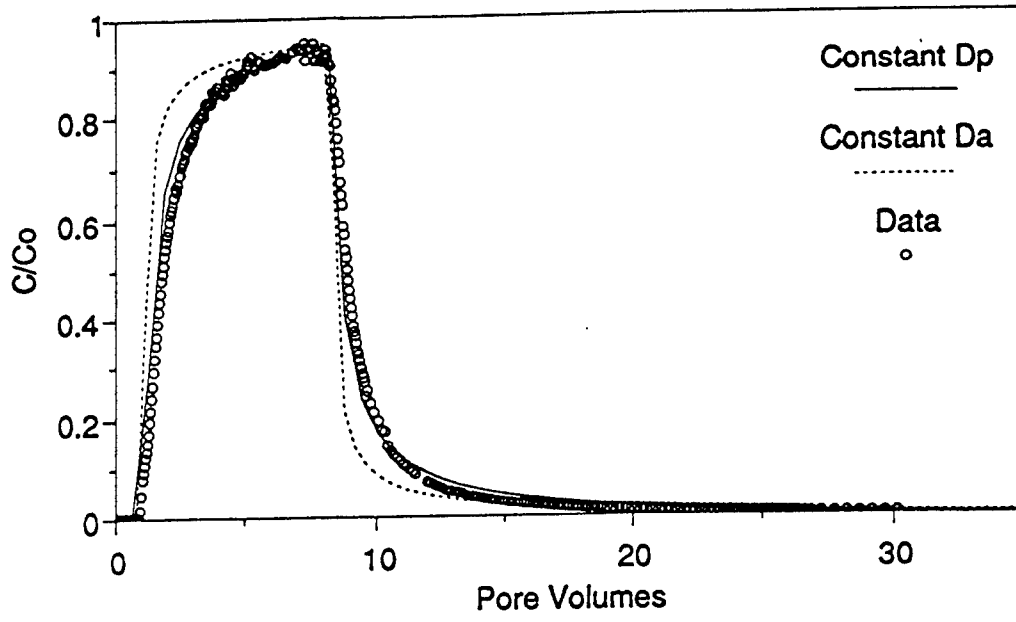
Figure 8. Comparison of the pore diffusion model with the solid diffusion model under the slow-column condition.
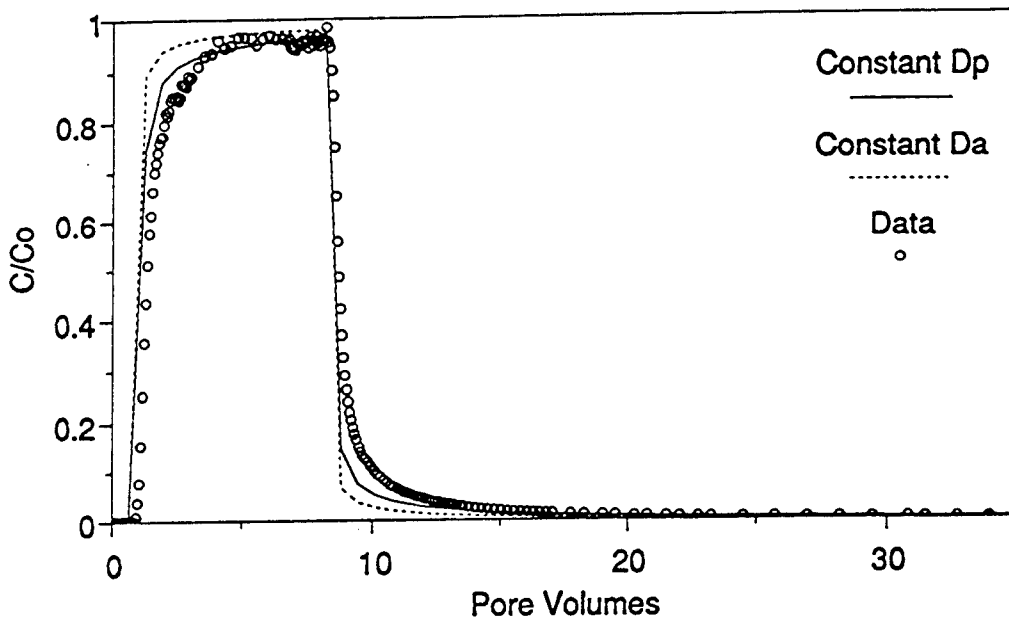

Figure 9. Comparison of the pore diffusion model with the solid diffusion model under the fast-column condition.
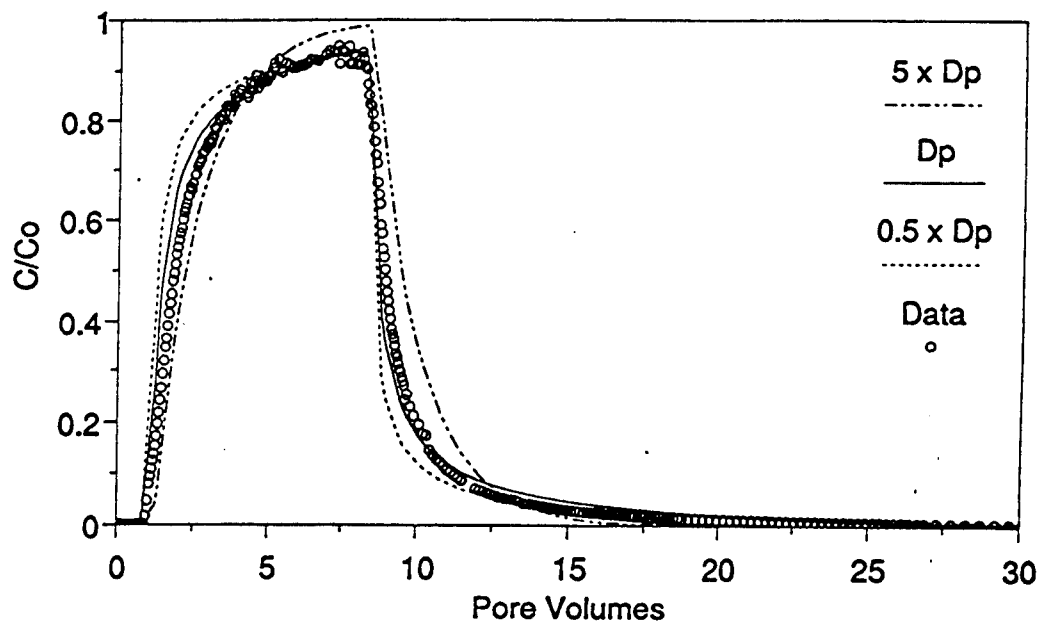
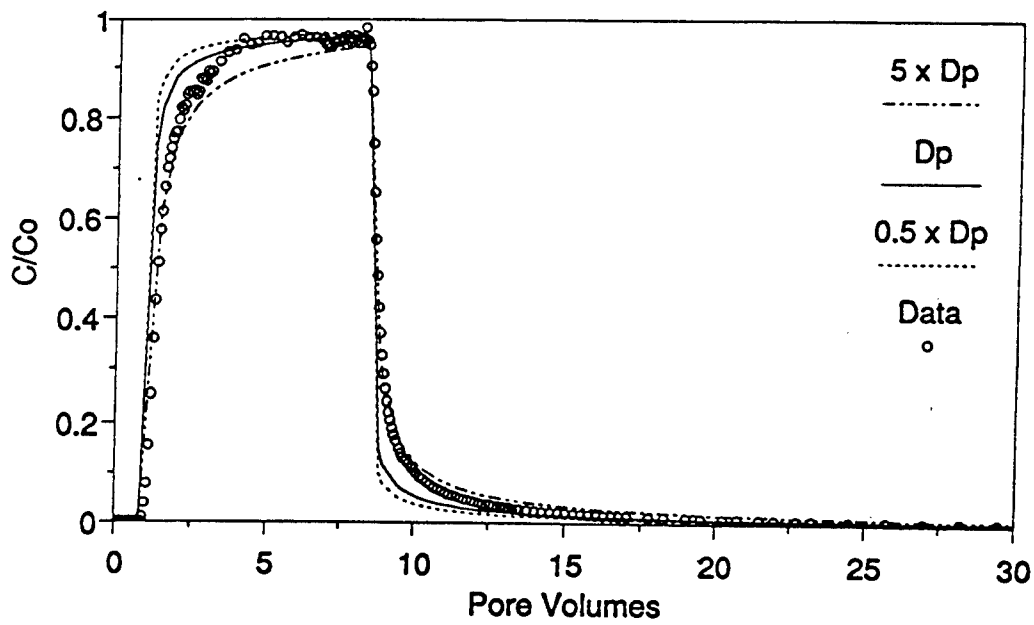Figure 10. Sensitivity of the pore diffusion model to D_p for the low velocity column.

Figure 11. Sensitivity of the pore diffusion model to D_p for the high velocity column.
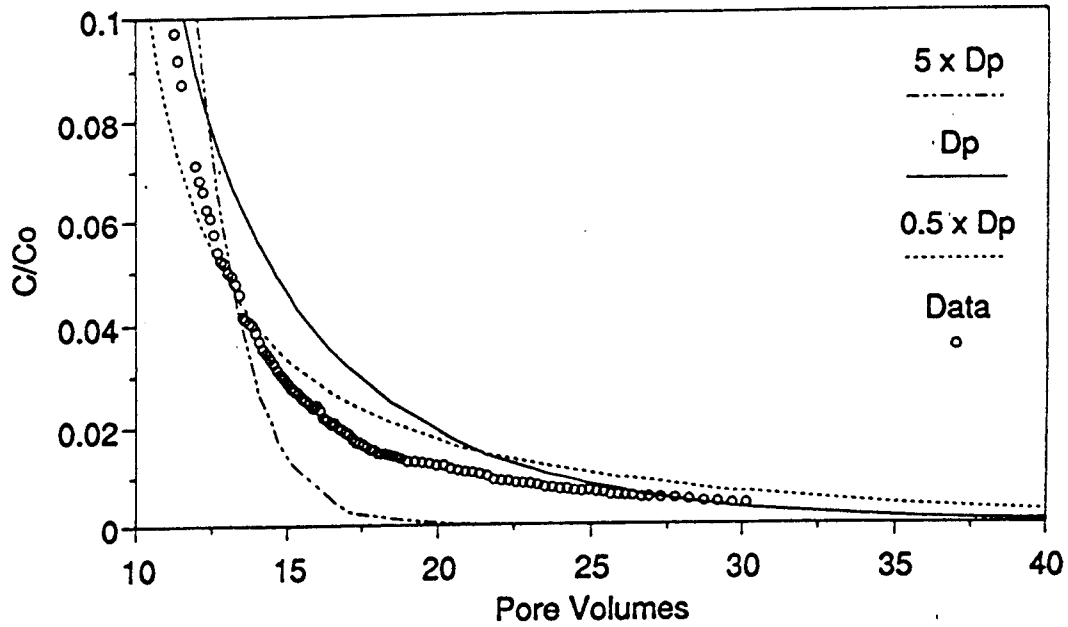
Figure 12. Sensitivity of D_p on the tailing edge of the low velocity breakthrough curve (magnification of Figure 8).
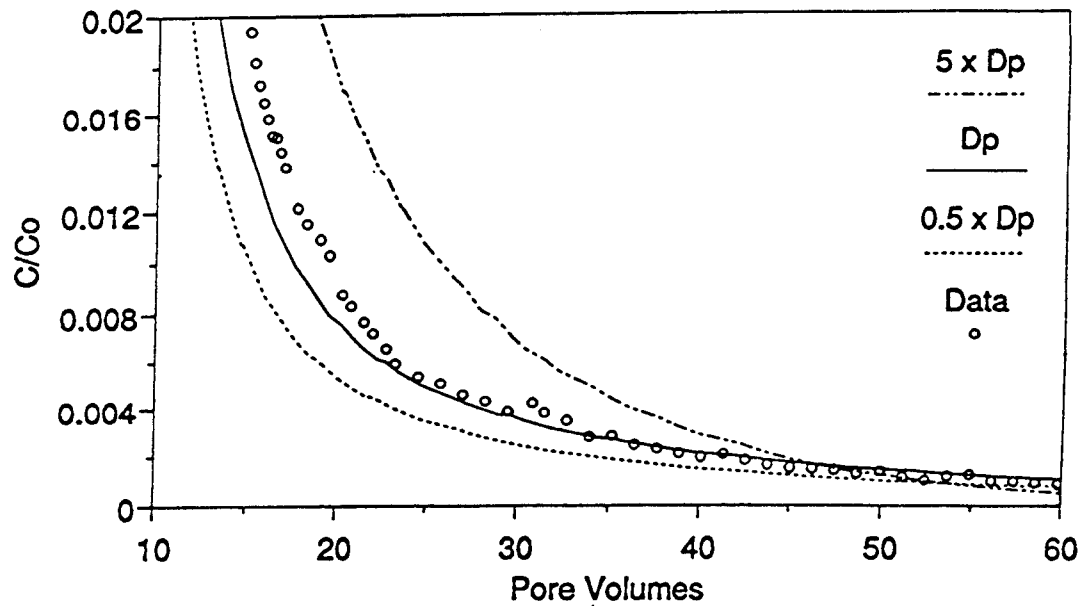
Figure 13. Sensitivity of D_p on the tailing edge of the high velocity breakthrough curve (magnification of Figure 9).

appropriate nonlinear sorption isotherm model to the column data presented here may be a fruitful avenue for future work.

PART 2: PARAMETER ESTIMATION FROM COLUMN STUDY

BACKGROUND

Part 1 of this paper dealt with the ability to predict the transport of contaminants through a soil column by measuring parameters in batch experiments. Part 2 of this paper deals with the ability to obtain these parameters by column experiments alone. Several commonly used methods to solve this inverse problem are explored, including least squares analysis (using the diffusion model and a first-order model) and the method of moments.

Least-Squares Analysis: Diffusion Model. The diffusion model described in Part 1 of this paper (Equations 10, 11, and 12) is often presented in dimensionless form to facilitate computations. The dimensionless form of these equations follow (Nkedi-Kizza et al., 1982):

$$\beta R \frac{\partial C_m}{\partial T} + (1-\beta) R \frac{\partial \overline{C_{im}}}{\partial T} = \frac{1}{P} \frac{\partial^2 C_m}{\partial Z^2} - \frac{\partial C_m}{\partial Z} \tag{18}$$

$$\frac{\partial C_{im}}{\partial T} = \frac{\gamma}{R(1-\beta)} \left[\frac{1}{\eta^2} \frac{\partial}{\partial \eta} \left(\eta^2 \frac{\partial C_{im}}{\partial \eta} \right) \right] \tag{19}$$

$$\overline{C_{im}} = 3 \int_0^1 C_{im} \eta^2 d\eta \tag{20}$$

where the dimensionless parameters are defined as follows:

$$\gamma = \frac{3 D_p L \left(1 - \frac{\theta_m}{\theta} \right)}{a^2 v} \tag{21}$$

$$T = \frac{vt}{L} \tag{22}$$

$$Z = \frac{x}{L} \tag{23}$$

$$P = \frac{vL}{D_H} \tag{24}$$

$$R = 1 + \frac{\rho K_d}{\theta} \tag{25}$$

$$\beta = \frac{\theta_m + f\rho_b K_d}{\theta \rho_b K_d} \tag{26}$$

$$\eta = \frac{r}{a} \tag{27}$$

For parameter estimation from column data, the most likely parameters are those which produce a minimum of the sum of the squares of the differences between the diffusion model and the data (Draper and Smith, 1981). (For the diffusion model, only the parameters γ and β were fitted). The function to be minimized may be written as

$$F_{min} = \sum_{i=1}^{n} (C_m - C_d)^2 \tag{28}$$

where F_{min} = function to be minimized

C_m^i = predicted model concentration at pore volume i

C_d^i = experimentally determined concentration at pore volume i

n = number of data points.

To the best of our knowledge, fitting of the diffusion model to column data derived from environmental soil samples has not been previously published. Thus, comparison of column-derived parameters to batch-derived parameters will be very useful in determining optimum methods for parameter estimation.

Least-Squares Analysis: First-Order Model. Since the diffusion model requires that the shape and size of the particle be known, a less complex first-order rate model, which greatly simplifies computation and does not require knowledge of the immobile zone geometry, is often used as an alternative model to describe column breakthrough subject to rate limitations. With the first-order model, the rate of solute mass transfer is a linear function of the concentration difference between the mobile and immobile regions, and thus uses a first-order mass transfer coefficient to approximate solute mass transfer. Since concentration gradients are assumed to be nonexistent in the immobile region, an average immobile concentration is used. Under these conditions, the rate-limited sorption term in Equation 18 (the second term) would be expressed as follows (Parker and van Genuchten, 1984):

$$\frac{\partial \overline{C_{im}}}{\partial T} = \frac{\omega}{(1-\beta)R}(C_m - \overline{C_{im}})$$

(29)

$$\omega = \frac{\alpha L}{v_m \theta_m}$$

(30)

This first-order model has been extensively used to fit data and derive parameters by least squares estimation. Parker and van Genuchten (1984) developed a computer program to fit the first-order model to column breakthrough data by the method of minimizing the sum of the square of the residuals. Their program, CXTFIT, allows adjustment of up to five parameters (R, ß, ω, P, and input pulse width) to find the optimum parameter combination.

Moment Analysis. An alternative method of estimating parameters from column data is to derive them from temporal moments. The nth moment is defined as follows (Valocchi, 1985):

$$M^n = \int_0^\infty Ct^n dt$$

(31)

where M^n = the nth moment

t = time.

Normalization of the nth moment can be accomplished by dividing by the zeroth moment, which is equivalent to the amount of solute mass passing through the column. The normalized n^{th} moment takes the following form:

$$m^n = \frac{\int_0^\infty Ct^n dt}{\int_0^\infty C dt}$$

(32)

The first normalized moment is the mean residence time of solute in the column and is independent of the model chosen. When time is expressed as pore volumes, the retardation factor can be readily determined from the first normalized moment by subtracting the first normalized moment of the input pulse,

$$R = m^1 - m_{in}^1$$

(33)

where m^1_{in} = first normalized moment of the input pulse.

Since laboratory experiments cannot be conducted to infinite time as the above expressions require, error in the moment-determined retardation factor will result and will be a function of the truncation time of the column experiment. Lin (1992) explored in detail the effect of truncation on the apparent retardation factor using computer-generated data. The effect of this error on laboratory-generated data is investigated below.

METHODS

Diffusion Model Fits. The fitting for the diffusion model was accomplished by coupling the fitting routine described by Equation 28 to the intraparticle pore diffusion finite-difference program used in Part 1. The parameters γ and β were varied over an extensive range to assure that the absolute minimum of the sum of the squares of the residuals was found. Column data collection and all other input parameters were taken as those described in Part 1.

First-Order Model Fits. Fitting of the first-order model was accomplished by applying the program, CXTFIT, developed by Parker and van Genuchten (1984). One (ω), two (ω and β), and three (ω, β, and R) parameters were optimized to the data.

Moment Analysis. The first normalized moment of the column data was calculated using Equation 33, where the integral was approximated from time zero to the final time of the column experiment. The area below the breakthrough curve was approximated by assuming trapezoidal configurations between data points.

RESULTS AND DISCUSSION

Diffusion Model Fits. The minimization of the function in Equation 28 for both sets of column data (v = 3cm/hr and v = 31 cm/hr) resulted in pore diffusivities that were 1.8 and 3.9 times greater than the batch-determined values, respectively (see Table 4). Possible reasons for these differences are the subject of on-going research but may include the effects of nonlinearity as described in Part 1, as well as the likely possibility that columns exhibit somewhat different rate limitations than do batch tests. The factor of two difference in the fitted D_p/a^2 for the two column velocities may also imply that diffusive rate limitations are functions of velocity, but such observations may also be due to the insensitivity of column experiments at high velocities as discussed in Part 1.

For both low and high velocity data sets, the fitted parameter β, which represents the fraction of solute that is at equilibrium with the mobile phase, was calculated to be 0.40, which compares very favorably with the batch determined value of 0.39.

Table 4. Summary of parameters. (*Italicized values indicate approximations made using Equation 34.*)

	D_p/a^2 (s^{-1} x 10^5)	α (s^{-1} x 10^6)	β	R
Batch Experiments	3.1	*5.5*	0.39	2.65
Column Experiments				
Diffusion Model Fits				
v = 3 cm/hr	5.6	*9.9*	0.40	--
v = 31 cm/hr	12.1	*21.4*	0.40	--
First-Order Fits				
v = 3 cm/hr				
1-parameter fit	*8.9*	15.8	–	--
2-parameter fit	*5.3*	9.5	0.51	–
3-parameter fit	*7.5*	13.3	0.52	2.33
v = 31 cm/hr				
1-parameter fit	*32.2*	57.0	–	--
2-parameter fit	*18.9*	33.4	0.47	–
3-parameter fit	*43.4*	76.8	0.70	1.63
Moment Analysis (calculated from final pore volume)				
v = 3 cm/hr	--	--	--	2.66
v = 31 cm/hr	--	--	--	2.34

First-Order Fits. Fitted parameters using the first order model are summarized in Table 4. One, two and three parameter fits were made for both the low and high velocity column data. Depending on the column velocity and the number of parameters fitted, the mass transfer coefficient α varied from 9.5×10^{-6} to 76.8×10^{-6} s^{-1}, while the term β varied from 0.47 to 0.70.

Though the first-order coefficient, α, is not directly comparable to the term D_p/a^2, approximations are often made to relate these two rate parameters. For instance, Gluekauf (1955) derived the following expression relating the two terms (rewritten here in the terminology of Ball (1989)):

$$\alpha \approx \frac{15\theta_{im}D_p}{a^2} \tag{34}$$

Gluekoff (1955) made the above approximation by equating the amount of mass sorbed of both models over a relatively long time period and under batch conditions. Parker and Valocchi (1986) came up with the same approximation as Gluekauf (1955) but derived the approximation for column conditions by equating the second moments of the two models. Approximations using this relationship were made here so that first-order coefficients could be compared (roughly) to the batch-derived diffusion coefficient. Values derived using this relationship are presented in Table 4 and are shown in italics. Clarification of this relationship is the subject of on-going research.

As Table 4 shows, alpha is clearly a function of column pore water velocity. On average, the value of alpha increases by more than 4 times as the velocity increases from 3 to 31 cm/hr. (This increase is twice as much as the corresponding increase of the fitted diffusion coefficient in the diffusion model, as discussed above). Such an effect is consistent with a diffusion mechanism (Rao et al. 1980; Do and Rice, 1986; Buzanowski and Yang, 1989) and reveals one of the weaknesses in approximating diffusion by a first-order process, that is, that a first-order coefficient determined at one velocity does not apply to a system at a different velocity.

Moment Analysis. As described above, parameters derived from moment analysis are expected to be a function of truncation of the column experiment. This fact is exhibited in Figures 14 and 15, which shows the effect of truncation on the determination of retardation factor for the slow and fast columns, respectively. The curve above the breakthrough curve represent the apparent retardation factor that would be calculated if the experiment were truncated at the respective pore volume. This curve is given as a ratio of the apparent retardation factor (R_a) to the batch-determined value (R_b). This apparent retardation factor underestimates the batch-derived value with the error increasing as truncation increases or as flow rate increases. For example, for the slow column (Figure 14), 30 pore volumes were required to correctly estimate R. At 20 pore volumes, when the effluent
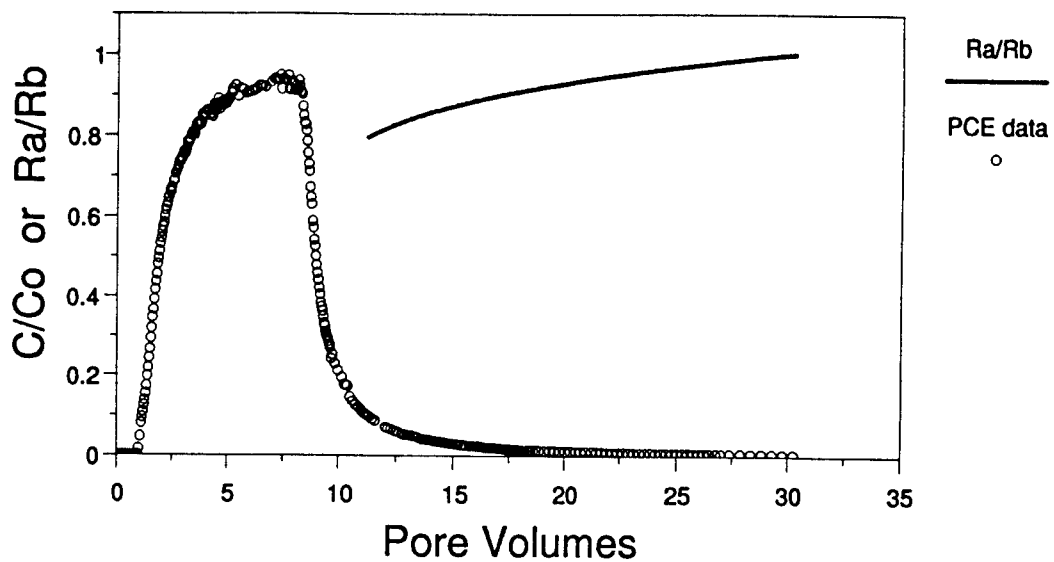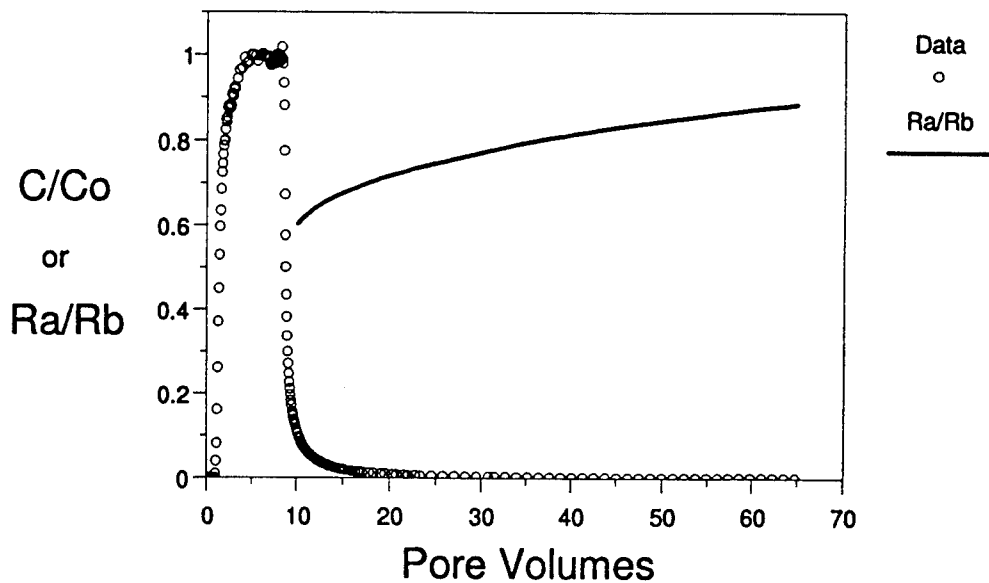
Figure 14. The effect of column experiment truncation on the apparent retardation factor when the retardation factor is calculated from the first moment. The low velocity column is shown (v= 3 cm/hr).

Figure 15. The effect of column experiment truncation on the apparent retardation factor when the retardation factor is calculated from the first moment. The high velocity column is shown (v= 31 cm/hr).

concentration was 1 percent of the influent pulse, the apparent retardation factor was 93 percent of the batch value. For the high flow column, even at 65 pore volumes, when the effluent was only 0.08 percent of the influent, the apparent retardation was only 88 percent of the batch value, and t 30 pore volumes, the apparent retardation was 77 percent of the batch value.

Early truncation will not only give incorrect retardation factors but will also affect p ameters derived from fitting techniques if the incorrect retardation factor is used as a "known" valu . For example, if the column data for the slow velocity column were truncated at 20 pore volumes, the retardation factor would be calculated to be 2.47. Now, if this value were entered into the CXTFIT fitting routine along with the truncated data set, the resulting first-order coefficient (α) would be 11.0 x 10^{-6} s^{-1} and ß would be 0.52. These values compare reasonably well with the fitted values derived from the full data set of 9.5 x 10^{-6} s^{-1} and 0.51, respectively. However, at the higher velocity, the fitted value derived from the data set truncated at 20 pore volumes gives α and ß values of 45.8 x 10^{-6} s^{-1} and 0.63 , which compare less favorably to the values derived from the full data set -- 33.4 x 10^{-6} s^{-1} and 0.47, respectively.

SUMMARY OF PARTS 1 AND 2

The following findings have resulted from this investigation:

• For this sorbate/sorbent system, nonlinear sorption isotherms are apparent when data are taken over a broad concentration range. However, in narrower concentration ranges, sorption behavior was sufficiently linear that a simple K_d approach could be successfully applied toward solute transport prediction.

• For this uniform size fraction of aquifer solids, a simple pore-diffusion transport model with independently determined parameters did an excellent job of predicting column breakthrough data at both high and low velocities. In addition, further evidence of a retarded pore-diffusion process was found in that the same intraparticle pore-diffusion coefficient (D_p) characterized the sorption rate at both high and low concentrations (where effective sorption distribution coefficients differed by 70 percent). In contrast, a sorbed-phase diffusion model could predict the results only if the sorbed-phase diffusion coefficient were assumed to vary with contaminant concentration.

• At high flow rates, rate-limited sorption models are much less sensitive to th equilib ium partitioning coefficient (K_d). Moreover, rate interpretation can be quite sensitive to p ntial rs in K_d. For these reasons, caution should be used when interpreting data from columns cc cted flow rates which are high relative to rates of sorption and desorption.

• The most sensitive data for detecting and characterizing the slow elution of sorb g contaminants is the tail of the breakthrough curve. The column technique outlined in   s pap

enables prolonged experiments of a design which may be especially useful for characterizing the sorption parameters responsible for prolonged tailing in groundwater remediation.

- A least squares fit of the transport model incorporating intraparticle pore diffusion to the low and high velocity columns gave diffusion coefficients that were 1.8 and 3.9 times greater than the batch-determined values.

- Fits of the first-order model gave a wide range of parameter values, depending upon the number of parameters fitted and the velocity of the column. On average the fitted first-order coefficient increased by a factor of four as the column velocity increased by 10 times.

- Error in calculating the retardation factor by the method of moments is a strong function of experiment truncation and column velocity.

In future efforts, the experimental capability developed under this project will be applied to estimate sorption-related transport parameters for volatile organic chemicals with a variety of different aquifer materials. Of particular interest is application of the developed methods in a field project being contracted with the USAF. This project has been designed to study the effects of contaminant sorption and mass transfer on aquifer remediation by pump-and-treat techniques, and will provide an important opportunity to apply laboratory based testing toward field-scale understanding.

REFERENCES

Ball, W.P., 1989. *Equilibrium Sorption and Diffusion Rate Studies with Halogenated Organic Chemicals and Sandy Aquifer Material*, Ph.D. Dissertation, Stanford University.

Ball, W.P., Buehler, Ch., Harmon, T.C., Mackay, D.M., and Roberts, P.V., 1990, "Characterization of a Sandy Aquifer Material at the Grain Scale", *J. Contaminant Hydrology*, 5, 253-295.

Ball, W. P., and P. V. Roberts, 1991a. "Long-Term Sorption of Halogenated Organic Chemicals -- Part 1. Equilibrium Studies", *Environ. Sci. & Technol.* 25(7), 1223-1237.

Ball, W. P., and P. V. Roberts, 1991b. "Long-Term Sorption of Halogenated Organic Chemicals -- Part 2. Rate Studies", *Environ. Sci. & Technol.* 25(7), 1237-1249.

Ball, W. P., and P. V. Roberts, 1991c. "Diffusive Rate Limitations in the Sorption of Organic Chemicals", Chapter 13 in *Organic Substances and Sediments in Water: Volume 2, Processes and Analytical*, R.A Baker (ed.), Lewis Publishers, Inc., Chelsea, MI pp. 273-310.

Bouchard, D.C., Wood, A.L., Campbell, M.L., Nkedi-Kizza, P., and Rao, P.S.C., 1988. "Sorption Nonequilibrium During Solute Transport", *J. Contaminant Hydrology*, 2(1), 209-223.

Brusseau, M.L., 1992. "Nonequilibrium Transport of Organic Chemicals: The Impact of Pore-Water Velocity", *J. Contaminant Hydrology*, 9, 353-368.

Brusseau, M.L. and Rao, P.S.C., 1989. "Sorption Nonideality During Organic Contaminant Transport in Porous Media" *CRC Critical Reviews in Environmental Control*, 19(1), 33-99.

Brusseau, M.L., Jessup, R.E., and Rao, P.S.C., 1989. "Modeling the Transport of Solutes Influenced by Multiprocess Nonequilibrium", *Water Resour. Res.*, 25(9), 1971-1988.

Brusseau, M.L., Jessup, R.E., and Rao, P.S.C., 1991. "Nonequilibrium Sorption of Organic Chemicals: Elucidation of Rate-Limiting Processes", *Environ. Sci. & Technol.*, 25(1), 134-142.

Buzanowski, M.A. and Yang, R.T., 1989. "Extended Linear-Driving-Force Approximation for Intraparticle Diffusion Rate Including Short Times", *Chemical Engineering Science*, 44(11), 2683-2689.

Crittenden, J.C., Hutzler, N.J., Geyer, D.G., Oravitz, J.L., and Friedman, G., 1986. "Transport of Organic Compounds With Saturated Groundwater Flow: Model Development and Parameter Sensitivity" *Water Resour. Res.*, 22(3), 271-284.

Curtis, G.P., Roberts, P.V., and Reinhard, M., 1986. "A Natural Gradient Experiment on Solute Transport in a Sand Aquifer. 4. Sorption of Organic Solutes and its Influence on Mobility," *Water Resour. Res.* 22(13) 2059-2067.

Do, D.D. and Rice, R.G., 1986. "Validity of the Parabolic Profile Assumption in Adsorption Studies", *AIChE J.*, 32(1), 149-154.

Draper, N.R. and H. Smith, 1981. *Applied Regression Analysis*, John Wiley and Sons, New York.

Garbarini, D.R. and Lion, L.W., 1985. "Evaluation of Sorptive Partitioning of Nonionic Pollutants in a Closed System by Headspace Analysis", *Environ. Sci. & Technol.* 19(11), 1122-1128.

Gluekoff, E., 1955. "Part 10.-- Formulae for Diffusion into Spheres and Their Application to Chromatography", *Transactions of the Faraday Society*, 51, 1540-1551.

Goltz, M.N. and Roberts P.V., 1986. "Interpreting Organic Solute Transport Data from a Field Experiment Using Physical Nonequilibrium Models", *J. Contaminant Hydrology*, 1(1), 77-93.

Hemry, M.S., 1992. *Evaluation of a Headspace Method to Determine VOC Soil: Water Distribution Coefficients*, Masters Thesis, School of Engineering, Duke University, Durham, NC

Karickhoff, S.W., 1984. "Organic Pollutant Sorption in Aquatic Systems", *J. Hydraulic Engineering, ASCE*, 110(6), 707-735.

Larsen T., Christensen, T.H., and Brusseau, M.L., 1992. "Predicting Nonequilibrium Transport of Naphthalene through Aquifer Materials using Batch-Determined Sorption Parameters", *Chemosphere*, 24(2), 141-153.

Lee, L.S., Rao, P.S.C., Brusseau, M.L., and Ogwada, R.A., 1988. "Nonequilibrium Sorption of Organic Contaminants During Flow through Columns of Aquifer Material", *Environmental Toxicology and Chem.* 7, 779-793.

Lin, Yi-Chang, 1992. *Factors Affecting the Calculation of Temporal Moments from Breakthrough of Organic Chemicals in Laboratory Columns*, Master's thesis, Department of Civil and Environmental Engineering, Duke University, Durham, NC.

MacIntyre, W.G., Stauffer, T.B., and Antworth, C.P., 1991. "A Comparison of Sorption Coefficients Determined by Batch, Column, and Box Methods on a Low Organic Carbon Aquifer Material" *Ground Water*, 29(6), 908-913.

Miller, C.T. and Pedit J.A., 1992. "Use of a Reactive Surface-Diffusion Model to Describe Apparent Sorption-Desorption Hysteresis and Abiotic Degradation of Lindane in a Subsurface Material", *Environ. Sci. & Technol.*, 26(7), 1417-1427.

Miller, C.T. and Weber, W.J., 1986. "Sorption of Hydrophobic Organic Pollutants in Saturated Soil Systems", *J. Contaminant Hydrology*, 1(1/2), 243-261.

Nkedi-Kizza, P, Rao, P.S.C., Jessup, R.E., and Davidson, J.M., 1982. "Ion Exchange and Diffusive Mass Transfer during Miscible Displacement Through an Aggregated Oxisol" *Soil Sci. Soc. Am. J.*, 46, 471-476.

Nkedi-Kizza, P., Brusseau, M.L., Rao, P.S.C., and Hornsby, A.G., 1989. "Nonequilibrium Sorption During Displacement of Hydrophobic Organic Chemicals and 45-Ca Through Soil Columns with Aqueous and Mixed Solvents", *Environ. Sci. & Techn.*, 23(7), 814-820.

Parker, J.C. and Genuchten, M. Th., 1984. "Determining Transport Parameters from Laboratory and Field Tracer Experiments", *Bulletin 84-3*, Virginia Agricultural Experiment Station, Virginia Polytechnic Institute and State University, Blacksburg, VA.

Parker, J.C. and Valocchi, A.J., 1985. "Constraints on the Validity of Equilibrium and First-Order Kinetic Transport Models in Structured Soils", *Water Resources Research*, 22(3), 399-407.

Pignatello, J.J., 1989. "Sorption Dynamics of Organic Compounds in Soil and Sediments" in *Reactions and Movements of Organic Chemicals in Soils*, B.L. Sawhney and K. Brown (Eds.), Soil Sc. Soc. Am., Inc. and Am. Soc. of Agronomy, Inc., Madison, WI, pp. 45-80.

Rao, P.S.C., Jessup, R.E., Rolston, D.E., Davidson, J.M., and Kilcrease, D.P., 1980. "Experimental and Mathematical Description of Nonadsorbed Solute Transfer by Diffusion in Spherical Aggregates", *Soil Science Society of America J.*, 44, 684-688.

Valocchi, A.J., 1985. "Validity of the Local Equilibrium Assumption for Modeling Sorbing Solute Transport Through Homogeneous Soils", *Water Resour. Res.*, 21(6), 808-820.

van Genuchten, M.Th. and Wierenga, P.J. and O'Conner, G.A., 1977. "Mass Transfer Studies in Sorbing Porous Media", *Soil Sci. Soc. Am. J.*, 41(2), 278-285.

Wu, S. and Gshwend, P.M., 1986. "Sorption Kinetics of Hydrophobic Compounds to Natural Sediments and Soils", *Environ. Sci. & Technol.*,Goltz and Roberts (1986) 20(7), 717-725.

CHARACTERIZATION OF 4-NITROPHENOL BIOTRANSFORMATION

Joseph H. Dreisbach
Professor
Chemistry Department

University of Scranton
Scranton, PA 18510-4626

CHARACTERIZATION OF 4-NITROPHENOL BIOTRANSFORMATION

Joseph H. Dreisbach
Professor
Chemistry Department
University of Scranton

Abstract

Oxidative degradation of 4-nitrophenol (PNP) by JS443 and JS402 through 1,2,4-benzenetriol (BT) was studied in order to characterize the early steps in the biodegradation pathway. The compound 4-nitrocatechol was identified as a product of PNP degradation in these systems. Previous research has shown that 4-nitrocatechol is converted to BT. Another possible product from monooxygenase catalyzed reaction of PNP is 4-nitroresorcinol but this compound was not identified in any of the experiments performed in this study. These results support the fact that JS443 possesses monooxygenase activity against PNP but it remains to be determined if the product of this reaction, 4-nitrocatechol, is an intermediate on the major PNP degradation pathway of induced JS443.

Attempts to obtain cell free activity against PNP were not successful although these cell free preparations possessed very active dioxygenase activity against BT.

Results from this project also reveal that JS443 and JS402 rapidly degrade 4-chlorophenol, 4-bromophenol and 4-iodophenol through BT. This pathway has not been demonstrated prior to this study.

INTRODUCTION

The release of nitroaromatic compounds into the environment is a result of the use of these compounds in the manufacture of a variety of materials including pesticides, explosives and solvents. An understanding of the biodegradation pathways of nitroaromatic compounds provides a sound basis for the potential application of bioremediation processes when addressing environmental contamination. One important group of nitroaromatics is the nitrophenols. The compound 4-nitrophenol (para-nitrophenol, PNP) is of particular interest since it is produced from the hydrolysis of parathion, a common insecticide. Even more important, from a military perspective, is the fact that PNP is an excellent model compound for investigations of biodegradation of nitrotoluenes. Nitrotoluenes are major components of explosives.

Although a number of groups have studied the degradation of nitrophenols, details on the biochemical pathways of degradation of these compounds have been elucidated in only a few cases. A thorough understanding of these catabolic pathways is critical prior to the development of a practical application of any bioremediation process.

Removal of the nitro group from the isomers of nitrophenol by aerobic processes has been reported for 2-nitrophenol (ortho-nitrophenol, ONP) (4,6), 3-nitrophenol (meta-nitrophenol, MNP) (9) and 4-nitrophenol (2,3,5). In the case of ONP catabolism, strains of _Pseudomonas putida_ were shown to convert the substrate to catechol which subsequently undergoes ortho ring fission to yield cis, cis-muconic acid (4). The same strain of _Ps. putida_ was also shown to release nitrogen from MNP as ammonium ion through a separate, reductive process.

Studies with _Flavobacterium_ sp. degradation of 4-nitrophenol suggested that 4-nitrocatechol may be an intermediate on the pathway (5) and other studies on oxidative metabolism of PNP revealed that certain strains of pseudomonads may produce hydroquinone as an intermediate (7,9). In one of these studies it was hypothesized that the hydroquinone intermediate is further hydroxylated to 1,2,4-benzenetriol (BT) prior to ring fission (9). More recently it has been shown conclusively that a _Moraxella_ sp. converts PNP to hydroquinone to yield nitrite

through an NADPH-dependent monooxygenase reaction (2,3). Hydroquinone undergoes ring fission directly to yield γ-hydroxymuconic semialdehyde (3). Although a number of the earlier studies provide some evidence for the identification of intermediates in the degradation pathways of nitrophenols, the study with _Moraxella_ sp. is the only one which details the reaction pathway including nitro group release and fission of the aromatic ring.

Studies performed under the direction of J. C. Spain at the U. S. Air Force Civil Engineering Laboratory at Tyndall Air Force Base, Florida involved three gram positive bacterial isolates which demonstrated active PNP degrading capabilities. Results from these studies revealed a PNP degradation pathway different from those previously described in the literature. The pathway involves catabolism of PNP through 1,2,4-benzenetriol (BT). This intermediate subsequently undergoes dioxygenase catalyzed ortho ring fission to yield maleylacetate. The pathway is described in Figure 1. Small amounts of hydroquinone which accumulate in the reaction medium indicate that this compound is produced through a minor, dead end path.

The objectives of this project were to further characterize the pathway of PNP degradation by isolates 443 and 402. The project involved three distinct approaches. One approach focused on the isolation and characterization of the enzyme responsible for reaction with PNP substrate. Another approach involved growing the bacterial strains under different conditions and analyzing the growth media in attempts to identify transient intermediates which may be on the pathway. The isolates were also examined for the capability of degrading compounds similar to PNP. If such similar pathways exist it may then be possible to identify intermediates analogous to those on the PNP pathway.

RESULTS AND DISCUSSION

Induction of JS443 and 402 with 4-nitrophenol. Previous results indicate that JS402 and JS443 cells which are grown on a PNP containing medium metabolize PNP rapidly and no intermediates were detected. It is possible that cells which
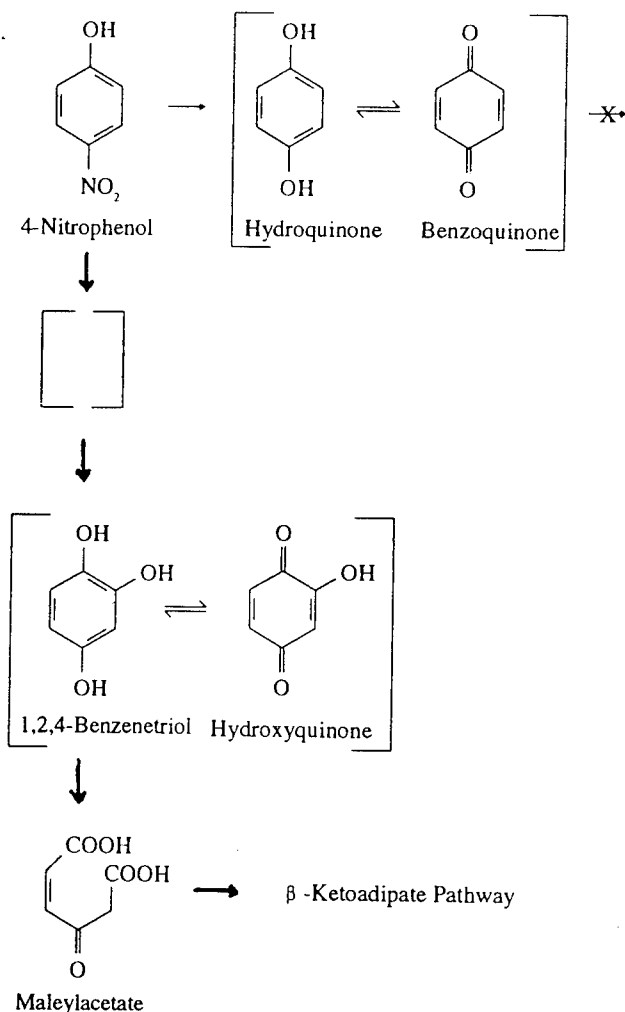
FIGURE 1. Biodegradation of 4-nitrophenol by JS402 and JS443. Bold arrows describe the main catabolic route. Results do not allow for identification of the oxidation state of the enzymatically formed compound and the equilibrium between the redox states of hydroquinone and 1,2,4-benzenetriol are shown in brackets. Empty brackets describe a possible and unidentified intermediate. Small amounts of hydroquinone which accumulate in the experiments indicate that this is a minor, dead end route.

are in the early stages of induction to use PNP might metabolize subsequent intermediates at a lower rate during the initial stages of induction. Washed, resting cells of yeast extract-grown JS443 cells were induced with PNP in an attempt to detect transient intermediates on the PNP degradation pathway. Supernatants from the induced culture were periodically removed and analyzed for

the presence of intermediates using reversed-phase high performance liquid chromatography. Results for JS443 are shown in Figure 2. Results using JS402 are similar but not included in this report. The induction experiment revealed a significant lag phase after which PNP was quickly degraded with stoichiometric release of nitrite. Significant amounts of 4-nitrocatechol (4NC) are detected early in the induction experiment but rapid PNP degradation and nitrite release does not occur until the latter stages of the experiment.
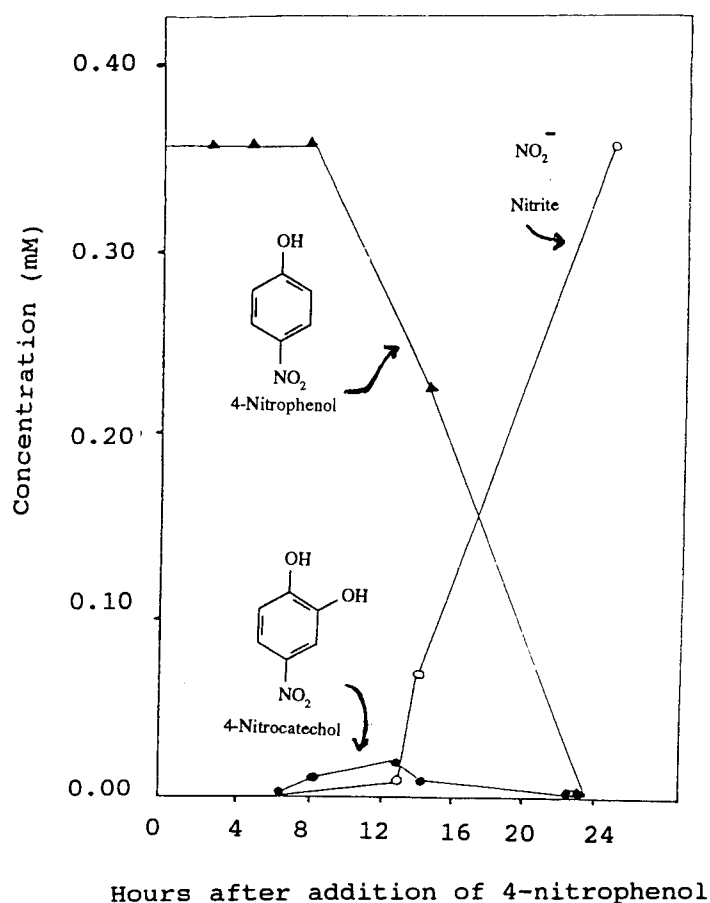
Figure 2. Induction of JS443 by 4-nitrophenol. Washed, yeast extract-grown JS443 cells are resuspended in 0.02 M phosphate buffer, pH 7.0. Addition of 50 ppm (0.36 Mm) 4-nitrophenol occurs at time zero. Aliquots are removed for analysis of 4-nitrophenol, 4-nitrocatechol and nitrite.
These results indicate that 4NC is a product of PNP oxidation by JS443.

Because of the initial slow rate of nitrite release which occurs during 4NC formation, however, one cannot conclude that 4NC is an intermediate in PNP degradation by JS443. That is, 4NC may not be present in a steady state condition in this experiment. These results suggest that further reaction of 4NC to BT and PNP to BT occur after another enzyme system is induced.

Reaction of JS402, JS443 and JS1490 with other substituted phenolic substrates. Results from studies on PNP degradation by JS443 indicate that induced cells rapidly degrade PNP. One possible reason for the rapid rate of PNP degradation by JS443 may be due to the fact that the nitro group is an excellent leaving group in aromatic nucleophilic substitution reactions (11). Halogen atoms are somewhat less electron withdrawing in this type of reaction. For this reason the monohalogenated phenols were used in an attempt to identify of intermediates on these degradation pathways. Activity of PNP grown JS443 was noted with 4-chlorophenol (4CP), 4-bromophenol (4BP) and 4-iodophenol (4IP). Slow degradation of 4-fluorophenol (4FP) was also noted. Results from oxygen uptake studies with PNP-grown JS443 are shown in Table 1. Similar rates of degradation were noted from experiments in which substrate degradation was monitored using HPLC analysis of substrates and intermediates (data not shown).

TABLE I. Oxygen consumption by PNP grown JS443.

Substrate (1.33×10^{-4} M)	Rate (μmoles/min/mg protein)
4-fluorophenol	< 1
4-chlorophenol	11
4-bromophenol	14
4-iodophenol	18

HPLC analysis of the reaction media was performed to identify intermediates in JS443 degradation of the halogenated phenols. Compounds with HPLC retention times corresponding to the 4-halogenated catechols were observed as transient intermediates in these experiments. GCMS analysis was used to identify the compound 4-chlorocatechol in ethyl acetate extracts of reaction media in which 4CP was used as substrate.

A mutant of JS443 which accumulates BT and also the oxidation product of BT,

hydroxybenzoquinone (HBQ), when incubated with PNP also accumulates HBQ when incubated with 4CP, 4BP and 4IP. These results support the hypothesis that JS443 and JS402 metabolize 4CP, 4BP and 4IP through BT in a pathway that appears to be the same as with PNP. As with the PNP pathway it remains to be determined if the 4-substituted catechol intermediate is in a steady state and on the major degradation path or if this compound is on a minor route of degradation.

In any case, these results reveal a newly identified pathway for 4-halophenol degradation which has not been previously identified. Our preliminary results indicate that 4-chlorophenol supports growth of JS443.

<u>Activity of cell-free extracts against substrates</u>. A variety of protocols were used in attempts to obtain cell-free extracts with enzymatic activity against PNP. A freeze-thaw procedure followed by sonication yielded cell-free extracts with high benzenetriol dioxygenase activity. No activity against PNP was observed in these experiments. A variety of cofactors including NAD$^+$, NADP$^+$, FAD, FMN, the reduced form of these compounds and a number of sulfhydryl reducing agents were used in the attempts without success.

<div align="center">SUMMARY</div>

The study of PNP degradation by a <u>Moraxella</u> sp. revealed the presence of an NADPH-dependent monooxygenase catalyzed step in the release of the nitro group as nitrite (2,3). In a study on the biodegradation of 2,4-dinitrotoluene by a <u>Pseudomonas</u> sp. it was demonstrated that a diooxygenase catalyzed step is responsible for release of the nitro group in the 4 position (13). The process results in release of nitrite and formation of 4-methyl-5-nitrocatechol. These results indicate that oxidative release of the aromatic nitro group can occur through either monooxygenase or dioxygenase catalyzed reactions.

This study on the degradation of PNP and other substituted aromatic compounds by JS443 and JS402 reveal the presence of an active monooxygenase enzyme which converts PNP to 4-nitrocatechol and 4CP to 4-chlorocatechol. The compound 4-nitrocatechol is subsequently converted to BT with release of nitrite. Our results also indicate that conversion of 4-chlorocatechol to BT is

the most likely route for degradation of this compound and we are currently developing a protocol to detect the chloride ion release which would be concomitant with such a scheme.

The slow rate of nitrite release after initial appearance of 4-nitrocatechol in uninduced cell systems (Figure 1), however, does not support the hypothesis that 4-nitrocatechol is an intermediate on the major PNP degradation route. Although 4-chlorocatechol was similarly observed in 4CP degradation by JS443 (data not shown), its appearance along with very slow 4CP degradation rates by uninduced cells is not conclusive evidence that a monooxygenase catalyzed reaction is the key step in the major degradation route of this compound by induced JS443.

The alternate monooxygenase product from PNP is 1,3-dihydroxy-4-nitrobenzene (4-nitroresorcinol, 4NR). No 4NR or 4-haloresorcinol was detected in any of the bacterial systems which were studied here. Substitution ortho to the hydroxy group on 4-substituted phenols is the predicted reaction based on the orientation and reactivity of the substituents on the aromatic ring. The OH group is an activating ortho-para director and the nitro group is meta directing and deactivating (11). Based on these activity rules, a monoxygenase catalyzed electrophilic aromatic substitution of PNP would be expected to yield 4-nitrocatechol. The compound 4-nitroresorcinol would not be expected as a product of such a reaction and is not observed.

Results from this project reveal the presence of an active monooxygenase system in induced JS443 and JS402. The monooxygenase system converts PNP to 4-nitrocatechol and 4CP to 4-chlorocatechol. These compounds are subsequently converted to BT. Degradation of PNP and 4CP through BT has not been previously reported. It remains to be determined if the monooxygenase catalyzed reactions are on the main route of PNP degradation through BT or if another enzymatic system is primarily responsible for the high rates of PNP degradation through BT by induced JS443 and JS402.

REFERENCES

1. Chapman, P. J., and D. W. Ribbons. 1976. Metabolism of resorcinylic compounds by bacteria: Alternative pathways for resorcinol catabolism in *Pseudomonas putida*. J. Bacteriol. 125:985-998.

2. Spain, J. C., O. Wyss, and D. Gibson. 1979. Enzymatic oxidation of p-nitrophenol. Biochem. Biophys. Res. Commun. 88:634-641.

3. Spain, J.C. and D. Gibson. 1991. Pathway for biodegradation of p-nitrophenol in a *Moraxella* sp.. Appl. Environ. Microbiol. 57:812-819.

4. Zeyer, J., and P. C. Kearney. 1984. Degradation of o-nitrophenol and m-nitrophenol by a *Pseudomonas putida*. J. Agric. Food Chem. 32:238-242.

5. Raymond, D. G. M., and M. Alexander. 1971. Microbial metabolism and cometabolism of nitrophenols. Pesticide Biochem. Physiol. 1:123-130.

6. Suzuki, K., T. Gomi, T. Kaidoh, and E. Itagaki. 1991. Hydroxylation of o-halogenphenol and o-nitrophenol. J. Biochem. 109:348-353.

7. Simpson, J. R., and W. C. Evans. 1953. The metabolism of nitrophenols by certain bacteria. Biochem. J. 55:xxiv.

8. Sudhakar-Barik, R. Siddaramappa, and N. Sethunathan. 1976. Metabolism of nitrophenols by bacteria isolated from parathion-amended flooded soil. Antonie van Leeuwenhoek 42:461-470.

9. Munnecke, D. M., and D. P. H. Hsieh. 1974. Microbial decontamination of parathion and p-nitrophenol in aqueous media. Appl. Microbiol. 28:212-217.

10. Spanggord, R. J., J. C. Spain, S. F. Nishino, and K. E. Mortelmans. 1991. Biodegradation of 2,4-dinitrotoluene by a *Pseudomonas* sp. 57:3200-3205.

11. March, J. 1968. Advanced Organic Chemistry. McGraw Hill, New York.

BUDGET

Personnel

Joseph H. Dreisbach, Ph.D Principal Investigator	$5,400.00
Christopher Shelley, B.S. Graduate Research Assistant	1,800.00
Stephanie Nilsen Undergraduate Research Assistant	1,800.00
Mary McHugh Undergraduate Research Assistant	2,000.00
Andrea V. Dreisbach, Ph.D. Postdoctoral Research Associate	1,900.00
Total Personnel	$12,900.00

Equipment

Linear Dual Channel Recorder	$ 1,133.24
HPLC Columns, Guard Cartridges, Column Stand	1,072.00
Eppendorf Micropipettes	997.15
LabLine Shaker Incubator	2,959.09
Shaker Clamps	333.20
Amicon French Pressure Mini Cell and Spacer	1,294.00
Bellco Shaker Flasks	708.84
Liquid-Liquid Extractor	232.70
Total Equipment	**$ 8,730.22**

Reagents and Consumable Supplies

General Substrates and Reagents	$ 324.10
^{14}-C Labelled 4-Nitrophenol (50 μCi)	541.00
^{18}-O$_2$ (99% enriched, 2 Liters) and Tank Charge	925.00
Electrophoresis Reagents	83.30
HPLC Grade Water and Solvents	104.95
Culture Tubes and Stoppers	147.24
Microbiological Media	175.85
Rheodyne Injector Syringe and Needles	72.00
Linear Recorder Chart Paper	102.00
PTFE Frit for HPLC Pump	18.40
HP Print Cartridges	71.70
Total Reagents and Consumable Supplies	**$ 2,565.54**

Total Expenditures from USAF-RDL RIP Grant #92-108 and University of Scranton Matching Funds	$24,195.76
Total Line Item Budget Originally Proposed	$24,000.00

TREATMENT OF NICKEL ELECTROLESS PLATING BATH WASTE
BY POLYMER COMPLEXATION

Douglas G. Klarup
Assistant Professor
Department of Chemistry

University of Montana
Missoula, MT 59812

TREATMENT OF NICKEL ELECTROLESS PLATING BATH WASTE BY POLYMER COMPLEXATION

Douglas G. Klarup
Assistant Professor
Department of Chemistry
University of Montana
Missoula, MT 59812

Abstract

The feasibility of using polymer-metal complexation in the treatment of spent electroless nickel plating bath solutions was explored. A twenty-eight equation equilibrium model was developed to model the polymer-metal interactions occurring in the bath solution. Approximately 60 g/L of polyethylenimine will complex virtually all of the metal found in the bath solution--nickel as well as contaminant zinc. Ultrafiltration to remove the polymer from the bath was not successful. However, dialysis with polyethylenimine isolated from the bath was successful in pulling out the metal. The addition of glutaraldehyde to the polymer-metal complex creates a gelatinous metal-polymer precipitate. This precipitation reaction has potential to remove all of the nickel and zinc from the bath solution.

Development of a phosphonomethylated poly(vinyl amine) polymer, capable of specifically complexing zinc and not nickel, was initiated. Preliminary results are encouraging, although much more characterization and development is required. This polymer, in conjunction with flow through dialysis, should be pursued as a means of recycling spent electroless nickel plating bath solutions.

TABLE OF CONTENTS

INTRODUCTION

Background

Metal plating baths are used in many Air Force installations to modify various parts to desired specifications. The baths function in different ways, but in general consist of large vessels containing the primary plating metal as well as supporting chemicals. The electroless nickel bath is a convenient bath for many reasons, but one disadvantage is that they become contaminated and require rather frequent disposal and replacement. Replacement of the baths is expensive (several thousand dollars per bath) and disposing of the old bath--which must be treated as hazardous waste--is also expensive. During the 1980's the Air Force supported research which tested the feasibility of chelation ion exchange as a means of recycling spent electroless plating baths.[1] In this technique the spent bath is pumped through a column containing a chelation ion exchange resin which, theoretically, will remove only contaminant ions and leave constituent ions, such as nickel and background electrolyte ions. The most promising resin was Duolite ES-467, manufactured by Rohm and Haas, which removed virtually all of the primary contaminant metal, zinc, while removing approximately thirty percent of the nickel. Unfortunately, regeneration of the resin (using HCl solution) proved to be difficult, and the resin fouled easily. The end result was contaminated resin, which needed to be disposed of as hazardous waste. Attempts at using chelation ion exchange to recycle electroless nickel plating baths have been abandoned, although this technique is used to treat acid etch baths.

The 1991 summer research project carried out by this researcher at Tyndall Air Force Base involved evaluation of complexation-ultrafiltration as an alternative to both chelation ion exchange and precipitation techniques for treatment of electroless nickel plating baths. In complexation-ultrafiltration a large polymer or macromolecule is present in a flow-through ultrafiltration cell. In theory the filter at the exit end

of the cell is fine enough to prevent the transmission of the polymer. The contaminated solution is pumped through the cell where the metals form a complex with the polymer. Those metal ions complexed are retained in the cell, of course, and effectively separated from the bulk solution.

The complete description of this research and its results can be found in the report entitled "The Comparison of Complexation-Ultrafiltration to Chelation Ion Exchange in the Treatment of spent Electroless Nickel Plating Baths" submitted to Research and Development Labs in September, 1991. In brief, we were able to show that complexation-ultrafiltration has the potential to treat spent electroless nickel plating baths but the quantitative numbers obtained were from limited data and a simplified model. In addition, the polymer used, polyethylenimine, was selective toward nickel over zinc, the reverse of the ideal situation.

RIP Project

The flow chart shown in Figure 1 describes the organization of the research we have used over the past year to extend the work done in Summer, 1991. We had three main goals: (1) show conclusively whether or not complexation-ultrafiltration could be used to remove metals from the electroless plating bath, (2) develop chemical equilibrium models which allow detailed understanding of the complexation process in the nickel electroless bath, and (3) synthesize a phosphonomethylated poly(vinyl amine) (PPA) polymer which would be highly selective toward zinc over nickel for use in complexation-removal of zinc, the primary cause of the need for bath disposal and replacement.

The first two of these goals have been completed, while the third is partially completed but needs further characterization. A detailed description of our results follows.

COMPLEXATION-REMOVAL

Ultrafiltration

The work completed the summer of 1991 showed that complexation-

ultrafiltration had the ability to remove metals from the electroless bath. However, no experiments were completed showing that all of the metal could be removed, i.e., zero discharge was not investigated. Therefore, we needed to know whether or not all of the metal waste could be collected using complexation-ultrafiltration. We chose polyethylenimine (PEI) as our model polymer, because of its availability and proven metal-complexation capability.[2]

Several experiments were performed by adding varying amounts of PEI to a clean (no contaminants) nickel electroless plating bath. We did not include contaminants so as to minimize difficulties in results interpretation. As the PEI was added, the pH rose and the color of the bath moved from green to blue. After PEI addition, the treated samples were placed in an ultrafiltration cell, the cell pressurized, and the effluent from the cell analyzed for Ni using Atomic Absorption Spectroscopy (AAS).

Initial results showed that, as was found in the Summer of 1991, PEI complexed much of the nickel. However, we had severe leakage through the ultrafilter. 20,000 dalton Nominal Molecular Weight Cut Off (NMWCO) filters were used initially, then 1000 NMWCO filters, but in either case leakage was observed. The color of the effluent indicated that it was the polymer-complex breaking through the filter, not that free nickel ions were present.

Figure 2 is a schematic of an cellulose-ester ultrafiltration membrane. There is a range of pore sizes present in these filters. It is our belief that some of the pores are large enough, and probably some fraction of the PEI small enough, to allow some passage of the polymer complex, perhaps spurred on by concentration-polarization[3] within the ultrafiltration cell. Concentration-polarization results from making the solution inside an ultrafiltration cell increasingly concentrated and then pushing this solution toward the filter.

For some applications, a small amount of leakage could be tolerated,

but here we are trying to remove all of the metal, and because each polymer has many metal atoms complexed with it, leakage of even a small amount results in significant metal transport across the membrane.

Another problem encountered with ultrafiltration was filtration time. Particularly with the 1000 NMCO filter, it took approximately 48 hours to filter even a small amount of solution. This is unacceptable in any practical application.

Dialysis

Given the problem with ultrafiltration, we turned to straight dialysis (see Figure 3). Here one is still depending upon the use of a membrane to separate large from small molecules, but the driving force is molecular diffusion, not pressurization. Experiments were conducted as follows (see Table I): A solution with PEI was placed in a large test tube. A dialysis bag (1000 MWCO) containing straight bath solution was lowered into this PEI solution. Equilibration of the solution was complete within 24 hours, but usually 48 hours were allowed to pass before analysis using AAS.

Table I

Mass Bath Solution	Mass Water Outside	Mass PEI Outside	ppm-Ni
16.697	71.155	1.270	24 - in 1254 - out
16.981	71.146	1.267	0 - in 1062 - out
19.656	37.27	.734	0 - in 2046 - out

This process proved to be very satisfactory. We observed no polymer leakage across this membrane, allowing virtually complete removal of the

nickel from the bath solution and ensuring we had reasonable numbers to check our equilibrium models (see below).

Based on these experiments, we have concluded that complexation-ultrafiltration using cellulose-ester filters does not allow complete removal of metals from nickel electroless plating baths. Evidently, concentration-polarization within the ultrafiltration cell places a high concentration of metal-polymer near the filter, resulting in small but significant leakage through the filter. Additionally, the amount of pressure required and length of time filtration takes probably make this technique prohibitive.

Dialysis shows, on the other hand, that the chemistry of this process is quite valid, and separation is feasible. There are industrial applications of dialysis, so this could be applied to the nickel plating bath as well.

Dialysis experiments using zinc and PEI were also carried out. As was found in the summer of 1991, however, zinc does not complex as readily with PEI as nickel, so removal of only zinc using complexation-dialysis and PEI is not feasible.

Reaction with glutaraldehyde

In the presence of glutaraldehyde, PEI will form very stable ring structures around transition metal ions[4], resulting in a "fixed" metal. We explored this reaction as a means of removing metals from the waste stream in a quantitative fashion.

The experiments were done by adding stoichiometric amounts of PEI (assuming 4 amine groups bind to a single metal ion) and glutaraldehyde to a solution of nickel plating bath containing 200 ppm zinc contaminant. The mixture immediately formed a yellow-green sludge, which upon heating turned brown. It was heated for 2.5 days at 70-80°C. After centrifugation d filtration through a 1 μm filter, the remaining solution showed nick and zinc concentrations of 18% and 41% of the original, respectively. K ping in mind that some of the precipitate probably came through the 1 μm filter,

it is apparent that this reaction does work although the selectivity of Ni over Zn means it is not a logical treatment choice if bath recycling is desired. It would be effective for total metal removal, but is probably not cost effective when compared to conventional treatment options.


ELECTROLESS PLATING BATH COMPLEXATION -- MODEL

In order to better understand the chemistry of the plating bath, and the complexation between the polymers and metals in the baths, detailed equilibrium models have been developed. The models are based on using PEI as the complexing polymer, but now that they are developed, they could easily be applied to other polymers as well. We have considered what most probably are the most relevant chemical interactions is the system.

Electroless Nickel Plating Bath--Description

The electroless nickel bath used by the Air Force consists of the following reagents and their amounts:

$NiSO_4$	24 g/L
$Na_3C_6H_5O_7$	85 g/L
NaH_2PO_2	10 g/L
NH_4Cl	50 g/L

and the chemical reaction responsible for the plating action is:[5]

$$NiSO_4 + 3H_2O + 3NaH_2PO_2 \text{ --- } Ni(0) + 3NaH_2PO_3 + 2H_2 + H_2SO_4$$
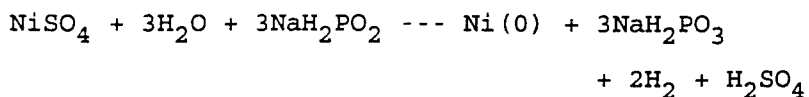
The bath is a high ionic strength, buffered bath with a pH of 4.4-4.6. The hypophosphite is the reducing agent used to convert nickel(II) to nickel(0). This reaction requires a catalytic surface: the piece being plated. Even with the catalytic surface, the above reaction is slow, so the bath is heated to 180° F to speed the reaction up. To maintain stability in the bath at this temperature, a complexing agent, in this case citrate, is added. Without this complexing agent, the reduction reaction

occurs spontaneously, and catalytic particles of Ni metal form in the solution.

As the bath ages several things begin to happen. Small particles form in the solution either as a result of dust contamination, spontaneous reaction, or metal phosphite precipitation. These small particles may serve as catalytic surfaces. In addition, since the solution is acidic with a complexing agent, metal atoms from the plating pieces are dissolved into the solution, contaminating it. Eventually, the degradation of the bath occurs to such a degree that it no longer functions as effectively as desired, and must be replenished, recycled, or replaced. Macroscopic techniques such as filtration can remove the particulate contaminants, but they will not remove the metal ion contaminants.

Chemical Equilibrium Model Using PEI

Table II shows the equilibrium species and reactions used in developing a model describing the addition of PEI to a synthetic solution of electroless plating bath (see Appendix I). The hypophosphite is neglected, primarily because of its relatively small concentration, particularly in the spent solution. This model is a 28 equation model designed for the nickel-PEI interaction. We assume that the dominant species is the NiL_4, indicating that four amine groups from the PEI bind to a single Ni ion. The amine groups were split into three different types: 1,2,3, each with different KHL and $KNiL_4$ constants. The ratio of concentration of these groups was 1:2:1, following the number of primary, secondary, and tertiary amine groups found in commercial PEI.

The model was tested by following the pH of a solution of bath while titrating with PEI and comparing the experimental pH to that predicted by the model. Titrations were done under N_2 to minimize CO_2 absorption. The initial result is shown in Figure 4, where literature values of KHL and $KNiL_4$ are used in the model and only one type of ligand is assumed. As the figure clearly shows, agreement between model and experiment is quite poor.

Table II

Species	Equation		Species	Equation
L_1	$L_{1\text{-total}}$		H_2Cit^{-1}	$KCit_2$
L_2	$L_{2\text{-total}}$		$HCit^{-2}$	$KCit$
L_3	$L_{3\text{-total}}$		Cit^{-3}	$Citrate_{\text{-total}}$
HL_1+	KHL_1		$NiOH^+$	$KNiOH$
HL_2^+	KHL_2		$NiNH_{31}^{2+}$	$KNiNH_{31}$
HL_3^+	KHL_3		$NiNH_{32}^{2+}$	$KNiNH_{32}$
NiL_{41}^{2+}	$KNiL_{41}$		$NiNH_{33}^{2+}$	$KNiNH_{33}$
NiL_{42}^{2+}	$KNiL_{42}$		$NiNH_{34}^{2+}$	$KNiNH_{34}$
NiL_{43}^{2+}	$KNiL_{43}$		$NiNH_{35}^{2+}$	$KNiNH_{35}$
Ni^{2+}	Ni_{total}		$NiNH_{36}^{2+}$	$KNiNH_{36}$
OH^-	K_w		NiH_2Cit^+	$KNiH_2Cit$
NH_4^+	KNH_4		$NiHCit$	$KNiHCit$
NH_3	$NH_{3\text{-total}}$		$NiCit^-$	$KNiCit$
H_3Cit	$KCit_1$		H^+	Charge Balance

Where L is the amine ligand of PEI (three different types), and equations beginning with K indicate dissociation equilibrium constant expressions generally, but formation constant expressions for the metal-polymer formation.

Predicting how much PEI would be required to complex all of the nickel is not going to be accurate unless better values to use in the model are found. The fact that even the initial pH, before any PEI is added, is so far from the experimental value indicates that the problem is not restricted to the PEI itself.

The difficulty comes from using literature values for theequilibrium constants. These literature values are measured under much more ideal conditions than those found in the nickel electroless plating bath. Figure 5 shows the result of changing the ionic strength on the pH of a solution of citrate. The effect is quite large, and combined with all of the interactions no doubt going on in the high-salt bath solution, no doubt can account for the large discrepancy found between model and experiment. In the interests of time we found that by arbitrarily increasing the amount of acid in the solution, the model behaved much better, as can be seen in Figure 6.

Arbitrarily adding acid improves the general match of the pH value, but as can be seen in Figure 6, the points at which curvature occurs is still poor. This is due to the model maintaining constant $KNiL_4$ and KHL values. Complexed PEI is a polyelectrolyte, and as the amount of positive charge accumulates on an individual molecule of PEI, it becomes increasing difficult to complex more metal or H^+. We need to have some way to account for this.

The first step to correct for this polyelectrolyte effect was to get values for KHL which would reflect the effect. To do this, we titrated PEI with HCl (Figure 7) in a 1.9 M ionic strength solution (Figure 8 shows that ionic strength will also effect these titrations). We assumed three different types of amine groups, and fitted three KHL values to get a close match between the model prediction and the experiment. The values obtained, assuming L ratios of 1:2:1, were 4.64e-11, 1e-8, 2.15e-4 (pKa's of 10.33, 8.0, and 3.67) (See Appendix II).

These three values were then used in the bath-polymer model. Figure

9 shows the results of using these KHL values, and fitting three $KNiL_4$

values to get agreement between experiment and model. The model results

give $KNiL_4$ values of 3.16e5, 1e14, and 1e37. The value of 1e37 suggests

that the formation constant at the beginning of the complexation is quite

high. Its actual value is questionable, since the reason the match came in

so high was to match pH values in the latter half of the titration, when

the nature of the solution has changed significantly from the first half,

when the acid value in the model was arbitrarily adjusted. If fact, if the

model is fitted to complexed nickel data, then the KNiL4 values become

5.0e4, 7.1e14, and 2.5e10, more realistic numbers. Figure 10 shows the

result of using these KNiL4 values to model the experimental titration. It

is apparent that the pH values calculated are worse than those found with

the larger KNiL4, but the predicted amount of nickel which is complexed by

the PEI remains the same. Also, the portion of the titration where the pH

match is bad is in the non-nickel solution, where the adjustments made to

force the model to fit (the arbitrary addition of acid to the model) are no

longer be valid.

Figure 11 shows the model prediction of the ionic strength as PEI is

added to solution. It is apparent that with such changes in solution

character, conditional equilibrium constants made at one point in the

titration are likely to be different at another point.

This perhaps seems like a lot of model adjusting, in order to get a

match. However, Figure 12 shows that the extent of complexation predicted

by the model is reasonably good, and our fiddling is empirically confirmed.

This figure shows the results of dialysis experiments where bath with and

without PEI was placed on either side of a 1000 MWCO membrane, allowed to

come to equilibrium and analyzed with AAS.

Although the model predicts the behavior or PEI in the nickel bath

solution, measurement of all equilibrium constants used in the model, under

the type of conditions experienced in the plating bath, would provide a

better theoretical basis for the model.

If warranted, a similar model can be developed for any metal, and then a large model for many metals developed. This is not really justified if only PEI is considered, since it preferentially binds nickel over zinc, forcing the removal of all of the metal to remove the contaminant, but may be justified, eventually, with the PPA polymer currently under development. With these models in hand, we should be able to understand and predict the bath behavior with PPA quite well and determine the feasibility of using this polymer to treat spent electroless nickel plating bath solutions.

The model and experiments done to date with PEI suggest that with the addition of enough PEI to make an L/M (amine group/metal ion) ratio of 10/1 will remove virtually all of the metal. In a typical plating bath, containing 8 g/L nickel and .2 g/L zinc, this would require the addition of about 60 g/L PEI. This is quite different than one would predict if trying to remove metal from a non-bath solution, where no citrate or ammonia complexes exit. The citrate and ammonia keep the metals from complexing with the polymers, meaning additional polymer is required. This is a similar phenomenon as is found with conventional precipitation treatments[6], and is accounted for in the model.

DEVELOPMENT OF THE PHOSPHONOMETHYLATED POLY(VINYL AMINE)

The use of PEI as a complexing polymer was useful for many reasons. It allowed us to check the viability of ultrafiltration and dialysis as means of removing metals form the nickel electroless plating bath. In addition, it made it possible to develop a methodology to modeling and understanding the interactions between the bath constituents and the polymers used for complexation. However, if PEI is the polymer used for bath treatment, the goal must be to remove all of the metal present in the solution. This is because the affinity between nickel and PEI is so very high.

Clearly, it is desirable to develop a way to either remove only the contaminants from the bath (as was attempted with chelation ion exchange), or at the very least extend the lifetime of a given bath. To do this, a

different polymer must be used. Ultimately we would like to use this better polymer to either (a) add to the bath solution to complex the zinc and "remove" this contaminant from the bath chemistry, or more likely (b) use it in conjunction with dialysis to remove the zinc, leaving the nickel behind in solution. This latter use would mimic the attempts made with chelation ion exchange, except there would be no resin to foul and the overall cost should be less. Some metal waste would still exist, but it would be much reduced.

To develop this polymer, we looked to find one which had the functional groups similar to Duolite-467, the Rohm and Haas chelation ion exchange resin which successfully selected zinc over nickel. The main difficulty with the resin was regeneration, a step we are not concerned with. The other problem with the resin was the removal of about 30% of the nickel. We found this does occur when the pH of the solution is 4.5. However, if the pH is dropped to 3-3.5, then virtually no nickel is complexed. Therefore, we feel the functional group found on this resin is the best place begin our polymer development.

The chemical literature gave one cite[7] concerning a polymer with the relevant function group, a phosphonomethylated amine ($-NH-CH_2-PO_3H_2$). It was listed in German patent literature, but is not commercially available. After failing to get BASF (the owners of the German Patent) to synthesize some of this polymer for testing, we decided to undertake the synthesis ourselves. Unfortunately, the starting material, n-vinyl formamide, is not readily available. It was not until September of 1992 that we were able to obtain any at all, and this was sent to us from Mitsubishi in Japan. Therefore, the synthesis of this polymer is still in the beginning stages. Initial attempts have resulting in polymer formation, but much more characterization is required.

The PPA synthesis is as follows. A solution of acrylic acid and n-vinyl formamide and a solution of t-butyl perethylhexanoate in isopropanol were simultaneously dropped into refluxing isopropanol. Nitrogen gas

flowed over the solution the entire time. The solution was refluxed for two hours, during which the polymer $[-CH_2-CH(CO_2H)-]_4 - [-CH_2-CH(NHCHO)-]$ formed. At this point, the solution was treated with concentrated hydrochloric acid, then phosphorous acid and formaldehyde and refluxed. Upon neutralization, the solid polymer salt drops out of solution. After filtering and repeated washing with methanol, the polymer $-[-CH_2-CH(CO_2H)-]_4 -- [-CH_2-CH(NHCH_2PO_3H_2)-]$ is formed.

Bidentate chelation to a transition metal ion such as nickel or zinc occurs between the nitrogen atom and an oxygen atom of the phosphono group. Our results of complexation of these metals to this polymer are preliminary only, but we do see complexation of zinc occurring. For example, in a dialysis experiment where contaminated bath was inside a 1000 MWCO bag, and [2.8 mg PPA Na-polymer/g solution] outside, we found that whereas no nickel was complexed (the nickel concentrations were the same inside as outside the bag), the final zinc concentration outside the bag was 170% higher that inside, and higher than the expected concentration if no complexation had occurred. However, this did not happen when a solution of polymer and bath, rather than just polymer and water, was outside the dialysis bag, so further investigation and explanation is required. We plan to answer these questions in the near future, but at this point it does appear somewhat encouraging.

CONCLUSIONS and FUTURE WORK

Polymer complexation remains a potential means of recycling and treating nickel electroless plating bath solutions. Polyethylenimine, the polymer used most in this study, is able to complex virtually all of the nickel in the bath solution, so theoretically could be used to separate or concentrate the waste metals from the waste stream.

Ultrafiltration with cellulose-ester filters, however, does not allow sufficient separation to enable zero-discharge to occur. Also, the filtration times are very long. Both of these facts suggest that complexation-ultrafiltration is not suitable for bath treatment. It may be

that radiation formed filters (Nucleopore), which have more uniform pore sizes, could provide better separation, although the filtration time will most likely still be quite long.

The addition of glutaraldehyde to the polyethylenimine created a sludge product which removed much of the metal from the spent bath solution. However, the selectivity remained similar to that of polyethylenimine alone, so no real advantage, in terms of bath recycling, is gained. If total metal removal is required, polyethylenimine with glutaraldehyde provides a viable alternative to conventional treatment processes, where a hazardous waste sludge is the result.

Although ultrafiltration does not appear promising at this point, we had good success with straight dialysis. We were able to remove all of the nickel from the bath solution using PEI in water outside a dialysis bag containing the nickel bath. In an industrial setting, this would probably work using a flow through dialysis system, where the bath is passed by a dialysis membrane, the other side of which resides the water/PEI solution. The flow through experiment should be done to determine the feasibility of this method.

We feel quite confident of the ability of PEI to remove or concentrate metals, so this polymer would be appropriate if total metal removal is the goal. However, ultimately, we would like to be able to remove only contaminant metal and the leave the nickel alone; we want to recycle the bath, not dispose of it. PEI is not an appropriate polymer for this, since nickel complexes with PEI quite readily. Recycling calls for a different polymer, and we have taken initial steps towards its synthesis. We have a polymeric material, PPA, which in a water solution does pull zinc through a dialysis membrane. However, much more characterization of the polymer and the dialysis process are required before we can claim success.

When we have convinced ourselves that we have synthesized the PPA polymer, evaluation of the polymer's ability to complex zinc in the nickel bath is the next step. This is where the work reported here with PEI will

be so valuable. We know that we need to characterize the acid/base characteristics of the PPA, just as was done with PEI. We have a equilibrium model which can be easily modified for PPA. And we have a solid experimental protocol to follow. This PPA line of research looks encouraging, and we plan to pursue it vigorously in the upcoming months.

REFERENCES

1. (a) "Purifying Air force Plating Baths by Chelate Ion Exchange", Report No. AFE-0277-FMI-8340-1, July 16, 1985.; (b) "Selective Ion Exchange Pilot Plant Demonstration Project", prepared for the Air Force Engineering and Services Center, Tyndall Air Force Base by Battelle Columbus Division, January 12, 1989.

2. Kobayashi, Shiro, Hiroishi, Kazuhisa, Tokunoh, Masazumi, and Saegusa, Takeo. Macromolecules **20** (1987), 1296-1500.

3. Mulder, Marcel. Basic Principles of Membrane Technology, Kluwer Academic, Boston, 1991.

4. Suh, Junghun; Cho, Younghee; Lee, Kyung Joo. "Macrocyclic Metal Complexes Built on Polyethylenimine," J. Am. Chem. Soc., 1991, 113, 4198-4202.

5. Murphy, James A., ed., Surface Preparation and Finishes for Metals, Society of Manufacturing Engineers, Maple Press Company, Caledonia, 1971.

6. (a) Peters, Robert W. and Ku, Young. Particulate Science and Technology **6 (1988)**, 421-439. (b) Peters, Robert W. and Ku, Young. Particulate Science and Technology **6 (1988)**, 441-466.

7. Mohr, Juergen, et. al. "Phosphonomethylated poly(vinyl amines) as wash formulation additive and water-treatment chemicals." Ger. Offen. DE 3926059, 1991.

FIGURE CAPTIONS

Figure 1. A flow chart of the project. PEI refers to polyethylenimine and phosphono refers to the phosphonomethylated poly(vinyl amine) polymer (PPA in text. The project was designed to use PEI as a model polymer to help in testing equilibrium models and experimental techniques.

Figure 2. A schematic of an cellulose ester ultrafiltration membrane. Note the variety of pore sizes.

Figure 3. A schematic of the equilibrium dialysis experiment. In some of the experiments, the initial outside solution was simply the polymer in water.

Figure 4. The comparison of the equilibrium model predictions to the experimental results for the addition of PEI to a nickel plating bath solution. L represents amine groups. Literature values for the equilibrium constants were used. Note the large deviation of model predictions from the experimental results, even before the addition of PEI. The use of Debye-Huckle activity coefficients improves the model a slight amount, but the ionic strength of the solution is far beyond the applicable range for Debye-Huckel values.

Figure 5. The pH of a solution of trisodium citrate as a function of citrate formality and ionic strength. The boxes are the values found with a pure water solvent. The plus signs are the values found with the solvent 1 M KNO_3. Note the large difference between the two, indicating the dependence of equilibrium constants on ionic strength.

Figure 6. The comparison of the equilibrium model predictions to the experimental results for the addition of PEI to a nickel plating bath

solution. The acid concentration has been artificially adjusted in the model so that the initial (before the addition of PEI) pH value predicted matches the experimental value. L/Ni is the ratio of amine groups to nickel atoms in the solution.

Figure 7. The titration of PEI with hydrochloric acid. The experimental pH values are designated by the solid line. The circles represent the pH values found by fitting three K_a values to the data. The K_a values were fit assuming three different amine groups in the PEI with a ratio of 1:2:1. The initial ionic strength of the solution was 1.9 M (adjust with KNO_3). The polyelectrolyte effect is quite evident here, with no sharp break in the titration curve.

Figure 8. The titration of PEI with HCl as a function of ionic strength (adjusted with KNO_3). Note that as in all of the equilibria found in the bath system, the equilibrium constants involved will be ionic strength dependent.

Figure 9. The comparison of the equilibrium model predictions to the experimental results for the addition of PEI to a nickel plating bath solution. Three formation constants for the Ni-PEI complex have been used to fit the pH value data, assuming three different amine groups with a 1:2:1 ratio. The fit is quite good. The 10^{37} value is reached by the fitting program due to trying to fit all of the points--even those after virtually all of the nickel has complexed. Any fitting accomplished on these latter points is suspect, because the conditions under which the program were optimized (the acid artificially added) are much different than those found at this point of the titration. Fitting to the actual amount of nickel complexed (Figure 10) does not lead to this high number.

Figure 10. The comparison of the equilibrium model predictions to the

experimental results for the addition of PEI to a nickel plating bath solution. The Ni-PEI formation constants were fit to the complexed-Ni data found via dialysis experiments. The pH fit is adequate during the initial portion of the titration, but quite poor in the latter half. We believe this is because the nature of the solution has changed significantly by this point, and our equilibrium constant values are no longer correct.

Figure 11. A plot of the ionic strength of the solution as a function of PEI addition to the nickel plating bath. Note that the ionic strength after the complexation of the nickel is significantly different than that found before the addition of PEI. This may account for the poor model pH value prediction near the end of the PEI addition, since the model was optimized (acid artificially added) before the addition of any PEI.

Figure 12. The comparison of the equilibrium model predictions to the experimental results for the addition of PEI to a nickel plating bath solution. Two model results are shown. The model using only literature equilibrium constants, and the model after optimizing at the initial point (artificially adding acid) and assuming three different amine groups, each with a different K_a and Ni-PEI formation constant. The optimized model fits the experimental data much better.

Figure 1

Figure 2

DIALYSIS BAG CLIP

BATH SOLUTION
WITH POLYMER

DIALYSIS BAG
[1000 MWCO]

BATH SOLUTION
WITHOUT
POLYMER

TEST TUBE

Figure 3

PEI in Ni Bath

Figure 4.

Figure 5

3-27

PEI in Ni Bath
NO3 Adjusted

Figure 6

K1=4.6e−11
K2=1.0e−8
K3=2.2e−4
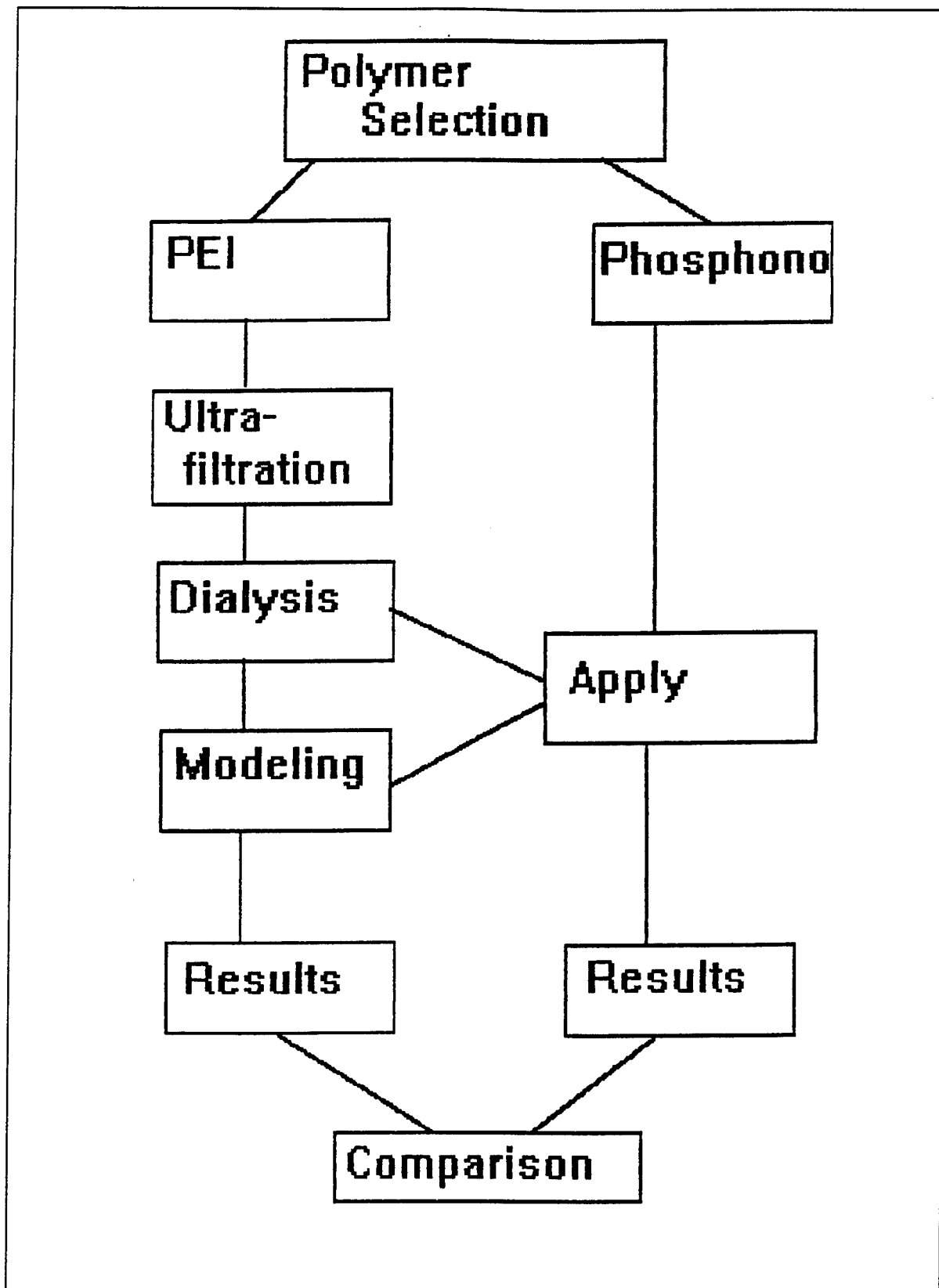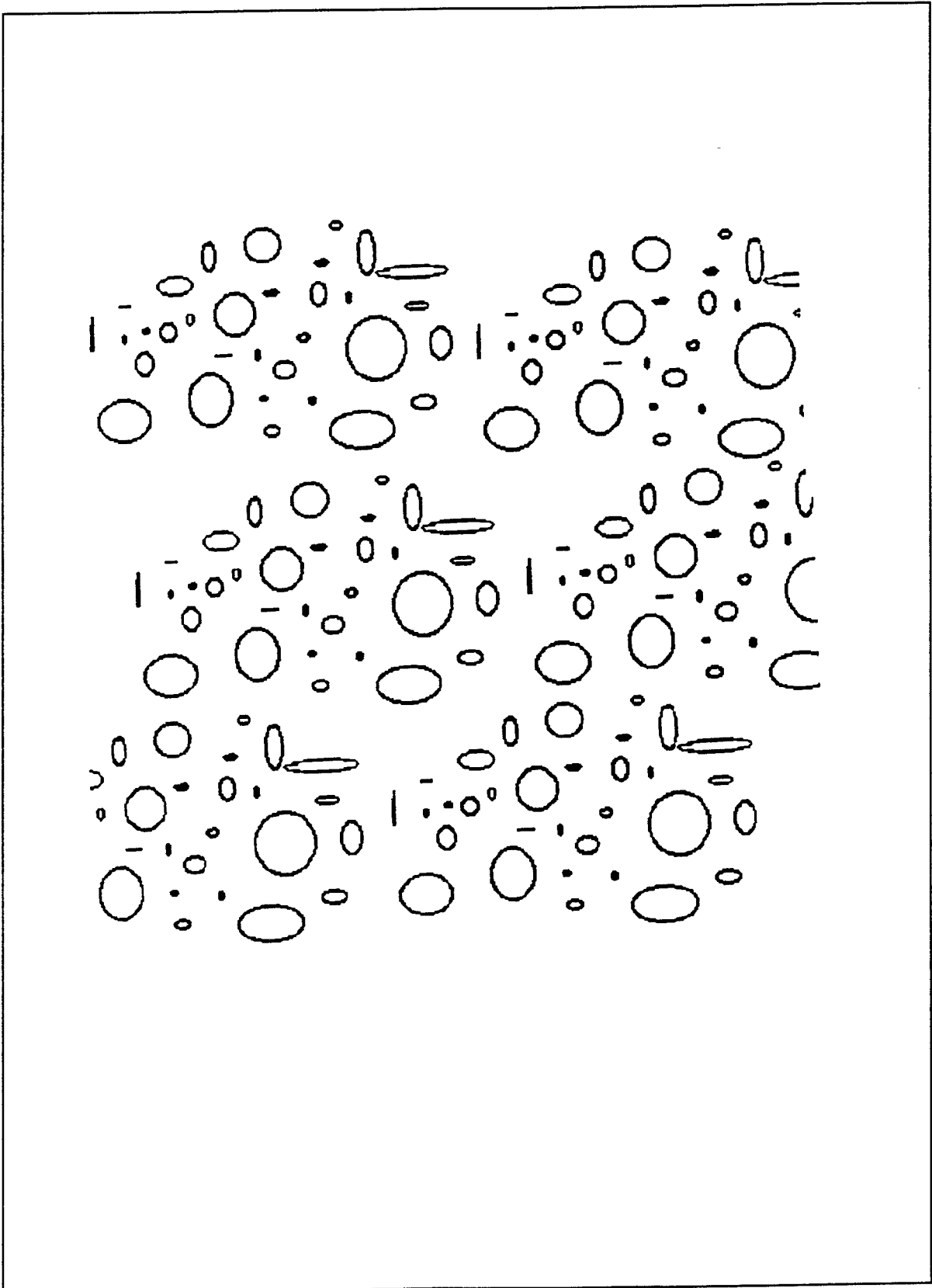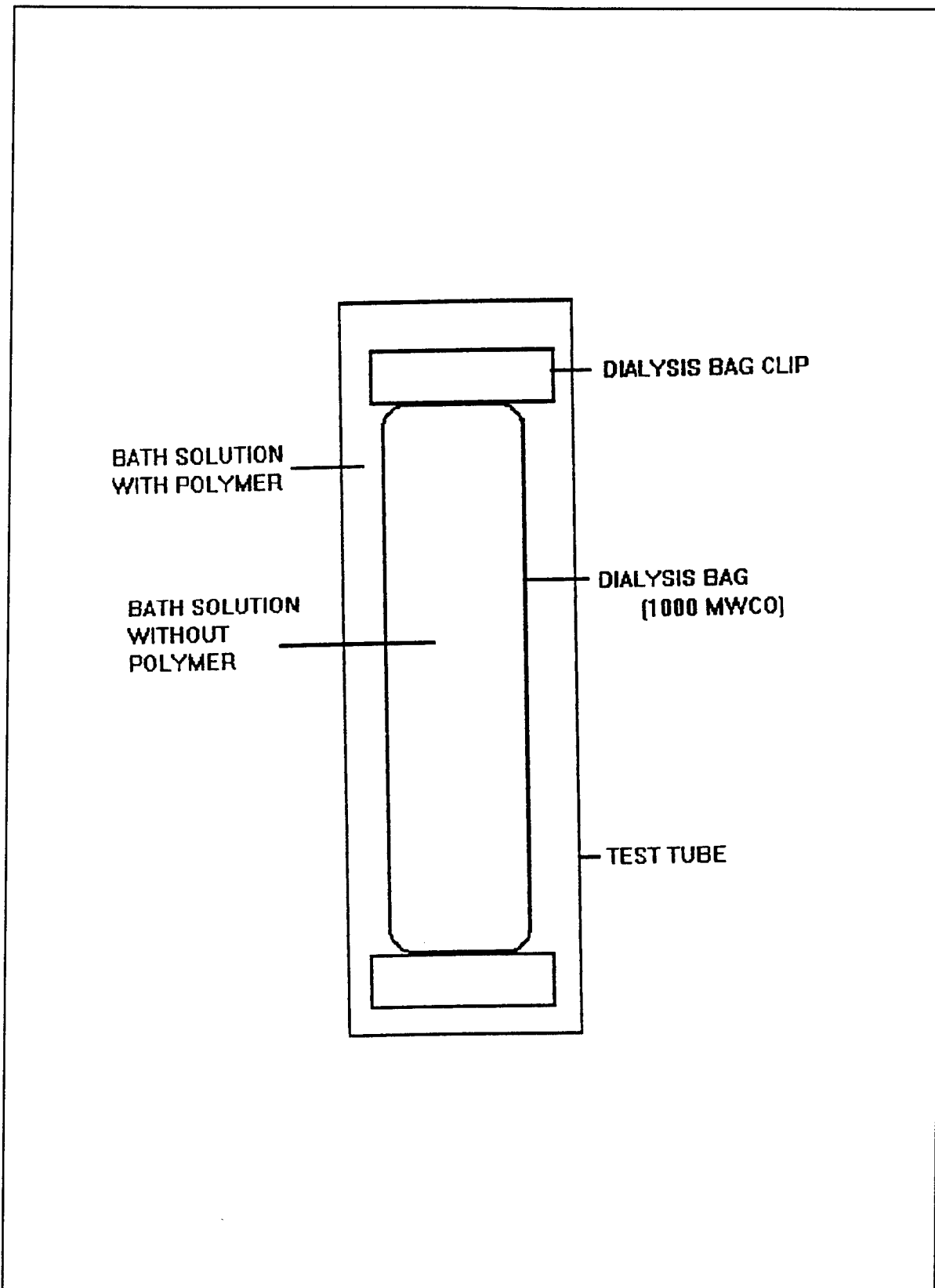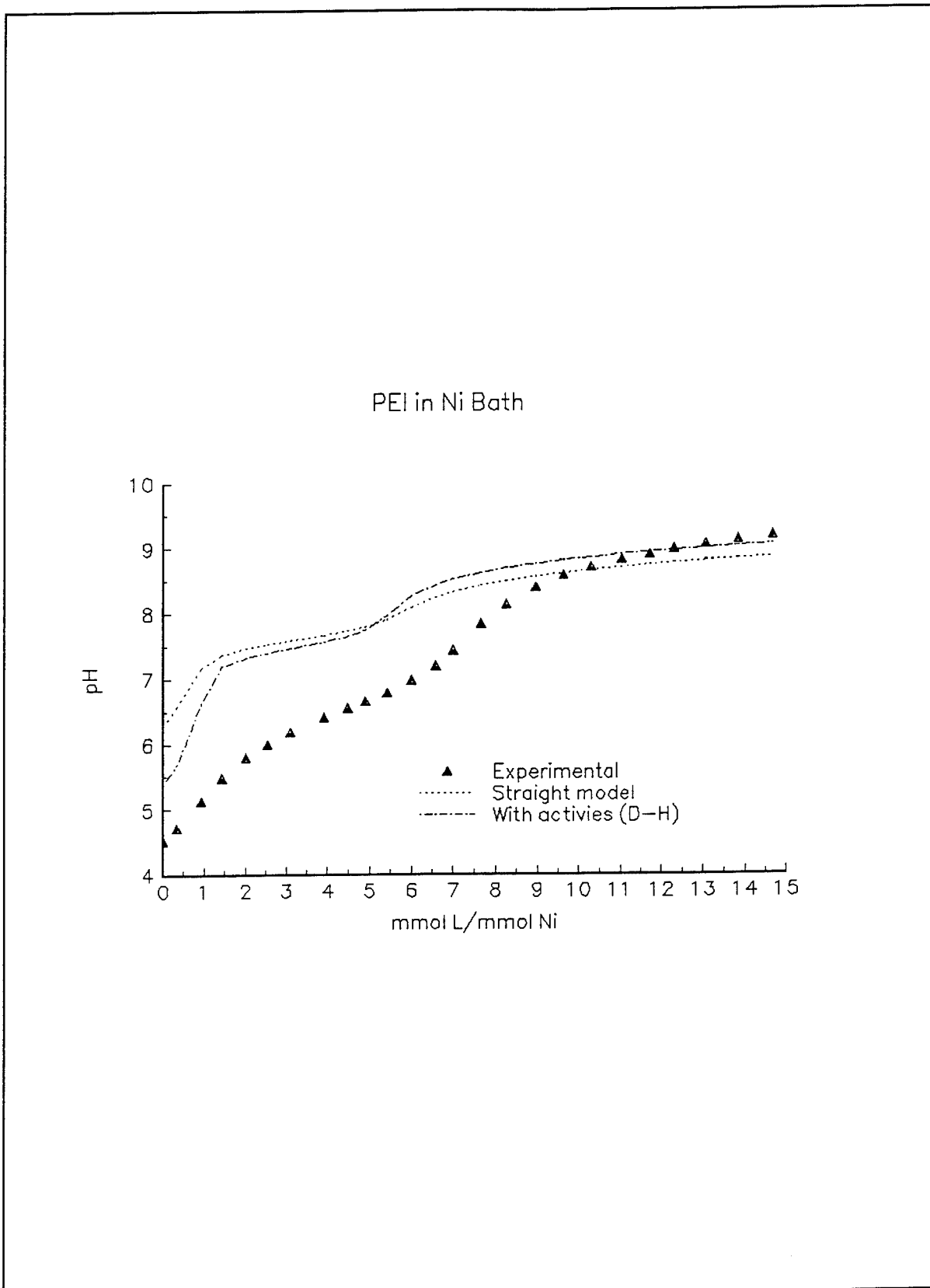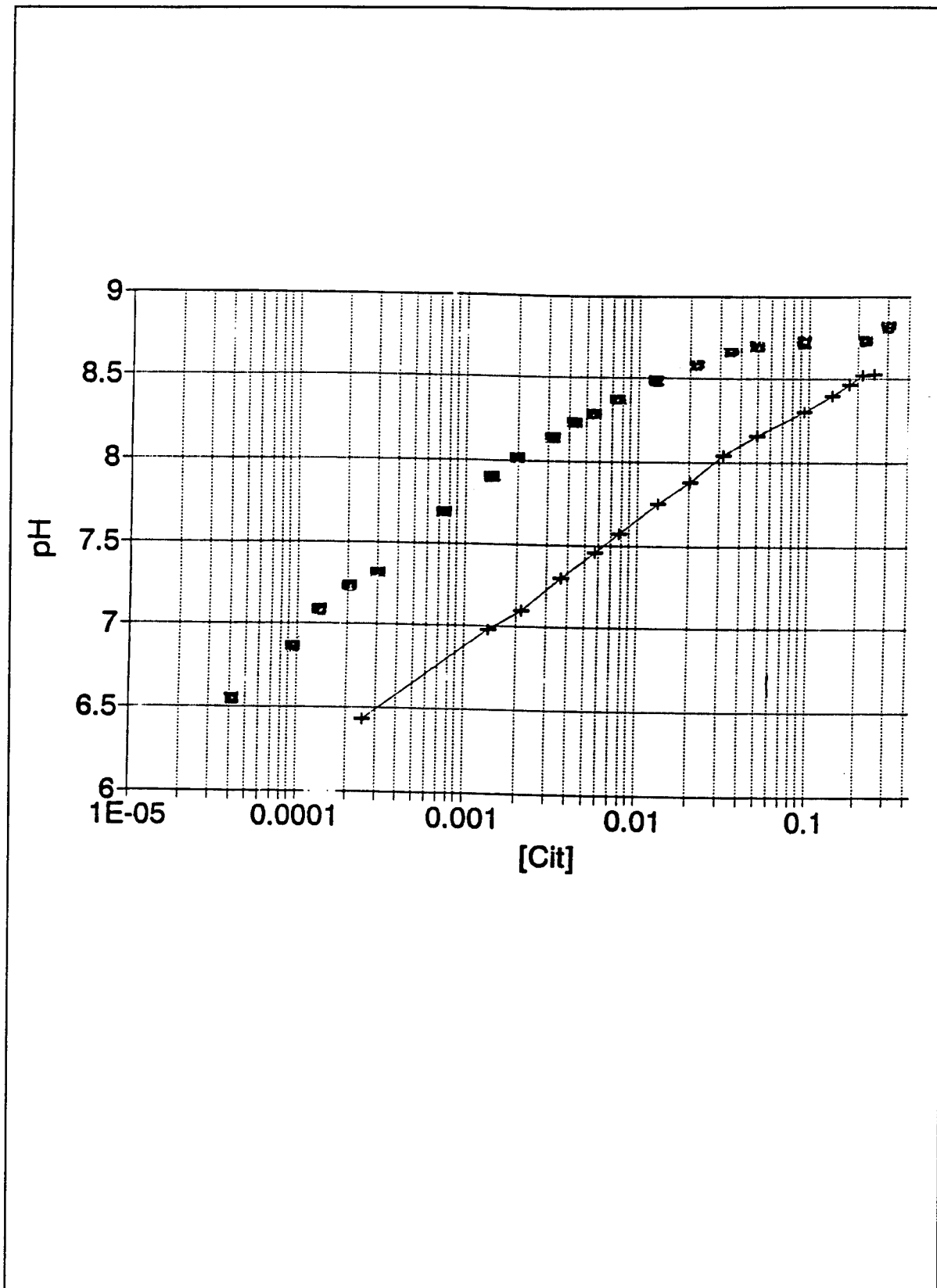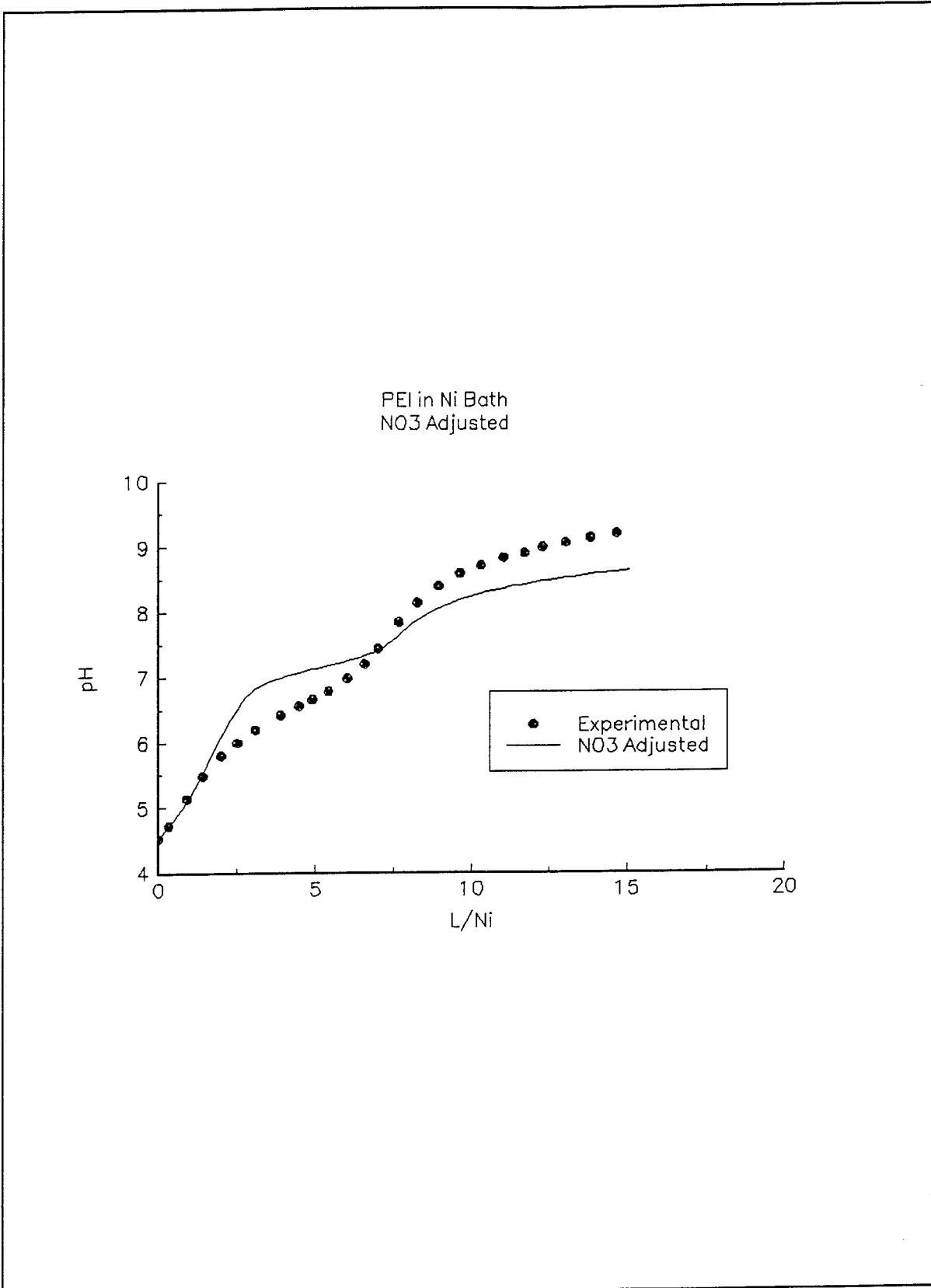
Figure 7

PEI Titrations
Ionic Strength Effect

Figure 8
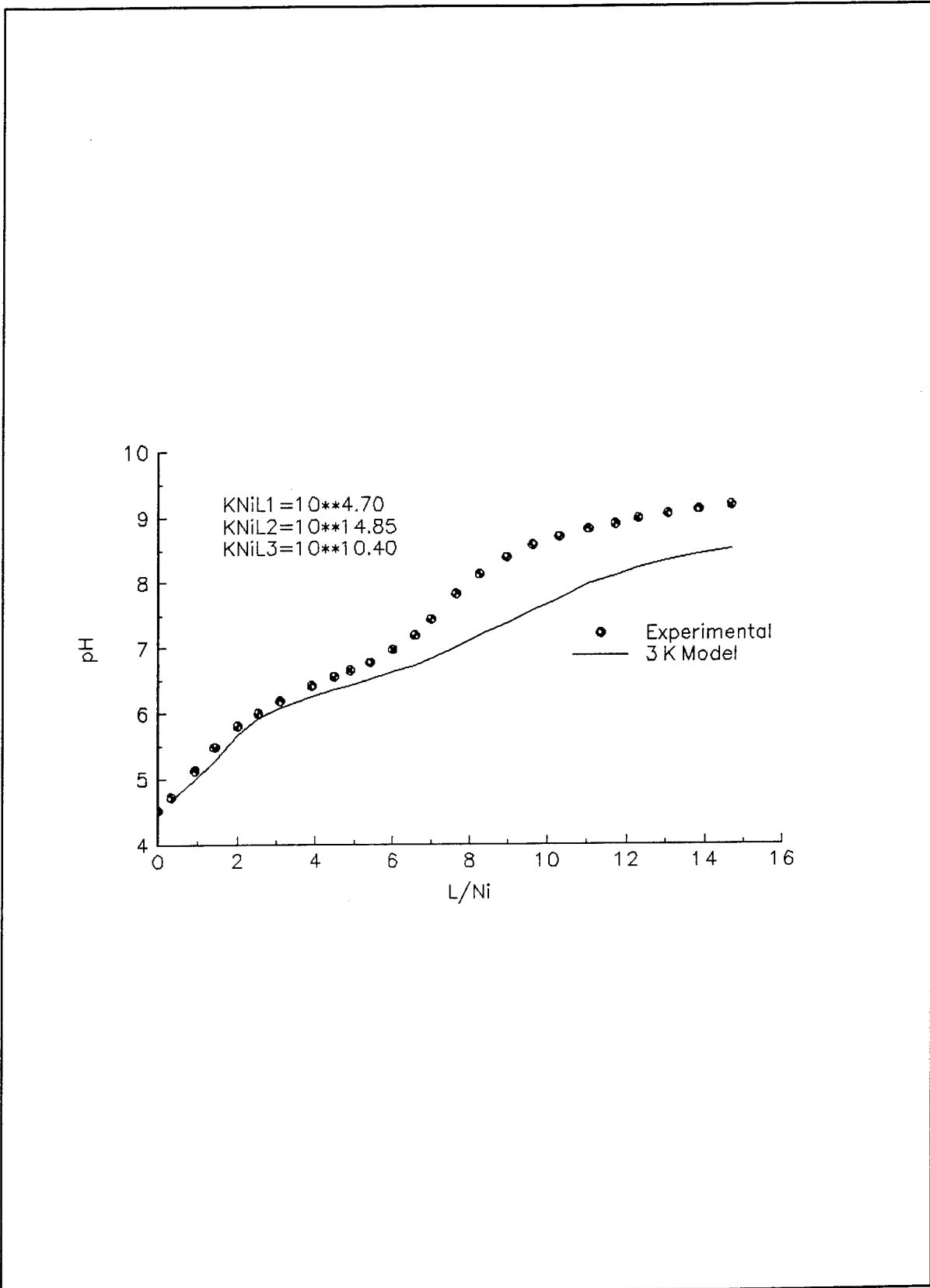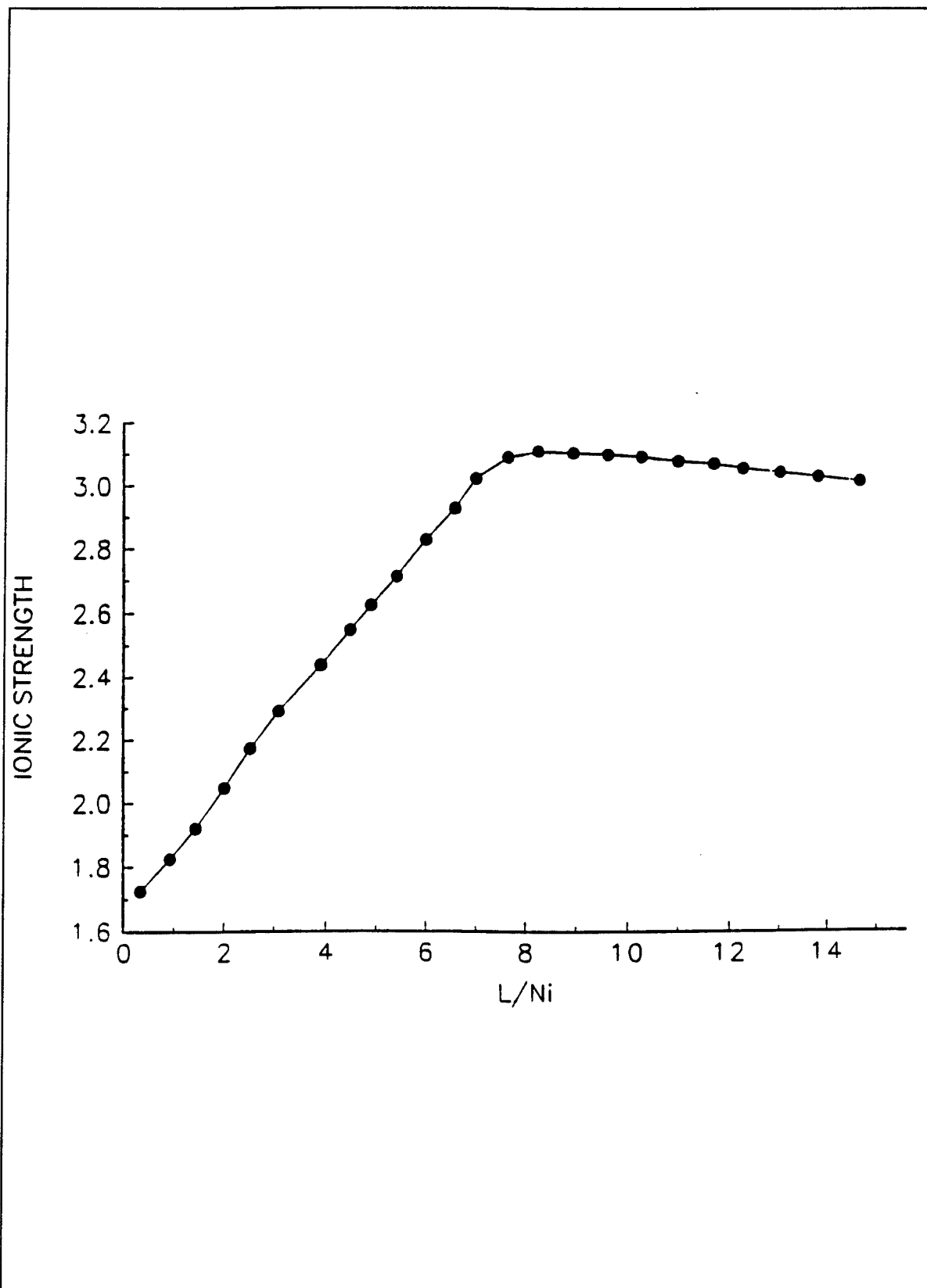
Figure 9

KNiL1 =10**4.70
KNiL2=10**14.85
KNiL3=10**10.40
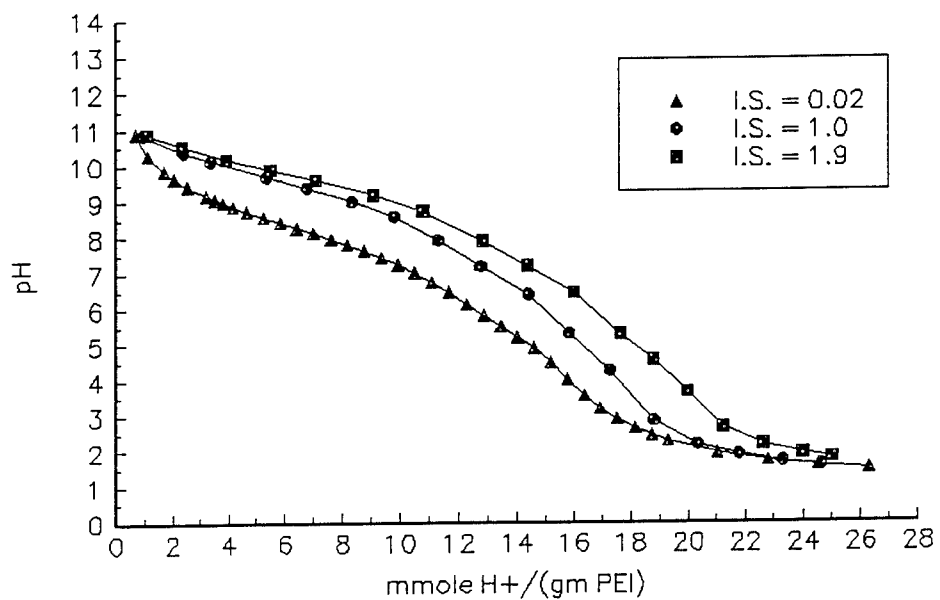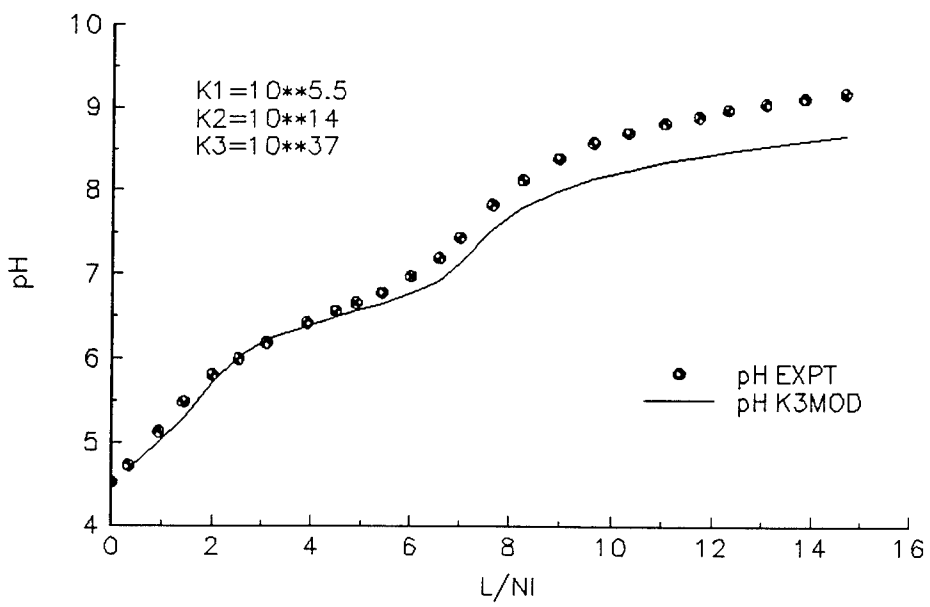
Figure 10

Figure 11

PEI in Ni Bath
Soluble Nickel

.... Literature Knl
—·—·— pH and Knl Adjusted
▲ Experiment
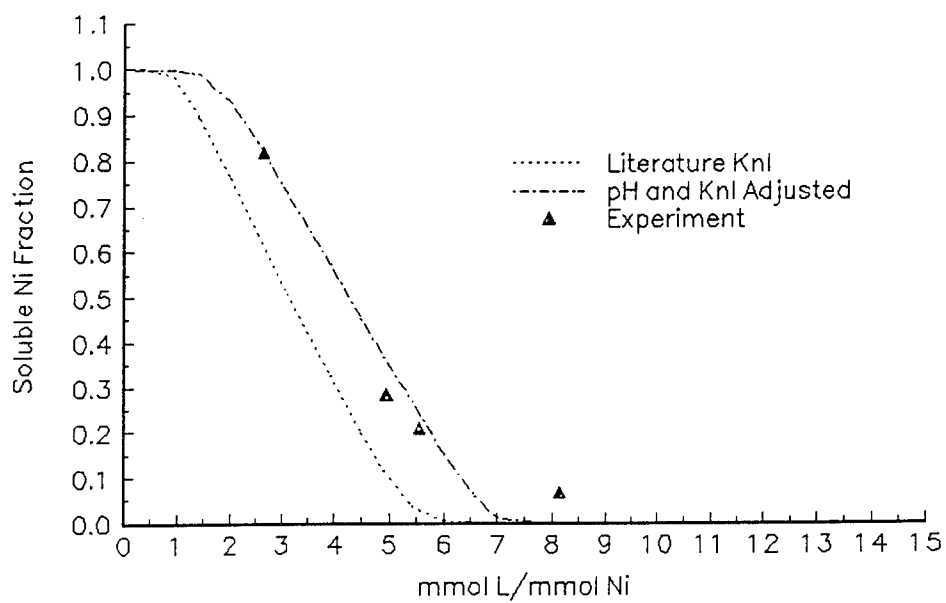
Figure 12

FORTRAN program calculated model pH and nickel complexed with PEI

```
        DOUBLE PRECISION ALPHA(28,28),BETA(28),INDX(28),VV(100)
        DOUBLE PRECISION X(28),COMNI,SOLNI,PH,RNIL41,RNIL42
        DOUBLE PRECISION SUM,ERRF,ERRX,LOGARG,RNIL43
        DOUBLE PRECISION TOLX,TOLF
        DOUBLE PRECISION A,B,C,XSAVE(28),LOGDEN
        DOUBLE PRECISION REVY(769,6),EMULT,ERRSUM,ERRTRACK
        REAL CK(24)
        REAL MA,MB,MC,CSET,BSET
        COMMON Y(6)
10      FORMAT(E40.26)
11      FORMAT(F12.6,4F9.6)
12      FORMAT(4E20.10)
13      FORMAT(F12.6)
14      FORMAT(3F6.2,2E20.8)
C       COMMENTS
        N=28
        NP=N
        LOGARG=10
        LOGDEN=LOG(LOGARG)
C       READ IN CHECK VALUES
        OPEN(UNIT=1,FILE='KNUCKS.PR')
        DO 16 I=1,24
        READ(1,13) CK(I)
16      CONTINUE
        CLOSE(1)
C       READ IN GUESS VALUES
          OPEN(UNIT=2,FILE='KNILCAL8ORIG.DAT')
            DO 30 I=1,NP
          READ(2,10) X(I)
30      CONTINUE
        CLOSE (2)
C   IMPORT Y VALUES, WITH ORDER CITTOT, NH3TOT, NO3,
C   NITOT,LTOT
C
C         OPEN FILE FOR RESULTS
        OPEN (UNIT=5, FILE='KNILTEST.REC')
C       ASSIGN KNIL4 VALUES HERE
        RNIL41=10**(5.50)
        RNIL42=10**(14.00)
        RNIL43=10**(37.00)

        OPEN (UNIT=3,FILE='KNIFAORIG.PR')
        DO 3000 NUM=1,769
          READ(3,11) Y(1),Y(2),Y(3),Y(4),Y(5)
C
          NTRIAL=1000
          TOLX=1E-16
          TOLF=1E-16
40      CONTINUE
        CALL MNEWT(NTRIAL,X,N,TOLX,TOLF,RNIL41,RNIL42,RNIL43)
C
        PH=-(LOG(X(28))/LOGDEN)
C
        DO 80 I=1,24
        IF (Y(5).EQ.CK(I)) WRITE(5,12) Y(5)/Y(4),.5*(
     ++X(4)+X(5)+X(6)+X(11)+X(12)+X(15)+X(18)+X(26)
```

```
        ++X(27)+X(28)+4*(X(7)+X(8)+X(9)+X(10)+X(16)+X(19)
        ++X(20)+X(21)+X(22)+X(23)+X(24))+9*X(17)+3*Y(1)+Y(3)
        ++4*Y(4))
80      CONTINUE
3000    CONTINUE
        CLOSE(3)
        CLOSE(5)
        END
        SUBROUTINE MNEWT(NTRIAL,X,N,TOLX,TOLF,RNIL41,RNIL42,RNIL43)
        PARAMETER (NP=28)
        DOUBLE PRECISION X(NP),ALPHA(NP,NP),BETA(NP),INDX(NP)
        DOUBLE PRECISION ERRF,ERRX,SUM,TOLX,TOLF
        DOUBLE PRECISION RNIL41,RNIL42,RNIL43
        INTEGER NTRIAL,K,N
C
10      FORMAT(E20.10)
        DO 13 K=1,NTRIAL
        CALL USRFUN(X,ALPHA,BETA,NP,RNIL41,RNIL42,RNIL43)
        ERRF=0
        DO 11 I=1,N
          ERRF=ERRF+ABS(BETA(I))
11      CONTINUE
C       PRINT *, 'ERRF='
C       WRITE(*,10) ERRF
C       WRITE(*,10)
        IF (ERRF.LE.TOLF) RETURN
        CALL LUDCMP(ALPHA,N,NP,INDX,D)
        CALL LUBKSB(ALPHA,N,NP,INDX,BETA)
        ERRX=0
        DO 12 I=1,N
        ERRX=ERRX+ABS(BETA(I))
        X(I)=X(I)+BETA(I)
12      CONTINUE
C       PRINT*, 'ERRX='
C       WRITE(*,10) ERRX
C       WRITE(*,10)
        IF (ERRX.LE.TOLX) RETURN
13      CONTINUE
        RETURN
        END
        SUBROUTINE USRFUN(X,ALPHA,BETA,NP,RNIL41,RNIL42,RNIL43)
        DOUBLE PRECISION X(NP),ALPHA(NP,NP),BETA(NP)
        DOUBLE PRECISION RNIL41,RNIL42,RNIL43
        COMMON Y(6)
        DOUBLE PRECISION SODIUM,CL,MF,AH,RNIL4
        DOUBLE PRECISION H,OH,LTOT1,LTOT2,LTOT3
        PARAMETER (RCIT1=7.44000000E-4,RCIT2=1.73E-5,RCIT3=4.02E-7)
        PARAMETER (RNH4=5.70E-10,RW=1.0E-14)
        PARAMETER (RNIHCIT=5.0125E-4,RNIH2CIT=1.7857E-2)
        PARAMETER (RNINH31=2.1368E-3)
        PARAMETER (RNINH32=7.5188E-3,RNIOH=2.5119E-5)
          PARAMETER (RNINH33=2.439E-2,RNINH34=8.547E-2)
        PARAMETER (RNINH35=2.3641E-1)
        PARAMETER (RNINH36=1.2346)
        PARAMETER (RNICIT=3.9811E-6)
        PARAMETER (RHL1=4.6419E-11,RHL2=1E-8,RHL3=2.1528E-4)
C
        SO4=Y(4)
        SODIUM=3*Y(1)
C
        CL=Y(2)
        LTOT1=.25*Y(5)
```

```
        LTOT2=.5*Y(5)
        LTOT3=.25*Y(5)
        DO 10 I=1,NP
        BETA(I)=0
        DO 8 J=1,NP
        ALPHA(I,J)=0
8       CONTINUE
10      CONTINUE
        BETA(1)=-(LTOT1-X(1)-X(4)-4*X(7))
         ALPHA(1,1)=-1
         ALPHA(1,4)=-1
         ALPHA(1,7)=-4
        BETA(2)=-(LTOT2-X(2)-X(5)-4*X(8))
         ALPHA(2,2)=-1
         ALPHA(2,5)=-1
         ALPHA(2,8)=-4
        BETA(3)=-(LTOT3-X(3)-X(6)-4*X(9))
         ALPHA(3,3)=-1
         ALPHA(3,6)=-1
         ALPHA(3,9)=-4
        BETA(4)=-(RHL1*X(4)-X(1)*X(28))
         ALPHA(4,4)=RHL1
         ALPHA(4,1)=-X(28)
         ALPHA(4,28)=-X(1)
        BETA(5)=-(RHL2*X(5)-X(2)*X(28))
         ALPHA(5,5)=RHL2
         ALPHA(5,2)=-X(28)
         ALPHA(5,28)=-X(2)
        BETA(6)=-(RHL3*X(6)-X(3)*X(28))
         ALPHA(6,6)=RHL3
         ALPHA(6,3)=-X(28)
         ALPHA(6,28)=-X(3)
        BETA(7)=-(RNIL41*X(10)*X(1)**4-X(7))
         ALPHA(7,7)=-1
         ALPHA(7,10)=RNIL41*X(1)**4
         ALPHA(7,1)=RNIL41*X(10)*4*X(1)**3
        BETA(8)=-(RNIL42*X(10)*X(2)**4-X(8))
         ALPHA(8,8)=-1
         ALPHA(8,10)=RNIL42*X(2)**4
         ALPHA(8,2)=RNIL42*X(10)*4*X(2)**3
        BETA(9)=-(RNIL43*X(10)*X(3)**4-X(9))
         ALPHA(9,9)=-1
         ALPHA(9,10)=RNIL43*X(3)**4
         ALPHA(9,3)=RNIL43*X(10)*4*X(3)**3
        BETA(10)=-(Y(4)-X(7)-X(8)-X(9)-X(10)-X(18)-X(19)-X(20)
      +-X(21)-X(22)-X(23)-X(24)-X(25)-X(26)-X(27))
         ALPHA(10,7)=-1
         ALPHA(10,8)=-1
         ALPHA(10,9)=-1
         ALPHA(10,10)=-1
         ALPHA(10,18)=-1
         ALPHA(10,19)=-1
         ALPHA(10,20)=-1
         ALPHA(10,21)=-1
         ALPHA(10,22)=-1
         ALPHA(10,23)=-1
         ALPHA(10,24)=-1
         ALPHA(10,25)=-1
         ALPHA(10,26)=-1
         ALPHA(10,27)=-1
        BETA(11)=-(RW-X(11)*X(28))
         ALPHA(11,11)=-X(28)
```

```
      ALPHA(11,28)=-X(11)
   BETA(12)=-(RNH4*X(12)-X(13)*X(28))
     ALPHA(12,12)=RNH4
     ALPHA(12,13)=-X(28)
     ALPHA(12,28)=-X(13)
   BETA(13)=-(Y(2)-X(12)-X(13)-X(19)-2*X(20)-3*X(21)-4*X(22)
  +-5*X(23)-6*X(24))
     ALPHA(13,12)=-1
     ALPHA(13,13)=-1
     ALPHA(13,19)=-1
     ALPHA(13,20)=-2
     ALPHA(13,21)=-3
     ALPHA(13,22)=-4
     ALPHA(13,23)=-5
     ALPHA(13,24)=-6
   BETA(14)=-(RCIT1*X(14)-X(15)*X(28))
     ALPHA(14,14)=RCIT1
     ALPHA(14,15)=-X(28)
     ALPHA(14,28)=-X(15)
   BETA(15)=-(RCIT2*X(15)-X(16)*X(28))
     ALPHA(15,15)=RCIT2
     ALPHA(15,16)=-X(28)
     ALPHA(15,28)=-X(16)
   BETA(16)=-(RCIT3*X(16)-X(17)*X(28))
     ALPHA(16,16)=RCIT3
     ALPHA(16,17)=-X(28)
     ALPHA(16,28)=-X(17)
   BETA(17)=-(Y(1)-X(14)-X(15)-X(16)-X(17)-X(25)-X(26)-X(27))
     ALPHA(17,14)=-1
     ALPHA(17,15)=-1
     ALPHA(17,16)=-1
     ALPHA(17,17)=-1
     ALPHA(17,25)=-1
     ALPHA(17,26)=-1
     ALPHA(17,27)=-1
   BETA(18)=-(RNIOH*X(18)-X(10)*X(11))
     ALPHA(18,18)=RNIOH
     ALPHA(18,10)=-X(11)
     ALPHA(18,11)=-X(10)
   BETA(19)=-(RNINH31*X(19)-X(10)*X(13))
     ALPHA(19,19)=RNINH31
     ALPHA(19,10)=-X(13)
     ALPHA(19,13)=-X(10)
   BETA(20)=-(RNINH32*X(20)-X(19)*X(13))
     ALPHA(20,20)=RNINH32
     ALPHA(20,19)=-X(13)
     ALPHA(20,13)=-X(19)
   BETA(21)=-(RNINH33*X(21)-X(20)*X(13))
     ALPHA(21,21)=RNINH33
     ALPHA(21,20)=-X(13)
     ALPHA(21,13)=-X(20)
   BETA(22)=-(RNINH34*X(22)-X(21)*X(13))
     ALPHA(22,22)=RNINH34
     ALPHA(22,21)=-X(13)
     ALPHA(22,13)=-X(21)
   BETA(23)=-(RNINH35*X(23)-X(22)*X(13))
     ALPHA(23,23)=RNINH35
     ALPHA(23,13)=-X(22)
      ALPHA(23,22)=-X(13)
   BETA(24)=-(RNINH36*X(24)-X(23)*X(13))
     ALPHA(24,24)=RNINH36
     ALPHA(24,23)=-X(13)
```

```fortran
      ALPHA(24,13)=-X(23)
     BETA(25)=-(RNIH2CIT*X(25)-X(10)*X(15))
      ALPHA(25,25)=RNIH2CIT
      ALPHA(25,10)=-X(15)
      ALPHA(25,15)=-X(10)
     BETA(26)=-(RNIHCIT*X(26)-X(10)*X(16))
      ALPHA(26,26)=RNIHCIT
      ALPHA(26,10)=-X(16)
      ALPHA(26,16)=-X(10)
     BETA(27)=-(RNICIT*X(27)-X(10)*X(17))
      ALPHA(27,27)=RNICIT
      ALPHA(27,10)=-X(17)
      ALPHA(27,17)=-X(10)
     BETA(28)=-(X(4)+X(5)+X(6)+2*(X(7)+X(8)+X(9)+X(10))-X(11)+X(12)
    +-X(15)-2*X(16)-3*X(17)+X(18)+2*(X(19)+X(20)+X(21)+X(22)+X(23)
    ++X(24))+X(25)-X(27)+X(28)+SODIUM-CL-Y(3)-2*SO4)
      ALPHA(28,4)=1
      ALPHA(28,5)=1
      ALPHA(28,6)=1
       ALPHA(28,7)=2
      ALPHA(28,8)=2
      ALPHA(28,9)=2
      ALPHA(28,10)=2
      ALPHA(28,11)=-1
      ALPHA(28,12)=1
      ALPHA(28,15)=-1
      ALPHA(28,16)=-2
      ALPHA(28,17)=-3
      ALPHA(28,18)=1
      ALPHA(28,19)=2
      ALPHA(28,20)=2
      ALPHA(28,21)=2
      ALPHA(28,22)=2
      ALPHA(28,23)=2
      ALPHA(28,24)=2
      ALPHA(28,25)=1
      ALPHA(28,27)=-1
      ALPHA(28,28)=1
     RETURN
     END
     SUBROUTINE LUDCMP(ALPHA,N,NP,INDX,D)
     PARAMETER (NMAX=100,TINY=1E-20)
     INTEGER N
      DOUBLE PRECISION ALPHA(NP,NP),INDX(N),VV(NMAX)
     DOUBLE PRECISION SUM,AAMAX,DUM
     D=1.
     DO 12 I=1,N
          AAMAX=0
        DO 11 J=1,N
        IF (ABS(ALPHA(I,J)).GT.AAMAX) AAMAX=ABS(ALPHA(I,J))
11    CONTINUE
     IF (AAMAX.EQ.0.) PAUSE 'SINGULAR MATRIX'
     VV(I)=1./AAMAX
12    CONTINUE
     DO 19 J=1,N
        DO 14 I=1,J-1
        SUM=ALPHA(I,J)
        DO 13 K=1,I-1
             SUM=SUM-ALPHA(I,K)*ALPHA(K,J)
13    CONTINUE
     ALPHA(I,J)=SUM
14    CONTINUE
```

```fortran
      AAMAX=0
      DO 16 I=J,N
      SUM=ALPHA(I,J)
      DO 15 K=1,J-1
          SUM=SUM-ALPHA(I,K)*ALPHA(K,J)
15    CONTINUE
      ALPHA(I,J)=SUM
      DUM=VV(I)*ABS(SUM)
      IF (DUM.GE.AAMAX) THEN
          IMAX=I
          AAMAX=DUM
      ENDIF
16    CONTINUE
      IF (J.NE.IMAX) THEN
      DO 17 K=1,N
          DUM=ALPHA(IMAX,K)
          ALPHA(IMAX,K)=ALPHA(J,K)
          ALPHA(J,K)=DUM
17    CONTINUE
      D=-D
      VV(IMAX)=VV(J)
      ENDIF
      INDX(J)=IMAX
      IF (ALPHA(J,J).EQ.O) ALPHA(J,J)=TINY
      IF (J.NE.N) THEN
          DUM=1./ALPHA(J,J)
      DO 18 I=J+1,N
          ALPHA(I,J)=ALPHA(I,J)*DUM
18    CONTINUE
      ENDIF
19    CONTINUE
      RETURN
      END
      SUBROUTINE LUBKSB(ALPHA,N,NP,INDX,BETA)
      INTEGER N
      DOUBLE PRECISION ALPHA(NP,NP),INDX(N),BETA(N)
      DOUBLE PRECISION SUM
      II=0
      DO 12, I=1,N
      LL=INDX(I)
      SUM=BETA(LL)
      BETA(LL)=BETA(I)
      IF (II.NE.0) THEN
          DO 11 J=II,I-1
          SUM=SUM-ALPHA(I,J)*BETA(J)
11    CONTINUE
      ELSE IF (SUM.NE.0) THEN
          II=I
      ENDIF
      BETA(I)=SUM
12    CONTINUE
      DO 14 I=N,1,-1
      SUM=BETA(I)
      IF(I.LT.N) THEN
          DO 13 J=I+1,N
          SUM=SUM-ALPHA(I,J)*BETA(J)
13    CONTINUE
      ENDIF
      BETA(I)=SUM/ALPHA(I,I)
14    CONTINUE
      RETURN
      END
```

FORTRAN program fitting three KHL values for use in equilibrium model.

```
          DOUBLE PRECISION ALPHA(8,8),BETA(8),INDX(8),VV(100)
          DOUBLE PRECISION X(8),A,B,C,XSAVE(8)
           DOUBLE PRECISION REVY(705,5),EMULT
          DOUBLE PRECISION SUM,ERRF,ERRX,ERRSUM,ERRTRACK
          DOUBLE PRECISION TOLX,TOLF,PHX,PHY,LOGDEN
          REAL MA,MB,MC,CSET,BSET
          COMMON R(3)
          COMMON Y(5)
10        FORMAT(E20.5)
11         FORMAT(3E13.5)
12         FORMAT(3E13.5)
13           FORMAT(5E15.5)
14           FORMAT(3E20.5)
15        FORMAT(5E15.5)
          N=8
          NP=N
          LOGDEN=2.3025851
C   IMPORT GUESS VALUES FOR SOLVING SYSTEM
          OPEN (UNIT=1,FILE='FFIT.DAT')
          DO 20 I=1,8
          READ(1,10) X(I)
20        CONTINUE
          CLOSE (1)
C   ASSIGN MINIMUM ERROR VALUE
          ERRTRACK=5
C   OPEN FILE FOR RESULTS
          OPEN (UNIT=4,FILE='K123FIT.DAT')
C   NEED TO GENERATE EQUIL. VALUES FIRST (R VALUES)
          DO 5000 MA=6,30
           A=12-(MA/6)
          R(1)=10**A
           DO 4990 MB=6,24
           B=10-MB/6
           IF (BSET.EQ.1) B=MB/6+5
          R(2)=10**B
           DO 4980 MC=6,40
         DO 30 I=1,8
          XSAVE(I)=X(I)
30        CONTINUE
           C=10-MC/6
           IF (CSET.EQ.1) C=MC/6+2.333333
          R(3)=10**C
C   SET ERROR SUM VALUE TO ZERO AND EMULT TO ONE
          ERRSUM=0
          EMULT=1.0E+00
C   NEXT NEED TO GET CNSTS FOR EACH POINT
C   THESE ARE CNSTS H(TRUE),CL,L1TOT,L2TOT,L3TOT
          OPEN (UNIT=3, FILE='FITCNSTB.DAT')
           DO 4000 NUMCNST=1,705
           READ(3,FMT=13) Y(1),Y(2),Y(3),Y(4),Y(5)
          NTRIAL=1000
          TOLX=1E-16
          TOLF=1E-16
          CALL MNEWT(NTRIAL,X,N,TOLX,TOLF)
C   NEXT COMPUTE ADDITION TO RESIDUAL SQUARE SUM AND
C   MULT VALUE.  MULT WILL INDICAT IF ANY OF THE
C   VALUES WERE NEGATIVE, INDICATING A FALSE MINIMUM
C   IN THE SOLUTION SOMEWHERE
```

```fortran
          DO 100 I=1,8
          IF (X(I).LT.0) EMULT=-1.0E+00
100       CONTINUE
          IF (EMULT.EQ.-1) GOTO 4070
C   THIS SECTION SELECTS THOSE POINTS FOR USE IN FITTING
C   NEEDS SOME WORK TO IDENTIFY POINTS EVEN IF GOIN UP
          IF (Y(1).EQ.2.88E-11) GOTO 110
          IF (Y(1).EQ.2.86E-10) GOTO 110
          IF (Y(1).EQ.2.85E-9) GOTO 110
          IF (Y(1).EQ.2.86E-8) GOTO 110
           IF (Y(1).EQ.2.84E-7) GOTO 110
          IF (Y(1).EQ.2.91E-6) GOTO 110
          IF (Y(1).EQ.2.91E-5) GOTO 110
          IF (Y(1).EQ.2.64E-4) GOTO 110
          IF (Y(1).EQ.2.239E-3) GOTO 110
          GOTO 4000
110       PHX=-LOG(X(8))/LOGDEN
          PHY=-LOG(Y(1))/LOGDEN
          ERRSUM=(PHX-PHY)**2+ERRSUM
C   WRITE R1,R2,R3,ERRSUM TO RESULT FILE
4000  CONTINUE
          CLOSE (3)
C   INSPECTION PRINT TO SCREEN
C         WRITE(*,15) R(1),R(2),R(3),ERRSUM,EMULT
C   NOW A SECTION WHICH SHOULD ISOLATE ONLY THE BEST FITS
          IF (ERRSUM.GT.ERRTRACK) GOTO 4005
          WRITE (4,15) A,B,C,ERRSUM,EMULT
C         WRITE (*,15) R(1),R(2),R(3),ERRSUM,EMULT
          ERRTRACK=ERRSUM
4005  CONTINUE
C   THIS NEXT SECTION IS A ATTMPT TO REVERSE LINES
C   IN THE FITCNST DATA FILE.  iF SUCCESSFUL, THIS
C   SHOULD HELP INITIAL GUESS VALUES FOR EACH NUMR SET
          OPEN (UNIT=3,FILE='FITCNSTB.DAT')
          DO 4010 I=1,705
          READ (3,FMT=13) REVY(I,1),REVY(I,2),REVY(I,3),
         +REVY(I,4),REVY(I,5)
4010  CONTINUE
          CLOSE (3)
          OPEN (UNIT=3,FILE='FITCNSTB.DAT')
            DO 4020 I=1,705
            J=706-I
          WRITE(3,FMT=13) REVY(J,1),REVY(J,2),REVY(J,3)
         +,REVY(J,4),REVY(J,5)
4020  CONTINUE
          CLOSE(3)
C   NEED SECTION IN HERE WHICH WILL ALLOW R2 AND R3 TO SCALE BACK
C   DOWN
C   AFTER SCALIN UP TO 1E12.  THIS WILL HELP KEEP R VALUES CLOSE
C   TO PREVIOUS SET, SO GUESS VALUES SHOULD BE CLOSE.
          GOTO 4980
C   NEXT 3 LINES IN CASE SOLUTION FALSE, SO PROGRAM STOPS
4070  WRITE(4,10) XSAVE
          WRITE (4,15) A,B,C,ERRSUM,EMULT
          STOP
4980  CONTINUE
          IF (CSET.EQ.1) GOTO 4988
          CSET=1
          GOTO 4990
4988  CSET=0
4990  CONTINUE
          IF (BSET.EQ.1) GOTO 4998
```

```
          BSET=1
          GOTO 5000
 4998     BSET=0
 5000     CONTINUE
          CLOSE (1)
           WRITE(4,10) X
          WRITE(4,10)
          WRITE(4,10) Y
           CLOSE (4)
          END
          SUBROUTINE MNEWT(NTRIAL,X,N,TOLX,TOLF)
          PARAMETER (NP=8)
          DOUBLE PRECISION X(NP),ALPHA(NP,NP),BETA(NP),INDX(NP)
          DOUBLE PRECISION ERRF,ERRX,SUM,TOLX,TOLF
          INTEGER NTRIAL,K,N
C
 10       FORMAT(E20.10)
          DO 13 K=1,NTRIAL
          CALL USRFUN(X,ALPHA,BETA,NP)
          ERRF=0
          DO 11 I=1,N
            ERRF=ERRF+ABS(BETA(I))
 11       CONTINUE
          IF (ERRF.LE.TOLF) RETURN
          CALL LUDCMP(ALPHA,N,NP,INDX,D)
          CALL LUBKSB(ALPHA,N,NP,INDX,BETA)
          ERRX=0
          DO 12 I=1,N
          ERRX=ERRX+ABS(BETA(I))
          X(I)=X(I)+BETA(I)
 12       CONTINUE
          IF (ERRX.LE.TOLX) RETURN
 13       CONTINUE
          RETURN
          END
          SUBROUTINE USRFUN(X,ALPHA,BETA,NP)
          DOUBLE PRECISION X(NP),ALPHA(NP,NP),BETA(NP),RW
          COMMON R(3)
          COMMON Y(5)
           RW=1.0E-14
          DO 10 I=1,NP
          BETA(I)=0
          DO 8 J=1,NP
          ALPHA(I,J)=0
 8        CONTINUE
 10       CONTINUE
          BETA(1)=-(Y(3)-X(1)-X(4))
          ALPHA(1,1)=-1
          ALPHA(1,4)=-1
          BETA(2)=-(Y(4)-X(2)-X(5))
          ALPHA(2,2)=-1
          ALPHA(2,5)=-1
          BETA(3)=-(Y(5)-X(3)-X(6))
          ALPHA(3,3)=-1
          ALPHA(3,6)=-1
          BETA(4)=-(R(1)*X(8)*X(1)-X(4))
          ALPHA(4,1)=R(1)*X(8)
          ALPHA(4,4)=-1
          ALPHA(4,8)=R(1)*X(1)
          BETA(5)=-(R(2)*X(2)*X(8)-X(5))
          ALPHA(5,2)=R(2)*X(8)
          ALPHA(5,5)=-1
```

```fortran
      ALPHA(5,8)=R(2)*X(2)
      BETA(6)=-(R(3)*X(3)*X(8)-X(6))
      ALPHA(6,3)=R(3)*X(8)
      ALPHA(6,6)=-1
      ALPHA(6,8)=R(3)*X(3)
      BETA(7)=-(RW-X(7)*X(8))
      ALPHA(7,7)=-X(8)
      ALPHA(7,8)=-X(7)
      BETA(8)=-(X(8)+X(4)+X(5)+X(6)-Y(2)-X(7))
      ALPHA(8,4)=1
      ALPHA(8,5)=1
      ALPHA(8,6)=1
      ALPHA(8,7)=-1
      ALPHA(8,8)=1
      RETURN
      END
      SUBROUTINE LUDCMP(ALPHA,N,NP,INDX,D)
      PARAMETER (NMAX=100,TINY=1E-20)
      INTEGER N
       DOUBLE PRECISION ALPHA(NP,NP),INDX(N),VV(NMAX)
      DOUBLE PRECISION SUM,AAMAX,DUM
      D=1.
      DO 12 I=1,N
          AAMAX=0
        DO 11 J=1,N
        IF (ABS(ALPHA(I,J)).GT.AAMAX) AAMAX=ABS(ALPHA(I,J))
11    CONTINUE
      IF (AAMAX.EQ.0.) PAUSE 'SINGULAR MATRIX'
      VV(I)=1./AAMAX
12    CONTINUE
      DO 19 J=1,N
          DO 14 I=1,J-1
          SUM=ALPHA(I,J)
          DO 13 K=1,I-1
              SUM=SUM-ALPHA(I,K)*ALPHA(K,J)
13    CONTINUE
      ALPHA(I,J)=SUM
14    CONTINUE
      AAMAX=0
      DO 16 I=J,N
      SUM=ALPHA(I,J)
      DO 15 K=1,J-1
          SUM=SUM-ALPHA(I,K)*ALPHA(K,J)
15    CONTINUE
      ALPHA(I,J)=SUM
      DUM=VV(I)*ABS(SUM)
      IF (DUM.GE.AAMAX) THEN
          IMAX=I
          AAMAX=DUM
      ENDIF
16    CONTINUE
      IF (J.NE.IMAX) THEN
      DO 17 K=1,N
          DUM=ALPHA(IMAX,K)
          ALPHA(IMAX,K)=ALPHA(J,K)
          ALPHA(J,K)=DUM
17    CONTINUE
      D=-D
      VV(IMAX)=VV(J)
      ENDIF
      INDX(J)=IMAX
      IF (ALPHA(J,J).EQ.0) ALPHA(J,J)=TINY
```

```fortran
          IF (J.NE.N) THEN
              DUM=1./ALPHA(J,J)
          DO 18 I=J+1,N
              ALPHA(I,J)=ALPHA(I,J)*DUM
18        CONTINUE
          ENDIF
19        CONTINUE
          RETURN
          END
          SUBROUTINE LUBKSB(ALPHA,N,NP,INDX,BETA)
          INTEGER N
          DOUBLE PRECISION ALPHA(NP,NP),INDX(N),BETA(N)
          DOUBLE PRECISION SUM
          II=0
          DO 12, I=1,N
          LL=INDX(I)
          SUM=BETA(LL)
          BETA(LL)=BETA(I)
          IF (II.NE.0) THEN
              DO 11 J=II,I-1
              SUM=SUM-ALPHA(I,J)*BETA(J)
11        CONTINUE
          ELSE IF (SUM.NE.0) THEN
              II=I
          ENDIF
          BETA(I)=SUM
12        CONTINUE
          DO 14 I=N,1,-1
          SUM=BETA(I)
          IF(I.LT.N) THEN
              DO 13 J=I+1,N
              SUM=SUM-ALPHA(I,J)*BETA(J)
13        CONTINUE
          ENDIF
          BETA(I)=SUM/ALPHA(I,I)
14        CONTINUE
          RETURN
           END
```

EVALUATION OF RUTTING RESISTANCE
CHARACTERISTICS OF AIRFIELD FLEXIBLE PAVEMENTS
USING GYRATORY TESTING MACHINE

Cheng Liu
Professor
Department of Engineering Technology

The University of North Carolina at Charlotte
Charlotte, North Carolina 28223

Final Report for:
Research Initiation Program
Air Force Civil Engineering Support Agency

December 1992

EVALUATION OF RUTTING CHARACTERISTICS OF AIRFIELD FLEXIBLE PAVEMENTS USING GYRATORY TESTING MACHINE

Cheng Liu
Professor
Department of Engineering Technology
The University of North Carolina at Charlotte

Abstract

The objectives of this research are to explore the use of the gyratory testing machine (GTM) to evaluate and identify a paving material's resistance to in-service rutting and to study the feasibility of using the GTM in quality control and assurance testing of paving materials.

Two different asphalt mixtures were selected for use in this investigation. Both of them were plant mix samples from Tyndall test sections, which were built and trafficked by F-15 C/D load cart in 1988. Both mixes were tested in the GTM in accordance with ASTM D 3387 "Standard Test Method for Compaction and Shear Properties of Bituminous Mixtures by Means of the U.S. Corps of Engineers Gyratory Testing Machine" and were carried to 480 revolutions instead of 60 revolutions as suggested by ASTM.

The results of mix density (γ), roller pressure (p), and gyratory shear resistance of mix (S_G) were obtained. These laboratory results were then studied along with field data furnished by the Air Force (obtained during and after trafficking of the test sections). For the two different mixes studied in this project, it appears that a minimum gyratory shear resistance of 100 at 480 revolutions may be adequate and necessary to prevent rutting from the F-15 C/D aircraft.

EVALUATION OF RUTTING RESISTANCE CHARACTERISTICS OF AIRFIELD FLEXIBLE PAVEMENTS USING GYRATORY TESTING MACHINE

Cheng Liu

INTRODUCTION

With increases in wheel load and tire pressure of new generations of Air Force fighter aircraft, rutting of asphalt pavements has become a problem in recent years. Rutting in flexible pavements develops gradually with increasing wheel load applications. It generally appears as longitudinal depressions in the wheel path, accompanied by small upheavals to the sides. Rutting can occur in any one or more of the pavement's layers including the subgrade soil. It is caused by:

1.   Traffic densification of paving materials in the wheel paths (decrease in volume and, hence, increase in density) and

2.   Shear deformation or lateral movement of pavement materials from below the wheel paths (deformation flow without volume change) due to insufficient stability of paving materials.

In the initial stage of trafficking, the increase of irreversible deformation below the tires is distinctly greater than the upheaval zones. In this initial phrase, traffic compaction has an important influence on rutting. After the initial stage, the volume decrement beneath the tires is approximately equal to the volume increment in the adjacent upheaval zones. This is an indication that traffic densification is completed for the most part and that further rutting is caused essentially by displacement with constancy of volume (1). Shear deformation, rather than densification, is the primary rutting mechanism. However, it is imperative to place materials at high densities in order to minimize porosity and provide durability.

It was considered reasonable to use shear resistance characteristics of asphalt concrete mixtures as a measure of its resistance to rutting. From prior experience, it was known that the gyratory testing machine (GTM) had been used successfully for mix design and evaluation of the shear resistance of mixtures (2). The objectives of this research are to explore the use of the GTM to evaluate and identify a paving material's resistance to in-service rutting and to study the feasibility of using the GTM in quality control and assurance testing of paving materials.

Two different paving mixes furnished by the Air Force were tested in the GTM in accordance with ASTM D 3387, "Standard Test Method for Compaction and Shear Properties of Bituminous Mixtures by Means of the U.S. Corps of Engineers Gyratory Testing Machine (GTM)." They were carried to 480 revolutions instead of 60 revolutions as suggested by ASTM. Both mixes were tested in the GTM and the laboratory results of density (γ), roller pressure (p) and gyratory shear resistance (S_G) were collected and evaluated. These laboratory results were then studied along with field data furnished by the Air Force (obtained during and after trafficking of the test sections) to determine the feasibility of using the GTM for evaluation and design of asphalt mixtures for resistance to rutting. Conclusions derived from this study along with tentative evaluation criteria with regard to paving mixtures' resistance to service rutting are presented in this report.

This study is by no means definitive, since its scope is limited to the testing and evaluation of only two different mixes (twenty seven samples). However, the results of this study can and should be used to determine the feasibility of using the GTM in quality control and assurance testing of air field paving materials.

MATERIALS AND TEST PROCEDURES

A. MATERIALS (3)

The selected aggregate for the asphalt mixtures was supplied in three separate sizes, identified as #67, #8910, both Alabama limestones, and crushed limestone screenings from Dravo's Perry, Florida plant. Figure 1 illustrates the grain size distribution of the resulting blend (from the aforementioned three aggregates) and the limits of the Air Force aggregate specifications. The LA abrasion resistance of the blended material was 28.3% loss, which is well below the limit of 40% loss. The specific gravity of each aggregate is listed in Table 1 along with the weighted average for the aggregate mix.

Grade AC-20 asphalt cement was used in the design and production of the mixes. The properties of the asphalt cement used are as follows:

Penetration: 5.7 millimeters (ASTM D 5)

Specific gravity: 1.0293 (ASTM D 70)
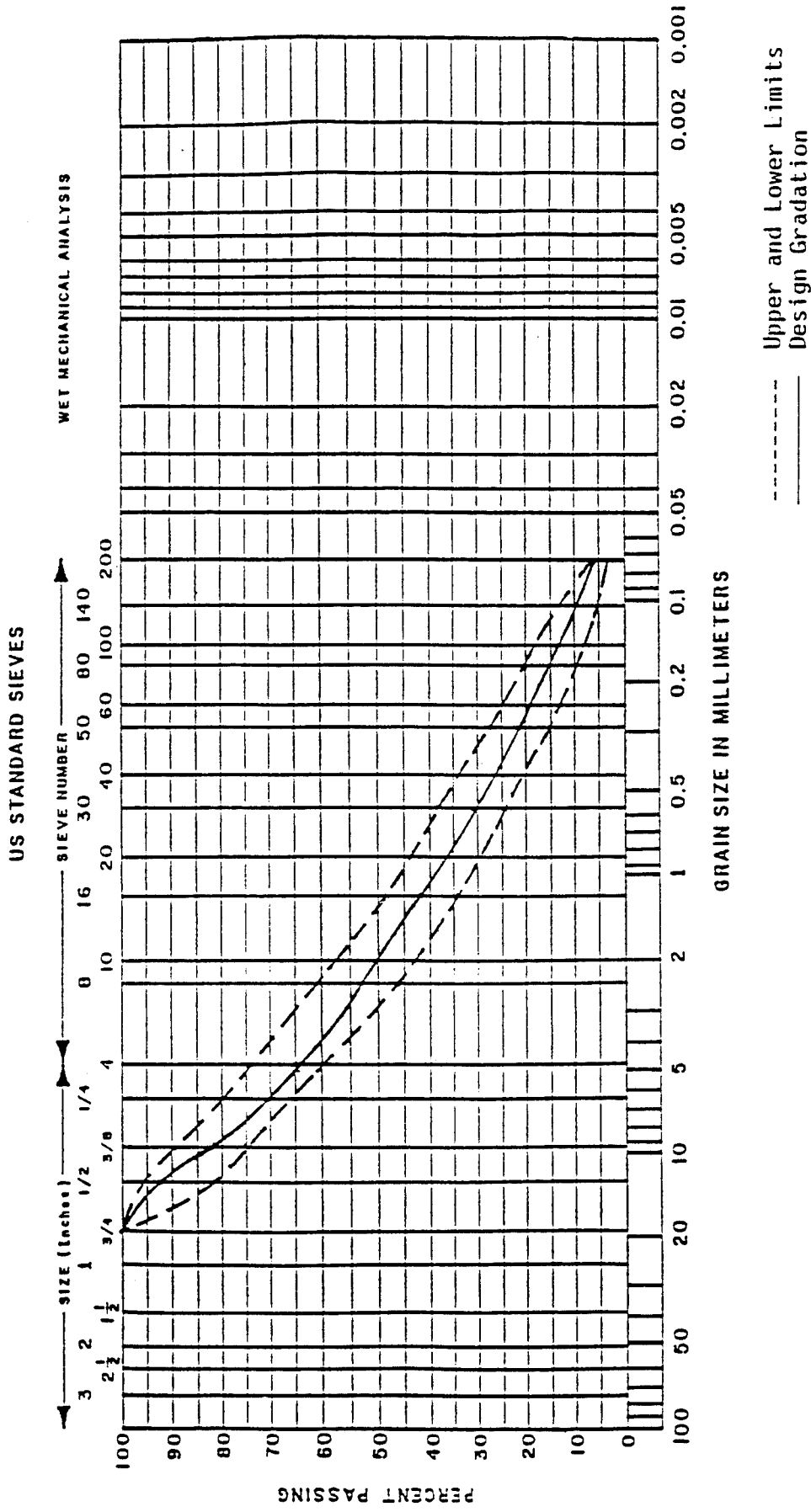
Figure 1. Asphalt Concrete Mix Design
Aggregate Blend Gradation (3)

| Kinematic Viscosity: | 471.8 Centistokes (ASTM 2170) |
| Softening point: | 128° F (ASTM D 36) |

Two different plant mixes were selected for use in this investigation. The mix that hereafter will be referred to as gyratory mix was designed with the Gyratory Testing Machine (ASTM D 3387), using 300 psi ram pressure. This mix performed well in the field and did not show significant rutting. The other mix, which will be referred to as Marshall mix, was designed with the Marshall method (Military Standard 620 A, Method 100) with 75 blow compaction. This mix performed poorly in the test sections . It exhibits medium to high rates of rutting. The resulting job mix formulas for asphalt contents for each mix are 6.4% of the total weight for the Marshall and 5.1% of the total weight for the Gyratory. The laboratory properties for each mix at the design asphalt content are summarized in Table 2.

B. TEST PROCEDURES (2) (4) (5)

"Draft of Proposed Revision, ASTM D 3387-83., STANDARD TEST METHOD FOR COMPACTION AND SHEAR PROPERTIES OF BITUMINOUS MIXTURES BY MEANS OF THE U.S. CORPS OF ENGINEERS GYRATORY TEST MACHINE (GTM)" (4) was generally followed. Before the plant mix samples were subjected to the GTM test, they were put in an oven and heated to 275 to 300°F for at least three to four hours. The temperature at the start of the GTM compaction corresponds to that anticipated to be used at the beginning of compaction in the field. The mold chuck heater was turned on to a 140°F setting for approximately 60 minutes prior to the start of testing.

The GTM parameter settings had to be calibrated before compaction and densification testing operations. The dial gage that measures sample height, the gyratory angle, and the oil-roller pressure gage were properly adjusted prior to each series of tests.

Sample heights can be measured to one-thousandth of an inch. To calibrate the dial gage, a steel block, 2.500 inches in height, is placed on the lower mold plate in place of a sample. The ram pressure is activated and when the steel block contacts the top mold plate the dial gage is set exactly to 2.500 inches.

TABLE 1. SPECIFIC GRAVITY VALUES OF AGGREGATE USED IN MIX (3)

MATERIAL	BULK	BULK SATURATED SURFACE DRY	APPARENT
#67	2.774	2.803	2.858
#8910	2.663	2.725	2.836
Screenings	2.423	2.474	2.553
Weighted Average	2.591	2.640	2.764

TABLE 2. MATERIAL PROPERTY SUMMARY OF DESIGN ASPHALT CONCRETE (3)

MATERIAL PROPERTY	MARSHALL	GYRATORY
Asphalt Cement Content	6.4%	5.1%
Unit Weight of Aggregate Only (pcf)	---	144.5
Density	148.7	153.9
Flow (.01 inch)	9.5	10.4
Gyratory Stability Index	---	1.02
Stability (lbs)	3000	5500
Voids Filled (%)	82.0	80.6
Voids Total Mix (%)	3.3	1.9

To set the initial gyratory angle of 1 degree, a dial (or knob) on the bottom roller is adjusted. Four turns of the dial are equivalent to a 1-degree change of the gyratory angle. When the dial has been set to the desired position, Hot mix is placed in the 4-in.-diameter heated mold and the mold is securely fastened in the GTM. The gyrograph recorder is turned on. Then, with the ram pressure at 300 psi the GTM is started and operated for about five revolutions. The machine is then stopped with the fixed oil-roller facing towards the front of the GTM. After a short time delay, the gyrograph produces a horizontal straight line, after which the carriage is rotated 180 degrees until the adjustable bottom roller is facing front. The gyrograph recorder pen produces another horizontal straight line on the chart paper. After counting the small divisions on the chart paper between the two horizontal straight lines, the angle of gyration can be determined. Each small division on the gyrograph equals 0.1 degree angle. So for a 1 degree initial gyratory angle, there should be 10 divisions between the horizontal straight lines. In the event the desired 1 degree angle (10 divisions) is not correct, adjustment can be made by using the adjustable bottom roller dial (knob).

The specimens were compacted at the anticipated design vertical stress (300 psi ram pressure) and 1 degree initial gyratory machine angle. Compaction continued to 480 revolutions, taking readings of heights of specimen and roller pressures at 30, 60, 120, 240 and 480 revolutions. The samples were then extruded from the mold,and the gyratory shear values and bulk density were computed.

The gyratory shear (S_G) value is a measure of the shear resistance of the asphalt concrete sample. S_G is computed using

$$S_G = \frac{4p}{h}$$

where p is the fixed oil-roller pressure in psi and h is the height of sample in inches. This equation was derived by taking moments about the center of the specimen as shown in figure 2. The moment equation is

$$S_G = \frac{2W.L}{A.h} = \frac{2 \times p \times a \times L}{A \times h} \qquad (1)$$

where S_G = gryatory Shear
    A = cross sectional area of specimen
    h = height of specimen
    L = length of roller lever arm
    W = load on roller = p x a
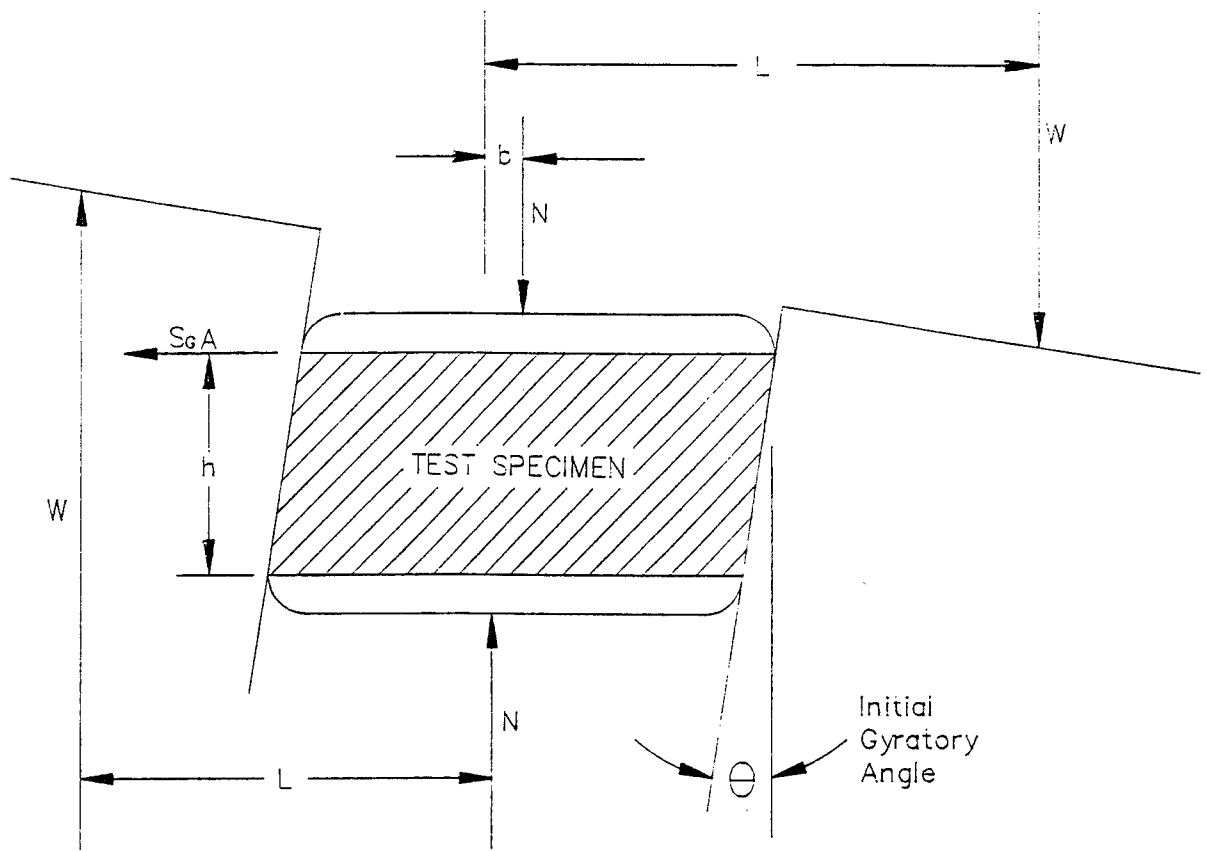
Figure 2.   Force Diagram For
GTM Specimen

where p = roller pressure, and
a = effective area of roller piston

N = vertical load on specimen = total load on ram

For GTM Model 4C:
$$a = 5.28 \text{ in}^2$$
$$L = 4.76 \text{ in}$$
$$A = \frac{\pi(4)^2}{4} = 12.57 \text{ in}^2$$

Substitute into Eq. (1) above

$$S_G = \frac{2 \times p \times (5.28)\,(4.76)}{(12.57)\,(h)} = \frac{4p}{h}$$

The effects of wall friction were not considered because its effect on S_G are not generally considered significant (2).

DATA ACQUISITION AND EVALUATION

Twenty seven asphalt plant mix samples were tested in the Air Force mobile GTM, which was brought to the University of North Carolina at Charlotte for this project. Twelve of them were gyratory mixes; the remaining fifteen were Marshall mixes. All twenty-seven samples were from Tyndall test sections, which were built and trafficked by F-15 C/D load cart in 1988. All mixes were tested in the GTM in accordance with the procedures described beforehand. The results of tests pertaining to gyratory shear resistance (S_G) at various GTM revolutions were listed in Table 3 and plotted in Figures 3 through 6. The results of tests pertaining to unit weight of total mix at various GTM revolutions were listed in Table 4 and plotted in figures 7 through 10. The capital letter "G" immediately following sample numbers (e.g TA 4-1 G) indicates that the sample is a gyratory mix. The capital letter "M" immediately following sample numbers (e.g. TA 9-1 M) signifies the material is a Marshall mix.

For all Marshall mix samples, except TB 12-1 M, substantial amounts of asphalt cement appeared around the edge of the upper head of the GTM after approximately 60 revolutions. This phenomenon indicated that the asphalt cement was being "squeezed" out of the test specimens after approximately 60 revolutions and the asphalt cement content of the test specimens subsequently decreased. At this point the specimens appeared to suffer significant reduction in shear resistance and they might be already at or

near failure at 60 revolutions. This is the reason that gyratory shear resistance values and total unit weights of all Marshall mixes (except TB 12-1M) were reported only up to 60 revolutions; the specimens had changed.

Marshall mix performed poorly at the Tyndall test sections. It exhibited early and excessive rutting in the field under F-15 C/D load cart. With the exception of TB 12-1M all Marshall mixes tested in the air mobile GTM had gyratory shear resistance values of less than 60 after 60 revolutions. (Table 3 and figures 3 through 6).

It was noted that TB 12-1 M contained more fine than the TA and TC samples. This excess fine tended to absorb some of the asphalt cement in this Marshall mix and made it less susceptible for asphalt cement content change. This is the reason that TB 12-1 M possessed higher gyratory shear resistance than other Marshall mix samples.

Gyratory mix performed very well at the Tyndall test sections. It showed little rutting in the field after extensive passes of F-15 C/D load cart (Table 5). All gyratory mixes tested in the GTM had gyratory shear values of over 130 at 60 revolutions and over 100 after 480 revolutions. (Table 3 and figures 3 through 6).

The unit weights or densities of both Marshall and gyratory mixes were about equal. They are all in the range of low 150's pcf at 30 to 60 revolutions and high 150's pcf at 480 revolutions. (Table 4 and figures 7 through 10).

CONCLUSIONS

The GTM can be used effectively to evaluate rutting resistance of asphalt concrete mixtures. Based on the tests conducted on two different paving mixes, a tentative gyratory shear value of 130 at 60 revolutions and 100 at 480 revolutions could be seen as an acceptable lower limit for airfield surface course mixtures scheduled for F-15 C/D traffic. This study is by no means definitive, since its scope is limited to the testing and evaluation of only two different mixes. Additional testing has to be performed to establish gyratory shear criteria with more certainty.

The most important performance characteristic of the asphalt mixtures in the GTM was their sensitivity to changes in asphalt content (2). The degree of sensitivity was readily identified by observing

drastic changes in the gyratory shear resistance value as the asphalt content was changed from 6.4% of Marshall mix to 5.1% of gyratory mix. (figure 3 through 6).

It is recommended that further testing on different types of mixtures be performed using the GTM to establish design or quality control criteria with regard to their potential rutting resistance on the airfield.

TABLE 3. GYRATORY SHEAR AT VARIOUS NO. OF GTM REVOLUTIONS

Sample No.	GTM Revolutions				
	30	60	120	240	480
TA 4-1 G	161.6	164.7	154.5	142.8	130.6
TA 4-2 G	141.1	138.5	130.8	124.0	108.5
TA 5-2 G	152.0	152.9	147.8	127.5	112.5
TA 6-1 G	139.5	133.2	126.7	117.9	108.3
TA 6-2 G	141.5	139.0	124.9	113.8	103.5
TA 7-3 G	143.5	137.4	136.9	121.8	108.8
TA 9-1 M	66.4	46.3			
TA 10-1 M	60.7	50.4			
TA 10-2 M	89.2	59.9			
TA 11-1 M	63.5	46.8			
TA 11-2 M	59.9	50.1			
TA 11-3 M	68.6	51.3			
TA 12-1 M	64.5	57.1			
TA 13-1 M	46.5	40.3			
TA 14-2 M	54.2	43.3			
TC 4-1 M	68.9	49.1			
TC 5-1 M	63.4	57.4			
TC 6-1 M	58.6	40.9			
TC 7-3 M	78.2	58.9			
TC 8-2 M	57.6	53.8			
TC 9-2 G	148.7	151.3	140.0	125.4	106.0
TC 10-1 G	170.1	163.3	151.2	132.6	120.2
TC 11-1 G	142.5	138.5	123.3	111.2	101.4
TB 3-1 G	141.9	145.4	149.2	151.5	153.4
TB 12-1 M	125.7	112.4	87.5	73.5	56.1
BB 4-1 G	147.8	151.0	154.6	150.2	146.2
BB 6-1 G	147.2	148.3	151.9	149.7	154.0

Gyratory Shear vs. No. of Revolutions

Gyratory Shear

Figure 3

Legend: TA 4-2 (Gyratory), TA 5-2 (Gyratory), TA 6-2 (Gyratory), TA 9-1 (Marshall), TA 12-1 (Marshall), TA 13-1 (Marshall), TA 14-2 (Marshall)
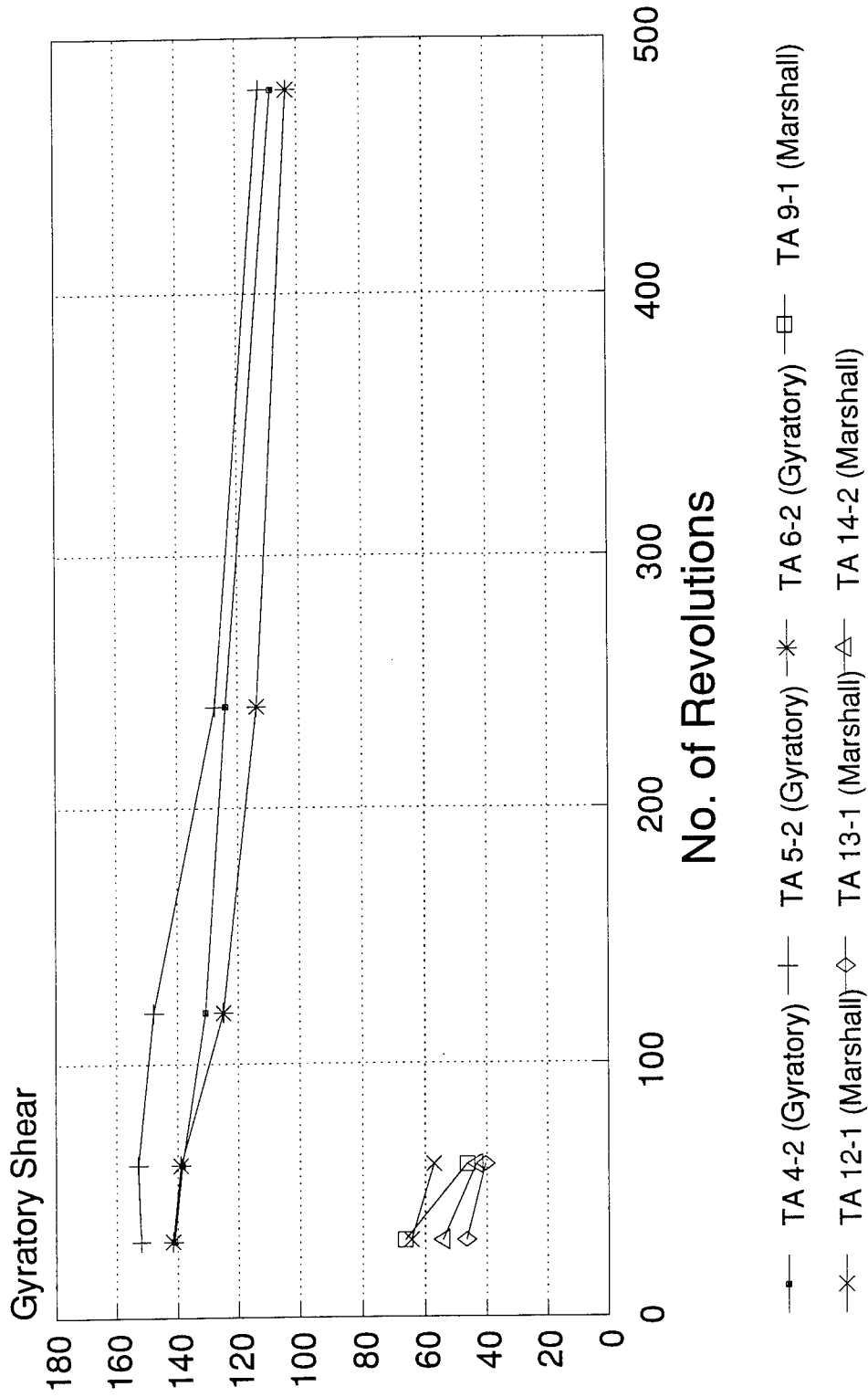
Gyratory Shear vs. No. of Revolutions
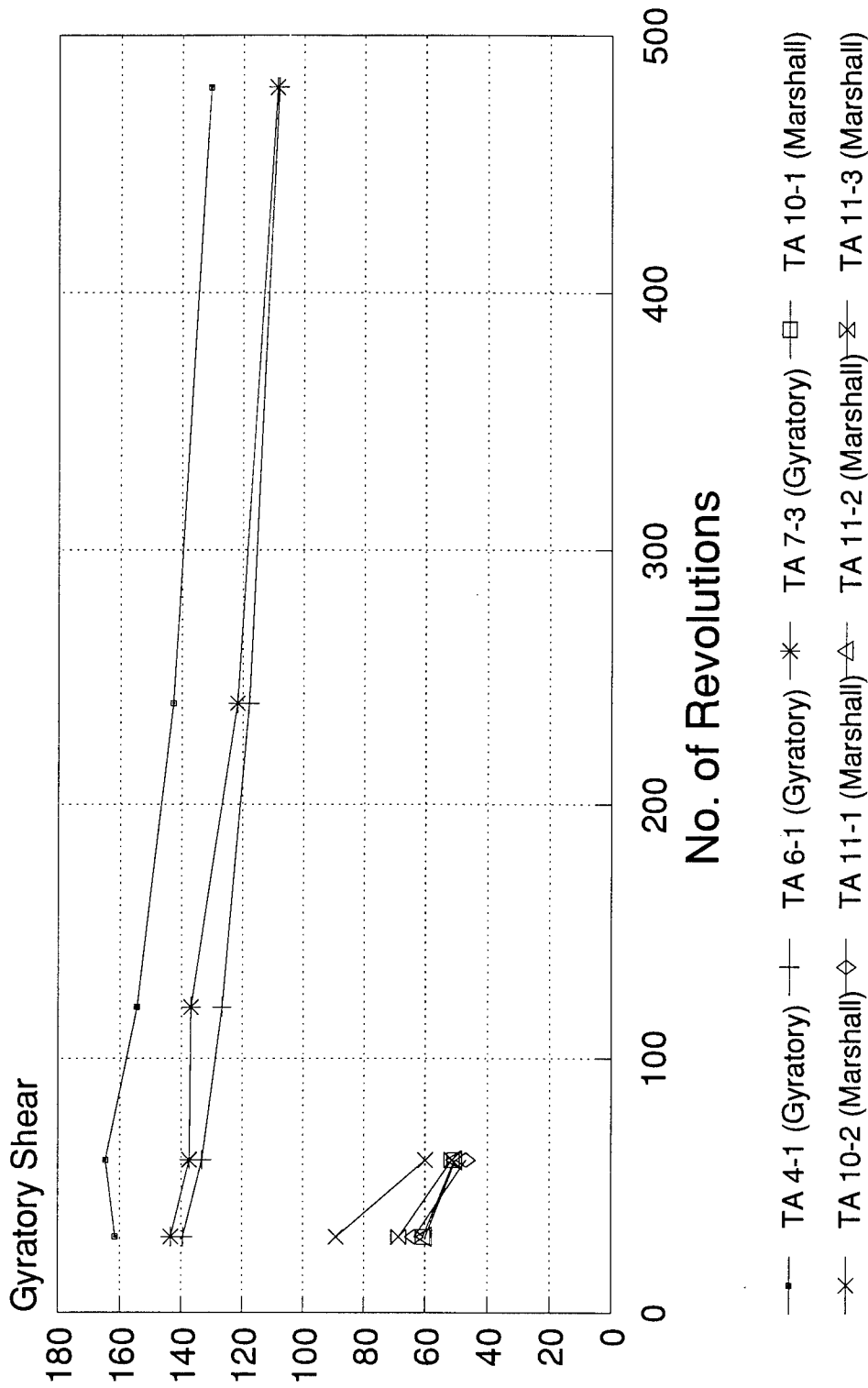
Figure 4

Gyratory Shear vs. No. of Revolutions

Gyratory Shear

No. of Revolutions

— TC 4-1 (Marshall) —+— TC 5-1 (Marshall) —*— TC 6-1 (Marshall) —□— TC 7-3 (Marshall)

—■— TC 8-2 (Marshall) —◇— TC 9-2 (Gyratory) —△— TC 10-1 (Gyratory) —⋈— TC 11-1 (Gyratory)
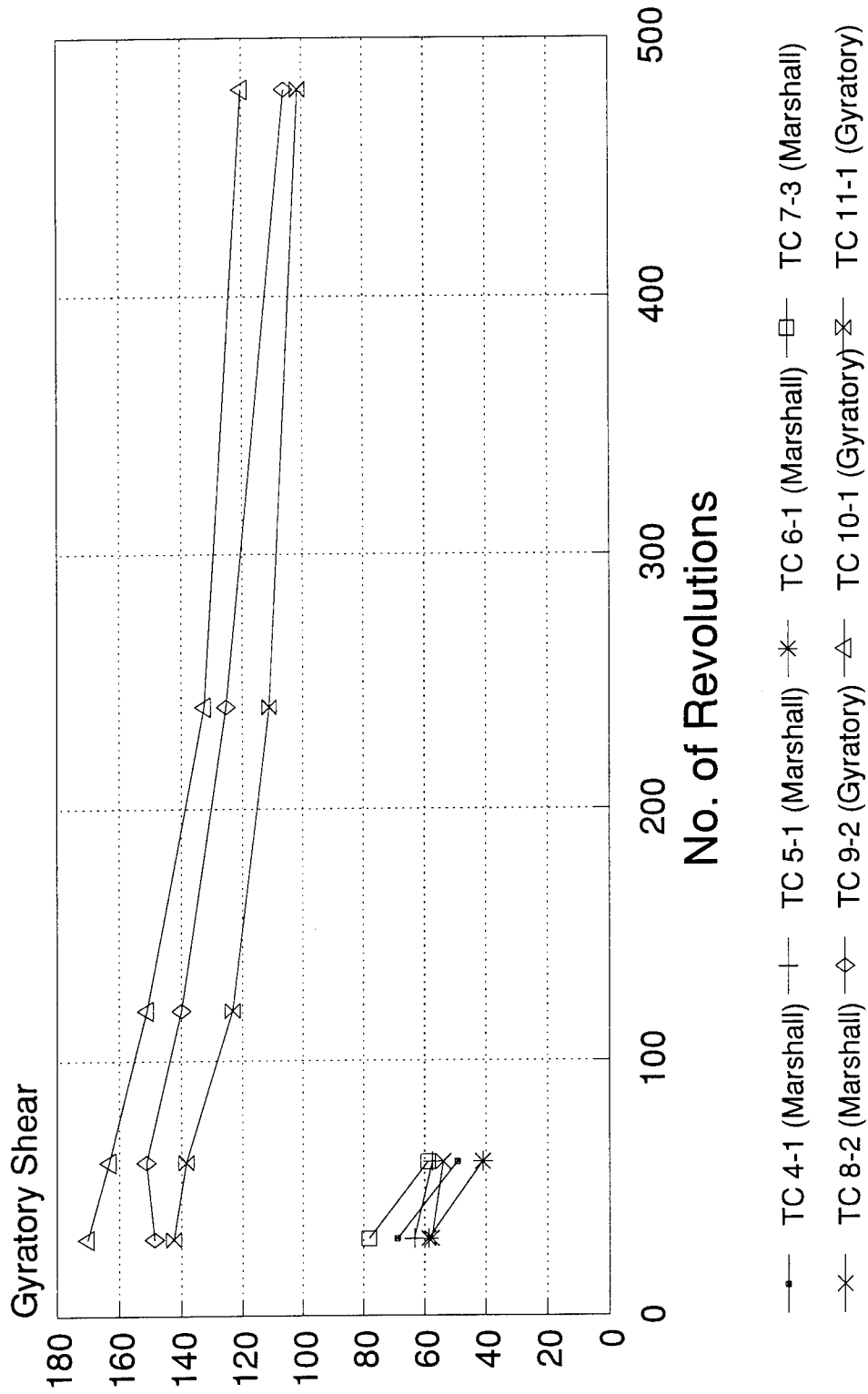
Figure 5

Gyratory Shear vs. No. of Revolutions

Gyratory Shear

Legend:
- TB 3-1 (Gyratory)
- BB 4-1 (Gyratory)
- TB 12-1 (Marshall)
- BB 6-1 (Gyratory)
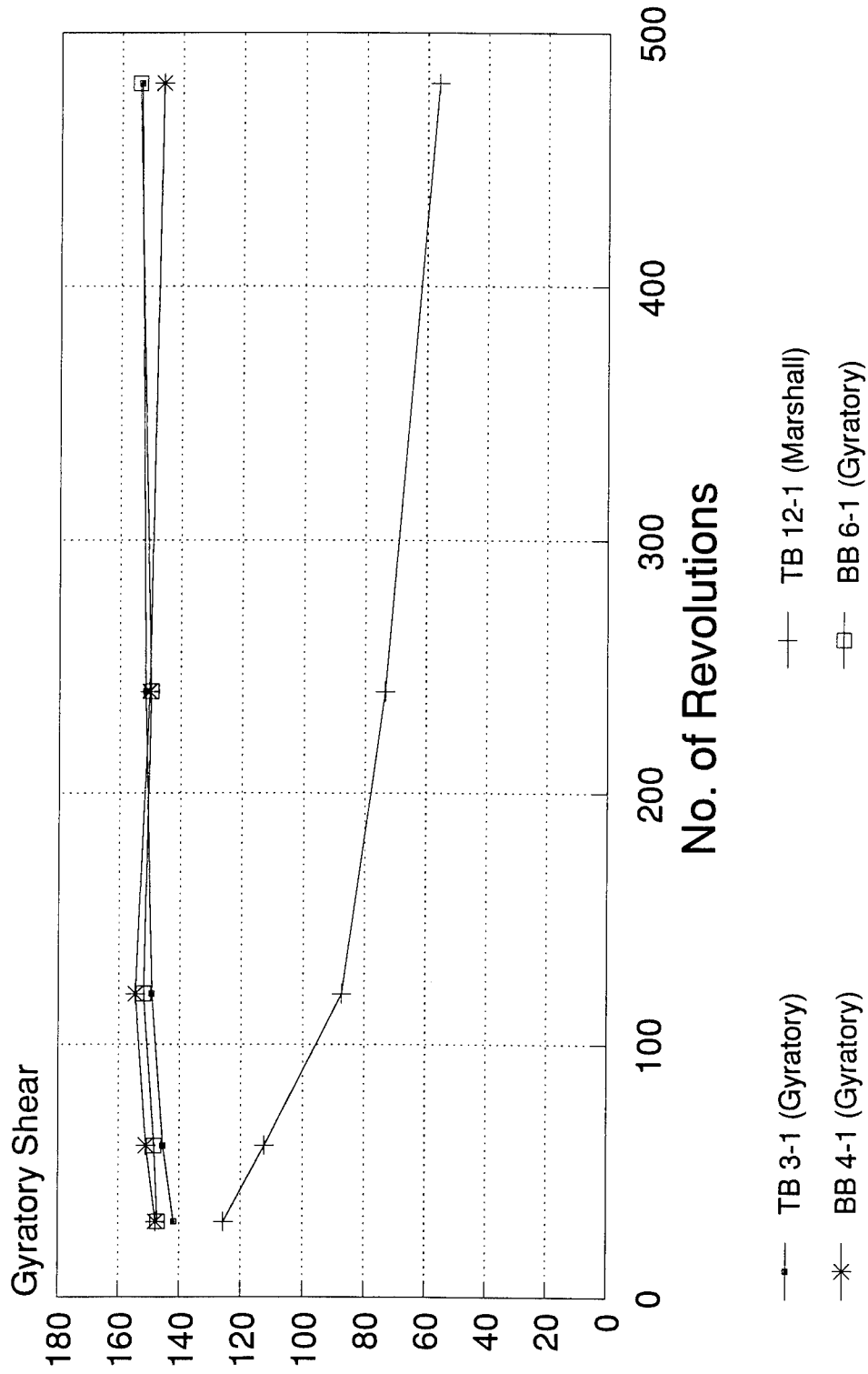
No. of Revolutions

Figure 6

TABLE 4. UNIT WEIGHT AT VARIOUS NO. OF GTM REVOLUTIONS

Sample No.	GTM Revolutions				
	30	60	120	240	480
TA 4-1 G	150.0	151.5	152.6	154.6	155.9
TA 4-2 G	152.8	154.1	155.6	157.1	158.5
TA 5-2 G	152.4	152.9	154.3	155.9	157.3
TA 6-1 G	153.2	154.4	155.6	156.8	157.8
TA 6-2 G	151.6	153.3	154.9	156.5	157.2
TA 7-3 G	152.4	153.9	155.4	156.5	157.7
TA 9-1 M	154.1	155.0			
TA 10-1 M	152.6	153.5			
TA 10-2 M	151.3	152.7			
TA 11-1 M	152.8	153.8			
TA 11-2 M	152.8	153.7			
TA 11-3 M	152.7	153.9			
TA 12-1 M	153.8	154.6			
TA 13-1 M	151.7	152.0			
TA 14-2 M	154.5	155.0			
TC 4-1 M	154.0	154.8			
TC 5-1 M	155.7	156.2			
TC 6-1 M	154.9	155.6			
TC 7-3 M	153.0	154.1			
TC 8-2 M	154.3	155.3			
TC 9-2 G	157.8	158.5	158.7	160.1	161.2
TC 10-1 G	152.9	154.9	156.7	158.0	159.2
TC 11-1 G	152.9	155.3	157.0	158.4	159.2
TB 3-1 G	148.6	149.9	150.9	151.7	152.4
TB 12-1 M	153.4	154.5	155.5	156.0	156.5
BB 4-1 G	150.6	152.2	153.5	154.7	155.1
BB 6-1 G	149.6	151.1	152.4	153.3	154.0

Unit Weight vs. No. of Revolutions

Figure 7

TA 4-1 (Gyratory)   TA 6-1 (Gyratory)   TA 7-3 (Gyratory)   TA 10-1 (Marshall)

TA 10-2 (Marshall)   TA 11-1 (Marshall)   TA 11-2 (Marshall)   TA 11-3 (Marshall)
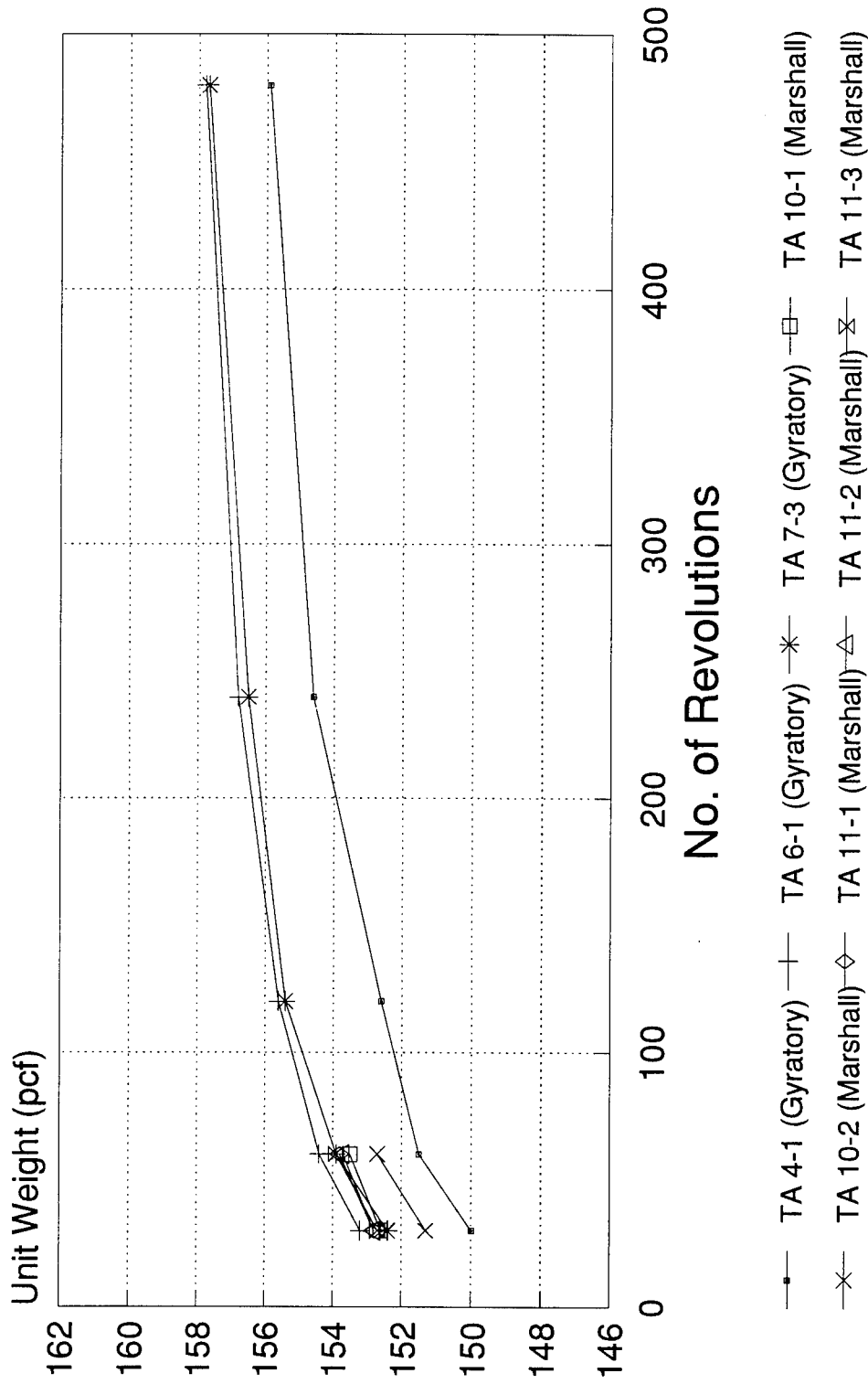
Unit Weight vs No. of Revolutions
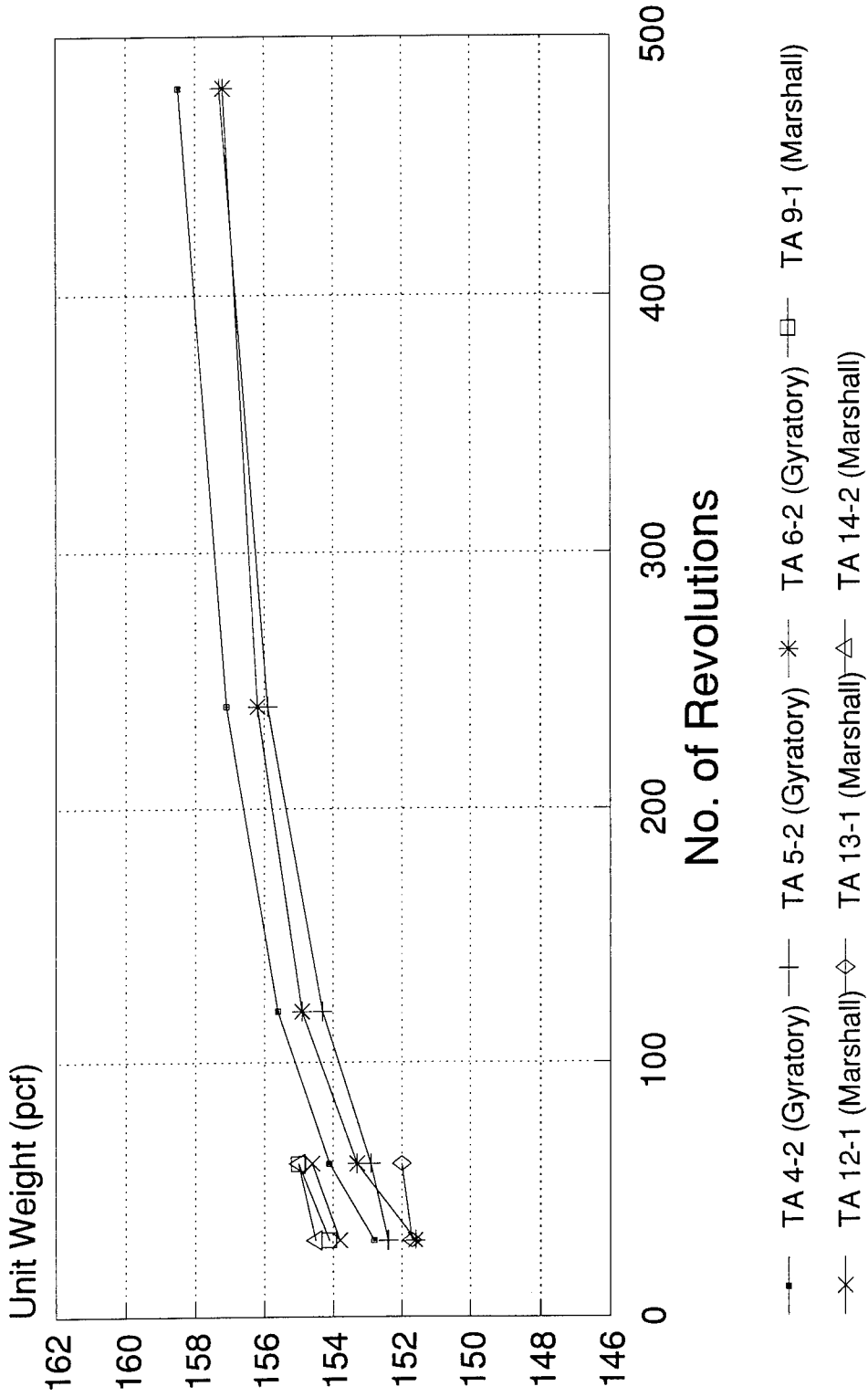
Figure 8

Unit Weight vs. No. of Revolutions
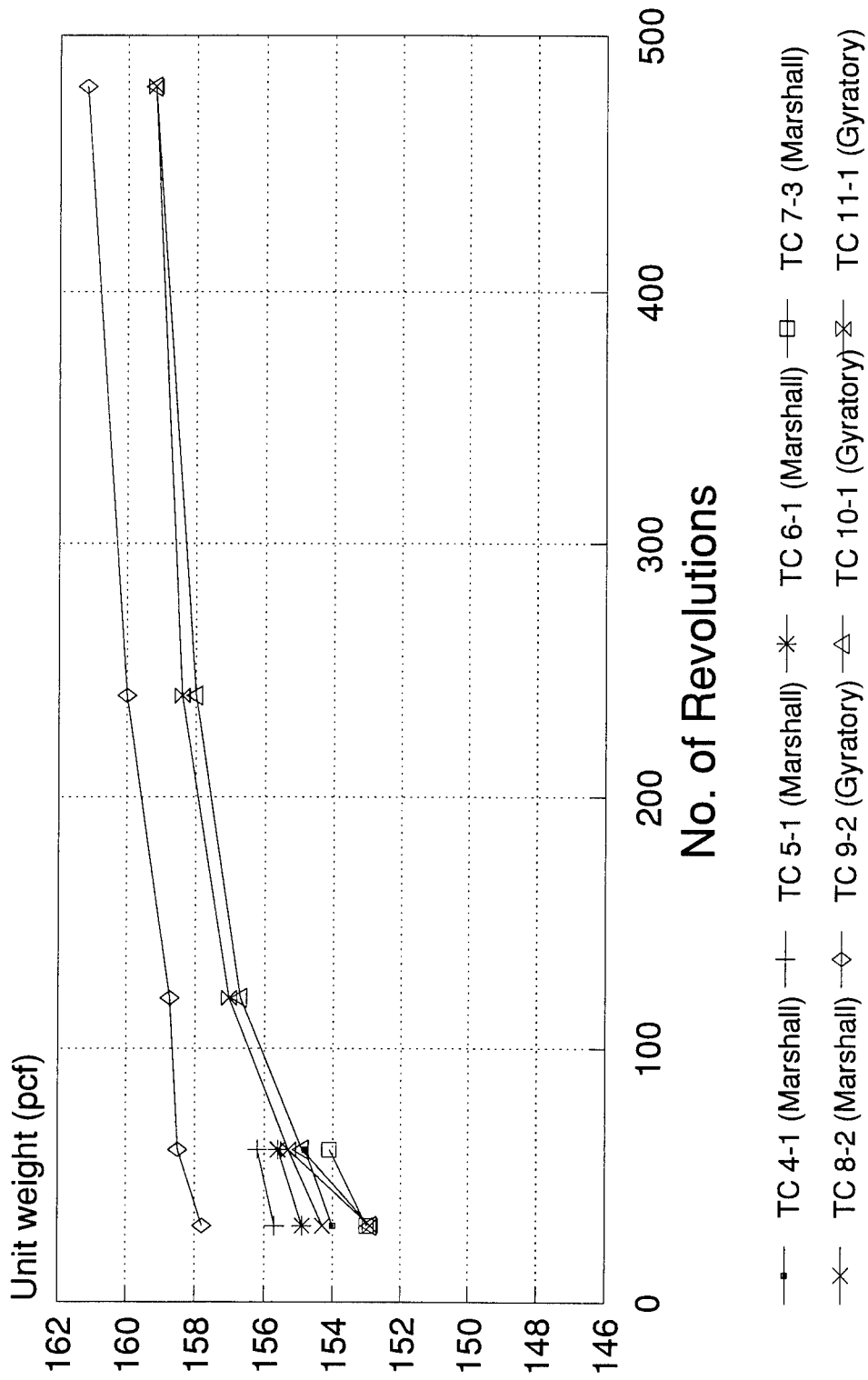
Figure 9

Unit Weight vs. No. of Revolutions

Unit Weight (pcf)

No. of Revolutions

TB 3-1 (Gyratory)   —+— TB 12-1 (Marshall)

—*— BB 4-1 (Gyratory)   —□— BB 6-1 (gyratory)
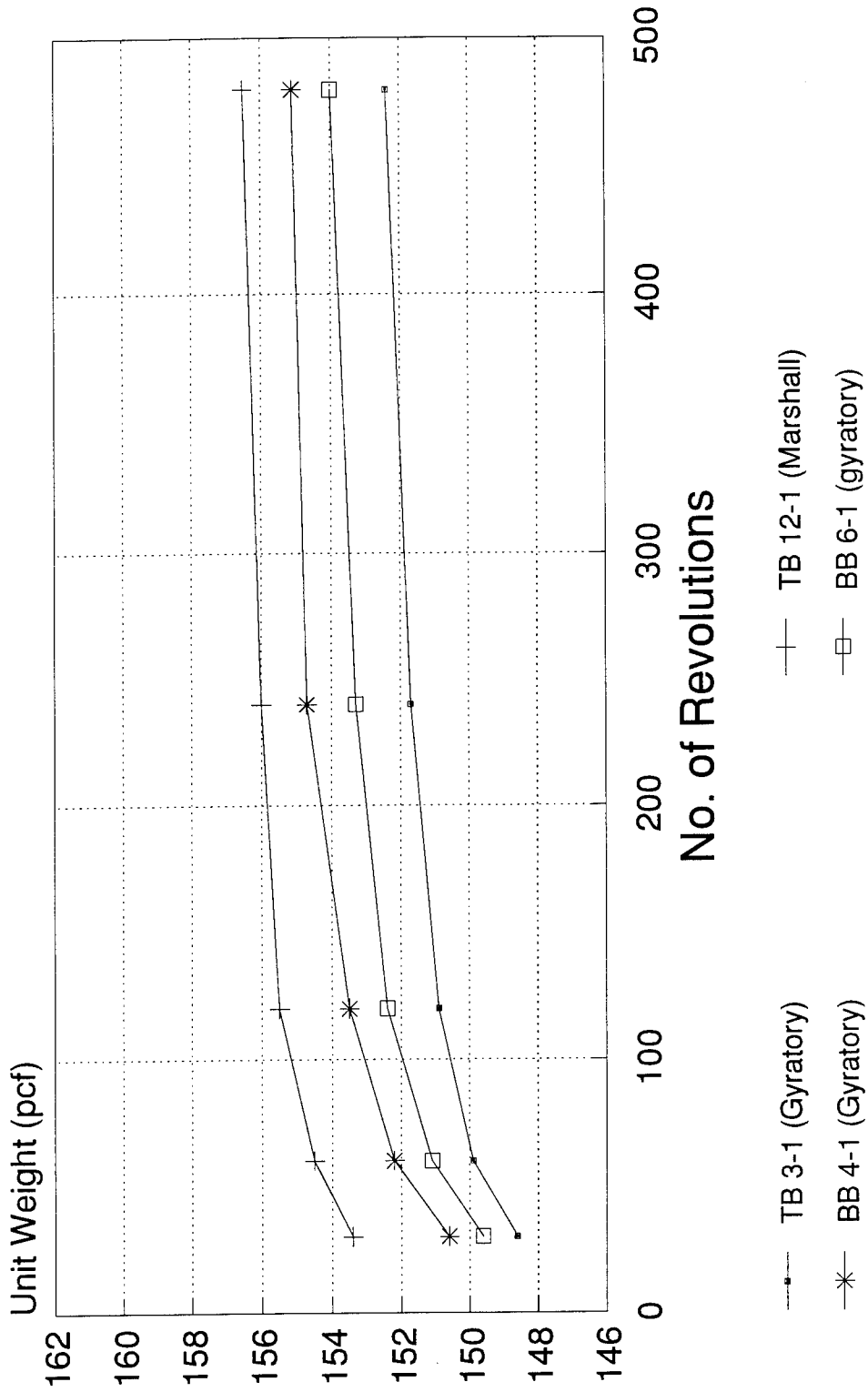
Figure 10

TABLE 5. RUT DEPTHS (FIELD MEASUREMENTS)[1]

SAMPLE NO.	STATION	PASS LEVEL[2]	MAX RUT DEPTH (IN)
TA 7 G	3+30	3286	-0.319
		5817	-0.321
	3+42	9715	-0.450
	3+44	448	-0.190
		9715	-0.450
	3+52	448	-0.160
		10350	-0.361
TA 6 G	4+08	10350	-0.320
	4+16	448	-0.204
		10350	-0.391
	4+18	10350	-0.322
	4+20	448	-0.115
		3286	-0.194
		10350	-0.327
TA 5 G	4+30	3286	-0.242
		10350	-0.353

[1]Data furnished by the Air Force.
[2]Highest pass level per station is the final pass level.

REFERENCES

1. J.B. Sousa, J. Crause and C.L. Monismith, Summary Report on Permanent Deformation in Asphalt Concrete, Strategic Highway Research Program, National Research Council, Washington D.C. February, 1991.

2. B.E. Ruth, M. Tia F.T. Najafi and S. Sigurjonsson, Final Report on Preliminary Investigation of Testing Procedures for Evaluation of Rutting Resistance, submitted to Florida Department of Transportation, February 1990.

3. Timian, D.A., "Design and Construction of Pavement Test Sections for the Study of High Pressure Tire Effects", Applied Research Associates Report to AFCESA, contract No. F08635-88-C-0067, Subtask 1.04, May 1989.

4. McRae, John, "Draft of Proposed Revision, ASTM D 3387-83, Standard Test Method for Compaction and Shear Properties of Bituminous Mixtures by Means of the U.S. Corps of Engineers Gyratory Test Machine (GTM)", 1992.

5. McRae, John, Gyratory Testing Machine Technical Manual, Engineering Development Co. Inc., Vicksburg, Mississippi, 1965.

ARNOLD ENGINEERING DEVELOPMENT CENTER

PERFORMANCE EVALUATION FOR PARALLEL INSTRUMENTATION SYSTEMS

Ben A. Abbott

Research Faculty

Department of Electrical Engineering

Vanderbilt University

400 24th Avenue South

Nashville, TN 37235

PERFORMANCE EVALUATION FOR PARALLEL INSTRUMENTATION SYSTEMS

Ben A. Abbott

Research Faculty

Department of Electrical Engineering

Abstract

This research concentrated on performance evaluation of new parallel processing platforms. In particular, experiments were performed using the Multigraph Programming Environment (MPE) on the Texas Instruments (TI) TMS320C40 Parallel Digital Signal Processor (DSP) and the Intel i860 HyperCube. The need for this research became apparent through participation in the 1991 Summer Research Program (SRP) at Arnold Engineering Development Center (AEDC). A major goal of the research was to suggest possible growth paths for the Computer Assisted Dynamic Data Monitoring and Analysis System (CADDMAS) project. Results of this performance study indicate that the TI 32C40 would be a good choice for many of the AEDC parallel instrumentation problems.

PERFORMANCE EVALUATION FOR PARALLEL INSTRUMENTATION SYSTEMS

Ben A. Abbott

INTRODUCTION

This research concentrated on performance evaluation of new parallel processing platforms. In particular, experiments were performed using the Multigraph Programming Environment (MPE) on the Texas Instruments (TI) TMS320C40 Parallel Digital Signal Processor (DSP) and the Intel i860 HyperCube. A major goal of the research was to suggest possible growth paths for the Computer Assisted Dynamic Data Monitoring and Analysis System (CADDMAS) project. Other AEDC instrumentation problems were also considered. Results of this performance study indicate that the TI TMS320C40 would be a good choice for many of the AEDC parallel instrumentation problems.

The need for this research became apparent through participation in the 1991 Summer Research Program (SRP) at Arnold Engineering Development Center (AEDC). This report documents the results of a follow-up grant (mini-grant) awarded as an extension of the SRP.

For the reader unfamiliar with CADDMAS or the Multigraph Programming Environment, background information may be found in the final reports delivered at the end of the Summer Faculty Research Programs (1988 through 1992) written by this same author. That reader may wish to read that background information before tackling the specific steps and results sections of this document. However, a quick description of the CADDMAS project and motivation for this research is

found in the next section.

Further, while this study performed tests on the TI TMS320C40 (C40) processor, it would be out of scope and quite lengthy for this document to try to describe all of the details of programming the C40. Rather, the reader will want to be familiar with the information found in the C40 data book [6]. This document describes the particular tests run on the C40 and their results.

MOTIVATION

Although performance evaluation is a fundamental research issue of parallel processing, a large-scale parallel application, CADDMAS, is responsible for the current focus. AEDC has developed and is currently using this large (200 Mega-Flops), transputer-based, parallel data acquisition and analysis system for turbine engine tests. However, a future system providing real-time monitoring with a performance in excess of 2 Giga-Flops is desired.

Several thousand sensors are commonly used during a turbine engine test. These devices generate large quantities of data that must be quickly analyzed and stored for later recall. On-line computations include: conversion to engineering units, filtering sensor readings, and computation of performance parameters such as Mach number, flow rates, and aggregate pressures. The previous Arnold computation platform consisting of a Cray 1-S and several Modcomp computers was incapable of meeting the real-time demands of current turbine tests.

Vanderbilt has cooperated in this effort since the Summer of 1988. The role of Vanderbilt is to provide a flexible/graphical programming environment (Multigraph) for this parallel system. The key principals of the Multigraph include:

- Providing a virtual machine consisting of a set of heterogeneous connected processors. The user should not be overburdened with the complexity of all the processors and their interconnections.

- Provide a multiple aspect modeling environment allowing the instrumentation system desired to be programmed (or modeled) in a declarative fashion rather than an algorithmic fashion. The declarative models are used by a special interpretation process to automatically generate the executable system.

The Multigraph has proven to be a quite valuable tool aiding the development of the CADDMAS software. However, performance metrics for parallel systems are the subject of considerable research. It is not always clear from vendor information exactly how fast or scalable a particular application might be on a certain type of new parallel processor.

The research effort outlined in the proposal for this grant was to use the Multigraph performance evaluation tools developed under previous research efforts to evaluate the next generation of parallel processing platforms with respect to how various instrumentation problems might be solved within the Multigraph Programming Environment.

Of particular interest was the next generation of transputer. The current CADDMAS uses INMOS T800 transputers of 1987 . It was expected that early in this research period, INMOS would release the T9 transputer. The T9 processor is expected to have various architecture changes as well as an order of magnitude performance increase in both computation and communication capability [3]. Repeated delivery delays for the INMOS T9 have been a major disappointment to the transputer community. The current, updated, delivery schedule places the processor unveiling over two years behind schedule. Simply by its tremendous schedule delays, the T9 has invalidated itself from this research effort.

Texas Instruments (TI), however, did release its new DSP/Parallel processor, the TMS320C40 (C40) [6]. The C40 was expected to be interesting since it is quite similar to the transputer and therefore might offer an easy upgrade path for the CADDMAS. This processor is part of the TMS320 family and has a well established software support library based on a quite similar mono-processing element of

the family, the TMS320C30. However, this is the first "parallel" processor of the TMS320 family. Due to the lack of a T9, the C40 processor became the major focus of this study. However, tests were run on the Intel i860 HyperCube as well.

Questions motivating the research included:

- Do the capabilities of these new platforms open areas where parallel instrumentation was not previously a viable solution?

- How does the performance increase impact the required processor count and architecture of instrumentation systems?

- How will the Multigraph perform with respect to the performance and architecture changes?

- What (if any) Multigraph kernel changes might better utilize these new architectures?

These questions are quite open and therefore can not be completely answered. However, performance evaluation of application systems running on these new platforms provides tremendous insight. Therefore, the basic approach of this research was to do a paper study of the available processors, purchase a chosen set, port the Multigraph and some pieces of application systems (e.g. CADDMAS, Spreadsheet, Image Processing), and then, evaluate the resulting performance.

This document proceeds by providing a step by step description and result discussions of the research steps performed. Then, the recommendations section attempts to combine this information into a concise summary.

STEP 1: EVALUATE EXISTING PROCESSORS

This step began by collecting information and prices from various vendors about these new parallel processors. As typically happens when a purchase is imminent,

vendors happily provided pounds of glossy paper describing there products. Processors lacking floating point support, parallel processing support, a C compiler, an interface for input/output devices, communication bandwidths an order of magnitude greater than T800 transputers, a reasonable future, or scalable solutions were not considered. Following these up and dropping out those processors which obviously did not fit, the following list was compiled:

1. Texas Instruments TMS320C40

   - *Type:* Digital Signal Processor / Parallel Processor

   - *Parallel Processing Support:* On the processor chip

   - *Primary Languages:* C, and Assembly

   - *Architecture:* Arbitrary (typically a hex mesh), scalable, six bidirectional 8 bit, 20 Mega-Bytes/second busses.

   - *Family:* TMS320

   - *Evaluation Board and Software Cost:* $6000 (Two Processor Board)

2. INMOS T9 transputer

   - *Type:* Parallel Processor / General Purpose

   - *Parallel Processing Support:* On the processor chip with an external routing chip

   - *Architecture:* Arbitrary (typically a mesh), scalable, four bidirectional 20 Mega-Bytes / second links. Virtual Channel Routing Chip.

   - *Primary Languages:* OCCAM, C, Fortran, Ada, Pascal, and Assembly

   - *Family:* transputer

   - *Evaluation Board and Software Cost:* N/A

3. Intel i860 HyperCube (not just an i860 accelerator since parallel processing is required)

- *Type:* Vector Processor / General Purpose / Parallel Processor

- *Parallel Processing Support:* External Chips

- *Architecture:* HyperCube, scalable by powers of two (up to 256 processors), Log2(Number of Processors) @ 10 Mega-Bytes / second links, Hardware Cube Routing.

- *Primary Languages:* Fortran, C, and Assembly.

- *Family:* None

- *Evaluation Board and Software Cost:* $10000 (approx. per node)

STEP 2: PURCHASE THE CANDIDATE PROCESSOR

Since the University owns an i860 HyperCube and the T9 was not available for purchase, the C40 was chosen to be the processor purchased for the study. Tests were run on the i860 as well as the C40. Due to price, a Spirit-40 board was purchased from Sonitech in Boston. The board contains two C40 processors each with 512K Bytes of Static Ram and a dual port memory interface with a PC ISA bus. The C40s communicate among themselves via their communication ports (8 bit busses). Along with the board, Vanderbilt received the full TI C environment including compiler, assembler, linker, run time library, and simulator. Further, Sonitech provided a run time library for the PC portion of the interface. $6070 was paid for the Spirit40 and software.

Board delivery was three months late. The Vanderbilt schedule was adjusted to work around this problem. The Spectron SPOX DSP operating system was also part of the purchase but has yet to arrive since their port has not been completed.

STEP 3: PORT THE MULTIGRAPH AND APPLICATIONS

The proposal stated quite clearly that there would not be time to make a complete port of any application or the Multigraph. Rather, a suitable subset of the pieces necessary for performance evaluation were ported.

Due to the time limitations, most of the effort focussed on the processor of primary interest, namely the C40. Only communication benchmarks, and a 3d image rendering application were ported to the i860. The i860 results were impressive from the computational aspect but communication overhead is on the order of 1 millisecond setup time to send a message. In the case of an image rendering application code, the i860 was only 10% faster than the C40. However, this application did not fully utilize the vector capabilities of the i860. Looking at cost, communication bandwidth and setup, scalability restrictions, and scalar operation performance, the i860 does not offer the advantages of the C40 for instrumentation problems. However, there is a tremendous wealth of linear algebra software available for i860 HyperCubes credited primarily to the work of Oak Ridge and Lawrence Livermore Labs. Thus, for numerical computations based on matrices, the Intel may be the best machine.

The following list gives details about the various pieces of application code that were successfully ported to the C40 and their resulting performance (all source code will be provided directly to AEDC along with this report):

- *C FFT*

  - *Description:* As is my habit with any new processor, the first benchmark to be run was a completely C code Fast Fourier Transform (FFT). The program performs a 1024 point complex FFT using 32 bit floating point numbers. It is not an extremely tricky code but is rather indicative of a normal numeric algorithm written in C. Lookup tables are precalculated and utilized for the Sin table. In the case of this program, the test was

run in the fashion described and supported by the Sonitech run time library [5]. That is, semaphores and shared memory were used to setup and run the program.

- *Optimization:* Full (other than register arguments)

- *Difficulties:* Finding all of the optimize switches is difficult at first. Programming in this fashion with shared memory is quite difficult to debug. The code of this program has since been converted to use the Multigraph message passing layer thereby allowing it to do the I/O itself.

- *Program Size:* 130 Lines of C Code.

- *Performance:* 16.8 milliseconds. Being a completely C program, this performance was quite impressive. The rated performance of the C40 for an assembly version of a complex 1024 point FFT is 1.54516 milliseconds [6]. A more general version that matches closer with the C algorithm implemented is also described in the data book. The general version of an assembly FFT is rated at 2.2554 milliseconds. This says straight C code can get within a multiple of 10 of raw machine performance. Further, looking at the C40 as a general purpose processor and comparing it with others adds further light. On a 486/33 DX machine using Turbo-C the same program requires 143 milliseconds. On a T800-25 transputer, this program takes 128 milliseconds.

  This type of calculation is indicative of many of the CADDMAS activities, as well as, those of image processing and engineering unit conversion.

- *Communication Benchmarks*

  - *Description:* The Sonitech example library [5] provides a set of communication benchmarks. Tests were run using these examples. Further, modifications were made to the DMA (direct memory access) based communication version of the examples to use the DMAs in their special

"split-mode" [6] so that bidirectional (full duplex) tests could be run. The logic behind running these tests was to get a feel for how the message passing system required by the Multigraph would best be implemented.

- *Optimization:* Full (other than register arguments)

- *Difficulties:* The "split-mode" DMA setup could not be done directly from C, rather, inline assembly had to be provided. TI provided no useful examples of how to program the DMA in split mode. There was a particularly vexing question as to how to restart only one side of the split DMA without disturbing the other currently active side. The TI hot line was of little help. Finally, I decided it just could not be done. Therefore, in the case of simply one side needing a restart, I issued a halt command to both sides of the DMA, waited for it to stop, reprogrammed the side of interest, and then restarted both sides. Recently, a release by TI onto their TI Bulletin Board System (TI BBS) giving source code to a message router confirmed my conclusion by using the same technique. This is a very sloppy way to have to program the DMA and causes considerable overhead in message setup time. While visiting in Sonitech in Boston, it was explained that the C40's can be destroyed by software if all connected processors are not reset at the same time. This has to do with the token passing mechanism of the communication bus. If it gets into an invalid state thinking that both of the processors own the bus at the same time, one of them may be destroyed. This difficulty causes the programmer to exercise extreme caution whenever working with communication software. One conclusion that may be drawn from these difficulties with communication manipulation is that TI is new into the parallel processing market and still has things to learn.

- *Program Size:* 50 lines of C code, 10 lines of assembly.

- *Performance:* Communication bandwidth results were quite surprising:

* Half duplex programmed input/output (I/O) checking the output empty obtained only 1.6 Mega-Bytes/second.

* Half duplex programmed input/output (I/O) checking the fifo full obtained only 2.2 Mega-Bytes/second.

* Interrupt driven Half duplex input/output (I/O) triggered on the fifo full/empty obtained 6.6 Mega-Bytes/second.

* Half duplex DMA (split or full mode) driven obtained 19.6 Mega-Bytes/second.

* Full duplex DMA (split mode) dropped back to 6.9 Mega-Bytes/second each direction.

Conclusions of this test quickly pointed to the need for any message passing system to use the DMA. The full duplex split mode was only expected to drop to 10 Mega-Bytes/second each direction since two processors were sharing the bus. The fact that the drop is even worse indicates multiprocessor systems developed on the C40 utilizing full duplex communication will experience dramatic nonlinearities in performance as the message passing loading increases and messages begin to bump in the bidirectional mode. More about this topic will be described in the summary of difficulties section.

● *Message Passing System*

   – *Description:* The multiprocessor version of the Multigraph kernel requires a message passing system to exist allowing it to create "streams" connected between processors regardless of hopping constraints [2]. Further, even the stand alone version requires that each processor be able to perform some basic input/output (I/O) functions (such as, opening a file or printing a string). Therefore, as part of the kernel port, this basic message passing system must be put in order. The approach used was to

take the PC side of the transputer version of this code and modify it such that it would work on the C40. The transputer side would be of little use since it was based on the internal scheduler capabilities of that processor. An interrupt mechanism (for DMA complete) had to be added to the PC version, as well as, all of the basic DMA setup functions. A new version of a message forwarding mechanism (similar to that of the transputer version) had to be implemented. Under a separate work, the Automatic Parallel Network Analyzer (APNA) tool was modified to be able to generate map files for the C40 networks (and eventually, mixed T800-C40 networks). The PC I/O server for the transputers had been based on the Logical Systems C compiler run time environment for transputers. This had to be replaced. A version of the Berkley Standard Distribution (BSD) C I/O libraries was modified for just this purpose and the I/O server was implemented. A loader ("ld-one") was put together such that each processor could be loaded with a different set of code and its node number was set into its memory. This loader has the limitation that all processors must be on the same ISA bus. The I/O server ("cio") was coded such that multiple copies of it could run simultaneously talking to different C40s under MS-Windows. As may be noted, the names of these programs were patterned after their LSC transputer version counterparts. All PC sides of the code were generated such that they could be compiled under Turbo-C or the 32 bit GNU-C for DOS. Considering the major changes made to the message passing system over the transputer PC version, it was deemed that serious testing was needed. Therefore, an interactive test monitor program was added. The commands of that monitor include:

```
r <hex address>              -> read a value from memory
. <hex address>              -> read a value from memory
                                (auto increment)
w <hex address> <hex value>-> write a value to memory
s <node> <value> <stream>    -> send an integer to a processor
t <node> <size> <stream>     -> toss (and catch) 100000 <size>
                                messages
b <stream>                   -> bounce everything on a stream
                                back to the sender
g <stream>                   -> test and get message on a
                                stream
d <stream>                   -> delay until get message on a
                                stream
a.                           -> wait for a server to connect
                                (Low)
o <node>                     -> open a stream to another node
                                (Low)
p <node> <channel>           -> set the path to a node out a
                                channel
```

When testing, the communication maps are set up so that each processor thinks it may get back to the host directly in its shared memory interface. Then, under MS-Windows, a separate version of "cio" is run to service each processor individually. With this setup, various test scenarios may be easily setup and verified.

— *Optimization:* Full (other than register arguments)

— *Difficulties:* byte packing had to be added since the TI cannot access bytes. The loader had a buf in that it did not clear the BSS segment of

the object module.

– *Program Size:*

* Basic Communication, Server, and Loader (basically all new):
boot.asm, bsdintf.c, cio.c, comm.c, comm386.c, commti.c, ld-one.c,
lowpc.c, lowti.c, memory.c, reset.c, stream.c, monitor.c, cio.h, comm.h,
revised.h, stream.h

total lines of code: 3799

* BSD Library Code (reused with small modifications):
_fmode.c, bcopy.c, bzero.c, clrerr.c, doprnt.c, doscan.c, fdopen.c, fgetc.c,
fgets.c, filbuf.c, findiop.c, flsbuf.c, fopen.c, fprintf.c, fputc.c, fputs.c,
fread.c, freopen.c, fseek.c, fstat.c, ftell.c, fwrite.c, getc.c, getchar.c,
getdtabl.c, gets.c, getw.c, printf.c, putchar.c, puts.c, putw.c, rew.c,
scanf.c, setbuf.c, setbuffe.c, setvbuf.c, sprintf.c, ungetc.c, vfprintf.c,
vprintf.c, vsprintf.c, aout.h, ar.h, assert.h, atexit.h, bool.h, bstring.h,
ctype.h, dir.h, dirent.h, dos.h, errno.h, fcntl.h, file.h, float.h, get-
pages.h, gppconio.h, graphics.h, grp.h, incremen.h, io.h, limits.h,
malloc.h, math.h, memory.h, mouse.h, obstack.h, osfcn.h, pc.h, pix.h,
pwd.h, random.h, regex.h, setjmp.h, signal.h, stab.h, std.h, stdarg.h,
stddef.h, stdio.h, stdlib.h, string.h, strings.h, swap.h, time.h, tzfile.h,
unistd.h, values.h, varargs.h, sys/cdefs.h, sys/dir.h, sys/dirent.h,
sys/errno.h, sys/fcntl.h, sys/file.h, sys/param.h, sys/register.h, sys/resource.h,
sys/signal.h, sys/stat.h, sys/stdc.h, sys/time.h, sys/times.h, sys/types.h,
sys/uio.h

total lines of code: 6912

– *Performance:* Once the monitor program was in place and the communication system began to work, several performance tests were run aimed at finding out the setup overhead (S), hop overhead (H) (when a message must pass through an intermediate processor on its way to another), and bandwidth (B). With this information, the time (T) to send a message of X bytes to another processor considering it must hop across N intermediate processors may be modeled as:

$$T = S + (N * H + (2 * (X/B)) + X/B$$

The numbers obtained via these tests are:

* $S = 40$ microseconds

* $H = 70$ microseconds

* $B = 19$ Mega-Bytes / Second (if no collisions)
   $B = 6.9$ Mega-Bytes / Second (if continual collisions)

Looking at this equation graphically shows that messages on the order of 4096 bytes are only slightly effected by the setup time overhead:

Effective Bandwidth of Adjacent Processors
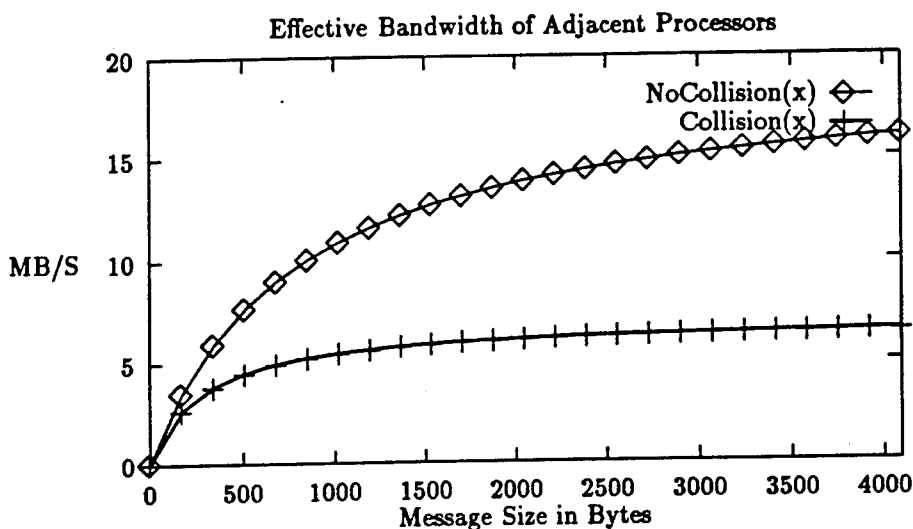
In the case of the CADDMAS, almost all of the message traffic is com-

posed of messages at least 4096 bytes since this is the size of 1024 floating point numbers that make up the basic ensemble. The bend in this curve is later than that of the transputer system which approaches maximum bandwidth at 1024k bytes, but is still quite encouraging since the actual bandwidth has increased by an order of magnitude. If the collision bandwidth can be accepted, the bend is smaller. It is important to note these two lines are the extreme cases, that is, partial collisions will cause the effective bandwidth to fall somewhere between the two lines. When collisions can not be tolerated, either the links needed can be hard coded and multiplexed by a special protocol thereby avoiding any full duplex activity or by programming the message passing via the APNA tool to only use that link in a one way fashion. The APNA tool and both the C40 and transputer versions of the message passing, support this variation on message paths.

Hop time is not a major concern for the CADDMAS system. It needs the throughput bandwidth to be preserved but does not have tight specifications on the time from an actual event till its full processing has been completed. One exception to this is the alarms. Alarms, when finally implemented must use the above equation to verify that the worst case response time is not exceeded.

- *Multigraph Benchmark*

  - *Description:* After the message passing layer existed, porting the Multigraph for a single C40 was a matter of recompiling. C40 complexities kept the multiprocessor port from being completed. The major benchmark desired for the Multigraph is the amount of overhead required to fire an actor. This test was done in the typically fashion by producing a graph with a single actor feeding data directly back to itself and counting the number of firings per second.

5-17

- *Optimization:* Full (other than register arguments)

- *Difficulties:* Porting the kernel to a testable version was not difficult. However, the port is not complete.

  Bytes can't be addressed on the C40. This causes the communication functions used by the Multigraph to require modification. The major change would have taken more time than this research effort was allotted. Memory size is an issue due to the byte addressing problem. The Multigraph requires just under 100K Bytes for code and static data space. However, the dynamic structures created by the kernel are often four times their comparable size on the transputer. Therefore, a safe size to assume for the CADDMAS application is 4 Mega-Bytes of RAM per typical processor. Further difficulties will need to be faced due to the strange floating point format used by the C40. While the C40 supports conversion to and from IEEE format, the Multigraph codes will need to be searched and modified to deal with this issue.

- *Program Size:* 18560 lines of C.

- *Performance:* The C40 is the fastest Multigraph machine ever tested! The scheduling overhead is only 40 microseconds per actor firing. This low overhead means that the normal actor script need only be on the order of 0.5 milliseconds before the kernel overhead becomes negligible. This number is called the granularity. The finer grain that can efficiently be used, the more generic scripts may become since they can be composed of smaller and smaller components.

- *Transient Data Processing Benchmark*

  - *Description:* As soon as the Multigraph was running, it was time to try the "Spreadsheet". In this case, only the single processor version could be tested.

- *Optimization:* Full (other than register arguments)

- *Difficulties:* The only difficulties encountered here were the same floating point format and byte size problems not completely solved in the Multigraph port described above.

- *Program Size:* 1230 lines of C are all that is needed to test the run time side of "spreadsheet". The user interface and builder do not need to be ported to the C40.

- *Performance:* As expected, the C40 was just about 10 times the speed of a T800-25. However, the test was limited to a small graph size due to memory limitations on the Spirit-40 (512K Bytes).

  It is expected that the multiprocessor version of the "spreadsheet" could use the broadcast bus described in the C40 databook [6] and thereby expand even further the possible scaling.

- *Engineering Unit (EU) conversion Benchmark*

  - *Description:* As a test of scaling performance, the equation: $h = g + x * (f + x * (e + x * (d + x * (c + x * (b + x * a)))))$
  was tested. This equation has 12 floating point operations.

  - *Optimization:* Full (other than register arguments)

  - *Difficulties:* Had to use the C keyword volatile to force the compiler to run this equation several times. The optimizer was correctly unrolling my loop and simply evaluating the equation once.

  - *Program Size:* 24 lines of C are all that were needed for this test since the message passing provided I/O.

  - *Performance:* In this test the C40 C compiler produced quite good code. 10 Mega-Flops were achieved. The machine code produced for this test follows:

```
        RPTB    L5
        LDF     @_X,R9
        MPYF    R10,R9,R0
        ADDF    R2,R0
        MPYF    R9,R0
        ADDF    R3,R0
        MPYF    R9,R0
        ADDF    R11,R0
        MPYF    R9,R0
        ADDF    R4,R0
        MPYF    R9,R0
        ADDF    R5,R0
        MPYF    R9,R0
        ADDF    R6,R0
L5:     STF     R0,@_h
```

While you might be able to code this with some parallel instructions, your first pass of hand coding this loop might be quite similar.

- *FORTRAN Benchmark*

  - *Description:* As a test for the transient data processing FORTRAN libraries, the AT&T F2C translator was ported to the C40. Then, an AEDC benchmark released during a supercomputer search was run.

  - *Optimization:* Full (other than register arguments)

  - *Difficulties:* C compiler size limitations forced the file to be broken into small subroutines.

- *Program Size:* F2C libraries are 5925 lines of C code. The AEDC benchmark is 6934 lines of FORTRAN code.

- *Performance:*

  In this test, the C40 completed computation in 196 seconds. The cut off to apply for the AEDC supercomputer contract was 100 seconds.

- *Image Processing Benchmark*

  - *Description:* In order to test the C40 on image processing applications, a 3d image rendering algorithm was ported to the C40. As well, the same code was ported to the IBM 320 and the Intel i860.

  - *Optimization:* Full (other than register arguments)

  - *Difficulties:* None.

  - *Program Size:* 643 lines of C code.

  - *Performance:*

    In this test, the C40 was able to render a 64 cubed image in 51.9 milliseconds. This was about twice the speed of the IBM 320 and just 10% slower than the i860.

DIFFICULTIES USING THE C40 IN A GENERAL PURPOSE FASHION

This section is intended to provide a summary of the types of difficulties foreseen in the transfer to the use of the C40:

- The biggest difficulty in porting existing code is the byte size addressing problem and the floating point format conversion. It is possible at the sacrifice of speed for a C compiler to solve this problem, but there is not one available.

Porting existing C code to the TI often proves to be difficult due to the "non-standard" sizeof(long) / sizeof(char) ratio. On the TI, the only addressable memory unit is a 32 bit word resulting in: sizeof(double) == sizeof(float) == sizeof(long) == sizeof(int) == sizeof(char) == 1. It is a common assumption of C programmers that: sizeof(double) == 8, sizeof(float) == sizeof(long) == 4, sizeof(int) == 4 or 2, and sizeof(char) == 1. This assumption has proven to be reasonable, until the TI. The result is that reuse of public / pre-existing code for the TI will often require a major rework. As well, all expected TI communication with other processors such as PCs or transputers must be carefully worked.

- Multiprocessing performance will hopelessly be tormented by the nonlinear loading problems of the communication system.

Use of the TI communication links in a half-duplex fashion (only sending one direction at a time) provides a 19 Mega-Bytes/Second bandwidth under DMA control. However, using full duplex transfers drops the aggregate bandwidth to 13.8 Mega-Bytes/Second (6.9 each direction). All of the AEDC/Multigraph applications regularly perform bidirectional transfers.

This nonlinear bandwidth drop will have dramatic effects on programs that load the communications heavily (even if the load is only a peak load). Linear prediction models will fail to correctly predict actual performance. Consider an application requiring 10 Mega-Bytes/second in one direction and only 4 Mega-Bytes/second in the opposite direction. This system might run perfectly for hours; as long as timing does not request a bidirectional transferring of data. However, if timing edges slowly such that a small bidirectional transfer overlap begins to occur, the overlap can then grow in an accelerated fashion since each added overlap portion decreases the overall possible bandwidth. At the overlap limit case for this example, the system would fail since 14 Mega-Bytes/second exceeds the bidirectional bandwidth available.

This problem did not exist in the transputer platforms since it provides "true" full duplex transfers.

The C40 crossbar switch currently being developed at UTSI is expected to suffer even worse from this issue since it will slow the bus turnaround time even further.

- From discussions I have had with other people coding message passing systems for the C40, it appears that bus starvation could become a very real problem. Specifically, the C40 memory bus bandwidth can be exceed if all of the DMA engines are communicating simultaneously.

  We saw a similar problem to this on the CADDMAS NPE where the Zoran would lock the bus for so long that the FEP would overflow its queue. The solution in that case was to add another processor into the pipeline, the FEPQUEUE processor. This issue must be kept in mind so that such surprises do not happen again.

- The possibility of destroying a processor by reaching an invalid communication bus state via incomplete system reset is particularly pernicious. Hardware system designs need to be very careful to try to lock these resets together. The Spirit-40 does not do it.

- The C compiler has a very good optimizer. Care must be taken to not assume a variable is always read if it appears in the code. The C keyword "volatile" should be used any time there is a need for a shared variable between two processes.

- The C40 is memory hungry due to the inability to access bytes.

- There are no tools such as the transputer programs "check" and "ld-net" for the C40.

- The Spirit-40 board and possible others does not support being put in a passive backplane since it does not have the ability to boot from the communication port. The C40 itself is capable of doing this.

- The C40 gets very hot. While I had eight processors in my 486, I was afraid to close up the box. Rather, I pointed a fan directly at the C40s.

RECOMMENDATIONS

I have no doubt that a C40 based CADDMAS and "spreadsheet" system could greatly exceed the current performance. It seems safe to say a reduction of processors on the order of four to one could be used with the exception of the NPE where the C40 seems only marginally faster. I like very much that the C compiler produces such good code. This opens the possibility of rapidly generating new hybrid signal processing functions without being forced into an archaic assembly language. In my opinion, this capability is directly in line with the AEDC mission since testing requirements are constantly being changed.

Four Mega-Bytes per C40 processor minimum is recommended for CADDMAS and other Multigraph instrumentation applications.

Care must be taken when putting together the first large C40 system to avoid the reset problems of boot from communication port and invalid bus state. Heat will be an issue in packaging.

An issue not directly addressed by specific tests came up near the end of this research. That is, many instrumentation applications could benefit from the broadcast bus capability of the C40. Consider for example the "spreadsheet", the "BTD bus" of CADDMAS, or an image "farming" algorithm, in this case the data must be flooded out to all of the consumers and then the results flow through to various locations. If the single master broadcast method described in the TI databook [6]

were used, full duplex collisions could be avoided and data delivery time reduced. I strongly suggest this method be investigated further. With such a bus, I am also confident that the C40 could be used to provide a formidable image processing machine.

Finally I am in the position to answer the questions posed as motivation for this research:

- *Do the capabilities of these new platforms open areas where parallel instrumentation was not previously a viable solution?* Quite definitely.

- *How does the performance increase impact the required processor count and architecture of instrumentation systems?* Four to one. Should use a broadcast bus.

- *How will the Multigraph perform with respect to the performance and architecture changes?* This is the fastest Multigraph machine ever tested!

- *What (if any) Multigraph kernel changes might better utilize these new architectures?* Byte accessing and floating point formats need to be generically supported by the Multigraph.

ACKNOWLEDGEMENTS

References

[1] Biegl, C.: "Design and Implementation of an Execution Environment for Knowledge-Based Systems" Ph.D. thesis, Department of Electrical Engineering, Vanderbilt University, Nashville, TN., Dec., 1988.

[2] Abbott, B., Biegl, C., Sztipanovits, J.: "Multigraph for the Transputer", Proc. of 3rd Conf. The North Amer. Transputer Users Group, Santa Clara, Calif., April 1990.

[3] This information was released over netnews by INMOS. The only way to get back to it is to dig through the news archive server.

[4] INMOS Limited: Transputer Reference Manual, 1989.

[5] SONITECH Interarntional, Inc: SPIRIT-40/ISA User's Guide, June, 1992.

[6] Texas Instruments Incorporated: TMS20C40 User's Guide, 1992.

[7] Zoran Corporation: ZR34345 32-Bit IEEE Floating-Point Vector Signal Processor User's Manual.

1992 USAF-RDL RESEARCH INITIATION PROGRAM

Sponsored by the

AIR FORCE OFFICE OF SCIENTIFIC RESEARCH

Conducted by the

Research and Development Laboratories

FINAL REPORT

Rocket Plume Image Sequence Enhancement
Using 3D Operators

Prepared by: Richard Alan Peters II, Ph. D.

Academic Rank: Assistant Professor

Department and   Department of Electrical Engineering
  University: Vanderbilt University

Research Location: Arnold Engineering and Development Center
                    Arnold AFB, TN 37389

USAF Researcher: J. A. Nichols

Contract No: F49620-88-C-0053

December 1992

Rocket Plume Image Sequence Enhancement Using 3D Operators*

Richard Alan Peters II
Department of Electrical Engineering
Vanderbilt University
Nashville, TN 37235

March 27, 1993

Abstract

We tested five 3D image operators in eleven configurations to determine which is best for the enhancement of image sequences of rocket plumes. We considered enhancement both for visual inspection and for radiometric characterization. We used real and synthetic imagery to test the operators under a number of conditions. We found that the best choice of operator depends on the amplitude distribution of the noise in the image sequence. In terms of SNR, long duration median filters with moderate spatial support appear to work best overall.

We also found that successful enhancement for visual inspection requires the original image data to be remapped prior to filtering. We found that this need not destroy the radiometric information in the imagery.

This paper describes some attributes of rocket plume image time sequences and the noise in them. It details our remapping procedure. It describes the operators we tested. It explains our methodology and presents the results of the numerous tests on synthetic imagery from which we draw our conclusions. It describes the application of our procedures to two real rocket plume image sequences.

6- 2

1 Introduction

Time-sequential imagery is an important tool for the evaluation of rocket firings. It is useful not only for the diagnosis of test firings but also for the tracking, detection and identification of rockets by an active defense system. The time-sequence of images from a rocket test is a time-sampled optical record of the evolution of the rocket plume. There is much information to be gleaned from such imagery, but often relevant information is obscured by noise or artifacts of the imaging system. Spurious information can also create false events in the record of a firing. This paper describes noise reduction techniques that improve the signal to noise ratio (SNR) in image sequences and greatly diminish spurious events.

Standard processing techniques for rocket plume imagery can be inadequate if they concentrate on the brightest, yet not necessarily most important information in the imagery. In this case much of the plume structure may be invisible. If the exact locations of various plume components are not known, the task of radiometric identification is complicated. Remapping the imagery to highlight the most important information bands can permit the precise location of various structures in the imagery. Then not only can radiometric assessment of the components be isolated, but also the non-plume regions of the imagery can be used to estimate the characteristics of the noise. As we will demonstrate, the characteristics of the noise determine which operator will best improve the SNR of the image.

Many of the enhancement and noise reduction procedures in common use are applied to the image time sequence on a frame-by-frame basis.[1] Frame-by-frame processing ignores a very important source of information – redundancy. The human brain probably uses temporal redundancy in discriminating real objects from the spurious within its visual field. For example, if one examines an image time-sequence, frame by frame, it can be difficult to decide which objects in the image are noise and which are the projections of features on real objects. However, if one views the sequence rapidly (i.e at video frame rates) it is easier to judge, albeit subjectively, which objects are real and which are noise. The brain apparently assumes that small, fleeting image objects (especially point objects) are noise whereas persistent features are real.

This is a reasonable assumption for processing rocket plume image sequences as well, since many types of noise are spatially uncorrelated and vary in time more rapidly than real objects. Some noise, notably the thermal noise in a CCD sensor array and the photomultiplier pulse noise, vary more quickly over time than a video or motion picture frame rate. If rather than processing on a frame-by-frame basis we process the sequence over a number of frames, we can use spatial coherence and temporal redundancy to discriminate true features from noise. Temporal redundancy becomes spatial coherence if the time sequence of images is treated like a 3-dimensional solid; that is, if the sequence of 2D images is taken to be a single 3D spacetime image. Then, 3D volumetric operators which emphasize spatial coherence can be used to enhance structures that have not only spatial support but also

---

[1]We use the term "frame" to mean a single image from a time sequence of images.

temporal persistence.[2]

We tested five 3D operators in eleven configurations. We state the dimensions of the operators as $x \times y \times t$, where x and y are spatial dimensions in pixels, and t is the time dimension in frames. The operators are :

1. (AVG113) $1 \times 1 \times 3$ average,

2. (AVG333) $3 \times 3 \times 3$ average (8-connected spatial neighborhood),

3. (AVG1115) $1 \times 1 \times 15$ average,

4. (AVG3315) $3 \times 3 \times 15$ average (4-connected spatial neighborhood),

5. (MED333) $3 \times 3 \times 3$ median filter (8-connected spatial neighborhood),

6. (MED1115) $1 \times 1 \times 15$ median filter,

7. (MED3315) $3 \times 3 \times 15$ median filter (4-connected spatial neighborhood),

8. (GMF9) 9 element 3D generalized morphological filter,

9. (GMF12) 12 element 3D generalized morphological filter,

10. (MMF) multistage median filter,

11. (LUM) lower-upper-middle filter.

The last four filters work in an $3 \times 3 \times 3$ spacetime neighborhood. Thus seven of the filters are short time duration and four are long duration.

We tested the operators on both real and synthetic imagery. We found that the statistical distribution of the luminance noise affects the results of the various operators. It is, perhaps, the most important criterion to consider in selecting an operator for noise reduction.

To obtain measurable results applicable to radiometry, we applied the operators to a synthetic image sequence of a rocket plume combined with noise of various strengths and measured the signal to noise ratio (SNR). We found the operators that maximize the SNR at each noise level. Although these might be the best for radiometric assessment of a rocket plume, the operators that were best in SNR did not necessarily *look* best. Presumably the human brain does not use an SNR criteria in judging image fidelity. More importantly it indicates that in choosing the best looking result, a researcher may select a suboptimal operator for radiometric assessment.

For our tests on real imagery, we remapped the data to enhance the visibility of plume structure. We applied the operators and, because the ground truth was unavailable, made a purely subjective assessment of the results. (I.e., which one looks best and why).

In this paper: We describe the characteristics of rocket plume imagery. We discuss the remapping the data from rocket plume sequences so that the most important information

---

[2]Note that in some situations, true features may be small and fleeting. However, for this work, we assumed that if an object has those characteristics, it is noise.

is visible. We describe the operators we tested for this paper. We describe the experiments we performed in testing synthetic data, including the effects of gaussian and non gaussian noise. We present the results of applying the filters to real data.

2   Characteristics of Time-Sequential Rocket Plume Imagery

This section discusses assumptions about the characteristics of plume objects and noise in time sequential imagery.

2.1   Characteristics of Rocket Plumes

We assume the following: A rocket plume consists of a bright core surrounded by a dimmer band. This outer band is often approximately parabolic in shape. Part of the outer band has a relatively sharp edge resulting from bow shock. Other edges of the outer band are diffuse. The plume is visible in every frame, although its exact position may vary considerably. The shape and luminance of the plume are mostly static except for occasional flare ups. During stage separation events. the plume shape and luminance are highly dynamic.

Figure 1 shows a synthetic image of a rocket plume generated by software at AEDC. We used this image to generate synthetic image sequences for our tests.

2.2   Characteristics of Noise

Rocket plume image sequences are notoriously noisy. Thermal processes in the image sensor, imperfections in the recording medium, atmospheric distortion, and various environmental factors degrade the imagery. The optics of the imaging system convolves a pointspread function with the imagery. In addition to being noisy, the images are usually jittery due to inaccuracies in tracking and other motion of the sensor platform. High-speed (with respect to the frame rate) jitter adds another pointspread function. Low-speed jitter causes the position of the rocket plume to change randomly from image to image within a sequence. Noise obscures important features of the plume and therefore should be removed or at least reduced. Jitter complicates noise cleaning because a pixel at a specific position does not image the same spatial location from frame to frame.

Noise is manifest in one or more of the following forms:

- **Dense noise.** This is an error from the true luminance value at every pixel im the image. It can result from atmospheric turbulence or aerosols as well as from thermal processes in the imaging system. Frequently, the noise intensity probability distribution is multimodal; rarely is it symmetric. The shape of an individual mode may be more or less gaussian in shape. The statistics are not necessarily time-stationary.

- **Photomultiplier pulse noise.** This phenomenon is generally called "popcorn" noise by the plume research community. It is the result of spurious emissions from the photocathode in a photomultiplier tube in the imaging system. The noise appears as spatiotemporally compact flashes with maximum luminance at random locations in

the image sequence. Generally a single pulse has spatial support of several pixels and persists for only a single frame.

- **Patterned noise.** This is often manifest as a periodic cross-hatching. It can result from vibration or electrical interference within the imaging system. It is generally difficult to estimate the intensity distribution of such noise. It is sometimes detectable as peaks in the 2D spatial frequency spectrum. The pattern may be fixed in position over time, or it may drift; It may or may not be amplitude modulated.

Pointspread functions and jitter also degrade the imagery. But we do not consider techniques for removing these.

In order to test the operators on a known quantity, we synthesized a dense noise processes, which we call LAL (for log-alpha-log) noise, as follows: Let $I(x,y)$ be a pixel in a noise free image. Let $G(x, y; \mu, \sigma)$ be a random variable whose amplitude is gaussian with mean $\mu = 0$ and variance σ^2 and whose spatial position in an image is given by (x, y).

$$N_s[I(x.y)] = \ln \{\alpha(1 + \ln [\lfloor I(x,y) + G(x,y; 0, \sigma) \rfloor])\}, \qquad (1)$$

where $\lfloor \cdot \rfloor$ represents clipping at zero. and α is a real constant. Thus if $I \equiv 0$, $N_s[I]$ has 50% of its pixels equal to zero and 50% given by the LAL distribution.

This is an *ad hoc* noise model. It was constructed to mimic the appearance of the noise in the real rocket plume image sequences (which it does). We based it on the presumed behavior of atmospheric noise and a typical imaging system. We assumed that noise due to atmospheric turbulence and aerosols is zero mean gaussian and additive to the rocket plume image. However, luminance cannot be negative so we clipped at zero. The log-alpha-log remapping was to mimic the response of the photocathode followed by a linear gain followed by the image sensor response. Further research should lead to less empirical noise models.

To mimic photomultiplier pulse noise, we placed white dots and random locations in some frames. We did not synthesize patterned noise nor did we convolve with a pointspread function.

3   Remapping of Image Data

There is a large variation in the dynamic range of the intensity measurements in unprocessed image sequences of rocket plumes. All information may be concentrated in one small amplitude band within the data words that represent the pixels. For example a 64-level (6-bit) image may be encoded in a 16-bit per word format. Those 64 levels may or may not be contiguous. The mapping from the 64 levels to the 65536 levels in the 16-bit words, although presumably monotonic, is arbitrary. That is, the data may be concentrated or it may be spread out over much of the available band.

On the other hand, the overall data amplitude band may be large but, that information which is *visually important* may exist only in a narrow band. For example, photomultiplier noise appears as very bright random impulses (popcorn noise) in an image sequence. If the

plume signal is dim and weak (having a very narrow amplitude band), it may appear not to exist at all, as it is drowned out by the intensity of the photomultiplier noise. This was the case in one of the two real image examples in this paper.

Additionally, the dynamic range as well as location of the amplitude band can change over time within an image sequence. Such dynamics can be the result of changing sensor characteristics. For example, some of the imaging systems have automatic gain adjust circuitry which attempts to keep the overall brightness of the image constant. If the plume is obscured momentarily, the gain of the system may increase causing visible flashes as the background noise is amplified to a level that matches the brightness of the plume.

The simplest function to map a long-pixel image to a short-pixel image for processing is a linear map of the form

$$v(x,y) = \max_v \left(\frac{u(x,y) - \min_u}{\max_u + \min_u} \right) - \min_v \tag{2}$$

where $u(x,y)$ is the original pixel, $v(x,y)$ is the remapped pixel, $(\min_u.\max_u)$ are the minimum and maximum pixel values in the original image and $(\min_v.\max_v)$ are the extrema for the remapped image. Usually, $(\min_v.\max_v) = (0, 255)$. The pair $(\min_u.\max_u)$ is often usually chosen to be the minimum and maximum values that can possibly be represented in the original image data word. (e.g., 0 and 65536 for 16-bit unsigned data). Alternatively, the pair might be chosen to be the actual minimum and maximum value present in the image.

The problem with these remapping strategies is that they ignore the range of the visually important data within the image. It is better to choose $(\min_u.\max_u)$ so that they bound the important data. Now, precisely what constitutes the important data is subjective. The graylevel histogram of the image often provides clues.

We have found the following approach adequate: We first average the gray level histograms of a number of frames (say 100) randomly selected from the sequence. Often the histogram exhibits a multimodal structure. One mode usually is near the bright end of the histogram. This is caused by either pixels in the plume core or photomultiplier noise. There may be another mode near zero where noise is clipped at the "floor" of the sensor. There is often a wider mode somewhere in between the two extremal modes. The center and extrema of this mode may vary quite a bit but the extrema for every frame usually are contained in some fixed interval A. We calculate the mean and standard deviation of the histogram restricted to A. we set $(\min_u.\max_u)$ to be within N standard deviations of the mean. We generally take $N = 2$ or $N = 3$. We then perform a linear mapping as per eqn (2). This is, admittedly, *ad hoc*, but through a careful examination of the raw data it is usually possible to find a good extrema pair.

Figure 2 demonstrates the results. Plots (a) and (c) are the logarithms of the gray-level probability distributions of two real rocket plume image sequences that have been linearly mapped from (min,max) to (0,255). In the first, the mode of the distribution is about 10, in the second, about 24. Images from these sequences appear mostly black with a few

bright spots.[3] If instead we remap the data to within 2 or 3 standard deviations of the mean frame-by-frame, we get the distributions shown in (b) and (d). Notice that there are spikes at either end of these distributions as a result of clipping. Whereas distribution (b) is dominately unimodal, distribution (d) has at least 5 modes. Neither is gaussian.

Linear mapping is not necessarily best for all data sets. If the most of the data is dark or light, it can be corrected by remapping along a gamma curve [12]. Or, if the histogram has many different modes, remapping for histogram equalization [6] makes optimum use of available gray levels.

Remapping the original data destroys the radiometric meaning of the value of the pixel. If the chosen mapping function is monotonic, it is invertible if it is one-to-one (not always the case due to quantization). Then the imagery can be remapped, processed, and then inverse mapped to regain the radiometric significance of the pixel values. Note that the remapping function may vary from frame to frame, so a frame-wise record must be kept if one is to employ this strategy. Another approach is to use remapping to delineate the plume structures in each frame. Then the original unmapped frames can be segmented into plume and non-plume regions. A noise distribution can be accumulated from the non-plume regions and an appropriate noise reduction operator can be used on the original frames. Then radiometric information is preserved.

4   3D Operators Tested

Morphological filters performed better than linear filters for noise reduction in most of the rocket plume image sequences. Mathematical morphology is the name applied to a collection of set theoretic operators defined on a abstract structure known as an infinite lattice. These operators, first examined systematically by Matheron [11] and Serra [13], [14], [15] in the 1960's, are an extension of Minkowsky's set theory. They are especially useful for image analysis and image enhancement. There are, in the general literature, a number of good tutorials on mathematical morphology for image processing [5], [7], [8], [9], [10], [14].

Morphological operators include, erosion, dilation, opening, closing, rank filters (including the median filter), tophat transforms, and generalized correlations. Three dimensional morphological operators are quite useful in processing 3D spacetime images. An appropriate operator, applied to a spacetime image can preserve the persistent shapes and discard those which change rapidly. We have observed that simple 3D morphological operations applied to a noisy time sequence can dramatically reduce the apparent noise.

We have used the following operators to reduce noise in image sequences: linear averaging, opening, closing, OCCO (pixelwise average of open-close and close-open), median filters, generalized morphological filters, the multistage median filter, and the LUM filter.

We used morphological tophat transforms (the difference between an image and its closing) [5] for background normalization in the real image sequences that we processed. This was done to further enhance the vivibility of the plume. We did not test its effect on SNR because it radiacally alters radiometric information.

---

[3]These are the distributions of the two real sequences described in section 6. c.f. figures 8 and 9

We found standard opening, closing, and OCCO to be not very useful under extreme noise conditions. They often produce completely black or completely white images given the high-amplitude noise in rocket test image sequences. Hence, we omitted those operators from the results presented here.

Our analysis of the operators includes both qualitative and quantitative aspects. We wanted to know which operator produces the "best-looking" results and which one maximizes the SNR of the output.

In the following, let $I(x, y, t)$ represent a pixel at spatial location (x, y) and frame t of a noise-free image sequence. Let $C(x, y, t)$ be the same pixel in a noise corrupted version of $I(x, y, t)$. The noise process which corrupts $I(x, y, t)$ is $N(x, y, t)$. It is reasonable to assume that $N(x, y, t)$ is independent with respect to t (if there is no patterned noise). It cannot, however, be assumed that $N(x, y, t)$ is identically distributed for each (x, y) since the value of $I(x, y, t)$ at that point could cause the distribution to saturate at an upper or lower clipping value (i.e. black or white). For the same reason $N(x_0, y_0, t)$, (x_0, y_0) fixed, can be considered identically distributed for each t only if $I(x, y, t)$ is constant with respect to t. $I(x, y, t) = constant$ w.r.t t only if the rocket plume is registered (i.e. exhibits no jitter) and is unchanging in shape.

4.1 Linear Averaging

The simplest and, perhaps, most obvious way to exploit time redundancy in an image sequence is to compute a running average of the frames. That is, if $C(x, y, t)$ is the noise corrupted image sequence, the output of the linear averaging filter, $\Phi_n[\cdot]$, is

$$A_n(x, y, t) = \Phi_n[C(x, y, t)] = \frac{1}{2n+1} \sum_{k=t-n}^{t+n} C(x, y, k). \tag{3}$$

If the underlying noise-free image sequence, $I(x, y, t)$ is constant with respect to t so that $C(x, y, t)$ is independent identically distributed with mean $\mu_{(x,y)}$ for each t, the law of large numbers implies that $A_n(x, y, t)$ converges in probability to $\mu_{(x,y)}$ as n gets large. Thus, if $I(x, y, t)$ is constant over time, and if $N(x, y, t)$ has mean zero, and if

$$C(x, y, t) = I(x, y, t) + N(x, y, t), \tag{4}$$

(i.e., the noise is additive and there is no clipping to skew the mean), a linear average will be close to $I(x, y, t)$ for sufficiently large n.

These conditions are rarely met. Rocket plumes are dynamic, even during stable periods there is usually some jitter in the image due to mistracking. This means $I(x, y, t)$ is not constant and therefore, the $C(x_0, y_0, t)$ are not identically distributed over t. Also, $C(x, y, t)$ often will be clipped due to the finite word length of the pixels, which causes the sample mean to be skewed away from the true mean.

These complications occur so frequently in practice that we have never found a running average to be the best method of noise reduction for an image sequence.

4.2 Median and Rank Filters

The median filter is a special case of the rank filter [9], a morphological operator which we now define:[4] Let Z_p be a morphological structuring element translated so that its origin lies at pixel location $p = (x, y, t)$ in the spacetime image $I(x, y, t)$. Assume that Z_p contains n pixels. $R_r(p)$, the rank filter of order r is computed by sorting the pixels in I covered by Z_p into descending order by value and picking the rth value from the list. This value is placed at pixel p in the output image. The value, $R_r(p)$, is also called the rth order statistic of the neighborhood defined by Z_p. If $r = \text{int}[(n + 1)/2]$, then $R_r(p)$ is a median filter.

The median filter was first described by Tukey [18] as an edge preserving noise filter. Median filters are most often used on 2D imagery to remove impulsive noise. The median filter has the property that if applied iteratively to a signal it reaches a fixed point (i.e., the signal is unchanged by application of the operator) after a finite number of iterations. Gallagher and Wise [4] called this fixed point a "median root," and proved an extistence theorem about it. In [2] Bovik defines what he calls an "order statistic filter" (OSF) as a linear combination of the order statistics. The median and rank filters are special cases of this. He found, for several noise distributions, coefficients for the OSF that minimize the MSE between a constant signal and a noise signal with mean equal to that constant. He found that for gaussian noise the coefficients should be equal; which is simply the average over the neighborhood. He also demonstrated that the more impulsive the noise, the more the coefficients tended toward a median filter. His noise distributions were all symmetric about the mean which means that his results do not necessarily apply to our situation where noise distributions are usually not symmetric.

Note that unlike the mean, the median of a distribution is unaffected by clipping the signal as long as the clip level is greater than the median when clipping from above, or less than the median when clipping from below. Half the pixels in the neighborhood are still less than the median and half are still greater. This generalizes to order statistics as follows:

Theorem 1 *Assume signal* $\{s(j)\}_{j=1}^{N}$ *takes on values in* $(-\infty, \infty)$. *Let the clipped signal* $c_{\alpha,\beta}(j)$ *be defined by*

$$c_{\alpha,\beta}(j) = \begin{cases} \alpha & \text{if } s(j) \leq \alpha \\ s(j) & \text{if } \alpha < s(j) < \beta \\ \beta & \text{if } s(j) \geq \beta \end{cases}$$

Let

$$OS\{s(j)\}_{j=1}^{N} = \left\{s^{(1)}, \ldots, s^{(N)}\right\}$$

be the the set of order statistics of $\{s(j)\}_{j=1}^{N}$. *That is,* $OS\{s(j)\}_{j=1}^{N}$ *is the set of elements* $s(j)$ *sorted into descending order. Let*

$$OS\{c_{\alpha,\beta}(j)\}_{j=1}^{N} = \left\{c_{\alpha,\beta}^{(1)}, \ldots, c_{\alpha,\beta}^{(N)}\right\}$$

---

[4]Morphological operators are defined in part by a structuring element (SE). For our purposes, this is best envisioned as a moving window or neighborhood delineator with one pixel – typically the center pixel – designated the origin.

be the order statistics for the clipped signal. Then,

$$c_{\alpha,\beta}^{(i)} = s^{(i)} \text{ for those } i \in (1,\ldots,N) \text{ such that } \alpha < s^{(i)} < \beta$$

That is, any order statistics between α and β are unchanged by clipping.

The proof is simple: If M elements in $\{s(j)\}_{j=1}^{N}$ are greater than β, these become $s^{(1)},\ldots,s^{(M)}$ in the order statistic list for $s(j)$. Then, $c_{\alpha,\beta}^{(1)},\ldots,c_{\alpha,\beta}^{(M)} = \beta,\ldots,\beta$ are the first M elements in the order statistic list for $c_{\alpha,\beta}(j)$. Similarly, if L elements in $\{s(j)\}_{j=1}^{N}$ are less than than α, these become $s^{(N-L-1)},\ldots,s^{(N)}$. The last L order statistics of the clipped signal are then $c_{\alpha,\beta}^{(N-L-1)},\ldots,c_{\alpha,\beta}^{(N)} = \alpha,\ldots,\alpha$. The other order statistics remain the same.

From this fact we see that if a constant sequence plus zero mean noise from a symmetric distribution is clipped unequally from above and below, The sample mean will not converge to the constant whereas the median will (providing the constant is not in one of the clip intervals). Since the distributions are often clipped in time sequential imagery of rocket plumes, a median filter will often be more accurate than simple averaging. If there is no clipping and the noise distribution is zero mean and symmetric, then both the mean and the median are unbiased estimators of the constant.

The above discussion applies directly to the situation where the rocket plume is registered and stable in shape. Then, a long-time median filter with spatial support of 1 pixel is an appropriate filter. The distance in probability of the sample median from the true value of the pixel sequence $I(x_0, y_0, t)_{t=-\infty}^{\infty}$ decreases as the length of the median filter increases. Thus, for stable imagery, the longer in time the median filter is the better the noise reduction will be.

However, real images of rocket plumes are dynamic. In that case, the likelihood of including spurious pixels in the median neighborhood increases with the duration of the filter. Thus, for dynamic imagery, the median filter should be kept short. Since rocket plume imagery is rather diffuse (does not exhibit drastic changes in luminosity between spatially neighboring pixels) one can use median filters with moderate spatial support to increase the total number of pixels in the median neighborhood without resorting to long duration filters. For example, we found that a $x \times y \times t = 3 \times 3 \times 15$, plus-shaped (4-connected spatial neighborhood) median filter works very well to enhance moderately time-stable structures that also have some spatial support.

4.3 The Multistage Median Filter

The multistage median filter (MMF) of Arce [1] combines the outputs of a several different median filters. There are a number of configurations possible depending on the choice of structuring elements. We have used the SE configuration shown in figure 3 (a). The filter comprises four median filters run in parallel. Each has a different structuring element that favors a specific spacetime configuration. Let M_j be the output of the jth median filter $j = 1,2,3,4$. Let $U(x,y,t) = \max_{j=1}^{4}\{M_j(x.y.t)\}$ and let $L(x,y,t) = \min_{j=1}^{4}\{M_j(x,y,t)\}$.

That is, U is the pixelwise maximum and L is the pixelwise minimum of $\{M_j(x.y.t)\}_{j=1}^4$. The output of the MMF is

$$\text{MMF}(x, y, t) = \text{median}\{I(x, y, t), L(x, y, t), U(x, y, t)\} \tag{5}$$

that is, the median of the set containing the pixel at (x,y,t) from the original image, the minimum median value, and the maximum median value. The MMF filter sets bounds on the behavior of a pixel, $I(x, y, t)$, based on the median behavior of pixels in various neighborhoods including the pixel itself. If $I(x, y, t)$ is out of the bounds given by $L(x, y, t)$ and $U(x, y, t)$, then the output pixel is which ever of $L(x, y, t)$ or $U(x, y, t)$ is closest in graylevel to $I(x, y, t)$.

4.4 The LUM Filter

LUM stands for lower-upper-middle. This filter was analyzed by Arce in [1]. This filter simply takes all the pixels in a neighborhood (with an odd number of pixels), sorts them, and finds the median of a lower order statistic, an upper order statistic, and the center pixel in the neighborhood. That is, let $m = (N + 1)/2$ where N is the number of pixels in the neighborhood. Then

$$\text{LUM}_k(x, y, t) = \text{median}\{I(x, y, t), L_k(x, y, t), U_k(x, y, t)\} \tag{6}$$

where $I(x, y, t)$ is a pixel from the original spacetime image which is in the center of the filter neighborhood, $L_k(x, y, t) = R_{m-k}(x, y, t)$ and $U_k(x, y, t) = R_{m+k}(x, y, t)$. L_k is the order statistic k below the median and U_k is the order statistic k above the median. This filter is similar to the MMF in that it compares the center pixel in a neighborhood to bounds determined by neighborhood statistics. If the center pixel is out-of-bounds, the filter returns the bounding value closest (in graylevel) to the center pixel. The LUM filter has a parameter, k that determines how tight the bounds are on the center pixel. If $k = 0$ the LUM filter is a straight median filter. If $k = m$ the filter does nothing to I. Thus, for increasing k the LUM filter becomes less stringent.

4.5 Generalized Morphological Filters

The generalized morphological filter is a hybrid linear / nonlinear filter, developed by Song and Delp and based on the cascade and combination of multiple morphological filters [16]. The basic filter consists of two stages, the OL stage and the CL stage. The OL stage applies in parallel a number of openings to the image. For each input pixel it orders and takes a linear combination of the results of the openings. The CL stage is similar, only it performs closings. In each of two possible configurations, one stage is the input to the other. Song and Delp defined and tested the filter in two dimensions. We have extended it to three dimensions for spacetime image processing.

We have tested a 9-element generalized morphological filter (GMF9) and a 12-element GMF (GM12). The number of elements corresponds to the number of structuring elements

used in each filter. Each set of SE's is designed to represent all possible motions of a specific configuration of pixels through space in a 3×3 neighborhood over three sequential images. The SE configurations are shown in figure 3 (b) and (c). Our implementation of the N-element GMF is as follows:

1. Open the input spacetime image, I, with each of the N SE's to create the N open images $\{O_j\}_{j=1}^N$ (OL stage).

2. Create an output image by taking the pixelwise maximum over all N opened images. I. e., $OL(x, y, t) = \max_j O_j(x, y, t)$. This in effect finds the best fitting SE at each pixel in I.

3. Close OL with each of the N SE's to create the N closed images $\{C_j\}_{j=1}^N$ (CL stage)

4. Create an output image by taking the pixelwise minimum over all N closed images. I. e., $CLOL(x, y, t) = \min_j C_j(x, y, t)$. This in effect finds the best fitting SE at each pixel in OL.

5. Save $CLOL$.

6. Repeat the first 5 steps only perform the CL stage on the original image followed by the OL stage on the CL output. This results in an image $OLCL$.

7. Form the output by taking the pixelwise average of $OLCL$ and $CLOL$.

GMF12 works quite well at finding visible structure while removing noise. In terms of SNR it performs second only to MED333. Upon visually comparing the outputs of the various filters, many people think the the 12 element GMF has the highest fidelity result. GMF9 improves the SNR only in very low noise situations.

5   Results on Synthetic Data

We performed a series of tests on synthetic data to determine the effects of the 11 operators listed in section 1. We tested the effect on noise alone and on synthetic plume image sequences, both noisy and noise-free. The noise-only sequences consisted of noise combined with a constant image. A comparative analysis of the input and output histograms indicates how well a given operator removes noise. With the synthetic plume sequences we were able to compare the SNR of the output to that of the input. We computed the SNR as follows:

$$\mathrm{SNR}(I, J) = 10 \log \frac{\langle I, I \rangle}{\langle (\alpha I - J), (\alpha I - J) \rangle}, \qquad (7)$$

where I is the noise-free image, J is the corresponding noisy or noise-cleaned image, $\langle \cdot, \cdot \rangle$ is the l^2 inner-product and α is a normalization factor given by

$$\alpha = \frac{\langle I, J \rangle}{\langle I, I \rangle}, \qquad (8)$$

which scales I to maximize the SNR. For each operator we plotted the SNR as a function of noise level. We also judged the (subjective) visual quality of the output.

5.1 Noise-only Sequences

We tested each operator on 22 image sequences each consisting of 30 frames of noise combined with a constant image. The images were 112 rows by 90, 8-bit pixels, grayscale. Eleven of the sequences had images of gaussian noise with mean 127 and variances 1, 2, 4, 8, 16, 32, 64, 128, 256, 512, and 1024. The other 11 were of LAL noise generated with equation 1 with $I \equiv 0$ and with the same variances as above. After applying the operators we had a total of 264 sequences. We computed the histograms of the 15 central frames in each sequence. (We used the 15 central frames out of 30 so as to avoid boundary effects in the results of the long-time duration operators.) We averaged the fifteen histograms to produce one per sequence.

Figure 4 shows the result of the various operators applied to the gaussian sequence with variance 1024. The widest, shallowest distribution in each of the four plots is the logarithm of the average probability distribution from the sequence. When applied to one of the gaussian sequences, a perfect operator would produce a sequence of constant images $J_k(i,j) = 127$. The probability distribution of one of the images would consist of a single spike at 127. As expected (by the law of large numbers), the averaging filters perform best on these sequences. Note in the figure that the probability that any given pixel has the correct value increases as a function of the number of pixels included in the average. The median filters perform nearly as well.

Table 5.1 demonstrates this as well. The "mean" column lists the average estimate of the the true pixel value made each of the operators. The median is the fiftieth percentile estimate. The third column lists the square root of the mean squared distance from the true value. The quality of the estimate varies inversely with this number.

Figure 5 shows the results of operating on the LAL noise sequence with $\sigma^2 = 1024$. The logarithm of the average probability distribution from that sequence is plotted on each of the four graphs in the figure. It consists of a spike of value $\log 0.5$ at zero and a wide, shallow distribution across the graylevels that peaks at about 180. The median filters perfom best on the LAL noise. Table 5.1 shows that 50% of the estimates are less than 1. Since 50% of the distribution is concentrated at zero, the mean of distribution indicates the "average" incorrect estimate. Thus, the median filters have the smallest average incorrect estimates. This same characteristic is reflected in the square root of the second moment (column 6).

A perfect operator applied to sequences with the other distribution would generate images constant at zero.

Table

5.2 Plume Sequences

To evaluate the 11 operators quantitatively with plume imagery, we tested them on image sequences containing the synthetic plume in figure 1. We generated five different types of

Table 1: Statistics of the output distributions.

Operator	Gaussian Noise			LAL Noise		
	mean	median	$\sqrt{E\{(x-127)^2\}}$	mean	median	$\sqrt{E\{x^2\}}$
AVG113	127.1766	128.0000	18.3739	58.6031	54.0000	69.8369
AVG1115	127.0230	128.0000	8.2494	58.4282	59.0000	60.8516
AVG333	126.3864	127.0000	5.9220	57.7970	58.0000	59.0274
AVG3315	126.3594	127.0000	3.5585	57.7561	58.0000	58.1800
GMF09	126.7023	128.0000	22.5409	53.0690	1.0000	79.5064
GMF12	125.8625	127.0000	8.9329	45.2757	51.0000	51.6739
LUM	122.1256	122.0000	13.2697	38.3798	1.0000	59.5937
MED1115	127.5756	128.0000	10.1639	36.4134	2.0000	56.5283
MED333	126.6795	128.0000	9.1579	30.0917	1.0000	48.1599
MED3315	127.1153	128.0000	5.0470	22.4665	1.0000	36.5406
MMF	122.0458	122.0000	18.9418	48.3077	1.0000	73.7270
Original	127.5219	128.0000	31.8327	58.8706	1.0000	88.3579

sequences all of which contained dense noise from model 1 and which exhibited various degrees of jitter. The statistics of the noise field were approximately constant throughout any one sequence, but the actual values of the noise field changed from frame to frame.

Type 1 Noise: synthetic photomultiplier pulses, star streaks, and dense noise.

      Jitter: one-pixel random walk (4-connected) from frame to frame.

      Plume Dynamics: stationary

Type 2 Noise: dense.

      Jitter: none.

      Plume Dynamics: stationary

Type 3 Noise: dense.

      Jitter: low – one pixel random walk (4-connected).

      Plume Dynamics: stationary

Type 4 Noise: dense

      Jitter: high – large variance random walk.

      Plume Dynamics: stationary

Type 5 Noise: dense.

      Jitter: low – one pixel random walk (4-connected).

Plume Dynamics: shape changes between frames

We computed the SNR of the 15 central frames in each of the 528 noisy and noise-cleaned sequences of types 2 – 4. We used the average of these 15 SNR's as the SNR estimate for the sequence.

We generated one sequence of type 1. It was created to mimic a real sequence convincingly for visual evaluation. We generated 12 each of types 2 – 4 with noise variances 0, 1, 2, 4, 8, 16, 32, 64, 128, 256, 512, and 1024. These were generated to find the operators that maximize the SNR under a variety of conditions. We applied each of the 11 operators to each of the 49 sequences. Thus, we had a total of 588 sequences of thirty frames each. Four of these were noise-free; 45 were noisy; and 539 were noise cleaned.

5.2.1 Subjective Visual Analysis

We visually evaluated sequence one and its 11 processed versions. We decided that teh results of MED3315 and GMF12 looked best. MED3315 completely removed pulse and star-streak noise. It created the blackest background. However, MED3315 stablized the plume image image at expense of the true shape. GMF12 completely removed the pulses. It greatly diminished the star streaks although they were visible when they intersected the plume. It made the background very black. GMF12 tracked the jitter and preserved the plume shape better than MED3315 but the plume image was not as strong. Figure 6 shows a single frame from the original sequence and the 11 operators. A subjective visual ranking of the results from best to worst is: (1) GMF12, (2) MED3315, (3) MED1115, (4) MED333, (5) AVG3315, (6) AVG1115, (7) LUM, (8) AVG333, (9) AVG113 (10) MMF, (11) GMF9, (12) original.

5.2.2 Quantitative Analysis: Noise-free Sequences

All of the operators degrade a noise-free sequence to a certain extent. Table 5.2.2 ranks the operators in terms of SNR for each of the sequence types 2 – 4.

In the stationary case, each image in the sequence is identical. and therefore represents the ideal. Only Avg3315 and Avg333 are noticeably visually degraded due to spatial blurring. (Avg333 is worse than Avg3315 because Avg333 averages a 9-pixel neighborhood per frame whereas Avg3315 averages a 5-pixel neighborhood.)

In the low-jitter case, the long-duration averages and medians, stabilize the image, which accounts for the diminished SNR. The other 7 operators track the motion with visible degradation effectively following the same ordering as the SNR.

The only filter that effectively tracks the high-jitter, noise-free signal is the MMF. It does this with a surprising high degree of visual fidelity even though the SNR is only 17.8dB. The LUM filter appears better than either of the GMF's although they have larger SNR's. The short-duration averages produce multiple images (ghosting) and the long-duration averages are very weak. The median filters outperform the averages visually as well as in SNR.

On the noise-free dynamic plume sequence, the short-duration filters tracked the changes whereas the long-duration filters enhanced the trends. Visually, we rank the results: MMF,

Table 2: Ranking by SNR of operators on signal with no noise.

Rank	Stationary	SNR	Low Jitter	SNR	High Jitter	SNR	Dynamic	SNR
1	GMF9	INF	GMF9	2067.2	MMF	17.8	GMF9	1252.5
2	MMF	INF	MMF	27.0	GMF9	9.0	MMF	26.6
3	Med1115	INF	LUM	23.4	GMF12	8.6	LUM	22.7
4	Avg113	INF	GMF12	18.9	LUM	8.1	GMF12	17.0
5	Avg1115	INF	Avg113	17.7	Med333	7.8	Avg113	16.0
6	GMF12	41.7	Med333	16.4	Med3315	7.5	Med333	15.8
7	LUM	37.6	Avg333	15.3	Med1115	7.4	Avg333	14.4
8	Med3315	36.1	Avg1115	12.5	Avg333	7.1	Med1115	12.3
9	Avg3315	20.0	Avg3315	12.4	Avg3315	7.0	Med3315	11.7
10	Med333	18.4	Med1115	12.3	Avg113	6.8	Avg3315	10.9
11	Avg333	17.1	Med3315	11.8	Avg1115	6.7	Avg1115	10.8

LUM, and Med333, followed by the GMF's and short-duration averages as having essentially equal fidelity (they differ in appearance).

While GMF9 and MMF are best at preserving a noise-free sequence, we will show that they are not good in terms of SNR at noise removal.

5.2.3 Quantitative Analysis: Noisy Sequences

Figure 7 shows the relative performance of 4 of the 11 operators when applied to noisy sequences. The operators are Med3315 (solid line), Med333 (dotted line), GMF12 (dashed line), and Avg3315 (dash-dot line). Each graph shows the average SNR of the outputs of each of the operators as a function of noise level for one of the sequence types. Each graph also contains a curve showing the average SNR of the unprocessed sequences (solid line with circles). We plotted only 4 of the operators to avoid clutter on the graph. We chose the 3 overall best performers together with the best performing averaging filter and the original for comparison.

The type 2 sequences have no jitter or variations in the plume; only the noise sample changes from frame to frame. Table 5.2.3 ranks the operators by SNR for $\sigma^2 = 1, 32,$ and 1024. Operators Med3315 and Med333 perform best overall. This is to be expected since the noise distribution is highly non-gaussian. The significantly better performance of Med3315 over Med333 is due to the larger neighborhood size (Med3315 covers 75 pixels whereas Med333 covers 27). Since, the plume is diffuse which means that most pixels are close in value to their neighbors. Note that in the worst case, Med3315 increases the SNR of the data by 7.69dB for noise level 11. The best performing averaging filter increases the SNR by 4.16dB. The MMF and LUM filters are not effective at removing high amplitude noise. While some observers agree that the result of GMF12 looks best, it is only slightly

Table 3: Ranking by SNR of operators on stationary image sequences.

Rank	Noise Level 1		Noise Level 6		Noise Level 11	
1	Med3315	20.64	Med3315	7.56	Med3315	-2.92
2	Med1115	14.50	Med333	3.90	Med333	-5.33
3	Med333	14.49	GMF12	2.49	GMF12	-5.54
4	GMF12	14.32	Med1115	2.03	Avg3315	-6.45
5	LUM	13.47	LUM	1.34	Avg333	-6.61
6	Avg3315	11.95	Avg3315	0.79	Med1115	-6.70
7	Avg1115	11.20	Avg333	0.53	Avg1115	-6.88
8	Avg333	11.06	Avg1115	0.17	LUM	-7.16
9	MMF	9.57	Avg113	-1.59	Avg113	-8.30
10	Avg113	8.92	MMF	-1.67	MMF	-9.03
11	GMF9	8.35	GMF9	-2.58	GMF9	-9.65
12	Original	5.86	Original	-4.23	Original	-10.61

better than averaging at increasing the SNR.

The type 3 sequences are low jitter. The results for $\sigma^2 = 1, 32, 1024$ are tabulated in table 5.2.3. The jitter in this case is a 1-pixel random walk on a 4-connected topology from frame to frame. Since most of the operators are defined on 3-by-3 neighborhoods, the results here should be similar to those for the stationary case. They are similar for sufficiently high level noise. For low noise levels Med333 outperforms Med3315.

The type 4 sequences are high jitter; the plume position varies greatly from frame to frame. Table 5.2.3 ranks the operators by SNR for $\sigma^2 = 1, 32$, and 1024. The SNR's of the results here are significantly lower than those from the no jitter or low jitter cases. This makes sense because there is little temporal redundancy. Although it is best at high noise levels, Med3315 does not perform significantly better than than Med333 or GMF12 at low noise levels.

The type 5 sequences feature a dynamic plume; its horizontal and vertical sizes vary greatly from frame to frame. Table 5.2.3 ranks the operators by SNR for $\sigma^2 = 1, 32$, and 1024. We expected the results of these experiments to closely match the high jitter case. Instead, they were close to the low jitter results. We atribute this to the behavior of the plume core in the sequences. In the high jitter sequences, the plume core changed position significantly from frame to frame. In the dynamic plume sequences the size of the core changed considerably but its position did not. In that respect the sequences more closely resembled those with low jitter.

Table 4: Ranking by SNR of operators on low-jitter sequences.

Rank	Noise Level 1		Noise Level 6		Noise Level 11	
1	Med333	13.49	Med3315	5.99	Med3315	-3.16
2	LUM	12.93	Med333	3.76	Med333	-5.38
3	GMF12	12.49	GMF12	2.35	GMF12	-5.55
4	Med3315	11.32	Med1115	1.53	Avg3315	-6.48
5	Avg333	10.64	LUM	1.26	Avg333	-6.61
6	Med1115	9.93	Avg3315	0.58	Med1115	-6.80
7	Avg3315	9.53	Avg333	0.53	Avg1115	-6.93
8	MMF	9.53	Avg1115	-0.05	LUM	-7.15
9	Avg1115	8.77	Avg113	-1.60	Avg113	-8.29
10	GMF9	8.46	MMF	-1.66	MMF	-9.01
11	Avg113	8.44	GMF9	-2.57	GMF9	-9.65
12	Original	5.96	Original	-4.18	Original	-10.57

Table 5: Ranking by SNR of operators on high-jitter sequences.

Rank	Noise Level 1		Noise Level 6		Noise Level 11	
0	MMF	8.23	Med3315	2.98	Med3315	-4.29
1	GMF12	7.32	Med333	1.58	Med333	-6.17
2	LUM	7.31	GMF12	0.87	GMF12	-6.34
3	Med3315	7.10	LUM	0.05	Avg3315	-7.25
4	Med333	6.95	Med1115	-0.09	Avg333	-7.32
5	Med1115	6.27	Avg333	-0.84	Med1115	-7.50
6	GMF9	5.74	Avg3315	-0.95	Avg1115	-7.67
7	Original	5.56	Avg1115	-1.49	LUM	-7.75
8	Avg333	5.52	MMF	-2.28	Avg113	-8.93
9	Avg3315	5.09	Avg113	-2.68	MMF	-9.51
10	Avg1115	4.60	GMF9	-3.23	GMF9	-10.14
11	Avg113	4.34	Original	-4.65	Original	-11.04

Table 6: Ranking by SNR of operators on dynamic plume sequences.

Rank	Noise Level 1		Noise Level 6		Noise Level 11	
0	Med333	12.94	Med3315	5.69	Med3315	-2.39
1	LUM	12.80	Med333	4.19	Med333	-4.53
2	GMF12	11.96	GMF12	2.94	GMF12	-4.54
3	Avg333	10.56	LUM	1.90	Avg3315	-5.48
4	Med3315	10.47	Med1115	1.85	Avg333	-5.58
5	MMF	10.10	Avg333	1.41	Avg1115	-5.95
6	Med1115	9.29	Avg3315	1.29	Med1115	-5.97
7	GMF9	8.83	Avg1115	0.66	LUM	-6.29
8	Avg3315	8.59	Avg113	-0.79	Avg113	-7.36
9	Avg113	8.58	MMF	-0.91	MMF	-8.13
10	Avg1115	8.01	GMF9	-1.83	GMF9	-8.75
11	Original	6.76	Original	-3.38	Original	-9.70

6 Results on Real Data

To test the 3D morphological filters on real data, we chose data from the UVPI set. This data set has proven itself to be difficult to enhance. It is impossible to test for radiometric accuracy of the filters on this dataset because the only record of the firing is the noisy one. Thus, we processed these sequences to maximize the visibility of plume structures.

Figure 8 is a single frame from a sequence taken by the UVPI tracker camera, together with the result of five enhancement procedures. The image sequence was captured by the UVPI tracker camera starting at the onset of the stage two burn in the rocket test.

Image (a) shows the original tracker camera image. Note that only the very center plume core is visible. This is because it is very much brighter than the rest of the plume. Throughout this entire sequence only this small point of light is visible if the data is quantized via linear mapping from min to max.

Image (b) shows the result of remapping the original image so that most of the data is moved into a visible range (See section 3). Now, plume structure is visible, but so is all of the low-level noise.

Images (c), (d), and (f) are the outputs of AVG1115, GMF12, and MED3315 respectively applied to the remapped sequence (b). All three of these remove much of the high frequency textured noise. In watching the sequence at video frame rate, it is apparent that the GMF12 best tracks the dynamic plume while MED3315 does the most smoothing. All three leave a graylevel bias and some background noise in the image sequence.

Using a morphological tophat transform [5] with a large structuring element (33 pixels in diameter) we removed the background bias without altering the plume structure. The result of this applied to the GMF12 sequence (d) is shown in (e). Visually, the difference

between (a) and (e) is significant.

Figure 9 shows the 195 to 295 angstrom UV Band from the stage 2 plume from the UVPI dataset. Image (a) is a frame from the original sequence. Mostly visible are random shot-noise events due to the camera photomultipliers. When viewed at frame rate, the linearly mapped sequence appears to contain nothing but this "popcorn noise".

Image (b) shows a remapping (per section 3) of the original image which puts most of the data in the visible range. Some plume structure is evident here. But, the imagery is dominated by background noise and photomultipier noise.

We applied a MED3315 filter to the remapped sequence to create (c). Much more plume core structure is visible, and most of the photo multiplier noise is gone. There is a significant background bias as well as some noise remaining in the background.

To remove this we used two different techniques. In the first, we segmented the processed sequence (c) into plume and background regions. Then we reprocessed sequence (b) after masking out the dynamic background. We segmented each frame of (c) individually by thresholding at the frame's mean gray level. This resulted in a noisy binary sequence which we opened using a $5 \times 5 \times 3$ cylinder to create a smoothly varying spacetime mask. This mask was used to extract a dynamic region of interest from sequence (b). The corresponding frame from this region of interest sequence is shown, remapped but otherwise unprocessed, in image (d).

Image (e) is a frame from the result of applying GMF12 to sequence (d). This smooths out much of the photomultiplier noise and leaves a more coherent plume core.

Sequence (f) was created from (c) by using a (large structuring element) morphological tophat transform to black out large, slowly varying section of the sequence. Notice that this preserves the plume core. More interstingly, it enhances a very faint bow structure in the plume that is utterly invisible in the original and remapped frames.

These examples demonstrate that a very high degree of enhancement is possible using careful remapping followed by processing with 3D operators. Although this enhancement alters the radiometric information from the unprocessed datasets, it shows where the plume structures are in data. This location information can be used to isolate and extract the pertinent radiometric information from the unprocessed data, something that could not have been done without the enhancement demonstrated above.

7   Conclusion

Based on the results of our SNR tests on synthetic data, we recommend the following: For a very noisy sequence, use a long-duration median filter with moderate spatial support. For a relatively clean sequence, use a long-duration median filter if the plume is stationary or a $3 \times 3 \times 3$ median if the plume is slightly jittery or dynamic. It is our opinion that the GMF12 filter best improves the appearance of a dynamic sequence. However, its computational complexity is much greater than that of the $3 \times 3 \times 3$ median filter. Moreover, the $3 \times 3 \times 3$ median has a higher SNR than the GMF12 in most situations. If the plume is highly jittery, register the images then apply the appropriate filter.

References

[1] Arce, G. R., "Multistage order statistic filters for image sequence processing," *IEEE Trans. Acoust., Speech, Signal Process.*, vol. ASSP-39, No. 5, pp. 1146-1163, 1991.

[2] Bovik, A. C., "A generalization of median filtering using linear combinations of order statistics," *IEEE Trans. Acoust., Speech, Signal Process.*, vol. ASSP-31, No. 6, pp. 1342-1350, 1983.

[3] Bovik, A. C., "Streaking in median filtered images," *IEEE Trans. Acoust., Speech, Signal Process.*, vol. ASSP-35, No. 4, pp. 493-503, 1987.

[4] Gallagher, N. C., and G. L. Wise, "A theoretical Analysis of the properties of median filters," *IEEE Trans. Acoust., Speech Signal Process.*, vol. ASSP-29, No. 6, pp 1136-1141, 1981.

[5] Giardina, C. R. and E. R. Dougherty, *Morphological Methods in Image and Signal Processing*, Prentice-Hall, Englewood Cliffs, New Jersey, 1988.

[6] Gonzalez, R. C., and R. E. Woods, *Digital Image Processing*, Addison-Wesley, Reading, Massachusetts, 1992.

[7] Haralick, R. M., S. R. Sternberg, and X. Zhuang, "Image analysis using mathematical morphology" *IEEE Trans. Pattern Anal. Machine Intell.*, vol. PAMI-9, No. 4, pp. 532-550, 1987.

[8] Maragos, P. and R. W. Schafer, "Morphological filters – part I: their set theoretic analysis and relations to linear shift invariant filters," *IEEE Trans. Acoust., Speech, Signal Process.*, vol. ASSP-35, No. 8, pp. 1153-1169, 1987.

[9] Maragos, P. and R. W. Schafer, "Morphological filters - part II: their relations to median, order-statistic, and stack filters," *IEEE Trans. Acoust., Speech, Signal Process.*, vol. ASSP-35, No. 8, pp. 1153-1169, 1987.

[10] Maragos, P. and R. W. Schafer, "Morphological Systems for multidimensional signal processing," *Proc. IEEE*, vol. 78, No. 4, pp. 690-710, 1990.

[11] Matheron, G., *Random Sets and Integral Geometry*, Wiley, New York, 1975.

[12] Schumacher, D., "Useful 1-to-1 pixel transforms," in *Graphics Gems*, Glassner, A. S., ed., Academic Press, San Diego, CA, 1990.

[13] Serra, J., *Image Analysis and Mathematical Morphology*, Academic Press, London, 1982.

[14] Serra, J., "Introduction to mathematical morphology," *Comp. Vision, Graph., Image Process.*, vol. 35, pp. 283-305, 1986.

[15] Serra, J., ed., *Image Analysis and Mathematical Morphology, Vol. 2: Theoretical Advances*, Academic Press, New York, 1988.

[16] Song, J., and E. J., Delp, "A Study of the Generalized Morphological Filter," submitted to *Circuits, Systems, and Signal Processing*, 1992.

[17] Sternberg, S. R., "Grayscale morphology," , vol. 35, *Comp. Vision, Graph., Image Process.*, pp. 333-355, 1986.

[18] Tukey, J. W., *Exploratory Data Analysis*, Addison-Wesley, Reading, MA 1971,

Figure 1: A synthetic rocket plume image.
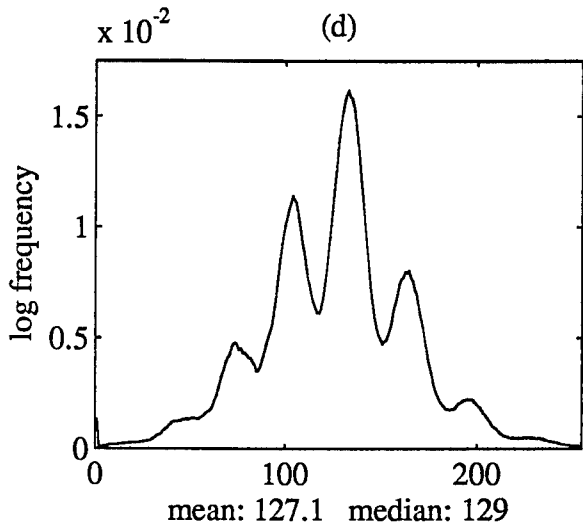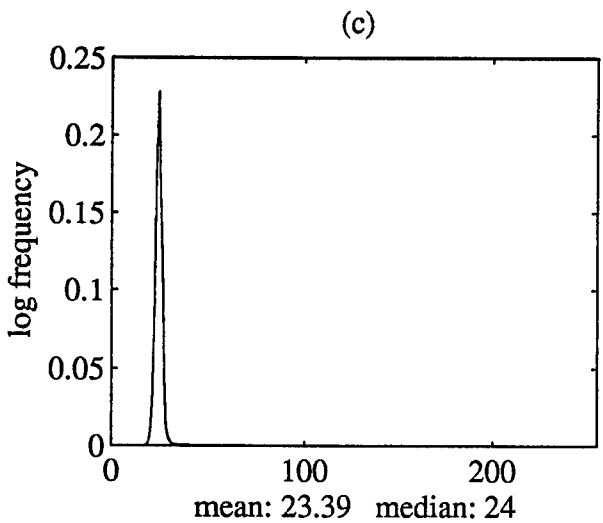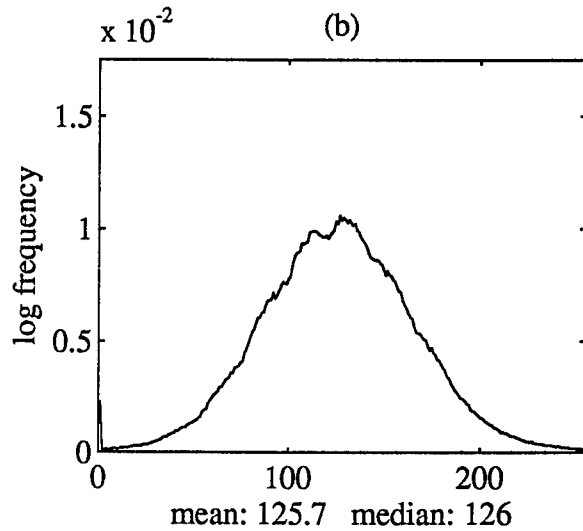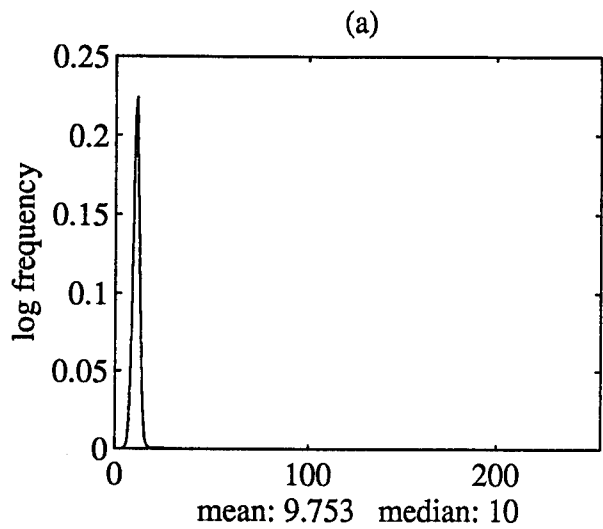
Figure 2: Accumlated graylevel probability distributions from (**a**) original UVPI tracker stage 2 sequence; (**b**) remapped version of (a) within mean ± 2 std. devs.; (**c**) original UVPI 191-291 UV bandstage 1 sequence; (**d**) remapped version of (c) within mean ± 3 std. devs.
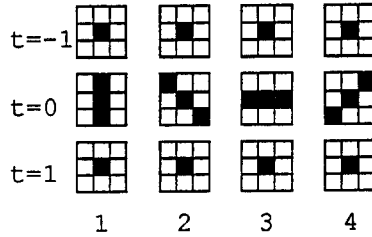
(a)   MMF filter neighborhoods
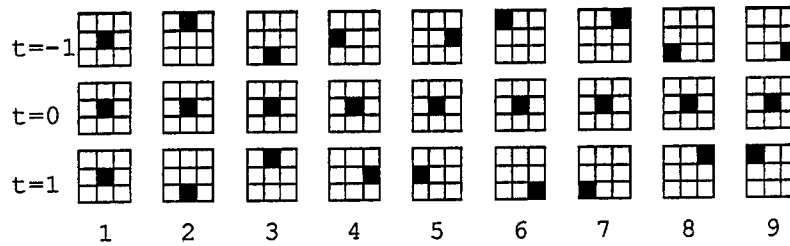
(b) GMF9 Structuring elements
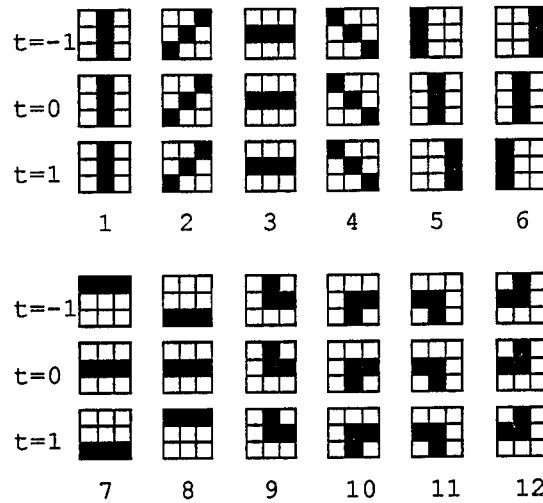
(c) GMF12 Structuring Elements

Figure 3: **(a)** Structuring element configurations for the multistage morphological filter (MMF). **(b)** Structuring element configurations for the 9-element generalized morphological filter (GMF9). **(c)** Structuring element configurations for the 12-element generalized morphological filter (GMF12).
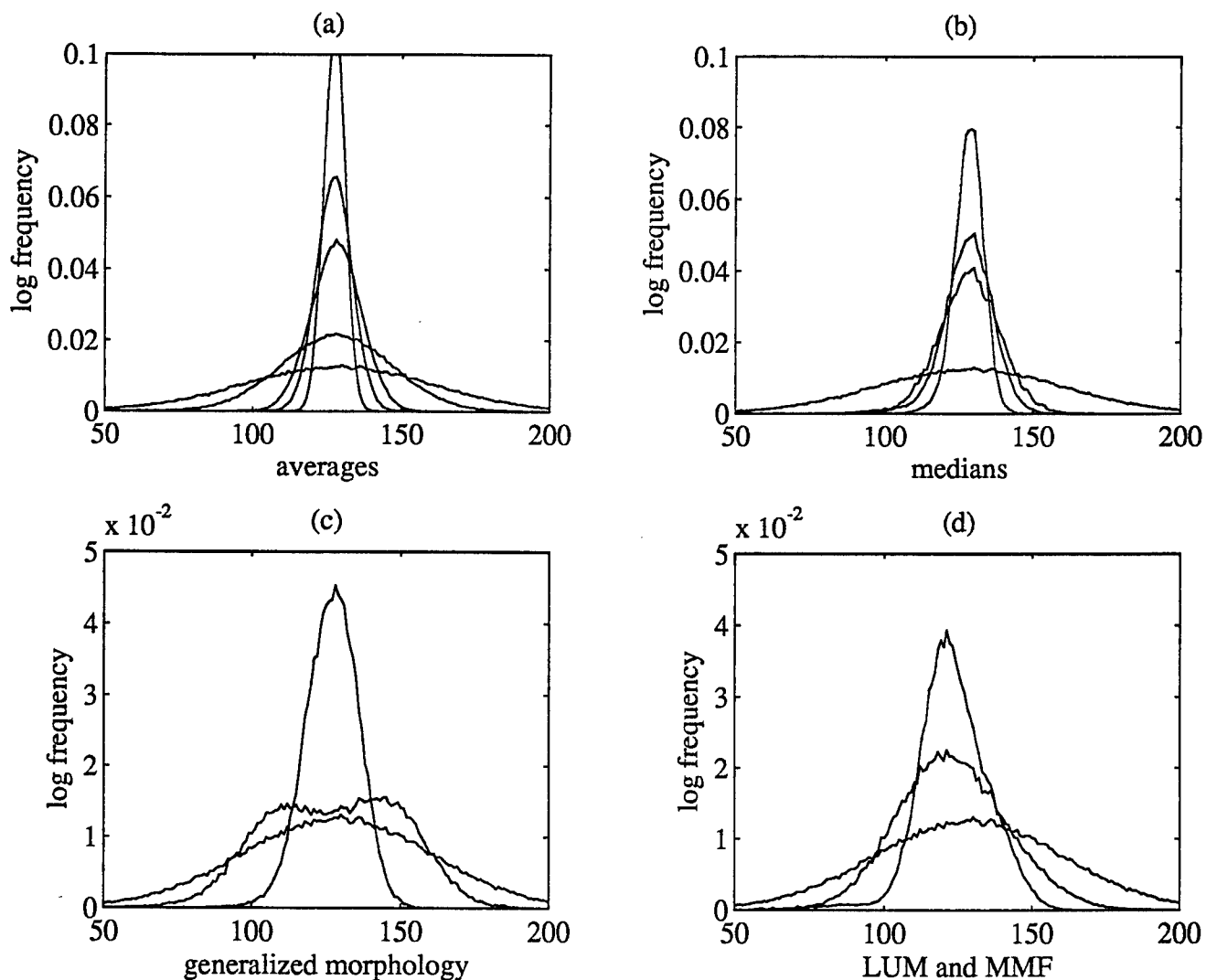
Figure 4: Average graylevel distributions of the sequences output by the 11 operators when applied to a sequence with a gaussian distribution. For each plot the operators are listed narrowest to widest. The original distribution is the widest in each plot. (a) Averaging operators: AVG3315, AVG333, AVG1115, AVG113, Original distribution. (b) Median operators: Med3315, MED333, MED1115, Original. (c) GM operators: GMF12, GMF9, Original. (d) Arce Operators: LUM, MMF, Original
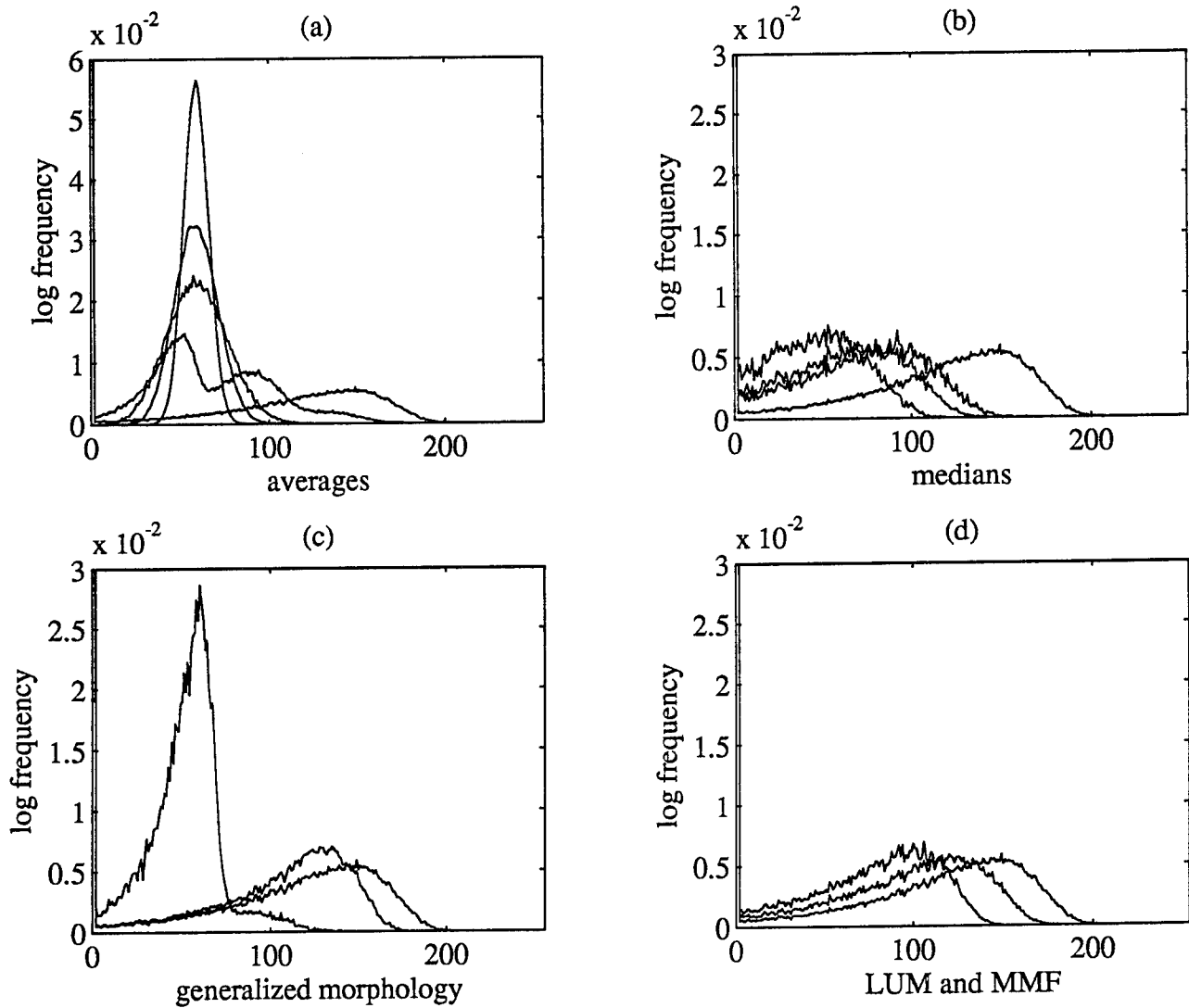
Figure 5: Average graylevel distributions of the sequences output by the 11 operators when applied to a sequence with an LAL distribution. For each plot the operators are listed narrowest to widest. The original distribution is the widest in each plot. (a) Averaging operators: AVG3315, AVG333, AVG1115, AVG113, Original distribution. (b) Median operators: Med3315, MED333, MED1115, Original. (c) GM operators: GMF12, GMF9, Original. (d) Arce Operators: LUM, MMF, Original.
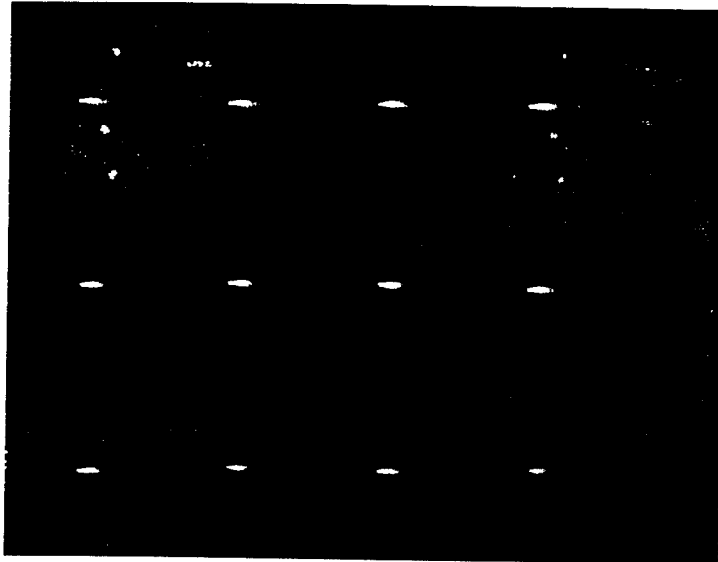
6

Figure 6: A frame frome a synthetic rocket plume image sequence with the corresponding outputs of 11 operators. Top row (l–r): Original, GMF9, GMF12, MMF; Middle row: MED333, MED1115, MED3315; Bottom row: AVG113, AVG333, AVG1115, AVG3315.
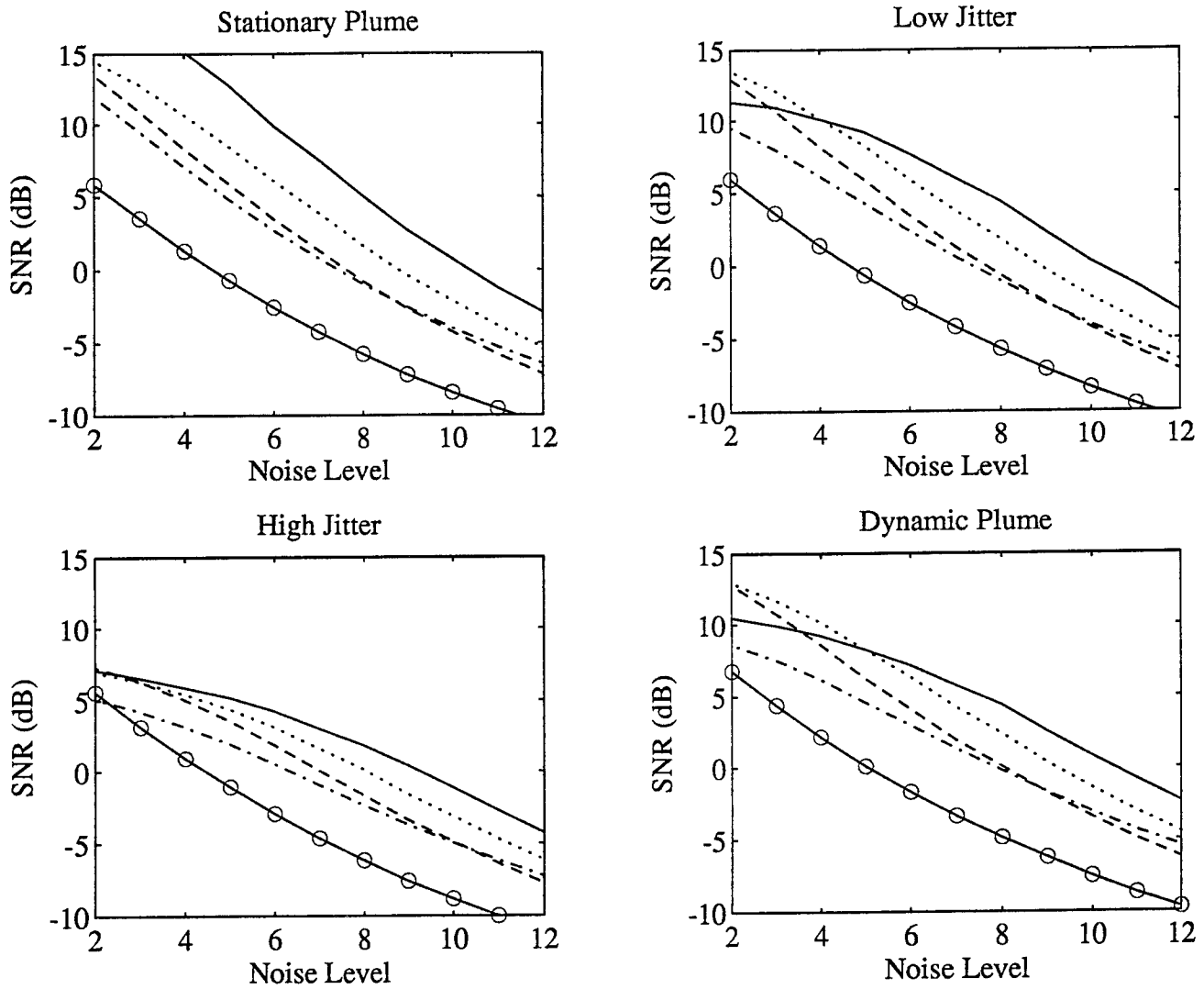
Figure 7: A comparison of the relative performance of 4 of the 11 operators when applied to synthetic noisy sequences. The operators are Med3315 (solid line), Med333 (dotted line), GMF12 (dashed line), Avg3315 (dash-dot line), Original (circle line.
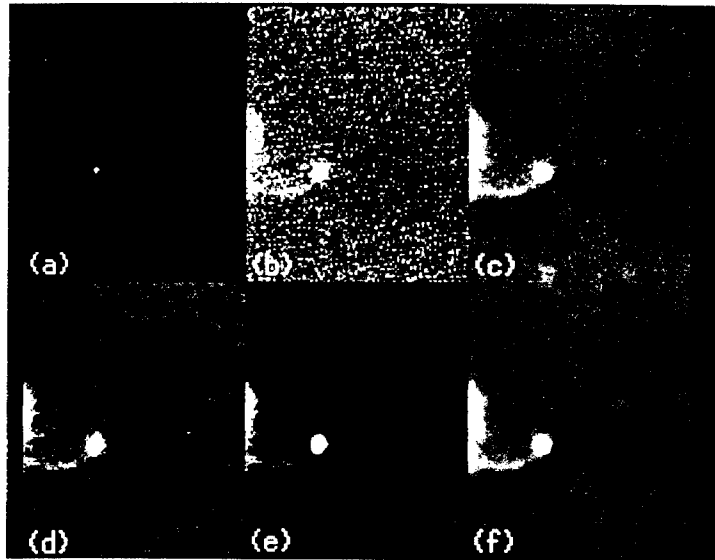
8

Figure 8: A single frame from a sequence taken by the UVPI tracker camera, together with the result of five enhancement procedures. (a) original UVPI tracker stage 2 sequence; (b) remapped version of (a); (c) AVG1115 of (b); (d) MED3315 of (b); (e) GMF12 of (b); (f) Background compensated GMF12 (e).
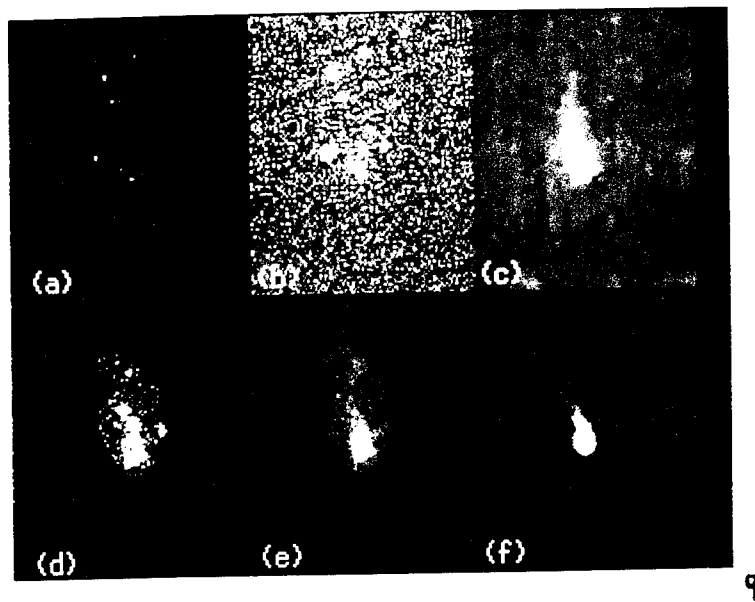
Figure 9: A single frame from a sequence taken by the UVPI 195 to 295 angstrom UV Band camera, together with the result of five enhancement procedures. (a) original UVPI 195 – 295 Åstage 2 sequence; (b) remapped version of (a); (c) MED3315 of (b); (d) Masked version of (b); (e) GMF12 of (d); (f) Background compensated MED3315 (c).

FRANK J. SEILER RESEARCH LABORATORY

Synthesis, Analysis and Reactions

of

Positively Charged Intermediates

Christopher M. Adams
Assistant Professor
Department of Chemistry

Oklahoma State University
Stillwater, Oklahoma 74078-0447

December 1992

Synthesis, Analysis and Reactions

of

Positively Charged Intermediates

Christopher M. Adams
Assistant Professor
Department of Chemistry, Oklahoma State University

Abstract

Semi-empirical PM3 calculations were performed on a number of nitrated heterocycles. which varied in stability to aqueous and non-aqueous isolation conditions. Analysis of the calculations suggest that the geometry of the nitro group with repect to the heterocyclic ring is crucial to compound stability. Structures for compounds **1-3** containing nitro groups oriented parallel to the ring system correlated with those compounds requiring an aqueous workup for isolation. Structures for compounds **5-8** containing nitro groups twisted or orthogonal to the ring system correlated to those compounds requiring a non-aqueous workup for isolation. These results suggest that p overlap with the ring nitrogen and resonance with the nitro group is required for aqueous workup. Compounds with more electrophilic nitro groups are oriented orthogonal to the π system and are susceptible to decomposition and hydrolysis.

Molecular mechanics (MM2) was employed to address intramolecular coupling and carbene addition pathways to cyclopropenyl cyclophanes. Comparisons of the calculated olefin strain energies (OS) suggest utilizing an intramolecular carbene addition of a cyclic acetylene to form the desired precursors.

Current methods available to modify or append alkyl groups to cyclobutadiene tricarbonyliron limit its use and study. Using selective alkylations and rearrangements on diisopropyl squarate, we developed simple and efficient routes to specific 1,3-disubstituted (**26**) and 1,2,3-trisubstituted (**27**) cyclobutadiene tricarbonyliron complexes. These methods represent the first direct syntheses of these complexes and provide new entries into potentially novel cyclobutadiene-derived synthons and complexes.

Synthesis, Analysis and Reactions
of
Positively Charged Intermediates

Christopher M. Adams

Introduction

The research described herein addresses two areas of interest to the Air Force and our research group. The first stems from the nitration of heterocyclic compounds using an aprotic nitronium species generated in situ and N-nitro compound stability.[1] The second explores small-ring cyclophanes and addresses through space interactions of molecular orbitals in the cyclophanes. These studies include computation modelling, analysis of intermediates as synthetic targets, and synthetic investigations.

Nitrated Heterocycles
Background

The nitration of heterocyclic compounds is of great importance to several fields of chemistry. Of primary interest to the armed services is the use of nitro compounds as propellants and energetic material binders and polymers.[2-5] Additionally, combustion cycles in aircraft, as well as land transportation systems, occur in the presence of nitrogen from our atmosphere and produce a variety of nitrogen oxides often observed as an orange smog hovering over crowded cities. A continuing area of recent interest in our laboratory is the stability, lability and reactions of reactive nitrogen oxide intermediates and compounds. The formation of nitro compounds in large quantities is of prime importance for their production; however, in the laboratory more convenient methods of nitration are required in order to form trial compounds for study. Many investigators, including ourselves, are interested in the stability of selected compounds and search for milder synthetic conditions and methodologies for compound synthesis in small quantities. Such conditions would allow modification of the trial compounds and the incorporation of more sensitive functionalities.

The introduction of nitro groups into organic molecules has been done using a variety of methods.[1,3] Often sensitive functionalities do not survive strongly acidic conditions or aqueous workup, limiting application of the reactions in specific compound syntheses. These conditions could also induce polymerization making the method not applicable to polymer precursors for energetic binders. Our earlier investigations improved the yields in the nitration of a variety of heterocycles using a reactive nitronium ion, NO_2^+, generated from tetrabutylammonium nitrate and trifluoromethanesulfonic anhydride (Tf_2ONO_2), Figure 1.[1]
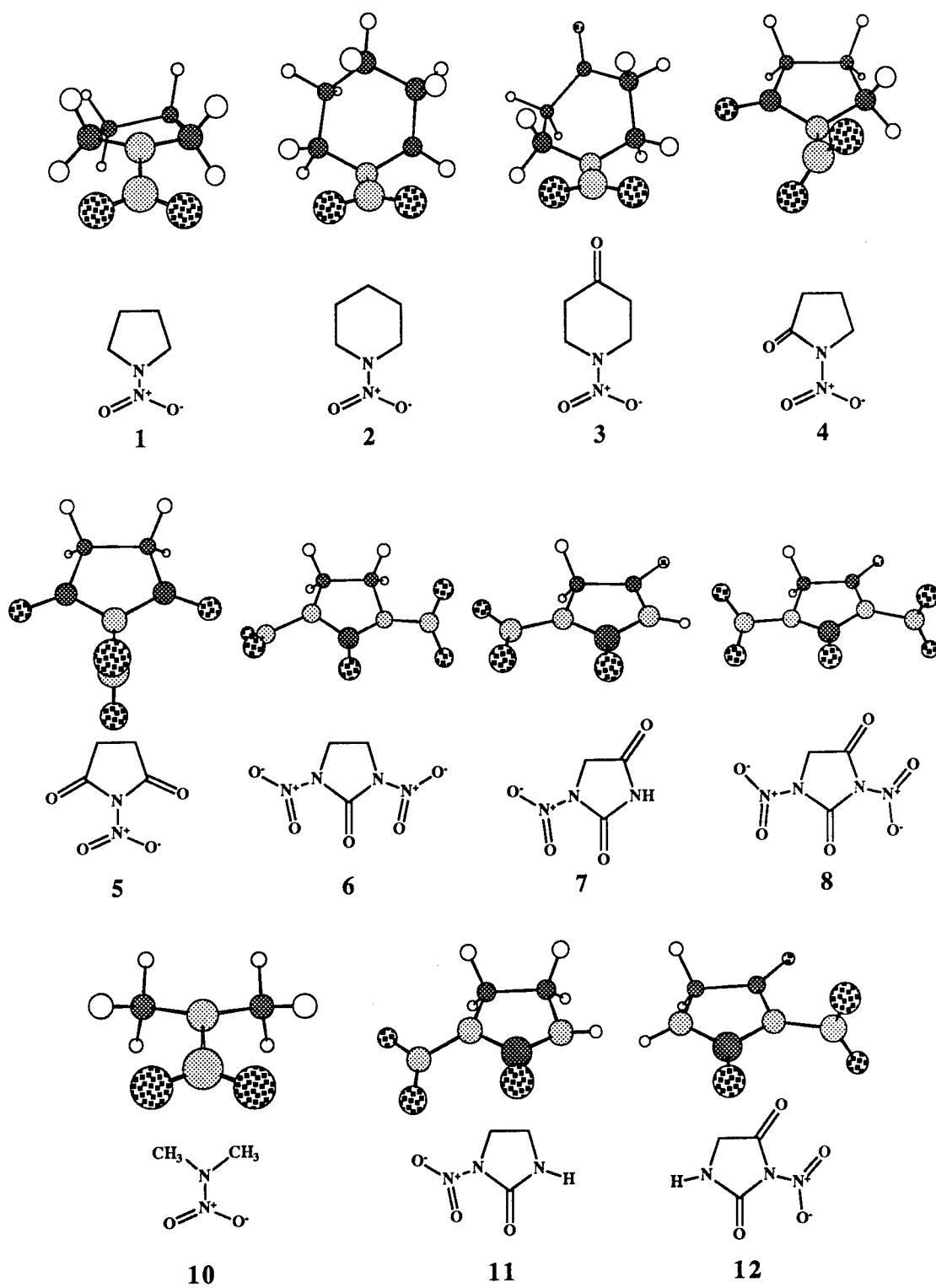
Figure 1. Geometric representations of the nitrated heterocycles in this study.

Facile nitration of the heterocycles in this modelling study were limited by sensitivity of specific compounds to aqueous workup.[1] While several of the compounds could be isolated using an aqueous workup, others were isolable only by non-aqueous methods. The nitrated heterocyclic products **1-8** are shown in Figure 1 and Table 1. On examination there are three nitro-amines (1-nitropyrrolidine (**1**), 1-nitropiperidine (**2**), 1-nitro-4-piperidinone (**3**)), one nitro-amide (1-nitropyrrolidinone (**4**)), one nitro-imide (N-nitrosuccinimide (**5**)), one nitro-imidazole (1,3-dinitro-2-oxotetrahydroimidazole (**6**)), and two nitro-oxazoles (1-nitro-hydantoin (**7**), 1,3-dinitrohydantoin (**8**)). By aqueous workup compounds **1-4** were isolated and by non-aqueous workup compounds **5-8** were isolated.[1] Compounds **1-3** were also isolable using non-aqueous conditions, however **4** was not. A reason for different isolation methods was sought using semi-empirical calculations of the corresponding structure models.

Methods

Semi-empirical calculations were performed using MOPAC6 developed by J. J. P. Stewart.[4] The PM3 hamiltonian parametrization was performed using the eigenvector minimization routine (EF) on the eight isolable compounds **1-8**, and four potential nitrated models **9-12**. The molecular mechanics correction MMOK in the minimization routine was applied to compounds **7**, **11**, and **12**, which contain a peptide linkage (-CO-NH-).

Results and Discussion

The minimized structures are shown in Figure 1. Several values were related: 1) the geometry of the nitro group with respect to the ring; 2) the nitrogen to nitro group bond distance; and 3) charge on the nitrated nitrogen in the ring. The N-O bond lengths were nearly identical in all cases due to resonance. The amine nitrogens in compounds **1-3** exhibited some pyramidal character. The nitro groups in compounds **1-3** were oriented parallel to the carbons attached to the nitrogen in the ring system. These observations are also observed in acyclic nitro-amine **10**. The $N-NO_2$ bond distances ranged from 1.465 to 1.491 Å.

Compounds **3-9** contain one or two carbonyls in the ring system. Compound **3** has the carbonyl isolated from the ring nitrogen and compounds **4-8** have carbonyls adjacent to the ring nitrogen, i. e. amide linkages. The nitro groups in compounds **4-8** are twisted, or nearly orthogonal, to the amide system. Nitro groups on nitrogens flanked by one carbonyl are twisted from planarity (0°-72°), and nitro groups on nitrogens flanked by two carbonyls are nearly orthogonal to the amide in the ring system. The $N-NO_2$ bond distances range from 1.494 to 1.618 Å.

The calculated structures for nitro-amines **1-4** correlate with their stability to aqueous workup. The nitro groups when oriented parallel to the ring carbons allow π overlap of the p

Table 1. Results of PM3 Calculations for Nitrated Heterocycles.

	Heterocycle	Bond N-NO$_2$ Å	Bond N-O Å	NO$_2$ Geometry	Atom Charge: NO$_2$	Atom Charge: N
1		1.465	1.21	parallel	1.246	-0.341
2		1.491	1.21	parallel boat form	1.231	-0.324
3		1.489	1.21	parallel	1.242	-0.346
4		1.528	1.20	twisted 70°	1.285	-0.407
5		1.582	1.19	orthogonal	1.342	-0.478
6		1.565	1.19	a)symmetrical twisted 72°	1.291 1.292	-0.390 -0.390
7		1.494	1.20	parallel flat	1.315	-0.425
8		a: 1.618 b: 1.541	1.19 1.20	a) orthogonal b) twisted 40°	1.355 1.302	-0.477 -0.404
	Model Compounds					
9	CH$_3$-NO$_2$	1.513	1.21	---	1.239	---
10	(CH$_3$)$_2$N-NO$_2$	1.496	1.21	parallel	1.231	-0.321
11		1.492	1.20	parallel	1.290	-0.389
12		1.589	1.19	orthogonal	1.349	-0.469
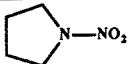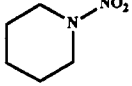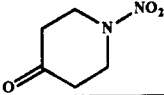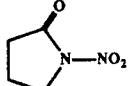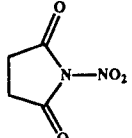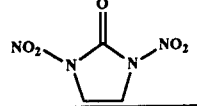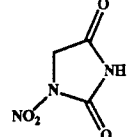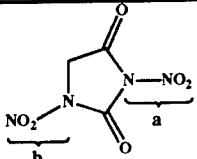
orbitals in the nitro group with the non-bonding electrons in the amine. This resonance stabilization is similiar to a peptide linkage, and the planar orientation of the nitro group gives a favorable stabilization, see structure **4**.

Compounds **5-8** contain an enforced planar orientation of the ring carbonyls with the ring nitrogen, see structure **13**. This enforcement allows delocalization of the electrons to dominate the system. It should be noted here, however, that the MMOK correction induces a barrier of nearly 14 kcal/mol,[4] forcing compounds **7** and **12** to be planar when constrained in the ring. Nitro groups attached to the amide nitrogens can adopt orientations at two extremes: in the plane of the cyclic amides, and orthogonal to the amides. When attached to an amide nitrogen flanked by two carbonyls, e. g. **5** and **8**, the nitro group is nearly orthogonal to the π system. This orientation removes the p orbital overlap and results in a lengthening of the N-NO_2 bond, cf Table 1. Of compounds **5**, **8**, and **12**, only **5** is stable over a period of time. In experimental attempts to synthesize **8**, we found **8** to be an orange compound, which on standing produced an orange-brown gas. Characterization of the resulting pale yellow solid gave only **7**. While compound **12** was never isolated, its existance during nitration must be considered. Its reactivity toward nitration must be greater than the starting material.

4   **13**

When a nitro group is attached to a nitrogen in conjugation with one carbonyl, e. g. **4**, **8**, and **11**, calculations suggest the nitro group is twisted from planarity. The nitro group itself must remain planar, thus any favorable through space bonding interaction or stabilization of the nitro group by the lone pairs on the carbonyl oxygen must be small. Compounds **7** and **11** remain anomalies. The nitro groups remain planar to the ring. This result is most probably due to the forced orbital overlap imposed by the MMOK correction.

The observation of nitrated heterocycle instability parallels the hydrolysis of the N-bromosuccinimide. Exposure of N-bromosuccinimide to HBr produces Br_2 and succinimide. Similiarly N-nitrosuccinimide (**5**) does not survive aqueous workup, hydrolyzing readily, showing that water may behave as a nucleophile.[5] Water should react with **5** to produce succinimide and nitric acid. This sensitivity and decomposition in water in compounds **5-8** is eliminated by the non-aqueous workup.

The susceptibility of the nitrated compounds to hydrolysis parallels the electrophilic nature of the nitrogen in the nitro group, see Table 1, Charge N-NO_2. Formally the nitro group nitrogen has a charge of +1, and any larger value corresponds to contributions from the

polarization of the N-NO$_2$ bond, i. e. a more electrophilic nitro group, Scheme I. In compounds **1-3** there is a smaller charge than for compounds **5-8**. This suggests a favorable p orbital overlap of the amine nitrogen with the π system in the ring, i. e. the ring nitrogen is tied up in conjugation with the ring systems for **5-8**. Compound **4** appears to be close to the crossover point of stability to hydrolysis. A similiar result is suggested by modelling of compounds **10-12**. The planarity in **11** allows favorable resonance stabilization, thus increasing the nucleophilic character of the remaining nitrogen. While orthogonality of the nitro group in **12** removes any favorable overlap, the remaining stabilized succinimide component allows increased nucleophilic character of the remaining amide nitrogen. These calculations would also indicate that **11** and **12** are more reactive and more readily form **6** and **8**, respectively. Another confirmation of the increased electrophilic character of the nitro group is the charge on the ring nitrogen. The increased negative charge on the nitrogen would suggest a greater stabilization of the charge by the flanking carbonyls.

Scheme I
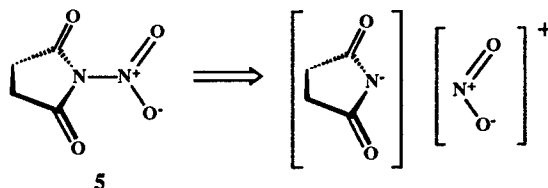
Conclusion

The results of the calculations on nitrated compounds **1-8** suggest one basic requirement to predict the method of choice for compound isolation. This requirement is the p orbital overlap and resonance stabilization. Nitrogen-nitro group resonance stabilization, by what can be termed a psuedo-amide functionality, favors use of an aqueous workup. Any removal of this stabilization by twisting the nitro group from planarity, or by increasing the stabilization of the electrons of the amide nitrogen by the attached carbonyls, generates a more electrophilic nitro group. The more electrophilic the nitro group, the more susceptible the nitrated heterocycle is toward hydrolysis. This would favor use of a non-aqueous workup.

Electrophilic Character of N-Nitrosuccinimide (5)

While the limitation of aqueous versus non-aqueous isolations can be circumvented, we are interested in reactions of N-nitrosuccinimide (**5**) with nucleophiles other than water. The most readily synthesized and handled nitrated derivative is N-nitrosuccinimide (**5**). In all experimental workups, **5** was readily hydrolyzed, or decomposed, by the addition of water. However, piperidine was found to displace the nitro group, generating N-nitropiperidine (**2**) in about 10% yield, Scheme II. Substitution of an alcohol, i. e. ethanol or β-naphthol, did not

decompose **5** and did not nitrate β-naphthol.[3] Utilization of an aromatic amine decomposed **5** and gave 4-methyl-2-nitroaniline (**14**), along with a number of other products in low yield. These results indicate N-nitrosuccinimide to be susceptible to hydrolysis by nucleophiles, and permits nitro group transfer to a limited extent.[5] We are continuing to explore the potential of **5** as a nitrating agent.

Scheme II
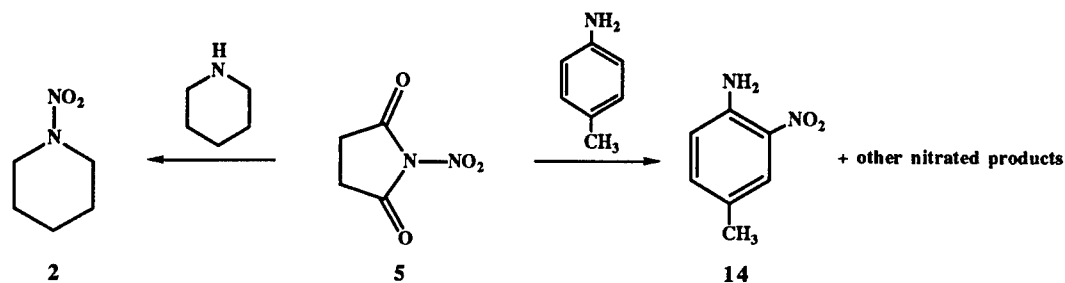
Cycloproprenium Systems
Background

Our research investigations extend to antiaromatic species. A broad view of these species incorporates a 3-dimensional component into the theories of metalloaromaticity, reactivity, and stabilization, and delocalized metalloaromatic complexes and polymers. Current research trends in modern electronic nanotechnology[6] concentrate on the development and fabrication of individual molecular equivalents which parallel large electronic components.[7] Molecular equivalent design depends on the preparation and exhibition of predictable electrical, optical, and magnetic properties, and is an expanding new field in chemistry.[7-9] The design of new materials has exploited the through-space interactions of molecular orbitals and the electron populations in the highest occupied molecular orbitals (HOMO). The genealogy of the theoretical and experimental research builds on the properties of aromaticity,[10] charge transfer complexes, and photo-induced charge separation.[11] Common to many known components is two-dimensionality within the molecule, and this characteristic extends to the macroscopic crystal or polymer. In many of the known charge-transfer systems the crystals exhibit conductivity coincident with the crystal planes. To increase the 3-dimensional macroscopic interactions within the crystal structure there has been increased interest in cyclophanes[12] and spiro-conjugated charge transfer partners[8] as new components of the materials. This work addresses the modelling of a new class of cyclophanes composed of face-to-face 3-membered rings, e.g. **15** and **16**, which are potential high-spin ferromagnetic materials,[13] three-dimensional D_{3h} cyclopropenyl charge transfer partners,[12,14] cyclopropenyl cyclophanes as electrolyte components, and conducting polymers.

7-9

The cyclopropenyl system, (CH)3, is unique among the conjugated cyclic systems investigated to date. It can be the smallest cyclic 4n+2 aromatic system, the smallest cyclic radical, or the smallest 4n antiaromatic system theoretically possible.[10,15,16] The synthesis and properties of the cyclopropenyl cation, and substituted cyclopropenyl cations, have been explored by Breslow.[17] The cyclopropenyl radical and cyclopropenyl anion are very reactive intermediates.[10,17,18]

15   16
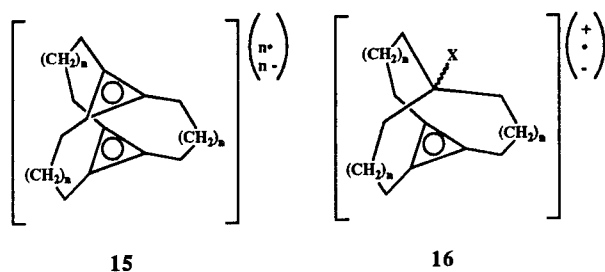
There has been considerable interest in σ conjugation in 3-centered, 2-electron bonds. Hydrogen bonds show 3-centered, 4-electron bonds. In many organometallic and inorganic compounds there are 4-centered, 4-electron bonds. Recent work by McMurry showed that an *in*-bicyclo[4.4.4]-1-tetradecyl cation **17** was a stable 3-centered, 2-electron C-H-C bond.[19] Molecular mechanics (MM2) showed the precursor "*in-* 5" isomer to be less strained than the "*out-* 5" isomer.[20] The negative olefin strain energy (OS) aided cation formation.[19] The cation showed a lower carbon chemical shift due to charge delocalization; the cation was a weak acid, on the order of acetic acid; the "*in-*" proton did not exchange, and the intermediate is the most stable cycloalkyl cation known.[19]

In another related 3-centered, 2-electron system **18**, one alkyl bridge was cinched to create a molecule with a hydrogen more equidistant between two bridgehead carbons.[21] The results suggested that the acidity is due to the difference [steric strain of the alkene precursor]- [steric strain of the cation] and that steric strain in the cation is less of a factor. The energy differences have been addressed through computational studies of hyperstable olefins.[20] Hyperstable olefins have negative olefin strain energies, that is the strain energy of the olefin is less than the parent hydrocarbon. The relationship of OS (a measure of the thermodynamic driving force for the reaction) and observed stabilities and reactivity was addressed by McMurry with compound **17**. To address a caged analog we modelled precursors to cyclophanes **16**.

17   18

7-10
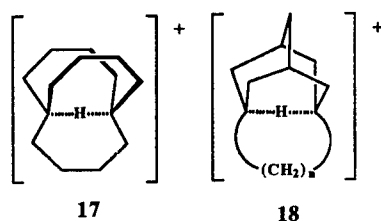
Results and Discussion

Using molecular mechanics (MM2) we modelled the products of intramolecular coupling of **19**, Scheme III.[22] Coupling of **19** would be expected to give **20** (the *in*-3° isomer) in accordance with observations for compound **17**, or **21** (the *out*-3° isomer). Our MM2 analyses of **20** and **21**, showed both these compounds to be hyperstable olefins.[22] The analyses also suggest for n = 1, 2, or 3 that **21** rather than **20**, would be exclusively formed. The prediction that **21** would be favored in the coupling initiated investigations of an alternative pathway to the "*in*-" isomers.

Scheme III
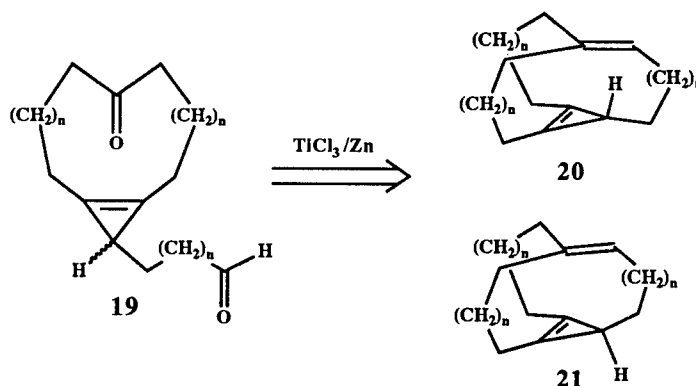
A plausible route for *in*- hydrogen compounds, circumventing cyclopropene ring formation prior to bridge formation, is to form the cyclopropene ring in a much later step, Scheme IV. Intramolecular carbene addition of diazoketone **22** would be expected to form the *in*-3° cyclophane **23**, or the *out*-3° cyclophane **24**. Our MM2 analyses of **23** and **24** showed for n = 2 or 3 that **23** is favored over **24** , but reversed for n=1.[22] Using these predictions the synthesis of **22** has been initiated.

Scheme IV
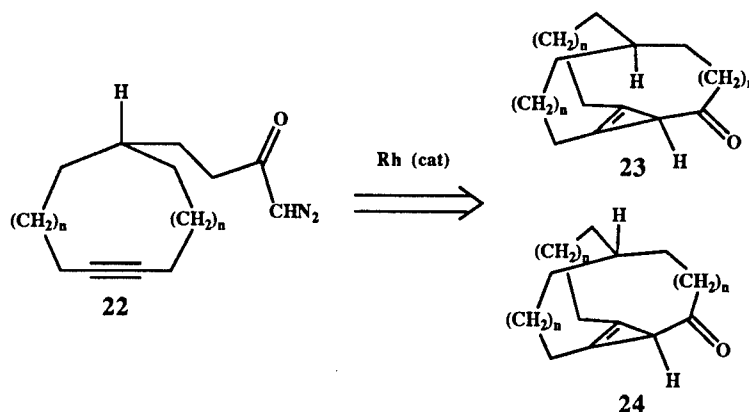
Small Strained-Ring Compounds[23]

Background

As part of our investigations of small ring π systems, our interest in cyclobutadiene compounds continued.[23] The paucity of methods to synthesize specific 1,2-, 1,3-, and 1,2,3-substituted cyclobutadiene complexes **25**, **26**, and **27**, respectively, limit their study and potential application as synthons in organic chemistry. The syntheses of the few known 1,3-disubstituted cyclobutadiene tricarbonyliron complexes, e. g. **25-32**, involve many steps from the parent cyclobutadiene complex **28**.[24] Early methods to synthesize disubstituted cyclobutadiene complexes have involved thermal and photochemical reactions to produce suitably substituted, 4-membered ring precursors. Notable examples of these reactions are the [2+2] thermal cycloadditions of perhaloethylenes with alkylacetylenes,[25] and dibromomaleic anhydride,[26] and [2+2] photochemical cycloaddition of vinylene carbonate with alkylacetylenes.[27] The regioselectivity of these reactions generally leads to 1,2-disubstituted products as components of complex mixtures. Such reactions are often plagued with undesired dimerizations, low yields, and difficulties with product isolation.[28] We recently reported new syntheses of 1,2-disubstituted cyclobutadiene tricarbonyliron complexes;[29] however, the 1,3-regioisomers do not lend themselves to facile synthesis through established thermal or photochemical reactions.

25: R^1,R^3 = alkyl; R^2 = H
26: R^1,R^2 = alkyl; R^3 = H
27: R^1,R^2,R^3 = alkyl
28: R^1,R^2,R^3 = H

29

30

31

32
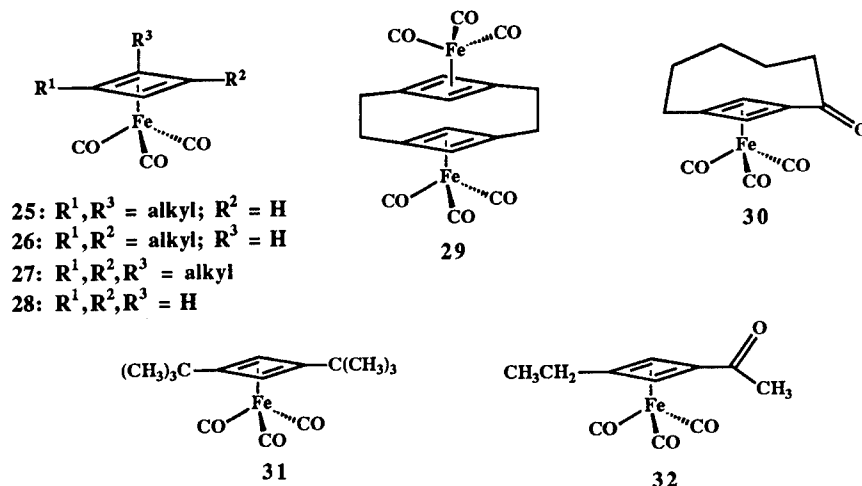
Results and Discussion

We sought to utilize and extend our facile preparative methodology for 1,2-disubstituted cyclobutadiene tricarbonyliron compounds to form cyclobutadiene complexes from ketoesters **33**.[30] Selective addition of an organolithium reagent to the carbonyl group of the α,β-unsaturated ketone versus that of the α,β-unsaturated ester in **33** establishes the desired 1,3-disubstitution pattern (Scheme V).[30] Methylation of **34** with sodium hydride and methyl iodide gave **35**. Reduction of **35** with lithium aluminum hydride, or Vitride, proceeded

smoothly to intermediate **36** in high yield. The crucial step to retain protection of the alcohol in **36** and yet rearrange the reduced ester was achieved by the selective rearrangement of allylic alcohol **36** with a mixture of trifluoroacetic anhydride and pyridine.[30] The mechanism for conversion of **36** to ketone **37** presumably involves the rearrangement of **36** to a hemiketal and hydrolysis, a mechanism previously suggested for substituted cyclobutenediones.[30] Cerium(III)-mediated reductions of ketones **37** with sodium borohydride or lithium aluminum hydride gave hydroxymethoxy derivatives **38** in high yields.[29,30] Bromination of **38** with phosphorus tribromide gave **39**, the desired precursor required to generate the final metal complex. Dibromides **39** were labile to chromatographic conditions and were sufficiently pure to allow their direct conversion to the corresponding iron complexes. Reductive elimination and complexation of **39** with $Fe_2(CO)_9$ gave the corresponding 1,3-disubstituted cyclobutadiene tricarbonyliron complexes **26** (Table II).[29]

Scheme V
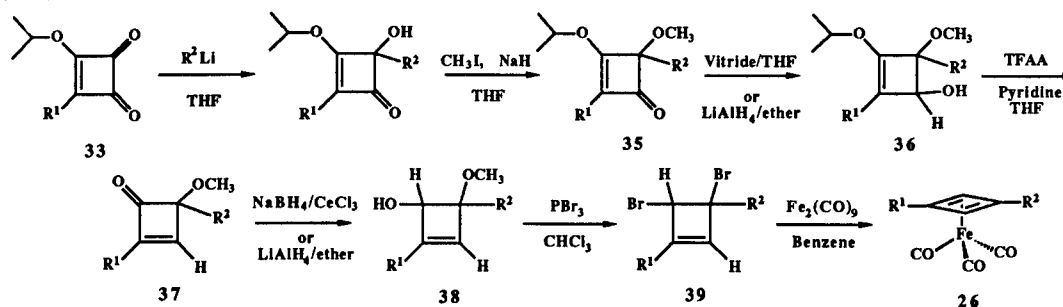
Table II. Preparation of 1,3-Dialkyl-Substituted Intermediates and Iron Complexes

Compound	R^1	R^2	Reduction Method[b]	Yield (%)[a]:						
				34	35	36	37	38	39	26
a	n-butyl	CH₃	1	99	71	76	40	85	52	84
b	n-butyl	n-butyl	2	68	99	82	76	99	42	50
c	t-butyl	CH₃	2	70	92	95	55	78	40	47

a) Yields refer to isolated, purified products.
b) Method 1 = Vitride/THF; Method 2 = LiAlH₄/ether.
c) Yields refer to crude products.

The reaction scheme was easily modified to allow formation of a 1,2,3-trisubstituted cyclobutadiene tricarbonyliron complex (Scheme VI). Addition of butyllithium to ester **35c** gave **40**, and rearrangement with acetic acid gave **41**. Reduction of **41** gave **42**, which slowly brominates with PBr₃ to give **43**. Reductive elimination and complexation of **43** with Fe₂(CO)₉ gave 1,2,3-trisubstituted cyclobutadiene tricarbonyliron complex **27**.

Scheme VI
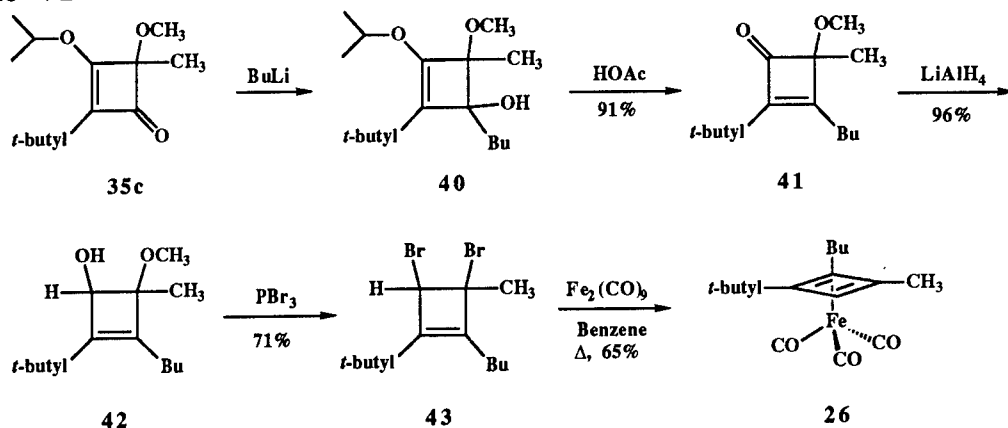
Conclusions

New approaches to the synthesis of pendant chain 1,3-disubstituted cyclobutadiene tricarbonyliron complexes allow choice in the placement of each chain, and a greater latitude in the syntheses of cyclobutadiene tricarbonyliron complexes. The complexes were derived from readily available diisopropyl squarate by using selective alkylations and rearrangements which yield specific 1,3-disubstituted (26) and 1,2,3-trisubstituted (27) cyclobutadiene tricarbonyliron complexes. We are continuing to explore the potential of the cyclobutadiene complexes made possible by the methods described herein.

Acknowledgement

References

1)   a) C. M. Adams; S. A. Shackelford, "New Reaction Transformations Using Nitronium Triflate", Air Force Office of Scientific Research, Final Report Research and Development Laboratories, Culver City, CA, 1991. b) Adams, C. M.; Sharts, C. M.; Shackelford, S. A. "Electrophilic Tetraalkylammonium Nitrate Nitration. I. Convenient New Anhydrous Nitronium Triflate Synthesis and In-Situ Heterocyclic N-Nitration", (manuscript submitted to *Tetrahedron Lett.*). c) Adams, C. M.; Sharts, C. M.; Shackelford, S. A. "Electrophilic Tetraalkylammonium Nitrate Nitration. II. Comparative Tetraethylammoniun Nitrate/Tetra-n-butylammonium Nitrate N-Nitration and Tetra-n-butylammonium Nitrate Aromatic Nitration in Hexane Solvent", (manuscript in preparation for *Tetrahedron Lett.*).

2)   a) Shackelford, S. A.; Goshgarian, B. B.; Chapman, R. D.; Askins, R. E.; Flanigan, D. A.; Rodger, R. N. *Propellants, Explosives, Pyrotechnics* **1989**, *14*, 93-102, and references cited therein. b) Rodgers, S. L.; Coolidge, M. B.; Lauderdale, W. J.; Shackelford, S. A.*Thermochemica Acta* **1991**, *177*, 151-168. c) Shackelford, S. A., "Mechanistic Investigations of Condensed Phase Energetic Material Decomposition Processes Using the Kinetic Deuterium Isotope Effect", Bulusu, S. N., Ed. Chemistry and Physics of Energetic Materials, Kluwer Academic Publisher, Netherlands, 1990, pp. 413-432. d) Shackelford, S. A., "Mechanistic Relationships of the Decomposition Process to Combustion and Explosive Events from Kinetic Deuterium Isotope Effect Investigations", Bulusu, S. N., Ed. Chemistry and Physics of Energetic Materials, Kluwer Academic Publisher, Netherlands, 1990, pp. 433-456.

3)   a) Suri, S. C.; Chapman, R. D. *Synthesis* **1988**, 743-745. b) Feuer, Henry and Nielsen, Arnold T., Eds. "Nitro Compounds: Recent Advances in Synthesis and Chemistry: Organic Nitro Chemistry Series", VCH Publishers, Inc., NY, NY., 1990. c) Barco, A.; Benetti, S.; Pollini, G. P.; Spalluto, G.; Zanirato, V. *Tetrahedron Lett.* **1991**, *32(22)*, 2517-2520. d) Lemaire, M; Guy, A.; Boutin, J. P. *Synthesis* **1989**,761-763. e) Lemaire, M; Guy, A.; Boutin, J. P. *Tetrahedron* **1987**, *43*, 835-844.

4)   a) Stewart, J. J. P. MOPAC, A Semi-Empirical Molecular Orbital Program, QCPE 455, 1983. b) Stewart, J. J. P *J. Comput. Chem.* **1989**, *10*, 221-264. c) Stewart, J. J. P *J. Comput. Chem.* **1989**, *10*, 209.

5)   a) Alcoholysis of some N-nitro derivatives have been reported: Koslova, I. K.; Luk'yanov, O. A.; Tartakovskii, V. A. *Izu. Akad. Nauk. SSSR Ser. Khim.* **1981**, *11*, 2556-2563. b) Koslova, I. K.; Luk'yanov, O. A.; Tartakovskii, V. A. *Izu. Akad. Nauk. SSSR Ser. Khim.* **1981**, *11*, 2563-2571.

6)   Feynman, R. P. *Saturday Review* **1960**, *43*, 45-47.

7)   a) Farazdel, A.; Dupuis, M.; Clementi, E.; Aviram, A. *J. Am. Chem. Soc.* **1990**, *112*, 4206-4214. b) Maslak, P.; Augustine, M. P.; Burkey, J. D. *J. Am. Chem. Soc.* **1990**, *112*, 5359-5360.

8)   a) Ducharme, S.; Scott, J. C.; Twieg, R. J.; Moerner, W. E. *Phys. Chem. Let.* **1991**, *66*, 1846-1849. b) Emmelius, M.; Pawlowski, G.; Vollman, H. W. *Angew. Chem. Int. Ed. Engl.* **1989**, *28*, 1445-1600. c) Tour, J. M.; Wu, R.; Schumm, J. S. *J. Am. Chem. Soc.* **1990**, *112*, 5662-5663. d) Hush, N. S.; Wong, A. T.; Bacskay, G. B.;

Reimers, J. R. *J. Am. Chem. Soc.* **1990**, *112*, 4192-4197. e) Ferringa, B. L.; Jager, W. F.; deLange, B.; Meyer, E. W. *J. Am. Chem. Soc.* **1991**, *113*, 5468-5470.

9) a) Heuer, W. B.; Mountford, P.; Green, M. L. H.; Bolt, S. G.; O'Hare, D.; Miller, J. S.; *Chem. Mater.* **1990**, *2*, 764-772. b) Miller, J. S.; Calabrese, J. C.; Harlow, R. L.; Dixon, D. A.; Zhang, J. H.; Reiff, W. M.; Chittipeddi, S.; Selover, M. A.; Epstein, A. J. *J. Am. Chem. Soc.* **1990**, *112*, 5496-5506. c) Broderick, W. E.; Thompson, J. A.; Day, E. P.; Hoffman, B. M. *Science*, **1990**, *249*, 401-403. d) Broderick, W. E.; Hoffman, B. M. *J. Am. Chem. Soc.* **1991**, *113*, 6334-6335. e) Miller, J. S.; O'Hare, D. M.; Chakrabroty, A.; Epstein, A. J. *J. Am. Chem. Soc.* **1989**, *111*, 7853-7860. f) Novak, J. A.; Jain, R.; Dougherty, D. A. *J. Am. Chem. Soc.* **1989**, *111*, 7618-7619. g) Manriquez, J. M.; Yee, G. T.; McLean, R. S.; Epstein, A. J.; Miller, J. S. *Science* **1991**, *252*, 1415-1417.

10) a) Garrett, P. J., Ed. "Aromaticity", Wiley-Interscience, N. Y., 1986. b) Breslow, R. *Chem. Engng News* **1965**, *43(26)*, 90-98. c) Borden, W. T.; Davidson, E. R. *Acc. Chem. Res.* **1981**, *14,* 69-76. d) Streitweiser, A. "Molecular Orbital Theory for Organic Chemists", J. Wiley, New York, N.Y. 1961.

11) For a review see Gray, H. B. *Aldrichimica Acta* **1990**, *23*, 87-94, and references cited therein.

12) a) Plitzko, K. D.; Rapko, B.; Gollas, B.; Wehrle, G.; Weakley, T.; Pierce, D. T.; Geiger, W. E. Jr.; Haddon, R. C.; Boekelheide, V. *J. Am. Chem. Soc.* **1990**, *112*, 6545-6556. b) Plitzko, K. D.; Wehrle, G.; Gollas, B.; Rapko, B.; Dannheim, J.; Boekelheide, V. *J. Am. Chem. Soc.* **1990**, *112*, 6556-6564. c) Keehn, P. M.; Rosenfield, S. M., Eds. "Cyclophanes", Academic Press, N. Y., 1983, Vol. 1 and 2, and references cited therein. d) Boschke, F. L. Ed. "Topics in Current Chemistry", Springer-Verlag, N. Y., 1983, Vol. 113 and 115, and references cited therein. e) Greenberg, A.; Liebman, J. F., Eds. "Strained Organic Molecules", Academic Press, N. Y., 1978, Vol. 38, and references cited therein.

13) a) Sixth International Symposium on Novel Aromatic Compounds, Osaka Japan, August 20-25, 1989, Pure Appl. Chem. 1990, 62, 1-574, and references cited therein. b) Symposium on Ferromagnetic and High Spin Molecular Based Materials; 197th American Chemical Society National Meeting; April 9-14, 1989; Dallas, TX. Proceedings: *Mol. Cryst. Liq. Cryst.*, and references cited therein. c) Synder, G. J.; Dougherty, D. A. *J. Am. Chem. Soc.* **1989**, *111*, 3927-3942. d) Snyder, G. J.; Dougherty, D. A. *J. Am. Chem. Soc.* **1989**, *111*, 3942-3954. e) Ham, S. W.; Chang, W.; Dowd, P. *J. Am. Chem. Soc.* **1989**, *111*, 4130-4131. f) Du, P.; Hrovat, D. A.; Borden, W. T. *J. Am. Chem. Soc.* **1989**, *111*, 3773-3778. g) LePage, T. J.; Breslow, R. *J. Am. Chem. Soc.* **1987**, *109*, 6412-6421. h) Stone, K. J.; Greenberg, M. M.; Blackstock, S. C.; Berson, J. A. *J. Am. Chem. Soc.* **1989**, *111*, 3659-3671.

14) a) Boekelheide, V. *Pure Appl. Chem.* **1986**, *58*, 1-6, and references cited therein. b) Plitzko, K. D.; Boekelheide, V. *Organometallics* **1988**, *7*, 1573-1582. c) LeVanda, C.; Bechgaard, K.; Cowen, D. O.; Mueller-Westerhof, U. T. Eilbracht, P.; Candella, G. A.; Collins, R. L. *J. Am. Chem. Soc.* **1976**, *98*, 3181-3187. d) Hopf, H.; Raulfs, F. W. *Tetrahedron* **1986**, *42*, 1655-1663, and references cited therein. e) Hopf, H.; El-Tamany, S.; Raulfs, F. W. *Angew. Chem. Int. Ed. Engl.* **1983**, *22*, 633-634. f) Katz, T. J.; Slusarek, W. *J. Am. Chem. Soc.* **1980**, *102*, 1058-1063. g) Laganis, E. D.; Finke, R. G.; Boekelheide, V. *Tetrahedron Lett.* **1980**, *21*, 4405-

4408. h) Laganis, E. D. ; Voegeli, R. H.; Swain, R. T.; Finke, R. G.; Hopf, H.; Boekelheide, V. *Organometallics* **1982**, *1*, 1415-1420. i) Burdett, J. K. Canadell, E. *Organometallics* **1985**, *4*, 805-815. j) Rausch, M. D.; Kovar, R. F.; Krachanzel, C. S. *J. Am. Chem. Soc.* **1969**, *91*, 1259-1260. k) Hedberg, F. L.; Rosenberg, H. *J. Am. Chem. Soc.* **1969**, *91*, 1258-1259. l) Katz, T. J.; Acton, N.; Martin, G. *J. Am. Chem. Soc.* **1969**, *91*, 2804-2805. m) Kasahara, A.; Izuma, T.;Yoshida, Y.; Shimizu, I. *Bull. Chem. Soc. Jpn.* **1985**, *55*, 1901-1906. n) Klavetter, F. L.; Grubbs, R. H. *J. Am. Chem. Soc.* **1988**, *110*, 7807-7813. o) Swager, T. M.; Dougherty, D. A.; Grubbs, R. H. *J. Am. Chem. Soc.* **1988**, *110*, 2973-74.

15) Breslow, R. *Acc. Chem. Res.* **1973**, *6*, 393-398.

16) a) Hess, B. A.; Ewig, C. S.; Schaad, L. J. *J. Org. Chem.* **1985**, *50*, 5869-5871. b) Hückel, E. *Z. Phys.* **1931**, *70*, 204. c) Breslow, R. *Chem. Engng News* **1965**, *43(26)*, 90-98.

17) a) Byun, Y. G.; Saebo, S.; Pittman, C. U., Jr. *J. Am. Chem. Soc.* **1991**, *113*, 3689-3696, and references cited therein. b) D'yakonov, I. A. *Zhur. Obshchei. Khim.* **1959**, *29*, 3848. c) Breslow, R.; Hover, H.; Chang, H. W. *J. Am. Chem. Soc.* **1962**, *84*, 3168-3174. d) Breslow, R.; Lockhard J.; Chang, H. W. *J. Am. Chem. Soc.* **1961**, *83*, 2367-2375. e) Breslow, R. ACS National Meeting, 1957, Abstract No. 30. f) Breslow, R. *J. Am. Chem. Soc.* **1957**, *79*, 5318. g) Breslow, R.; Yuan, C. *J. Am. Chem. Soc.* **1958**, *80*, 5991-5994.

18) a) Anet, F. A. L.; Trova, M. P.; Paquette, L. A. *Tetrahedron Lett.* **1989**, *30*, 6469-6472. b) Dai, S.; Wang, J. T.; Williams, F. *J. Am. Chem. Soc.* **1990**, *112*, 2835-2837. c) Breslow, R.; Gal, P. *J. Am. Chem. Soc.* **1959**, *81*, 4747-4748. d) Roth, H. D.; Raghavachari, K. *J. Am. Chem. Soc.* **1989**, *111*, 7132-7136. e) Hess, B. A., Jr.; Schaad, L. J.; Carsky, P. *Tetrahedron Lett.* **1984**, *25*, 4721-4724.

19) a) McMurry, J. E.; Lectka, T.; Hodge, C. N. *J. Am. Chem. Soc.* **1989**, *111*, 8867-8872. b) McMurry, J. E.; Hodge, C. N. *J. Am. Chem. Soc.* **1984**, *106*, 6450-6451. c) McMurry, J. E.; Lectka, T. *J. Am. Chem. Soc.* **1990**, *112*, 869-870. d) McMurry, J. E. *Chem. Rev.* **1989**, 1513-1524. e) McMurry, J. E. *Acc. Chem. Res.* **1974**, *7*, 281-286. f) McMurry, J. E.; Dushin, R. G. *J. Am. Chem. Soc.* **1989**, *111*, 8928-8929. g) McMurry, J. E.; Dushin, R. G. *J. Am. Chem. Soc.* **1990**, *112*, 6942-6949. h) McMurry, J. E.; Matz, J. R. *Tetrahedron Lett.* **1982**, *23*, 2723-2724. i) Seebach, D.; Betschart, C. *Chimica* **1989**, *43*, 39-49.

20) McEwen, A. B.; von Rague Schleyer, P. *J. Am. Chem. Soc.* **1986**, *108*, 3951-3960.

21) Sorensen, T. S.; Whitworth, S. M. *J. Am. Chem. Soc.* **1990**, *112*, 8135-8144.

22) Adams, C. M. unpublished results. MM2 calculations were performed using MMX from Serena Software, Indiana, on a Macintosh IIsi.

23) a) Adams, C. M.; Joslin, S. A.; Crawford, E. S.; Schemenaur, J. E. "Cyclobutadiene Tricarbonyliron Complexes: Formation of 1,3- and 1,2,3- Substituted Derivatives", (*Organometallics* Accepted, In Press). b) Preliminary work was presented in part at the 203rd ACS National Meeting, San Francisco, CA, April 5-10, 1992, Division of Organic Chemistry, Abstract No. 305.

24)   a) Adams, C. M.; Holt, E. M. *Organometallics* **1990**, *9*, 980-986. b) Adams, C. M.; Crawford, E. S.; Salim, E. *Tetrahedron Lett.* **1992**, *33*, 3963-3966. c) Reeves, P.; Henery, J.; Pettit, R. *J. Am. Chem. Soc.* **1969**, *91*, 5888-5890. d) Marcinal, P.; Hannoir-Guisez, N.; Cuingnet, E. *Trav. Soc. Pharm. Mont.* **1973**, *33*, 281-288.

25)   a) Smutny, E. J.; Caserio, M. C.; Roberts, J. D. *J. Am. Chem. Soc.* **1960**, *82*, 1793-1801. b) Brune, H. A.; Hanebeck, H.; Hüther, H. *Tetrahedron* **1970**, *26*, 3099-3112. c) Bloomquist, A. T.; LaLancette, E. A. *J. Org. Chem.* **1964**, *29*, 2331-2334.

26)   a) Berens, G.; Kaplan, F.; Rimerman, R.; Roberts, B. W.; Wissner, A. *J. Am. Chem. Soc.* **1975**, *97*, 7076-7085. b) Roberts, B. W.; Wissner, A.; Rimerman, R. A. *J. Am. Chem. Soc.* **1969**, *91*, 6208-6209.

27)   a) Grubbs, R. H.; *J. Am. Chem. Soc.* **1970**, *92*, 6693. b) Grubbs, R. H.; Pancoast, T. A.; Grey, R. A. *Tetrahedron Lett.* **1974**, 2425-2426. c) Grubbs, R. H.; Grey, R. A. *J. Chem. Soc., Chem. Commun.* **1973**, 76-77.

28)   a) Efraty, A. *Chem. Rev.* **1977**, *77*, 691-743 and references cited therein. b) Watts, L., Fitzpatrick, J. D.; Pettit, R. *J. Am. Chem. Soc.* **1965**, *87*, 3253-3254. c) Emerson, G. F.; Watts, L.; Pettit, R. *J. Am. Chem. Soc.* **1965**, *87*, 131-133.

29)   Adams, C. M.; Schemenaur, J. E.; Crawford, E. S.; Joslin, S. A. *Synth. Commun.* **1992**, *22(10)*, 1385-1396.

30)   a) Liebeskind, L. S.; Fengl, R. W.; Wirtz, K. R.; Shawe, T. T. *J. Org. Chem.* **1988**, *53*, 2482-2488. b) Liebeskind, L. S.; Baysdon, S. L. *Tetrahedron Lett.* **1984**, *25*, 1747-1750. c) Reed, M. W.; Pollart, D. J.; Perri, S. T.; Foland, L. D.; Moore, H. W. *J. Org. Chem.* **1988**, *53*, 2477-2482. d) Krysan, D. J.; Gurski, A.; Liebeskind, L. S. *J. Am. Chem. Soc.* **1992**, *114*, 1412-1418. e) Heerding, J. M.; Moore, H. W. *J. Org. Chem.* **1991**, *56*, 4048-4050. f) Xu, S. L.; Tiang, M.; Moore, H. W. *J. Org. Chem.* **1991**, *56*, 6104-6109. g) Xu. S. L.; Xia, H.; Moore, H. W. *J. Org. Chem.* **1991**, *56*, 6094-6103. h) Luche, J.-L. *J. Am. Chem. Soc.* **1978**, *100*, 2226-2227. i) Rubin, Y.; Knobler, C. B.; Diederich, F. *J. Am. Chem. Soc.* **1990**, *112*, 1607-1617.

NONLINEAR BICHROMATIC WAVE PROPAGATION
IN PERIODICALLY POLED OPTICAL WAVEGUIDES

Marek Grabowski
Associate Professor
Department of Physics

University of Colorado
1420 Austin Bluffs Parkway
Colorado Springs, CO 80933-7150

NONLINEAR BICHROMATIC WAVE PROPAGATION
IN PERIODICALLY POLED OPTICAL WAVEGUIDES

Marek Grabowski
Associate Professor
Department of Physics
University of Colorado at Colorado Springs

Abstract

The energy exchange process between the fundamental and its second harmonic fields copropagating in an optical medium is facilitated by the spatially periodic DC poling field. The nonlinear dynamics of this system is investigated in the context of an effective Hamiltonian formalism. The explicitly included cross and self phase modulation nonlinear terms lead to the bifurcation instability interpreted as a new switching phenomenon in which both up and down conversion efficiencies can be precisely controlled by the external field. Experiments testing predicted effects are suggested.

NONLINEAR BICHROMATIC WAVE PROPAGATION
IN PERIODICALLY POLED OPTICAL WAVEGUIDES

Marek Grabowski

INTRODUCTION

Many interesting phenomena associated with the propagation of electromagnetic waves in spatially periodic nonlinear media have recently been studied in the context of such diverse branches of physics as nonlinear dynamics [1,2], semiconductor physics [3,4], and nonlinear optics [5,6]. These investigations led to a fairly complete understanding of the regular (periodic), localized (solitons), and chaotic behavior of monochromatic waves in one-dimensional geometries. However, the full picture of spatio-temporal nonlinear phenomena is still missing.

As a first attempt toward understanding the propagation of pulsed classical waves, co-propagating fundamental and second harmonic fields are studied in the slowly varying envelope approximation, but with an explicit account for nonlinear phase modulation effects [7]. For inversion symmetric systems, such as optical glasses, the energy transfer between the two fields is due to third order susceptibility and must be mediated by an electric dc-field of the appropriate periodicity. This spatially periodic dc-field can be either internally self-generated, or externally imposed.

Indeed, such a self-generated dc-field has been invoked as a possible explanation of a anomalous second harmonic generation observed in glass optical fibers [8] (for a review see Chapter 10 of Agrawal [9]). This spatially periodic space-charge electric field strongly depends on charge transport, and thus, it is sensitively time dependent. In contrast, Kashyap [5] reported phase-matched second harmonic generation in externally poled optical fibers,

thus allowing much more control over the resulting phenomena. Our approach in this paper is meant to model the latter situation.

PROPAGATION EQUATIONS

We consider the case of two optical fields: E_1 of frequency ω, and its second harmonic E_2 of frequency 2ω, copropagating along the z-direction in an inversion symmetric medium poled by a static, spatially periodic electric field E_0. The coupled propagation equations for these fields follow [6] from the macroscopic wave equation:

$$\left(\partial_x^2 + n_1^2\right)E_1 + \kappa\left[\left(E_0^2 + |E_1|^2 + 2|E_2|^2\right)E_1 + 2E_0E_2E_1^*\right] = 0$$

$$\left(\partial_x^2 + 4n_2^2\right)E_2 + 4\kappa\left[\left(E_0^2 + |E_2|^2 + 2|E_1|^2\right)E_2 + E_0E_1^2\right] = 0 \tag{1}$$

where $x = z\omega/c$, $\kappa = 12\pi\chi^{(3)}$ measures the nonlinear polarization of the medium, and n_j stands for the linear refractive index.

To present the main results as elegantly as possible, we find it advantageous to treat the Eq. 1 as arising from the following Lagrangian for complex scalar fields with the spatial coordinate x playing the role of time:

$$L(E_j, \partial_x E_j) = \sum_{j=1}^{2}\left(\left|\tfrac{1}{j}\partial_x E_j\right|^2 - \left|n_j E_j\right|^2\right) - \kappa V(E_j)$$

$$V(E_j) = \sum_{j=1}^{2}\left(E_0^2 + \left|E_{3-j}\right|^2 + \tfrac{1}{2}\left|E_j\right|^2\right)\left|E_j\right|^2 + 2E_0\,\mathrm{Re}\left(E_1^2 E_2^*\right) \tag{2}$$

In the above equation the nonlinear "potential" contains the external, self- and cross-phase modulation terms, as well as the term responsible for the dc-field mediated energy transfer between the fundamental and second harmonic fields.

The Lagrangian of Eq. 2 is globally gauge invariant and the associated conserved current can be identified as:

$$J = \sum_{j=1}^{2} \frac{1}{j} \mathrm{Im}(E_j^* \partial_x E_j)$$

(3)

Clearly, $\partial_x J = 0$, reflecting the constancy of the energy flow in the direction of wave propagation. This symmetry of the Lagrangian suggests the use of polar representation for the fields:

$$E_j(x) = \sqrt{P_j(x)/n_j} \; \exp\left\{ij\left[n_j x + \phi_j(x)\right]\right\}$$

(4)

where the fast oscillating components of the fields (those on the scale of wave number n_j) have been explicitly separated in preparation for the so-called *Slowly Varying Envelope Approximation* (SVE) *cf.* Ref. [10].

Indeed, for the periodic *dc*-field varying as:

$$E_0(x) = \sqrt{\mathcal{E}/n_2} \, \cos 2n_0 x$$

(5)

and with $n_2 > n_1 \gg n_0$, the backscattering of the fields by the long wavelength periodic potential is negligible and the SVE approximation is justified [10]. Consequently, upon substitutions of Eq. 4 and Eq. 5 the SVE Lagrangian becomes:

$$L_{SVE}(P_j,\phi_j,\partial_x\phi_j) = 2\sum_{j=1}^{2} P_j \partial_x \phi_j - \frac{\kappa}{n_1 n_2} H(P_j,\phi_j)$$

$$H(P_j,\phi_j) = P_1 \sqrt{\mathcal{E}P_2} \, \cos 2(\phi_2 - \phi_1 + \Delta x) + P_1 P_2$$

(6)

where $\Delta = n_2 - n_1 - n_0$ is the phase mismatch and the second term in the Hamiltonian H represents the contribution of the self- and cross-phase modulation terms (their significance will

be discussed shortly). In addition, we have neglected small terms of the order of $(n_2 - n_1) \ll 1$ (applicable in most optical materials).

The global gauge invariance of L_{SVE} becomes manifest if we introduce new variables – the total and relative phases :

$$\phi = 2(\phi_2 + \phi_1), \qquad \psi = 2(\phi_2 - \phi_1 + \Delta x), \tag{7}$$

Clearly, under the *SVE* approximation, the conserved current J of Eq. 3 is just the total intensity of the propagating fields $W = P_1 + P_2$. Using this constancy of W, and upon further rescaling of the variables as $p = P_2/W$ and $\varepsilon = \mathcal{E}/W$, we arrive at a conservative single degree of freedom system described by an effective Hamiltonian in the relative phase coordinate, with canonically conjugated "momentum" p:

$$h_\delta(p, \psi) = \sqrt{\varepsilon p}(1 - p)\cos\psi + (1 + 2\delta - p)p \tag{8}$$

where $\delta = n_1 n_2 \Delta/(\kappa W)$ measures the phase mismatch for the energy transfer term.

The equations of motion corresponding to the Hamiltonian of Eq. 8 can be easily written:

$$\partial_y p = \sqrt{\varepsilon p}(1 - p)\sin\psi$$

$$\partial_y \psi = \tfrac{1}{2}\sqrt{\varepsilon/p}(1 - 3p)\cos\psi + (1 - 2p) + 2\delta \tag{9}$$

with the independent coordinate rescaled as $y = (\kappa W/n_1 n_2)x$. These equations can be decoupled using the constancy of the Hamiltonian of Eq. 8. In particular, the first order differential equation for the intensity of the second harmonic wave becomes:

$$(\partial_y p)^2 = Q(p) = \varepsilon p(1 - p) - \left[h_\delta(p_0, \psi_0) - (1 + \delta - p)p\right]^2 \tag{10}$$

with p_0 and ψ_0 being the initial ($y = 0$) intensity and relative phase, respectively. Although the solutions to Eq. 10 can be written in terms of elliptic functions with parameters depending on the roots of the quartic polynomial $Q(p)$, these explicit expressions are not particularly informative and shall not be presented here. Instead, we proceed by "graphically" classifying the possible solutions to Eq. 9.

DISCUSSION OF RESULTS

The dynamical system given by Eq. 9 is clearly integrable. Consequently, its phase space representation proves quite illuminating and it is shown in Fig. 1. Specifically, we restrict our analysis to the perfectly phase matched propagation, i.e. $\delta = 0$. This condition makes the special effects discussed below most pronounced and otherwise it does not change the main conclusions. Clearly, all solutions are periodic. Moreover, for initial conditions restricted to $\psi_0 = 0$ (in-phase), the dynamics of the system resides on non-negative energy manifold ($h \geq 0$) and there are only two types of solutions: libration-like inside the separatrix and rotation-like outside of it. Notice also that the rotation-like solutions exist only due to self- and cross-phase modulation terms and thus are absent in the usually employed approximations (especially, in the most frequently used undepleted pump approximation, cf. Ref. [5], [10]).

Based on Fig. 1, two interesting phenomena can be predicted. For a given strength of the external dc-field $\varepsilon < 1$ and initial conditions $\psi_0 = 0$, $p_0 < p_c$, the second harmonic intensity oscillates between the initial value of p_0 and the maximum which is limited by ε, and is always less then p_s (the saddle point). The period of these spatial oscillations grows from the value of 2π at $p_0 = 0$, to infinity at the separatrix $p_0 = p_c$ (soliton-like kinks solutions). As the seed intensity p_0 increases past the critical one, p_c, the solutions switch to libration-like, with nearly doubled period and significantly increased up-conversion

efficiency up to the maximum as large as p_m (the upper branch of the separatrix). This is illustrated in Fig. 2 which shows $p(y)$ for two seed intensities chosen to emphasize the period doubling upon crossing of the separatrix. We shall refer to this behavior as *switching*.

The second type of phenomenon we shall address is *down-frequency conversion*. Since the energy flow direction between the ω and 2ω fields is in itself periodic along the propagation length (with the intensity of the fundamental mode given simply by $1 - p$), then for $p_0 > p_{e0}$ (cf. Fig. 1) one can regard the fundamental mode as a seed for down-frequency conversion. Consequently, similar to the discussion above, the efficiency of the down-frequency conversion switches abruptly upon crossing of the upper branch of the separatrix (i.e. for $p_0 = p_m$), and is accompanied by the spatial period doubling. Notice, however, a major difference between up and down conversion regimes: for $p_0 = 1$, i.e. for zero initial intensity of the ω-field, there is no energy exchange between the two fields! This is obviously consistent with the well known underlying physics [10] (two high frequency photons cannot spontaneously combine into a lower frequency one). Nevertheless, this simple fact is missing in models which ignore the nonlinear phase modulation terms, further emphasizing the importance of the asymmetry attributable to their presence.

It should also be clear that the emergence of the separatrix in the phase space of Fig. 1 represents a truly nonperturbative effect in ε as can be seen in Fig. 3. All the positive energy critical points bifurcate from the value of one-half at $\varepsilon = 0$ and then quickly saturate as $\varepsilon \to 1$. For the strength of the *dc*-field $\varepsilon > 1$ (not shown in Fig. 3) the saddle point p_s bifurcates further, and for large ε the energy transfer term in the Hamiltonian of Eq. 8 dominates the nonlinear phase modulation terms. Thus, in this limit standard approximation results are recovered. The switching effect is most prominent however, for small ε and in particular for $\varepsilon \approx 0.15$, where the maximum gain on switching reaches a maximum. Consequently, this is the region on which we shall concentrate in further discussion.

In practice, one would observe the intensity of the second harmonic field $p(L)$, at a fixed propagation length with L being the length of the optical fiber or waveguide. In Fig. 4 both of the phenomena defined above are illustrated. The solid curves represent the up-frequency conversion gain as measured at conveniently chosen $L = 3\pi$, with the optimal gain shown as dashed curves to serve as a guide to the eye. Notice the dramatic changes of the gain as the seed intensity p_0 is varied. Also, the negative gain for larger p_0 should be interpreted as the above mentioned down-frequency conversion. Although the down and up conversion regions appear nearly symmetrical, they are significantly different especially for zero seed intensities: the gain is zero for $p_0 = 1$, while for $p_0 = 0$ it is finite and depends on the strength of ε. The two curves shown in Fig. 4 for two different values of ε give an indication of how the conversion gain depend on that parameter. Generally, the oscillatory features are sharper for larger ε, including narrower switching range for both up and down conversion regimes. Finally, notice the wide plateau of zero gain for $\varepsilon = 0.15$ and p_0 around the elliptic fixed point reflecting the progressively decreasing importance of the phase modulation terms of libration-like solution for larger values of ε.

The switching behavior can also be observed for fixed seed intensity by adjusting the strength of the dc-field. This situation is perhaps easier to realize experimentally and is illustrated in Fig. 5. There again the solid curves show the conversion gain (with $p_0 = 0.05$ only the up-conversion takes place) as a function of ε at different propagation lengths: $L = 3\pi$ and 4π. Clearly, the conversion gain is sensitively dependent on propagation length with narrower switching region for larger L or, since L scales with the total intensity W, for higher field intensities.

CONCLUSIONS

In conclusion, the nonlinear cross-phase modulation that always accompanies the self-phase modulation in the case of more than one propagating field is shown to be responsible for a novel type of instability. The origin of this instability can be traced to the dynamical bifurcation of the system's fixed points and the emergence of the separatrix isolating different types of periodic solutions. Consequently, the energy exchange between the two copropagating fields is highly sensitive to all externally controllable parameters: the propagation length L (or alternatively, total field intensity W) set by the sample length, the phase mismatch δ controlled by the periodicity of the external static field, the initial seed intensity of the second harmonic field p_0, and the strength of the dc-field ε.

Finally, it should be noted that even though the results are presented in a fairly general context, the phenomena of switching and down frequency conversion should find exciting applications in the area of integrated opto-electronic devices. Moreover, the new findings of this study should encourage the reexamination of the experiments already performed [8,5] on second harmonic generation in optical fibers.

REFERENCES

[1] Marek Grabowski and Pawel Hawrylak, Phys. Rev. B **41**, 5783 (1990).

[2] François Delyon, Yves-Emmanuel Lévy, and Bernard Souillard, Phys. Rev. Lett. **57**, 2010 (1986).

[3] D.L. Mills and S.E. Trullinger, Phys. Rev. B **36**, 947 (1987).

[4] Pawel Hawrylak and Marek Grabowski, Phys. Rev. B **40**, 8013 (1989).

[5] Raman Kashyap, J. Opt. Soc. Am. B **6**, 313 (1989), Appl. Phys. Lett. **58**, 1233 (1991).

[6] Marek Grabowski, in Proceedings of the NATO ARW on Localization and Propagation of Classical Waves in Random and Periodic Structures, Crete, May 1992 (in print).

[7] Govind P. Agrawal, Phys. Rev. Lett. **59**, 880 (1987).

[8] Dana Z. Anderson, Victor Mizrahi, and John E. Sipe, Optics Lett. **16**, 796 (1991).

[9] Govind P. Agrawal, *Nonlinear Fiber Optics* (Academic Press 1989).

[10] Y.R. Shen, *Principles of Nonlinear Optics* (Wiley, New York 1984).

FIGURE CAPTIONS:

FIG. 1. Representative phase space trajectories of the solutions to Eq. 9 for $\varepsilon = 0.15$ and $\delta = 0$. Emphasized are: the separatrix (dashed line), zero energy boundary (thick line), and elliptic fixed points (dots).

FIG. 2. The intensity of the second harmonic field as a function of the propagation length for two initial intensities (indicated in the figure) straddling the critical intensity $p_c = 0.044$ for $\varepsilon = 0.15$.

FIG. 3. The characteristic points of the phase space as a function of the dc-field's strength. The solid curves represent the saddle (p_s) and the elliptic $\psi = 0$ (p_{e0}) or $\psi = \pi$ $(p_{e\pi})$ fixed points. The broken curves show the critical points: p_c and p_m. The dash-dotted line illustrates the maximum possible gain on switching defined as $g_{max} = p_m - p_s$.

FIG. 4. The up-frequency conversion gain $g = p(y) - p_0$ as measured at $y = 3\pi$, for two values of ε indicated. The broken line envelopes represent the maximum possible gain, while the solid bars indicate the switching regions.

FIG. 5. The conversion gain for seed intensity of $p_0 = 0.05$ as a function of the dc-field strength at two different propagation lengths. The broken line stands for the maximum possible gain, and the solid bars indicate the width of the switching region.
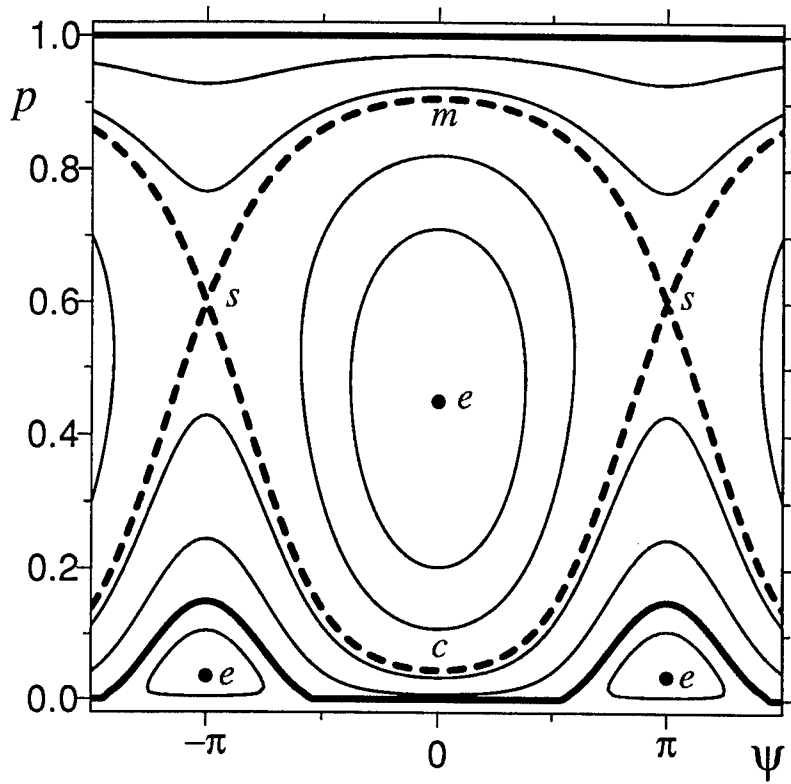
FIG. 1
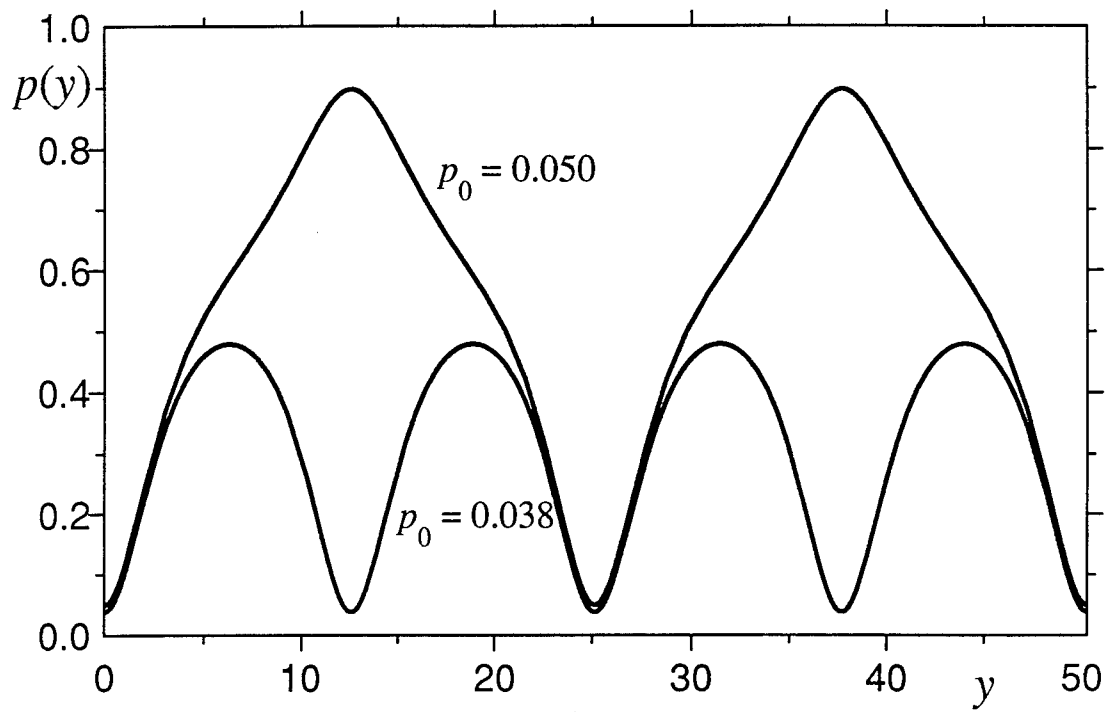
FIG. 2

FIG. 3

FIG. 4
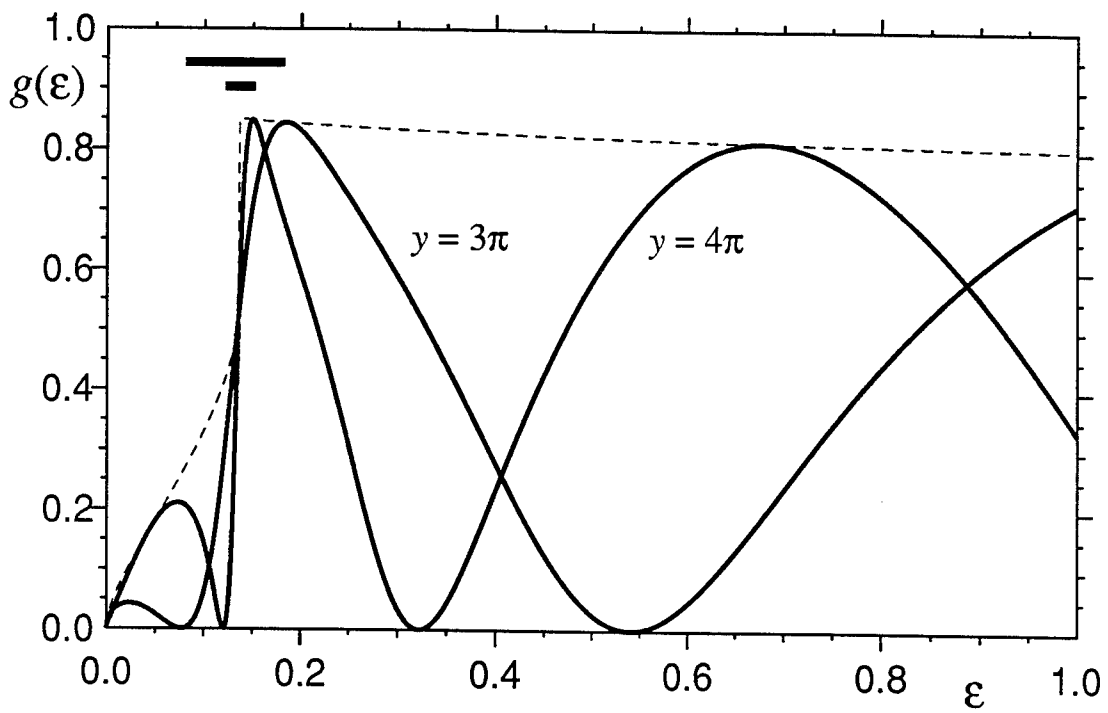
FIG. 5

AN *AB INITIO* STUDY

OF

LEWIS ADDUCTS OF POTENTIAL IMPORTANCE

IN

ROOM TEMPERATURE CHLOROALUMINATE MOLTEN SALTS

Gilbert J. Mains
Professor
Department of Chemistry

Oklahoma State University
Stillwater, OK 74078

AN *AB INITIO* STUDY

OF

LEWIS ADDUCTS OF POTENTIAL IMPORTANCE

IN

ROOM TEMPERATURE CHLOROALUMINATE MOLTEN SALTS

Gilbert J. Mains
Professor
Department of Chemistry
Oklahoma State University

Abstract

Quantum chemical methods have been employed to calculate the relative Lewis acidities for the dominant species in molten chloroaluminate at room temperature. The order of Lewis acidities were $Al_2Cl_7^- < Al_2Cl_6 < AlCl_3 < Na^+$ as determined using reactions with Cl^- as the reference Lewis base. This order was also obtained when $AlCl_4^-$ was employed as the reference Lewis base. It is shown that Cl^- is a better Lewis base than $AlCl_4^-$. Structures and electron density surfaces are given for $AlCl_3$, $AlCl_4^-$, Al_2Cl_6, and $Al_2Cl_7^-$.

AN *AB INITIO* STUDY

OF

LEWIS ADDUCTS OF POTENTIAL IMPORTANCE

IN

ROOM TEMPERATURE CHLOROALUMINATE MOLTEN SALTS

Gilbert J. Mains

INTRODUCTION

The search for batteries which exhibit a high energy is world wide,[1,2,3] and is of special interest to the U.S. Air Force where weight reduction permits the payload of electronic systems, armament, and weaponry to be increased in both manned aircraft and missiles. The Air Force has funded research, both in-house[4] and externally,[5,6] in this area for over a decade. This search focuses on a suitable solvent for use in the battery, since water based electrochemical cells must function in a very small electrochemical window. Most of the recent research has focused on the application of room temperature melts formed by the mixtures of solid aluminum chloride and organic quaternary salts, commonly 1-methyl-3-ethylimidazolium chloride [abbreviated $(MEI^+)Cl^-$]. The ion, MEI^+,
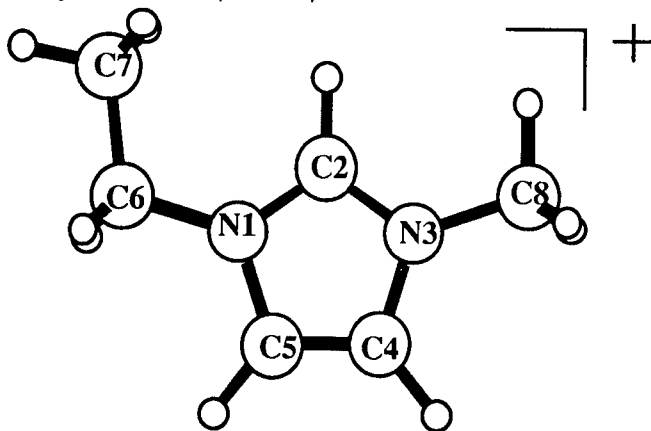
is aromatic and quite stable to both oxidation and reduction (electrochemical window circa 3.5 V). However, aluminum chloride compounds are very hydroscopic making handling and purification pose experimental problems. Important contributions by the F. J. Seiler Research Laboratory at the U. S. Air Force Academy have overcome many of the difficulties associated with aluminum

chloride chemistry.

Aluminum chloride is a white crystalline solid which melts at 193 °C at 1700 mm Hg into a molecular liquid, Al_2Cl_6, with low electrical conductivity. Room temperature addition of $(MEI)^+Cl^-$ results in a clear liquid melt, the properties of which depend upon the ratio of $AlCl_3$ to $(MEI)^+Cl^-$. Regardless of the ratio, the room temperature melt is an excellent conductor of electricity and is mostly ionic. If the ratio is exactly one, the species present are $(MEI)^+$ and $AlCl_4^-$. If the ratio is greater than one ($AlCl_3$ in excess), the mixture is termed <u>acidic</u>. Since there is then insufficient chloride ion to form $AlCl_4^-$ exclusively, the excess $AlCl_3$ shares a chloride ion forming $Al_2Cl_7^-$, a Lewis acid which can readily surrender $AlCl_3$. The cation is exclusively $(MEI)^+$ in the absence of impurities. If the ratio is less than one, the mixture is termed <u>basic</u>. Since there is insufficient $AlCl_3$ to form $AlCl_4^-$, excess chloride ion, Cl^-, a Lewis base, is also present with $(MEI)^+$. The equilibrium constants relating the species have been established.[7]

$$(MEI)^+Cl^- + (1/2)\ Al_2Cl_6 \longrightarrow (MEI)^+ + AlCl_4^- \qquad K_1 = 10^{19}$$

$$AlCl_4^- + (1/2)\ Al_2Cl_6 \longrightarrow Al_2Cl_7^- \qquad K_2 = 10^3$$
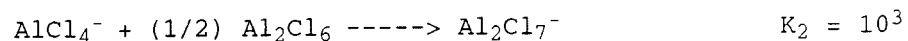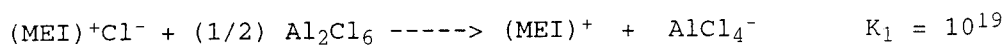
These can be combined to yield a third equilibrium as follows:

$$2\ AlCl_4^- \longrightarrow Cl^- + Al_2Cl_7^- \qquad K_3 = K_2/K_1 = 10^{-16}$$

Thus in neutral melt, the mole fractions of Cl^- and $Al_2Cl_7^-$ are quite small. The application of these melts for use as solvents in batteries is considerably complicated by changes in the chemical species as reactions occur that shift the equilibria. In an important breakthrough, this problem was solved by Wilkes et al.[7], who showed that the addition of NaCl buffered the system so that the only anions present were $AlCl_4^-$ and Cl^-. As expected, long range coulombic forces dominate the interactions between melt species. However, there is evidence for a kind of "H-bond" between the Lewis bases, Cl^- and $AlCl_4^-$, and hydrogens attached directly to the imidazolium ring.[8] It is clear that the Lewis acid strengths of Na^+, $AlCl_3$, Al_2Cl_6 and $Al_2Cl_7^-$ and the Lewis base strengths of Cl^- and $AlCl_4^-$ are of paramount importance in understanding these systems. These are questions which computational chemistry can address and are reported herein.

COMPUTATIONAL CHEMISTRY

Quantum chemical calculations have made enormous contributions to chemistry since Prof. John Pople developed the *ab initio* Gaussian series of

computer programs and shared them with the scientific community.[9] Prior to Gaussian 70, quantum chemists did not share their programs and only a few calculations, originating where the programs were developed, were reported. Wide dissemination of the *ab initio* programs resulted in an explosion of computational chemistry and has led to significant progress in many research areas. "*Ab initio*" means only the fundamental properties of atoms, e.g. nuclear charge and electron charge, were used in computing the molecular wave function. Pople has shown that it is possible to predict equilibrium structures of molecules with accuracies approaching the best experimental values of bond lengths and angles. Bond energies and enthalpies of reaction can be predicted to "chemical accuracy", circa two kcal/mol.[10] It is difficult to overestimate the impact that Gaussian 70 and its successors have had on chemistry. Despite the fact that *ab initio* programs require enormous amounts of computer time, the development of large high-speed computers permits calculations on molecules which have exceeded quantum chemists' dreams only a few years ago, e.g. clusters of one hundred carbon atoms (600 electrons) can be used to simulate diamond. Prior to the *ab initio* programs, Pople and others had developed semi-empirical programs which were parameterized and, while much, much faster in execution than the *ab initio* programs, were sometimes less reliable. An important family of semi-empirical programs were developed by Dewar and his colleagues that were both fast and capable of handling large molecules; the most popular semi-empirical program is the MOPAC series developed by J.J.P.Stewart.[11] We have employed both *ab initio* methods (Gaussian 88 and Gaussian 90) and semi-empirical methods (MOPAC6 and Extended Huckel) in the study reported here. In the *ab initio* studies the structures were optimized by using the 6-31G* basis set and correlation included at the MP2 level and, where possible, to the MP4(SDTQ) level. In the MOPAC6 semi-empirical studies the PM3 parametrization[11] was employed exclusively. The electron density plots, i.e. surfaces at which the electron density is 0.010 electrons/Å^3, were computed using STO-6G basis set resident in the Personal Cache Innovator Plus computer program[12] and using the 6-31G* *ab initio* basis set. The former (STO-6G) surfaces were Extended Huckel semi-empirical calculations and were performed at the geometries obtained by *ab initio* Hartree-Fock optimizations using the 6-31G* basis set. As is common

9-5

with semi-empirical calculations, only the valence shell densities were computed, whereas the *ab initio* computations calculates the all electron densities.

RESULTS

The structures for the aluminum compounds are presented in Figure 1. Except for $Al_2Cl_7^-$, the structures are well known and will not be discussed in detail here. We have discussed these in a recent paper[13] where it was shown that the dissociation energies of halogenated dialanes were readily correlated with Lewis acid/base properties of the constituent halogenated alanes. The utility of describing interactions in such dialanes, for example, Al_2Cl_6, as 2-electron 3-center bonds was questioned. See, also, McKee et al[14] in this regard. The structure of $Al_2Cl_7^-$ was first computed by Davis et al[15] using MOPAC, subsequently confirmed by Curtiss[16] at the HF/3-21G level, and by Bock et al.[17] at the HF/6-31G* level. The Extended Huckel and *ab initio* electron density surfaces, calculated for the atom configurations in Figure 1, are presented in Figure 2 and have not been reported previously. The $AlCl_3$ surfaces clearly depict the absence of electron density in the aluminum *p* orbital normal to the plane of the molecule. This orbital provides the driving force for most of the aluminum halide chemistry. Note that the semi-empirical computation finds no electron density on the aluminum atom nor any electron density shared between the aluminum atoms and the chlorine atoms, suggesting the structure is ionic. Indeed the bonds are very ionic but there is covalent electron density in the Al-Cl bond as can be seen by examining the HF/6-31G* surface. The shading of the surface is a measure of the gradient of the electron density normal to the surface at any point and, since it is not easily distinguished in black and white renditions, will not be discussed for any of the surfaces (the shading is omitted for the *ab initio* electron density surfaces). Observe that the crowding experienced in the sp^3 hybridization in $AlCl_4^-$ causes overlap between the 0.010 electrons/$Å^3$ chlorine surfaces in both the semi-empirical and *ab initio* calculations. The equivalence of t atom is readily seen from the identical gradients. This overlap is evide ls in Al_2Cl_6 where sp^3 hybridization also describes the coordination a nd e aluminum atom. However, although not obvious from the surfaces presented here, there is less electron density between the bridging chlorine atoms and the aluminum atoms that between the terminal chlorine atoms and the aluminum

atoms. However, observe that in $Al_2Cl_7^-$ the $AlCl_3$ moieties are more nearly planar and the overlap between the chorine atoms surfaces is less. We have reported previously[18] that the strength of a Lewis Acid/Base interaction in aluminum adduct systems is measured by the deviation of the $AlCl_3$ moiety from planar. Jansien[19] made a similar observation on related adducts. Now that computer programs are in hand which can graphically show the electron density contours, we plan a more quantitative study of the electron densities between the terminal and bridging chlorine atoms in both Al_2Cl_6 and $Al_2Cl_7^-$.

In order to explore the relative acid strengths of Na^+, $AlCl_3$, Al_2Cl_6 and $Al_2Cl_7^-$ we consider the energy changes for their reactions with a common base, Cl^-. Thus, we calculate the energy changes for the following reactions:

$$Na^+ + Cl^- -----> NaCl \qquad (1)$$
$$AlCl_3 + Cl^- -----> AlCl_4^- \qquad (2)$$
$$0.5\ Al_2Cl_6 + Cl^- -----> AlCl_4 \qquad (3)$$
$$Al_2Cl_7^- + Cl^- -----> 2\ AlCl_4^- \qquad (4)$$
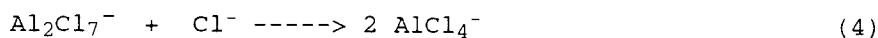
The results are presented in Table I. The order of increasing Lewis acidity is $Al_2Cl_7^- < Al_2Cl_6 < AlCl_3 < Na^+$. This order is not at all surprising. The weakest Lewis acid is $Al_2Cl_7^-$, which is structurally a loose association of two $AlCl_3$ molecules with a Cl^-. In a great excess of $AlCl_3$ one might anticipate the association of three $AlCl_3$ molecules with a single chloride ion, i.e. Cl^- $(AlCl_3)_3$, and such a structure was found using MOPAC.[20] In the presence of a stronger Lewis base than Cl, say F^-, one expects that $Al_2Cl_7^-$ would surrender one of the $AlCl_3$ immediately and the remaining $AlCl_3\cdots Cl^-$ would form $AlCl_4^-$ via reaction represented by equation (2). We have searched exhaustively and unsuccessfully for a transition state for this reaction, and conclude that the addition of Cl^- to $AlCl_3$ must occur with a very low energy barrier. Since the adduct $HCl\cdots Al\ Cl_3$ is quantum mechanically stable[21] at this same level of computation (HF/6-31G*), the absence of a barrier is interesting. We also note that an optimization that starts with a hydrogen ion replacing a sodium in $Na^+AlCl_4^-$ results in the formation of the $HCl\cdots AlCl_3$ adduct, i.e., the H and the nearest chlorine atom are pushed out to 2.97 Å above the aluminum atom as the residual $AlCl_3$ becomes more nearly planar. There is considerable interest in hydrogen speciation in chloroaluminate melts[5], where HCl is proposed in acidic melts and HCl_2^- in basic melts. The reaction

9-7

$HCl + Al_2Cl_7^- ----> AlCl_4^- + HCl \cdots AlCl_3$ is endothermic by 24.29 kcal/mol at the MP2/6-31G* level; this suggests that $HCl \cdots AlCl_3$ adduct is not important in acidic melts.

The order of Al_2Cl_6 and $AlCl_3$ acidity should be independent of the Lewis base chosen. Hence, we may check the above conclusions by using the other common base in these systems, $AlCl_4^-$. The reactions to be considered are represented as follows:

$$Na^+ + AlCl_4^- -----> NaAlCl_4 \tag{5}$$

$$AlCl_3 + AlCl_4^- -----> Al_2Cl_7^- \tag{6}$$

$$0.5\ Al_2Cl_6 + AlCl_4^- -----> Al_2Cl_7^- \tag{7}$$
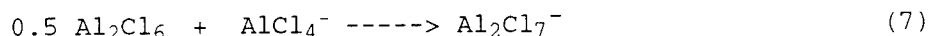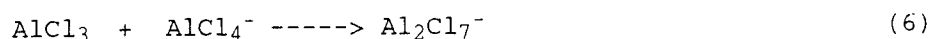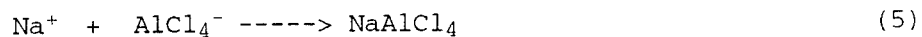
The results are presented in Table II. The order of acidity is, as expected, the same. The relative Lewis basicity of Cl^- and $AlCl_4^-$ can be inferred from the exothermicities of their reactions with a common acid, e.g. $AlCl_3$, the former, Cl^-, being the much stronger base. In systems which are buffered with NaCl, the excess Cl^- dominates the basicity and one cannot expect the acidic components, i.e. $AlCl_3$, Al_2Cl_6, or $Al_2Cl_7^-$, to be present.

In addition to the calculations reported here, we have computed most of the structures and energies for equivalent reactions of $EtAlCl_2$, ethylaluminum dichloride, used as an HCl "getter" in these chloroaluminate melts.[21] (Addition of $EtAlCl_2$ to a chloroaluminate melt containing HCl results in a reaction which produces $AlCl_3$ and ethane gas.) The preliminary data suggest that the substitution of an ethyl group for a chlorine on $AlCl_3$ does not substantially alter the stability of the dimers nor the acid properties of $EtAlCl_2$, $EtAl_2Cl_5$, $(EtAlCl_2)_2$, or $EtAl_2Cl_6^-$. Two additional publications, not discussed in detail here, were performed partially under the aegis of this RIP grant. One publication, noted earlier,[13] dealt with the structures and stabilities of halogenated dialanes. The other publication dealt with the dimerization of CH_3AlCl_2 and related compounds.[22]

Table I

RELATIVE LEWIS ACIDITY CHEMICAL REACTION	MOPAC[a] ΔH_{rx}	Ab Initio HF /6-31G*	MP2 /6-31G*	ΔE_{rx}[a] MP4SDTQ /6-31G*
$Na^+ + Cl^- \longrightarrow NaCl$	- 108.23	- 134.50	- 39.92	- 140.32
$AlCl_3 + Cl^- \longrightarrow AlCl_4^-$	- 85.52	- 80.56	- 85.42	- 84.94
$0.5\ Al_2Cl_6 + Cl^- \longrightarrow AlCl_4^-$	- 52.00	- 71.45	- 71.42	- 71.24
$Al_2Cl_7^- + Cl^- \longrightarrow 2\ AlCl_4^-$	- 37.90	- 54.90	- 54.17	nc

a. All energies in kcal/mol.

Table II

RELATIVE LEWIS ACIDITY CHEMICAL REACTION	MOPAC[a] ΔH_{rx}	Ab Initio HF /6-31G*	MP2 /6-31G*	ΔE_{rx}[a] MP4SDTQ /6-31G*
$Na^+ + AlCl_4^- \longrightarrow NaAlCl_4$	- 80.55	- 102.28	- 110.17	- 108.53
$AlCl_3 + AlCl_4^- \longrightarrow Al_2Cl_7^-$	- 47.62	- 25.66	- 31.25	nc
$0.5\ Al_2Cl_6 + AlCl_4^- \longrightarrow Al_2Cl_7^-$	- 14.09	- 16.54	- 17.25	nc

a. All energies in kcal/mol.

REFERENCES

1. Bard, A. J. (Ed), *Encyclopedia of Electrochemistry of the Elements*, Marcel
   Dekker, N.Y. (1976).

2. Volkov, S. V., *Chem. Soc. Rev.* **1990**, *19*, 21.

3. Gale, R. J.; Blomgren, G.; Kojima, H. (Eds), *Proc. of Eighth International
   Symposium on Molten Salts,* **1992**, Vol. 92-16, The Electrochemical
   Society, Inc., Pennington, N.J.

4. Wilkes, J. S.; Zaworotko, M. J., *J. Chem. Soc., Chem. Commun.,* **1992**, 963,
   and earlier publications by J.S. Wilkes.

5. Trulov, P.C.; Osteryoung, R. A., *Inorg. Chem.* **1992**, *31*, 3980, and earlier
   publications by R.A. Osteryoung.

6. Carlin, R. T.; Crawford, W.; Bersch, M., *J. Electrochem. Soc.* **1992**, *139*,
   2720, and earlier publications by R.T.Carlin.

7. Stuff, J. R.; Lander, Jr., S. W.; Rovang, J. W.; Wilkes, J. S., *J.
   Electrochem. Soc.* **1990**, *137*, 3865.

8. Carper, W. R.; Pflug, J. L.; Elias, A. M.; Wilkes, J. S., *J. Phys.Chem.*
   1992, *96,* 3828.

9. Gaussian 70, was released to the scientific community in 1970, and has been
   followed with Gaussian 76, Gaussian 80, Gaussian 86, Gaussian 88,
   Gaussian 90 and most recently, Gaussian 92.

10. See Radom, L., *J. Mass Spectrom. Ion Processes* **1992**, *118/119*, 339 for a
    recent review and applications to gas phase ion chemistry.

11. Stewart, J. J. P., *J. Computational Chem.* **1989**, *10*, 221.

12. CACHe Scientific, P.O. Box 500, Mail Station 13-400, Beaverton, Oregon

13. Bock, C.W.; Trachtman, M.; Mains, G. J., *J. Phys. Chem.* **1993** (scheduled
    for February issue.)

14. Cioslowski, J.; McKee, M. L., *J. Phys. Chem.* **1992**, *96*, 9264.

15. Davis, L. P., Dymek, C. J.; Stewart, J. J. P., Clark, H.P.; Lauderdale, W.
    J., *J. Am. Chem. Soc.* **1985**, *107*, 5041.

16. Curtiss, L. P., in *Proc. International Symposium on Molten   'ts,*
    Mamantov, G.;Mamnatov, C.; Hussey, C. Saboungi, M-L., Bla   , N.
    Wilkes, J.S.(eds), Vol. 87-7, The Electrochemical Society,   nc.,
    Pennington, N.J.

17. Bock, C.; Trachtman, M.; Mains, G. J. **1992** *unpublished results.*

18. Wilson, M.; Coolidge, M. B.; Mains, G. J., *J. Phys.Chem.* **1992**, *96,* 4851.

19. Jansien, P. G., *J. Phys.Chem.* **1992**, *96,* 9273.

20. Mains, G. J. **1992**, *unpublished results.*

21. Zawodzinski, Jr., T. A.; Carlin, R. T.; Osteryoung, R. A., *Anal. Chem.***1987**, *59,* 2639.

22. Mains, G. J.; Bock, C. W.; Trachtman, M.; Mastryukov, V., *J. Molecular Struct.(Theochem)*,**1992**, *247,* 277.
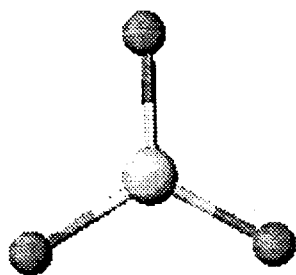
AlCl₃
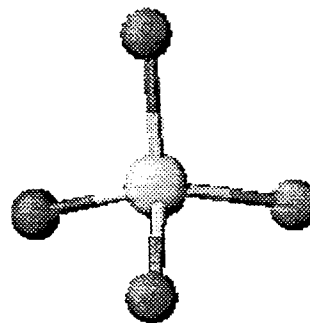
AlCl₄⁻
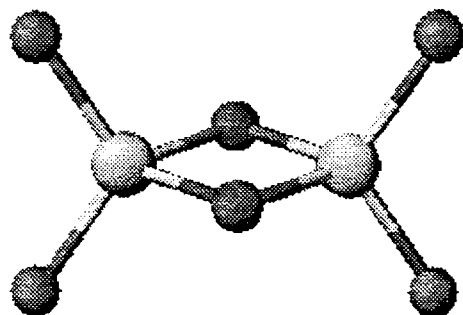
Al₂Cl₆
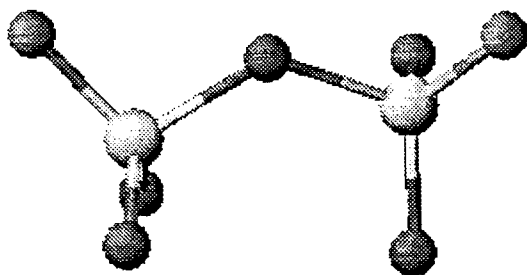
Al₂Cl₇⁻

Figure 1

Ball & Stick Representations
of AlCl₃, AlCl₄⁻, Al₂Cl₆ and
Al₂Cl₇⁻.
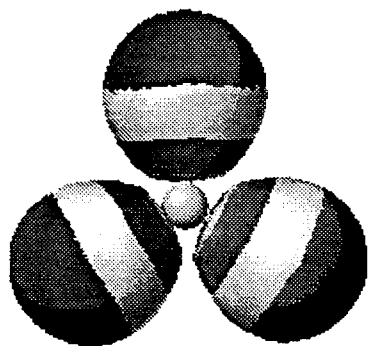
AlCl$_3$ Valence Shell Density
0.01 e$^-$/ Å^3
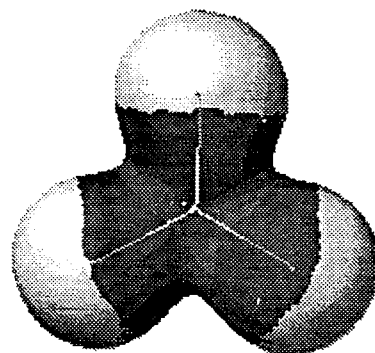
AlCl$_3$ HF/6-31G* *Ab Initio*
Density @ 0.01 e$^-$/ Å^3
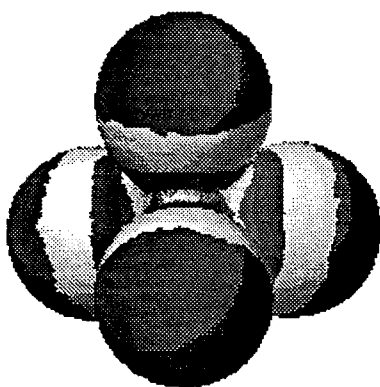
AlCl$_4^{-1}$ Valence Shell Density
0.01 e$^-$/ Å^3
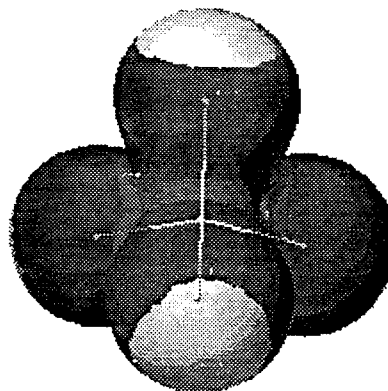
AlCl$_4^{-1}$ HF/6-31G* *Ab Initio*
Density @ 0.01 e$^-$/ Å^3

Figure 2

Extended Huckel and *Ab Initio*
Electron Densities for AlCl$_3$,

AlCl$_4^-$, Al$_2$Cl$_6$, and Al$_2$Cl$_7^-$.
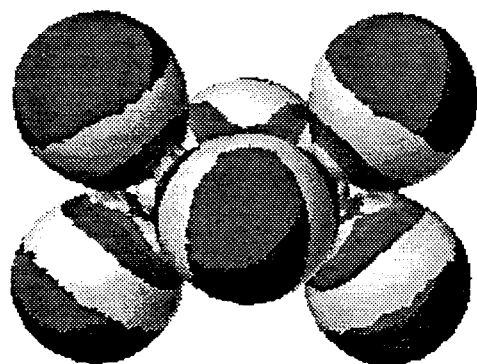
Al$_2$Cl$_6$ Valence Shell Density
0.01 e$^-$/ Å^3
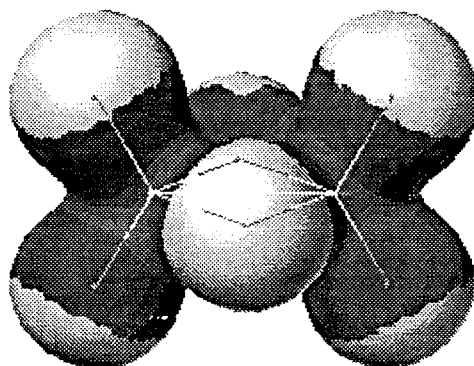
Al$_2$Cl$_6$ HF/6-31G* *Ab Initio*
Density @ 0.01 e$^-$/ Å^3
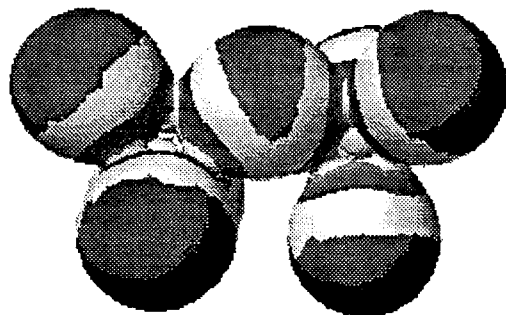
Al$_2$Cl$_7^-$ Valence Shell Density
0.01 e$^-$/ Å^3
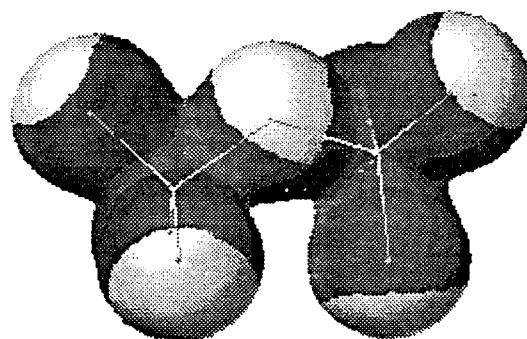
Al$_2$Cl$_7^-$ HF/6-31G* *Ab Initio*
Density @ 0.01 e$^-$/ Å^3

Figure 2   continued

Extended Huckel and *Ab Initio*
Electron Densities for AlCl$_3$,
AlCl$_4^-$, Al$_2$Cl$_6$, and Al$_2$Cl$_7^-$.

WILFORD HALL MEDICAL CENTER

FINAL REPORT
TO
AIR FORCE OFFICE OF SCIENTIFIC RESEARCH

RHEOLOGICAL, BIOCHEMICAL AND BIOPHYSICAL STUDIES OF BLOOD AT ELEVATED TEMPERATURES.

Prepared by: W. Drost-Hansen
                           Mag. scient. (Ph.D.)

Academic Rank: Professor

Department and University: Lab. for Water Research
                           Department of Chemistry
                           University of Miami
                           Coral Gables, FL. 33124

AIR FORCE LAB.
FOCAL POINT: COL. J.H. CISSIK, (Ph.D.)
                           CID/WHMC, LACKLAND
                           AFB, TX.

Period covered: Dec. 15, 1991 - Dec. 15, 1992

Date: April 9, 1993.

ABSTRACT

RHEOLOGICAL, BIOCHEMICAL AND BIOPHYSICAL STUDIES OF BLOOD AT ELEVATED TEMPERATURES.

W. Drost-Hansen
Laboratory for Water Research
Department of Chemistry, University of Miami
Coral Gables, FL, 33124.

In spite of over 70 years of use in clinical diagnosis, no theory exists which adequately describes the Erythrocyte Sedimentation Rate (ESR.) In an attempt to understand the dynamics of the ESR we have over the past four years studied a variety of parameters related to the ESR, including the rheology of blood plasma and model biopolymers (effects of temperature and shear-rate), red cell volumes, rate of diffusion of solutes and colloidal particles, and related physical parameters likely to play a role in the transport processes of whole blood. In the present study we have particularly studied rheological aspects of model macromolecules and bio-polymers as function of shear-rate and temperature. The main findings are: I) *large polymers in aqueous solution are "vicinal hydrated"* -- i.e., these polymers have hydration "shells" of interfacially modified water of the type expected at most (or all) solid surfaces. Small solutes in water are not similarly hydrated; hence it appears that *vicinal hydration of macromolecules occurs only for molecules larger than a certain critical minimum size, about 1 kDa.* Furthermore, we find that II) *the vicinal hydration of large macromolecules is strongly shear-rate dependent.* III) Once the vicinal structures have been disrupted by shear, *the original hydration structures reform only slowly;* this is in agreement with earlier findings by the Author and his coworkers. In all cases studied, IV) the *viscosity of the polymer solutions* (with MW above the critical range) *exhibit distinct* (and often dramatic) *changes as a function of temperature at the thermal transition temperatures (T_k) of vicinal water.* Finally, V) measurements by a Photon Correlation Spectrometric method of the *apparent particle diameters of solid, submicroscopic Polystyrene spheres yield values which decrease quite abruptly near 30°- 32 °C.* It appears that this effect is most pronounced in stagnant suspensions, and that stirring such suspensions remove the abrupt change at T_k in the apparent diameters; this view is consistent with the observation mentioned above that the vicinal hydration structures are very labil. It is conceivable that similar considerations may apply to erythrocytes in whole blood.

FILB: APRBP931

INTRODUCTION

The famous biochemist/biologist Albert Szent-Gyorgyi repeatedly stressed that water is the "mother and matrix" of life. It is indeed hard to overemphasize the "aqueous connection": most living organisms contain, on the average, about 70 % water but while this may seem high the truly aqueous nature of life becomes much more readily envisioned when it is realized that because of the low molecular weight of water, the mole-fraction of water in a living cell is overwhelming. Thus, in a typical assembly of eukaryotic cells, say a muscle, the number of ions and molecules (large and small) is *very* low compared to the number of water molecules. Thus, per 20 000 water molecules there are only about 100 small ions and non-electrolytes; somewhat fewer larger non-electrolytes and only 75 lipid molecules with one (or at most, two) protein molecules and one or a few other macromolecules (say polypeptides, nucleic acids, or polysaccharides.) In view of this, it seems reasonable to seek a description of *life in terms of the physical chemistry of aqueous interfacial systems.* Indeed, this is the underlying "leitmotif" for most of the work in the LABORATORY FOR WATER RESEARCH at the University of Miami.

For several decades we have investigated various aspects of the role of the aqueous phase in cell biology [a list of pertinent papers are given in the Reference Section at the end of this report.] These papers will serve to "set the stage" for the investigations to be described below. In the present report the main emphasis will be on the role of interfacial water in modeling hemorheology, both as far as the dynamics of transport processes are concerned, as well as external surface hydration effects which may affect the apparent volumes (and effective cross-sectional areas) of erythrocytes. To this discussion will be added some of the tentative conclusions reached from the results of three years of Summer Research Programs (sponsored by the AFOSR) and an integration sought between the various pieces of information obtained.

Hemodynamics is concerned with the flow of blood in the circulatory systems of those organisms which have a closed circulatory system -- from earthworms to fish, amphibians and reptiles, and from birds to mammals. In man, malfunction of the circulatory system, traceable to hemodynamics, accounts for a large fraction of all medical problems such as high blood pressure, ischaemic heart disease, peripheral arterial disease and stroke.

Hemorheology is concerned with the rheological aspects of the flow of the exceedingly complex fluid, the blood. The complexities are overwhelming; the blood is a non-homogeneous suspension of various types of living cells, all deformable and non-spherical (of different ages and in varying numbers) in an extremely complex fluid, the plasma, which is non-newtonian, containing high concentrations of both electrolytes and non-electrolytes, including a large number of different biopolymers in varying ratios, in which the number-density of the dispersed blood cells vary with shear rate. As an example of the role of hemorheology, consider the apparent correlation between blood plasma viscosity and ischaemic heart disease as recently discussed by Lowe et al., 1991. [Thrombosis and Haemostasis, 65, p. 851, abstract, 1991. also ibid., 67(5), p. 494 - 498, 1992.]

The Erythrocyte Sedimentation Rate (ESR or "sed rate") is a measure of the rate of hindred settling of red cells in whole, anti-coagulated blood. This quantity has been used empirically for about 70 years as a non-specific indicator of disease. Given the complexity of blood, indicated above, it is hardly surprising that no satisfactory theory is extant for the calculation of the ESR from first priniciples and added to the physico-chemical problems involved in calculating the rate of hindred settling (of non-spherical deformable "particles") under the conditions prev 'ing in whole blood one must add the complexity of rouleaux formation -- itself reflecting some complex, aqueous adsorption processes of biopolvmers on the red cell surface -- which dramatically affects the net obst ved sed rates.

10-4

While the ESR may seem a "subspecialty" within hemorheology (as part of the larger realm of hemodynamics) it is worth noting that ESR assumes a uniquely interesting position as bridging the gap between Chemical and Industrial Engineering on the one hand -- for instance through the processes of settling tanks in chemical industrial operations and hydrological considerations in reservoir Engineering for dams -- and the physical processes of hinderd settling as an exercise in theoretical hydrodynamics of heterogeneous dispersions on the other hand. Add to this difficult "mix" the likely role of classical, physico-chemical hydration aspects of solid surfaces in contact with an aqueous phase. Finally, as will be emphasized in the present report, to this decription must be added the unique features of "vicinal hydration" of the interface between a "solid surface" and the aqueous phase -- immensely complicating the dynamic description of the ESR.

One of the main objectives of the author's research is to elucidate the role of vicinal water in cell functioning. In the context of the AF Grant, our interest has primarily been in the role of vicinal water in the Erythrocyte Sedimentation Rate and rheological aspects of bood and aqueous solutions of biopolymers, such as plasma and serum. Independent of the AF Grant, the author has spent three summers at an AF clinical Laboratory (namely, the Clinical Investigation Directorate of Wilford Hall Medical Center at Lackland AFB) and has there had the opportunity to make a large number of ESR measurements and rheological observations. Since the results of these studies have greatly influenced the selection of topics pursued under the AF Grant to LWR it is important briefly to review these related studies as well as to mention significant results obtained from the literature.

IV. BACKGROUND.

The two main, interrelated themes of the present report are A) the dynamics of the Erythrocyte Sedimentation Rate [ESR] and B) the rheology of aq. polymer solutions and dispersions -- particularly those of biophysical interests, such as protein solutions, plasma, serum and whole blood. A vast literature exists on these subjects, yet our understanding of the transport properties in question is still incomplete and in certain aspects totally inadequate. However, the main point of the present study is not to attempt an extension of current insight by the study of further "classical" details but instead *to examine the likely role that interfacially modified water structures [the socalled vicinal water] may play in these areas.* In this respect, then, the research reported here breaks new ground and some previous "unusual results" now find natural explanations in terms of the vicinal water effects. As some readers may be unfamiliar with the current state of vicinal water research the next several Sections of this Report will attempt briefly to "set the stage" by reviewing the essence of vicinal water theory. This "diversion" is critically important in order to understand the selection of subjects chosen for AF Grant study and for the interpretation of the results we have obtained.

FILE: AFREP93H

VICINAL WATER

Notwithstanding a century of study, the structure of water has not yet been fully delineated -- and may indeed escape a rigorous description for several more decades. By the same token, our understanding of aqueous solutions also remain incomplete; thus not only do we not have adequate, quantitative theories for any but the most dilute electrolyte solutions but far less is known with certainty about solutions with multiple solutes, especially mixtures of electrolytes and non-electrolytes. Concentrated solutions - say a few molar - present additional significant problems and again mixtures of solutes in this concentration range are even less well understood. Finally, polymer behaviour in water is not only difficult because of the enormous complexity of the polymers themselves, but for lack of a detailed description of water structure our insight into the specifics of water/polymer interactions remain largely obscure (not withstanding decades of research.)

Consider now a typical living cell, say a eukaryotic cell. The most overwhelming aspect of all cells is not their vast biochemical complexity; instead, the two totally dominant factors are A) the enormous mole fraction of water compared to all other solutes (see ref. ..) and B) the gigantic interfacial area within the cell. In short, a living cell is essentially only a highly dispersed aqueous system serving as the structured medium in which the biochemical processes take place. The prevailing biochemistry, then, may not necessarily bear any resemblance to the relatively simple chemistry of the same molecular moities in a dilute, bulk solution. No wonder, then, that a study of cell functioning on the molecular level must now begin with an understanding of how interfaces in general affect the struture and properties of water (and aq. solutions.)

In the older literature (say, before 1925) - the idea that a solid surface might alter the structure of an adjacent liquid to a significant extent was quite readily appreciated -- notwithstanding the fact that the evidence provided for such structural effects was often rather weak or circumstantial. Since the mid twenties, however, the notion of "long-range ordering" in liquids near surfaces fell from favor for a variety of reasons. The Debye-Hückel theory of dilute aqueous solution of electrolytes was spectacularly successful without making any specific reference to the detailed structure of water - a fortunate circumstance as noteven on approximate, first-order theory of liquid water existed at the time of the original Debye-Hückel paper. At that time, most (but not all) studies of liquid water, for instance by x-ray diffraction, found no evidence whatever for long-range ordering in the liquid and thus it did not seem unreasonable to conclude that "water is water is water", right up to any interface, and that for many or most purposes water might be treated as a continuum dielectric fluid with no structural characteristics. As far as interfaces are concerned, the theory of Deryaguin-Landau-Verwey-Overbeek (early WW II) for colloidal systems was enormously successful without any reference to specific structural aspects of water. The idea that an interface might significantly affect the structure of the adjacent water became notably unpopular and only during the past one or two decades have serious attempts been made to re-examine the structure of interfacial water. However, at this time a considerable number of investigators would agree that there does indeed exist evidence for structural effects in water (and aq. solutions) induced by most interfaces. What is missing is a consensus opinion as how to far from the interface such structural effects may propagate into the liquid and what type of structural effects are indeed operating. Again, we are seriously hampered by not knowing the detailed structure of bulk water (and aqueous solutions.)

THE NATURE OF VICINAL WATER.

It appears that most (and possibly ALL) solid interfaces in contact with an aqueous phase create vicinal water. The properties of such interfacially modified water differ from the equilibrium and transport properties of the corresponding bulk water (and solutions) and hence it must be concluded that the structure of the vicinal water also differs from the (still unknown) structure of the bulk aqueous phases. The principal questions regarding vicinal water are: 1) to what extent do the properties differ from the bulk; 2) what is the geometric extent of the structurally modified layers; 3) how does the energetics of vicinal water differ from the bulk, and 4) what is the difference in structure between bulk and vicinal water. For detailed considerations of these and related questions the reader is referred to the writings by Etzler, Wiggins, Peschel, Low and others, as well as the studies by the present author. Below are outlined briefly some of the more unusual properties of vicinal water -- including the existence of thermal anomalies in a great variety of properties.

Etzler et al. have carefully measured the density of vicinal water in narrow pores of a silica gel. The density is distinctly lower than that of the bulk phase, -- by as much as 3 to 4 %. To compress bulk water to the same extent would require a pressure of about 750 atm. and to achieve a similar expansion of the bulk would require heating the water from about room temperature to 70 ^{o}C. The density of the vicinal water assumes its lowest value near the actual interface (or at least within a few molecular layers of the interface) and decreases (probably roughly exponentially) as a function of distance from the interface; a "decay-length" of say 30 (to 50) molecular layers may be involved (i.e. a drop of 50 % in the degree of "vicinal ordering" over distances of about 100 Angstrom = 10 nm, or 0.01 micron.) Such distances far exceed most previous estimates of the depth of structurally modified interfacial water which traditionally have been taken to be merely one to three molecular layers.

The low density of vicinal water has been used to explain an unexpected volume contraction observed when dispersions of rather inert particles settle out of an aqueous suspension. Thus we have shown by high-precision dilatometry that when suspensions of Polystyrene (PS) spheres settle, a

distinct volume contraction occurs. This observation is readily understandable if it is assumed that in the suspended state each particle is surrounded by a "vicinal hydration shell". As the particles settle, these hydration shells overlap and the modified water in the overlap-region is converted to bulk water; as the bulk water has higher density (and thus lower specific volume) a volume contraction takes place. From these volume contraction data is it possible to obtain rough estimates of the water layer thicknesses; typically values are of the order of 300 - 400 A (or about 100 molecular layers) in excellent agreement with independent estimates based on a variety of other methods. It is of interest to note that similar volume contactions were observed in a study of the settling of silica particles.

The specific heat of water is remarkably high (1.0 cal/gram ^{o}C) compared to most other liquids -- the result of its high degree of structure reflecting the extensive H-bonding. Measurements of the specific heat (c_p) of vicinal water have show that c_p is even larger than observed in the bulk, namely about 1.25 cal/gram ^{o}C or 25 % larger!! Thus it must be concluded that vicinal water is even more structured than the bulk. The fact that the specific volume of vicinal water is greater than that of the bulk, and the larger degree of structuring required to explain the enhanced specific heat suggest that vicinal water likely resembles ice (Ice-Ih) -- at least in the sense of being more open and more structured.

In connection with the increased values for c_p it is also of interest to point out that essentially identical values for c_p were obtained on water adjacent to such "unlike surfaces" as quartz, glass, activated charcoal, diamond and a zeolite. In fact, this behaviour has been confirmed in many other studies: the specific detailed chemistry of the solid interface plays only a minor role (if a role at all) in the formation of vicinal water structuring at inᴣ faces! This phenomenon has been named the "Paradoxical Effect" becaus ᴣf its unexpected nature. In this connection, however, it should be noted ᴁ of course the specific nature of the surface chemistry does indeed p a crucial role in the short-range, highly energetic interactions wᴑ.ch determines the nature and extent of the innermost ("primary") hydᴑ ᴑon structures -- i.e. the classical hydration of surfaces.

Over the past five to ten years, the evidence for vicinal water has become greatly strengthened through the studies by such investigators as Etzler, Kurihara and Kunitake, and several others. A recent example of an investigation suggesting truly long range effects of an interface on the adjacent water structure is the paper by Yanagimachi, Tamai and Masuhara Chem. Phys. letters, 201, p 115 - 119, 1993.) The authors have examined the rate of proton transfer of 1-naphthol at the sapphire/water interface by a total internal reflection fluorescence method. FIG. $\mathit{1}$ shows the rate constant as a function of the distance from the interface. A notable reduction in rate is observed over distances of the order of 100 to 200 nm - in other words 1000 to 2000 A or roughly 300 to 600 molecular diameters. Such large distances have been invoked earlier by other authors (for instance, Hühnerfuss et al.; see also Drost-Hansen, in "Biophysics of Water", F. Franks and S. Mathias, Eds., Wiley, 1982) and this range for the vicinal water is indeed consistent with our own Photon Correlation Spectroscopy data on Polystyrene sphere suspensions (see last Section of this Report.)

RATE CONSTANT OF THE PROTON TRANSFER
REACTION OF 1-NAPHTHOL IN AQUEOUS
SOLUTION AT THE WATER/SAPPHIRE INTERFACE.
DATA BY YANAGIMACHI ET AL., CHEM. PHYS. LETT.
201, p. 115 - 119, 1993. *NOTE THE LARGE DISTANCE*
FROM THE INTERFACE OVER WHICH THE REACTION
IS AFFECTED.
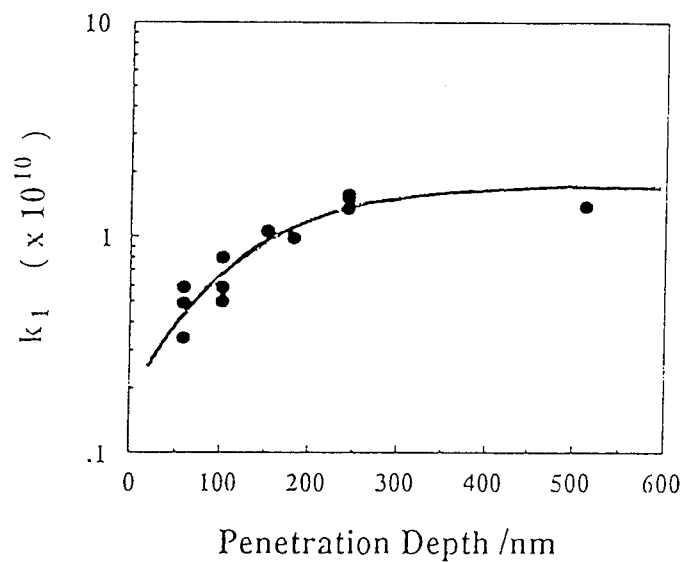
FIG. 1

THERMAL ANOMALIES.

One of the most characteristic features of vicinal water is the existence of thermal anomalies in the properties of large surface-to-volume ratio systems in which vicinal water is present. Typical examples of anomalies are more or less abrupt changes in the slope of a property [when plotted against temperature] over a rather narrow temperature range, say one (to two) Degrees. Between the melting and boiling points of water no less than four such transition ranges occur, namely around $14 - 16^o$, $29 - 32^o$, $44 - 46^o$ and $59 - 62^oC$. (The transition temperatures, T_k, are sometimes referred to as the "Drost-Hansen thermal anomaly temperatures".) While the anomalies are extremely well documented it is not at all obvious what molecular processes underlie these transitions; we have previously assumed that they represent higher-order phase transitions of the vicinal water structures but while not an unreasonable assumption we have no firm proof for this. (In fact, a recent neutron-scattering study [Davies, Dore, and Drost-Hansen, to be published, 1993] of water in porous silica gel did find that the water structure at the silica/water interface is indeed changed as expected for vicinal water, but no evidence was found for a phase transition (in any "crystallographic" sense) of this differently structured water near 30 ^oC.)

Over the years a great number of studies have been reported showing sometimes dramatic evidence for the thermal anomalies. Using an early version of a high-precision force-balance, Peschel and co-workers have measured the disjoining pressure between two highly polished quartz plates immersed in water and various dilute solutions. For pure water, for instance, the disjoining pressure as a function of temperature goes through very distinct, sharp maxima and minima (the minima occuring near T_k.) Similarly, the viscosity of the water between the plates goes through somewhat broader maxima and minima, again relating to T_k; see Fig.2 . In view of these extreme examples of temperature effects on the viscosity of vicinal water it is hardly surprising that the viscosity of a large number of aqueous polymer solutions also show dramatic temperature responses. By the same token, in fact, much of the rheology of aqueous dispersed

ARRHENIUS GRAPH: LOG(VISC.) VS. RECIPROCAL
ABSOLUTE TEMPERATURE; WATER BETWEEN QUARTZ
PLATES SEPARATED (IN ORDER TOP TO BOTTOM) 30, 50,
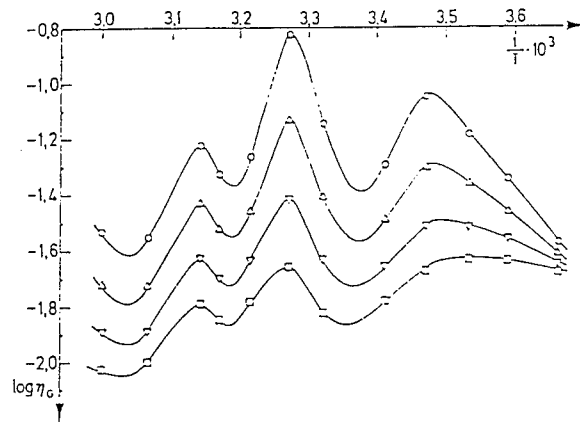70, AND 90 nm.DATA BY PESCHEL AND ADLFINGER, 1971.

FIG. 2

systems must be expected to show complicated responses to temperature; as will be discussed briefly below. Subsequent to the force-balance measurements by Peschel et al., Israelachvili has notably improved the force-balance method and the studies by Israelachvili and coworkers have revealed a wealth of information regarding the nature of the interfacially modified water. Regrettably, no detailed studies appear to have been published where this improved surface-force balance has been used for closely spaced temperature measurements as would be necessary to delineate the thermal anomalies of the vicinal water.

Among the many reported studies of thermal anomalies the results by Wiggins deserve special mentioning as the implications for cell physiology of Wiggins data are highly significant. Wiggins measured the distribution of K and Na ions (from equimolar solutions of the two kinds of salts) between the vicinal water in the pores of a silica gel and the outside, bulk solution. Her results are shown in Fig. 3 . Note first the values of the ion partitioning coefficient for K/Na: apparently the vicinal water enhances the concentration of the K ions at the expense of the Na ions. This is of course qualitatively exactly the essence of cell functioning in nearly all eukaryotic cells but achieved here without any membrane or membrane-situated, active transport "ion-pumps". Note also the sharp peaks in the partition coefficient near the thermal transition temperatures. Because of the signal importance these findings may have for cell volume regulation we have repeated Wiggins measurements (Huertado and Drost-Hansen, 1979) and confirmed, quantitatively, her findings for the K/Na ions. That similar processes may indeed play a major role in cell physiology is illustrated in Fig. 4 : instead of using silica gel Wiggins used slices of rat kidney cortex and once again measured the K/Na partitioning as a function of temperature. Note that qualitatively the results resemble those observed in Fig. 3 with the silica gel, namely sharp peaks near 15 and 30 ^oC. The obvious conclusion is that vicinal water must play a major role in the ion distribution between a cell and the surrounding fluid. For a discussion of these results see the papers by Wiggins et al., and by the present author. Independently, Etzler has demonstrated the existence of similar peaks in the distribution of Li and K ions between a silica gel and both aqueous solutions and D_2O solutions.

ION DISTRIBUTION: K^+/Na^+ FOR EQUIMOLAR
K AND Na SALTS IN THE VICINAL WATER OF
PORES IN SILICA GEL AS A FUNCTION OF THE
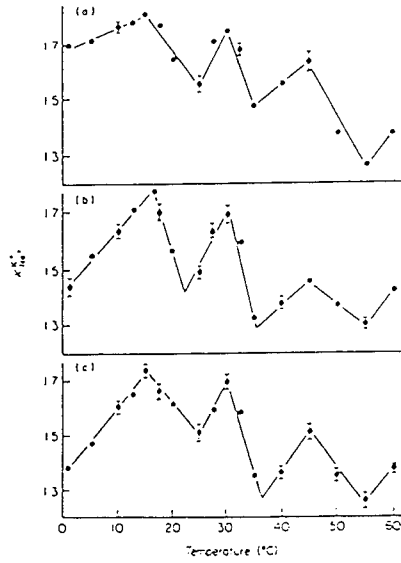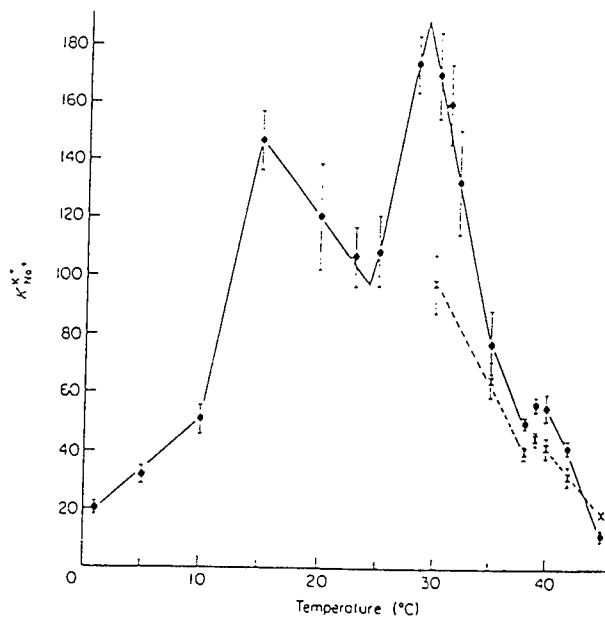TEMPERATURE. DATA BY WIGGINGS, 1975.

FIG. 3

FIG. 4

The experimental evidence for vicinal water structuring at the solid/water interface is now very substantial while the evidence for thermal anomalies in the properties of vicinal water is even more firmly established. It is obvious that the thermal anomalies reflect the presence of vicinal water and vice versa: the presence of vicinal water makes it likely that thermal anomalies exist in some properties of the system Note that the properties of *bulk* water (and bulk aqueous solutions of small solutes) do not reveal any anomalies as a function of temperature at T_k (i.e. at the temperatures of the thermal anomalies for vicinal water.) On the other hand, bulk aqueous solutions of some macromolecules, for instance many enzymes, do show anomalies at T_k, suggesting that these solutes are vicinally hydrated in (bulk) solution. In view of this it is of interest to consider if there exists a critical molecular size above which most (or all) macromolecules in solution are hydrated in the same manner that a solid surface is vicinally hydrated. We have considered this question for some time and based on an examination of data from the literature have concluded that indeed a critical molecular weight (MW) range may exist above which the molecules are vicinally hydrated. This critical MW range appear to be in the range from about 600 to a few thousand Dalton. The reader is referred to the references listed at the end of this report for more details about this conjecture; in the present study we have examined the viscosity of some polymer solutions, mostly Poly-ethylene oxides [PEO - sometimes also referred to as PEG, Polyethylene glycols] as function of MW using both capillary and variable shear-rate cone-&-plate viscometers. The question of vicinal hydration of the macromolecules in the cell is of obvious importance to all of cell biology considering the prevalence of biopolymers in cellular systems: solid-like interfaces abound in the cell, for example the endoplastic reticulum and the membrane surfaces of the cell wall and the various organelles. IF, in addition, to these vicinally hydrated "solid" surfaces the larger biopolymer molecules are also vicinally hydrated, it becomes difficult to see how one can be anywhere within a living cell without the aqueous environment being vicinal water!

FILE: AFR6P93L   3-22-93

10-18

A vast literature exists on the hydration of proteins, particularly in solution, but while these studies include extensive viscosity measurements there is a notable paucity of reports on the viscosity of macromolecules in aqueous solutions measured as a function of temperature, - especially at closely spaced temperature intervals. Interestingly, however, a number of other rheological studies have been reported on aqueous biopolymer systems at closely spaced temperatures, particularly by investigators in the food industry.

As an example, FIG. 5 shows the viscosity of a dilute actomyosin solution as a function of temperature during slow heating (1 $^{\circ}$C per min.) at a shear-rate of 1.02 sec^{-1}. Note the distinct minimum near 30 $^{\circ}$C and the very low value around 45 $^{\circ}$C. Somewhat similar results are shown in FIG. 6 and FIG. 7, respectively for the rigidity of actomyosin solutions during heating (at 1 $^{\circ}$C/min.) at low shear-rate: 0.0684 sec^{-1}, and changes in rigidity of actomyosin pastes (being heated at 1 $^{\circ}$C/min.) The anomalies at both 30 $^{\circ}$ and 45 $^{\circ}$C are pronounced.

Other rheological studies of concentrated protein/water systems from the Laboratory of Hamann and Lanier are shown in FIG. 8 where the modulus of rigidity of a minced fish paste is plotted as a function of temperature: again distinct minima near 28 $^{\circ}$- 29 $^{\circ}$C and 45 $^{\circ}$C are observed and these anomalies persist at different rates of heating as shown in FIG. 9.

Since 1991 we have measured the viscosities of a number of solutions of both model polymers and biologically important macromolecules. Thus measurements have been made with a Brookfield variable shear-rate cone-&-plate viscometer on solutions of such model polymers as Polyethylene oxide (PEO, = PEG), Polyvinyl pyrrolidone (PVP), and Dextran as well as on solutions of BSA, fibrinogen and cytochrome-c. Measurements have also been made on blood plasma and serum. In addition to varying the shear-rates in these experiments, we have also made measurements over

VISCOSITY OF ACTOMYOSIN SOLUTION.
HEATING RATE: 1 $^\circ$C/MIN. SHEAR-RATE
1.02 SEC^{-1}; CONCENTRATION: 14 MG/ML.
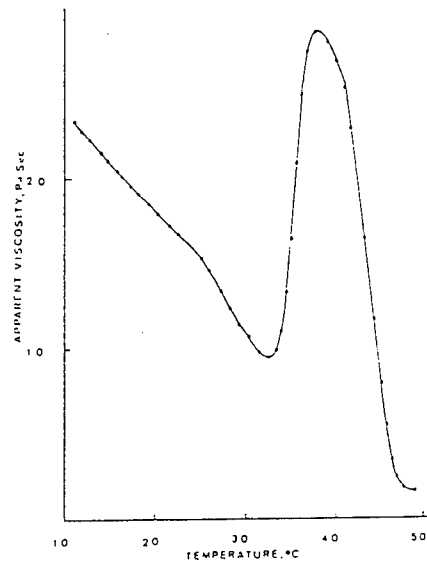DATA: WU ET AL., J.FOOD TECH., 50, 1985.

FIG. 5

VISCOSITY/RIGIDITY ACTOMYOSIN
SOLUTIONS; HEATING RATE: 1 °C/MIN.
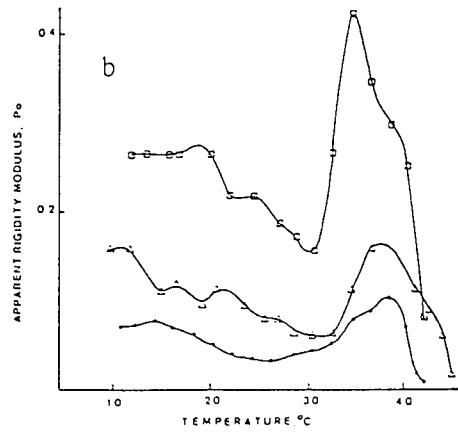SHEAR RATE: 0.0684 SEC^{-1}. DATA:
WU ET AL., (IBID)

FIG. 6

RIGIDITY OF ACTOMYOSIN PASTES
(AT DIFFERENT CONCENTRATIONS)
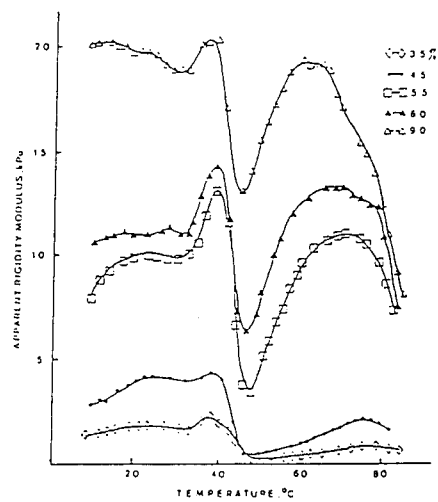DURING HEATING (!). 1 ºC/MIN. DATA:
WU ET AL., (IBID.)

FIG. 7

RIGIDITY OF MINCED FISH PASTE;
HEATING RATE: 0.5 ºC/MIN. DATA:
MONTEJANO ET. AL, JOURNAL OF
RHEOLOGY, 27 p. 557 - 579, 1983.
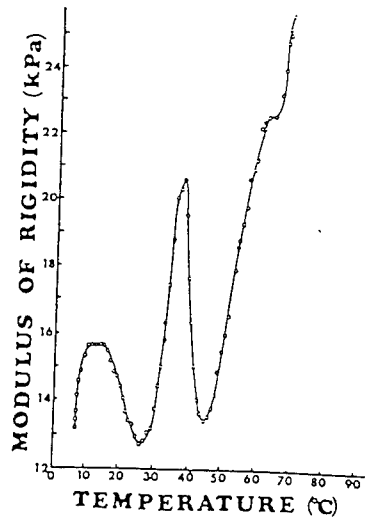
FIG. 8

RIGIDITY OF FISH PASTE FOR VARIOUS
HEATING RATES; MEASURED IN THE
ORDER: a, b, c. DATA BY MONTEJANO
ET AL., (IBID.)
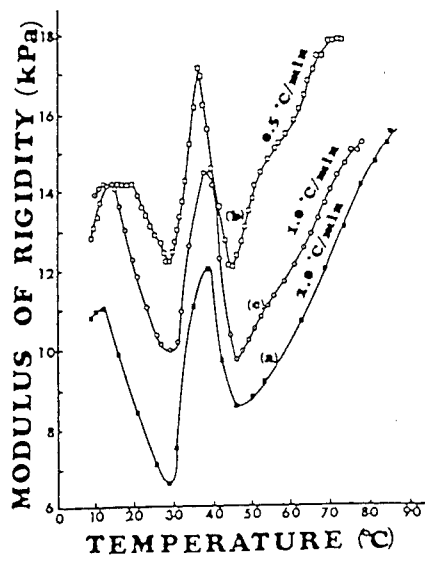
FIG. 9

rather large temperature intervals (usually from about 20 $^\circ$C and up to 50 or 60 $^\circ$C.) Nearly all measurements have been made at closely spaced temperatures: usually at two [or one] degree intervals.

The viscosities of solutions of larger polymers, including many of biochemical interest, usually depend very strongly on the temperature. Over the past three years we have collected a large amount of such data in connection with the AF SUMMER RESEARCH PROGRAMS. Meaurements have been made on aqueous solutions of a variety of model polymers (PEO, Polyvinyl pyrrolidone, Dextran, etc.) and biopolymers (such as albumin, fibrinogen, cytochrome-c and blood plasma and serum.) In all the cases, A) thermal anomalies have been found at one or more of the thermal transition temperatures for vicinal water (T_k); and B) the observed thermal anomalies are very strongly shear-rate dependent: as the shear-rate increases the degree of change in the viscosity decreases, specifically, the thermal anomalies become far less pronounced. Again this is consistent with the idea that the vicinal hydration structures are very readily disturbed or destroyed. As an example of the temperature effects on the viscosity of a polymer solution, FIG. /$\mathit{l}$shows the viscosity of a 5 % Dextran solution, (MW 82 kDa.) as a function of temperature. The anomaly near 30 $^\circ$C is pronounced. A detailed paper describing all our viscosity measurements is in preparation.

VISCOSITY OF 5 % DEXTRAN SOLUTION (MEASURED IN
BROOKFELD VISCOMETER) AS FUNCTION OF TEMPERATURE.
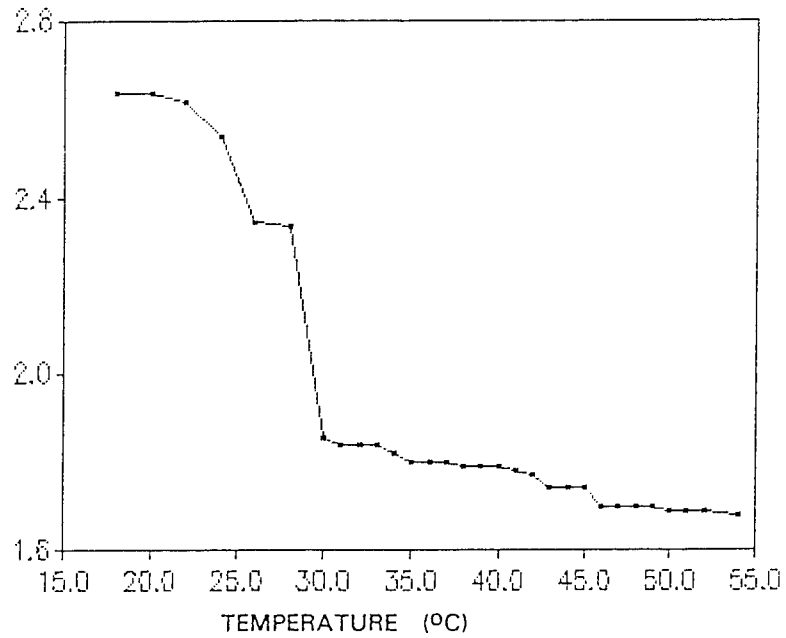SHEAR-RATE: 90 SEC^{-1}. DATA: DROST-HANSEN AND
CAMACHIO, UNPUBL. 1992.

FIG. 10

PHYSICO-CHEMICAL ASPECTS OF THE ESR: DYNAMICS OF HINDRED SETTLING.

Much of the impetus for the work performed under the AF Grant comes from a desire to understand the dynamics of hindred settling of red cells in whole anticoagulated blood. The reasons are two-fold: A) the ESR has a long, distinguished career as a cheap, "quick-and easy", non-specific indicator of disease, yet the dynamics of the process is still far from well understood, and B) settling of red cells in the body may occur at low flow rates in the venous system, and thus be an important factor in the overall hemodynamics of the patient, especially in those cases where the sed rate is notably elevated due to the presence of various diseases.

ERYTHROCYTE SEDIMENTATION RATE (ESR)

After 70 years the ESR continues to be a useful, if rather non-discriminating, indicator of disease. It is not only a cheap diagnostic test, but where more sophisticated biomedical Laboratory equipment is not available, it may still be an important aid to the physician. In other circumstances it may serve as a cheap, fast and relatively reliable monitor of the progress of a disease or as an indicator of the effectiveness of the therapies employed over a period of time.

No satisfactory theory of the ESR is presently available. This is hardly surprising as the dynamics is extremely complicated. Briefly, the initial settling rate is nearly zero (particularly in healthy subjects) until a significant degree of rouleaux formation has occurred. The rate of rouleaux formation itself must be a complicated function of the adsorption of various proteins on the red cell surface, and further depend on the rates of diffusion of the cells and the proteins involved in the binding between the cell surfaces. Only when the rouleaux formation has progressed sufficiently will these larger entities begin to settle: a process bearing very little resemblance to the simple settling af a single, spherical particle implied in the Stokes treatment of sedimentation. The process is further

complicated by the chemical and rheological complexity of the plasma, including the fact that the plasma is non-newtonian and the individual red cells are deformable. Even in those rare cases where a reasonably complete biochemical analysis is available of the proteins present in the plasma it is still difficult to predict the viscosity of the plasma with any degree of certainty.

Not withstanding the obvious shortcomings of the Stokes treatment of sedimentation when applied to whole blood, the "Stokesian approach" underlies all current theories of the ESR. It is important to point out that even the theory of hindred settling of perfect, non-interacting spherical particles in low concentration in newtonian liquids, is approximate (and extremely difficult mathematically) and does certainly not apply to concentrations corresponding to normal hematocrit values, nor to the less-than-rigid, totally non-spherical red cells or the rouleaux aggregates of red cells. On the other hand, it is intuitively reasonable that the viscosity of the plasma -- or of the whole blood itself -- must play a role, as must the "effective cross-sectional" area of the sedimenting entities. It is indeed for these reasons that much of our work has been concerned with viscosity measurements of protein solutions (and other polymers and biopolymers) and with the determination of the sizes of the (individual) red cells (as well as white cells and platelets.)

FILE: AF REP93G

The dynamics of transport processes in blood must depend on a variety of variables; in this and our earlier studies we have, somewhat arbitrarily, chosen to investigate the following parameters: the viscosity of the plasma; the surface hydration of the erythrocytes (in part modeled by Polystyrene spheres), and the volumes of the blood cells (red cells, white cells and platelets.) As will become apparent in the following sections, we are particularly interested in the effects of the hydration of macromolecules on the overall rheological properties. However, our primary interest is not in the "classical" aspects of polymer hydration [such as the first layer of water of hydration, frequently associated with the hydration of surface charges or surface dipoles.] Instead, we have proposed (Etzler & Drost-Hansen, 1983) that macomolecules in aqueous solution (at least those with a Molecular Weight, MW, larger than about 1000 Dalton) are VICINALLY hydrated, -- akin to the vicinal hydration of solid surfaces (please see the list of General Papers in the Reference Section.)

A ubiquitous aspect of vicinal hydration is the occurrence of thermal anomalies in the temperature dependence of many or most parameters. Thus, anomalies - such as more or less abrupt changes in the temperature coefficient - over rather small temperature intervals [say one to two degrees] are frequently seen. The temperatures of the anomalies (the "DROST-HANSEN THERMAL ANOMALY TEMPERATURES"), T_k, are near 15, 30, 45 and 60 $^\circ$C. Conversely, the occurrence of the these thermal anomalies strongly suggest the presence of vicinal water --- a point which is of crucial importance for the discussion which follows. Again the reader is referred to the list of General Papers.

EXPERIMENTAL. PART A: VISCOSITY MEASUREMENTS.

To elucidate the nature of macromolecular hydration in aqueous solutions - and its likely role in determining plasma viscosities - measurements were made on a number of polymer solutes as functions of concentration, temperature, molecular weight (MW) and shear rates. Most of the measurements were made on polyethylene oxide (PEO) polymers (= polyethylene glycols, PEG) with MWs ranging from about 300 to 300 000 Dalton.

As mentioned briefly in the Introduction, our preliminary studies have suggested that a distinct change in the nature of the hydration may occur for macromolecular solutes in water in the MW-range of about 1000 Dalton. To investigate this possibility for PEO, measurements were made on various PEO polymers covering the suggested critical MW-range at various temperatures (in some cases only two temperatures, - see below) in order to obtain the apparent energy of activation for the flow process ($\Delta E^{\neq}$) It was assumed that the flow of the PEO solutions were essentially newtonian, -- or, at least, that the non-newtonian effects would only slightly affect the <u>difference</u> in flow times at two relatively closely spaced temperatures (say, usually only two to six degrees apart.)

Unless otherwise stated, the meaurements discussed in this Part of the report were made with capillary viscometers of the Cannon-Fenske or Ubbelohde type with the following specifications:
Viscometer A size 150, serial # I795
                B size 200, serial # A284
                C size 100   # O 364
At each temperature at least three determinations were made with each viscometer. RSD were calculated and usually found to be 0.5 % or les

The viscosity measurements were all made in a constant temperature water bath with heavy external insulation (including the top surface of the bath) through which was cut an opening for use as a viewing port. Temperatures were generally constant throughout each run to within $+/-$ 0.01 °C (or better.)

Materials: the PEO samples were obtained from the Aldrich Company (except for the 14 100 Dalton sample from American Polymer Standards, Corp). The polymers were used as received without any purification or fractionation. The MW estimates listed are those provided by the Distributor. All solutions were prepared by weight.

To utilize the observed flow times (measured to within 0.01 sec.) for the calculation of relative viscosities, density measurements were made on all solutions prepared by simple pycnometry, using a Gay-Lussac type pycnometer; the samples were equilibrated in a separate water bath at various temperatures covering the range of temperatures used for the viscosity measurements. In general the estimated precision on the density meaurements is $+/-$ 0.0001 g/ml.

No surface tension or kinetic energy end-effect corrections were applied to the viscosity data as the primary use of these data were for comparative purposes on systems differing only slightly in the flow parameters; any corrections were estimated to be minimal.

FILE: AFREP93C

The two main features of vicinal hydration examined in this study are:

a)   the existence of thermal anomalies in solution viscosities at the vicinal water thermal transition temperatures, T_k, [the socalled "Drost-Hansen thermal anomaly temperatures"], and

b)   the possibility that a critical macromolecular size exists above which aqueous polymers are vicinally hydrated.

Once again the reader is reminded that our interest is not primarily in the "classical" type of primary polymer hydration but rather in the far more subtle type of vicinal hydration which is readily observed near most [or all] water/solid interfaces.

Fig. //__ shows the temperature coefficient of the flow times for a   5.0 % aq. solution of PEO, MW = 10 000 Dalton. The ordinate is the *change in flow time per two degree (^oC)*; the abscissa is the temperature. It is obvious that a change in slope occurs at 31 ($^+/_-$ 1) ^oC. As the densities of the solutions generally have been found to change in a perfectly smooth manner with temperature, the change in slope seen in Fig. //__ must be due to a change in the energy of activation for the viscous flow of this solution. The difference in the slopes below and above the transition temperature corresponds to a difference of 257 cal/mol in the energy of activation, or a change of 5.6 % (from $\Delta E^{\neq}$ = 4714 cal/mole to 4457 cal/mole.)
A comparison with the flow properties of pure water is shown in the table below;

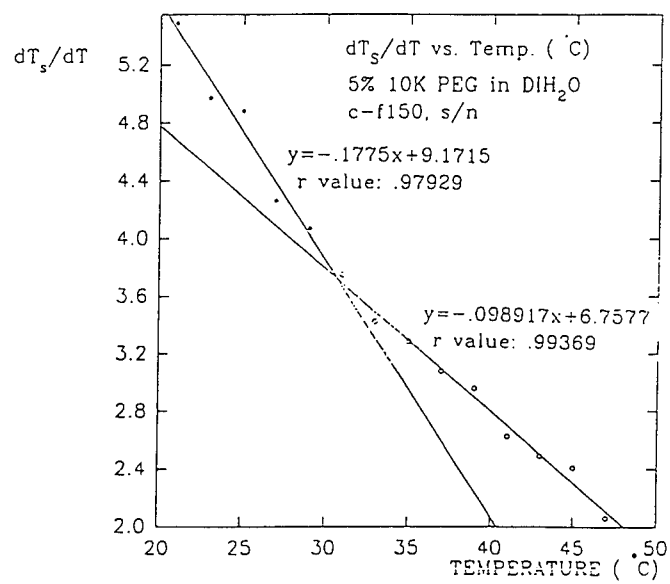| T_{av} (^oC)	25	38.5	Ratio [$25^o/38.5^o$]
$\Delta E^{\neq}_{water}$ (CAL/MOLE)	3700	3560	1.039
$\Delta E^{\neq}_{polym.}$ (CAL/MOLE)	4714	4457	1.058
Ratio [polym/water]	1.274	1.228	1.037

FIG. 11

As discussed above, it has been proposed (Etzler and Drost-Hansen, 1983) that macromolecules in aqueous solutions are vicinally hydrated - similar to the vicinal hydration of solid surfaces - but only if sufficiently large! The critical size appears to be around 1000 Dalton. This idea was suggested on the basis of a variety of measurements reported in the literature, such a the intrinsic viscosity of PEO as a function of MW, and the diffusion coefficient of some thirty solutes (Stein and Nir, 19) plotted as a function of MW. More recent examples of dramatic changes in solute properties have been reported by [Japanese authors ,19--] from a study of ultrasonic properties of dextrans of different MW. Because of the importance of the suggestion that a critical size of macromolecules in solution might exist we have investigated in detail the viscosities of a number of PEO samples with different MW, spanning a range from 300 to 300 000 Dalton. All the measurements were carried out two different temperatures (20 $^{\circ}$ and either 25 $^{\circ}$ or 26 $^{\circ}$C) -- so as to allow estimates to be made of the apparent energies of activation for viscous flow -- using capillary viscometers (sizes 100, 150, and 200) Some of the results are discussed below.

AMOUNT OF BOUND WATER (PER REPEAT UNIT)
IN 30 % PEO (AND MPEO) SOLUTIONS AS FUNCTION
OF MW. OPEN CIRCLES: PEO; CLOSED: MPEO.
DATA BY ANTONSEN AND HOFFMAN (IN HARRIS, ED.
"POLY(ETHYLENE GLYCOL) CHEMISTRY", PLENUM
PRESS, 1992.)
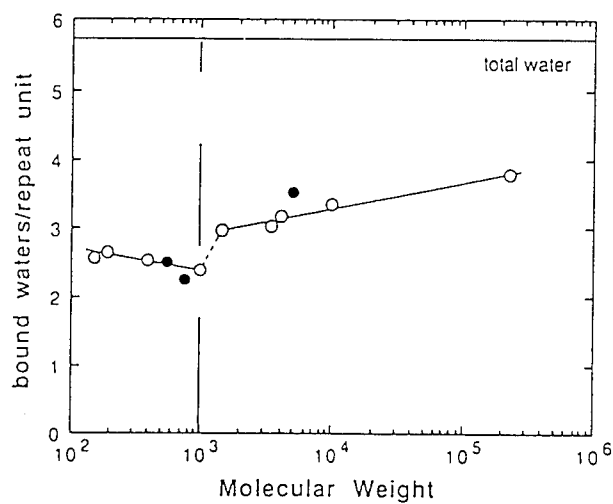
FIG. 12

AMOUNT OF BOUND WATER PER REPEAT UNIT
IN 30 % PEO SOLUTION AS FUNCTION OF MW. DATA
BY ANTONSEN AND HOFFMAN (IBID.)   NOTE:
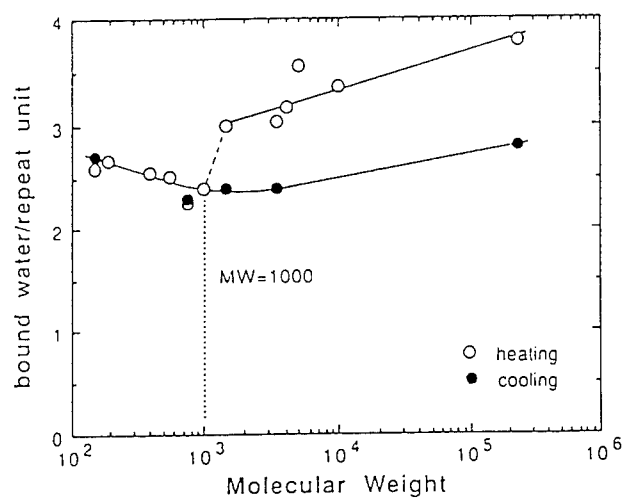DIFFERENCE BETWEEN HEATING AND COOLING.

FIG. 13

VISCOSITY OF 10 % PEO SOLUTIONS AS FUNCTION
OF MW AT 20 AND 26 ºC. [SIZE 150 VISCOMETER.]
DATA: VOUGHT AND DROST-HANSEN, UNPUBL.
NOV. 1992
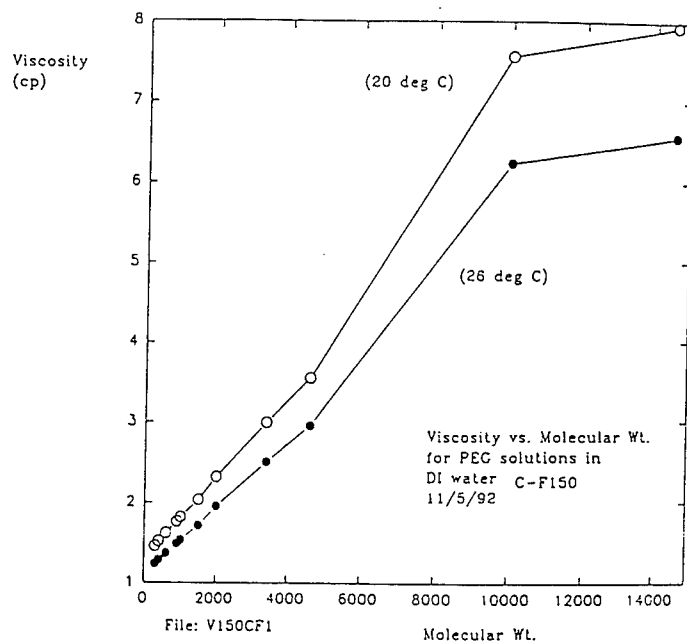
FIG. 14

VISCOSITY OF 10 % PEO SOLUTIONS AS FUNCTION
OF MW AT 20 AND 26 ºC. [SIZE 200 VISCOMETER.]
DATA: VOUGHT AND DROST-HANSEN, UNPUBL.
NOV. 1992
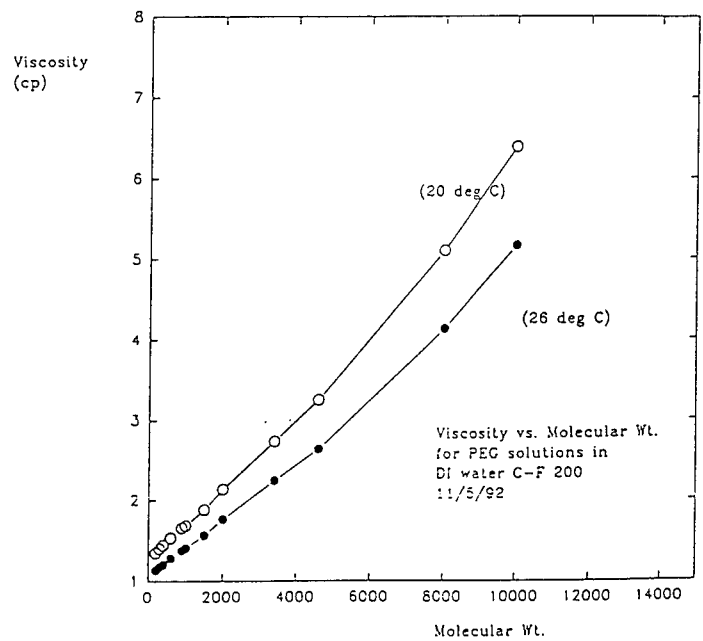
FIG. 15

APPARENT ENERGIES OF ACTIVATION FOR
VISCOUS FLOW OF PEO SOLUTIONS, 10 %, AS
FUNCTION OF MW. [SIZE 150 VISCOMETER.]
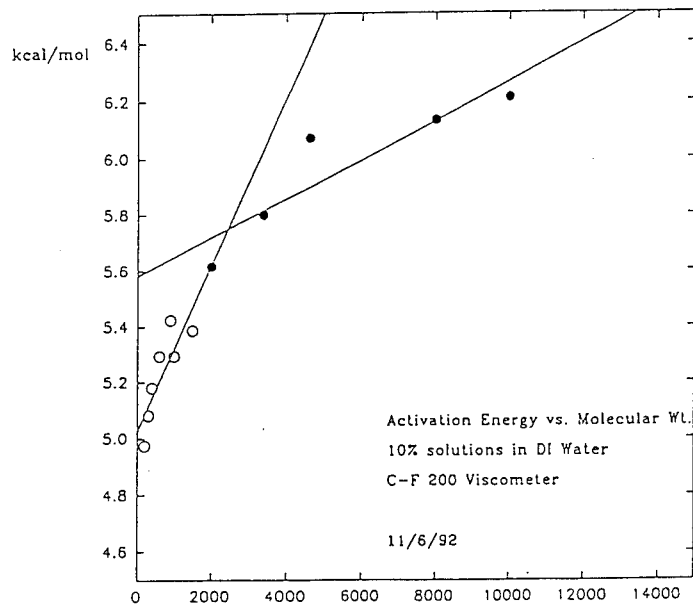DATA: VOUGHT AND DROST-HANSEN, UNPUBL.
NOV. 1992.
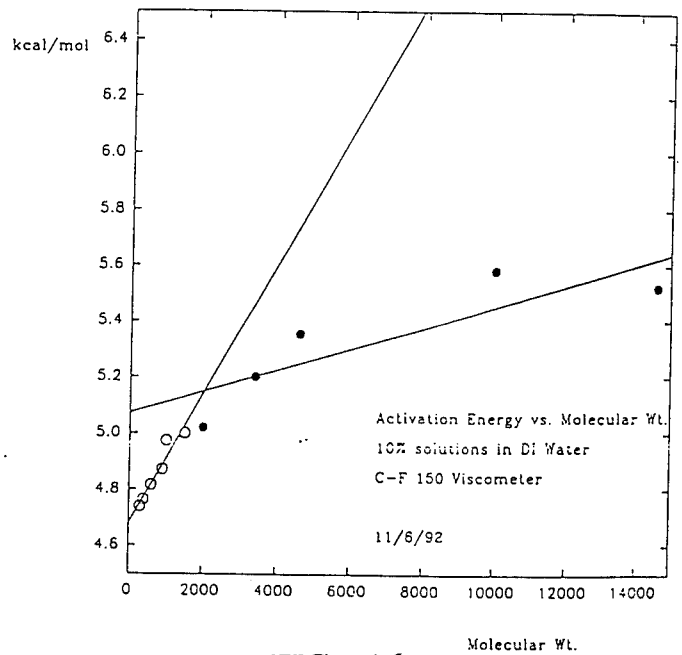
FIG. 16

APPARENT ENERGIES OF ACTIVATION FOR
VISCOUS FLOW OF PEO SOLUTIONS, 10 %, AS
FUNCTION OF MW. [SIZE 200 VISCOMETER.]
DATA: VOUGHT AND DROST-HANSEN, UNPUBL.
NOV. 1992.

FIG. 17

Other indications of notable differences in solute behaviour of PEO, respectively with MW below and above 1 kD, have come from a recent study by Antonsen and Hoffman (in"Poly(Ethylene Glycol) Chemistry", ed. J. Milton Harris, Plenum Press, 1992, pp.15 - 28.) These authors observe a small, but distinct jump in the amount of bound water/repeat unit between 1 and 2 kD. Similarly, transition temperatures from melts of the PEO in water show a dramatic increase around a MW of 1.2 kD and the heats of fusion a similarly distinct jump between 400 and 1000 kD. FIG. 12

It is of interest also in the study by Antonsen and Hoffman, that large differences exist between data collected upon heating the samples compared to data collected during subsequent cooling of the samples. This FIG. 13 is eminently consistent with our own measurements on vicinal water: upon heating, a particular vicinal water structure appears to be destroyed (and a new one formed) when heating a sample above one of the critical transition temperatures (T_k) for the vicinal water. Upon cooling, the vicinal water structure is only "regenerated" very slowly; sometimes 24 hrs may be necessary to reform the specific prior structure in question. For a discussion of such hysteresis see the discussions elsewhere by the present author

Bailey and Koleski reported a change in the slope of the intrinsic viscosity of PEO solutions (as a function of MW) near 2 to 3 kDa. In our own FIG. 14 work we have frequently plotted the *actual* viscosities of PEO solutions as FIG. 15 function of MW without noting any distinct change near this MW range. In an attempt to provide a more sensitive test of the MW dependence we have measured the viscosities of a series of PEO solutions with different MW, at two different temperatures, in order to examine the effects of the MW changes on the apparent energies of activation for the flow process. Some typical results are shown in FIG. *16* and FIG. *17*. The two sets of data were obtained using viscometers with two different capillary sizes (to estimate the effects of differences in shear-rates.) It appears that the apparent energy of activation levels off above some MW range around 2 kDa., but the scatter in the data for the larger solutes makes a quantitative comparison suspect. Nonetheless, it does appear that two different flow regimes do exist, respectively, below and above some critical MW range, centered around 2 kDa. *That the resulting hydration is indeed similar to the vicinal hydration which occurs at solid/water interfaces is supported by the occurrence of thermal anomalies in the properties of such solutions.* as discussed elsewhere in this Report.

An entirely different study of MW effects have been reported by Bayer and Rapp who measured the ^{13}C-NMR-Relaxation of free (and of bound) PEO as a function of the MW. Their results are shown in FIG. *18*. It is obvious that a decisive "levelling off" in T_1 occurs for the free PEO at about 1 - 2 kDa.

Finally, in the study by Antonsen and Hoffman a number of other characteristic properties of PEO solutions were investigated. In FIG. *13* is shown the observed amounts of "bound water" per repeat unit of PEO (and MPEO) as a function of MW. A small, but distinct change occurs near 1 kDa. Similarly, the amount of bound water in 30 % solutions of PEO increases distinctly near 1 kDa, as observed during experiments performed while heating the samples. Note, however, that this effect does not appear upon cooling the samples down. This examples nicely illustrates the hysteresis in vicinal water discussed elsewhere in this Report: once the structure of the vicinal water has been disturbed (destroyed) by heating past one of the transition temperatures (T_k), the structure reforms only very slowly when the temperature is returned below the transition point. On measuring the heat of fusion for frozen solutions of PEO Antonsen and Hoffman again observed the MW range from (400 to) 1000 to play an important role as seen in FIG. *19* . Finally, an abrupt change in the transition temperatures of 30 % PEO solutions at low temperatures also reveal a distinct MW dependency in the range around 1 kDa.; see FIG. *20*.

13C-NMR-RELAXATION TIMES T_1 OF FREE
PEO (a) AND OF PS-IMMOBILIZED PEO (b) AS
FUNCTION OF MW. DATA: BAYER AND RAPP,
(IN HARRIS, ED. "POLY(ETHYLENE GLYCOL)
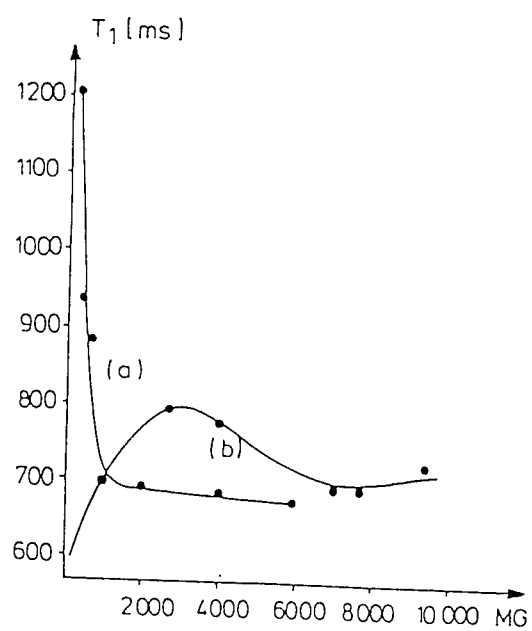CHEMISTRY" PLENUM PRESS, 1992.)

FIG. 18

TOTAL HEAT OF FUSION FOR 30 % SOLUTION OF PEO.
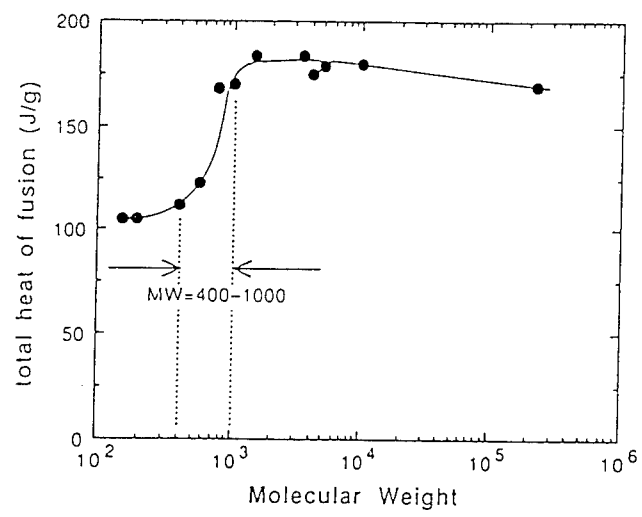DATA BY ANTONSEN AND HOFFMAN (IBID.)

FIG. 19

TRANSITION TEMPERATURE FOR 30 % PEO
SOLUTIONS AS FUNCTION OF MW. DATA BY
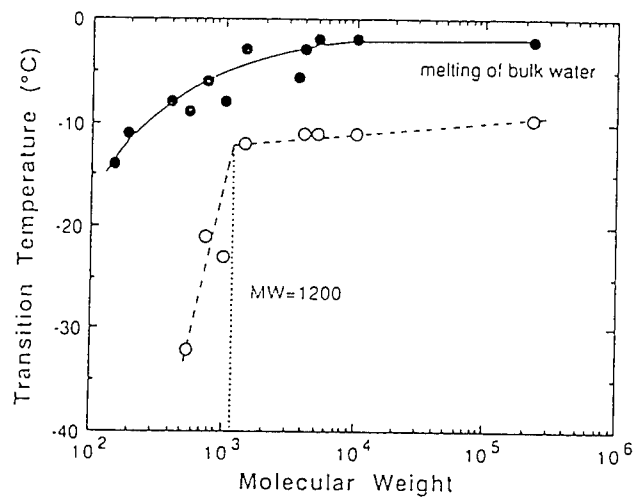ANTONSEN AND HOFFMAN (IBID.)

FIG. 20

We have demonstrated that the viscosities of aqueous polymer solutions (for polymers above a certain critical size) strongly suggest the vicinal hydration of the polymers. The significance of this finding to cell biology becomes particularly obvious when recalling the Walden rule: that diffusion coefficients and viscosities are inversely related. Thus it must be expected that the diffusion coefficients for solutes in the cytoplasm reflect the presence of the vicinal water. Mastro and Hurley (1985) have used an ingeneous technique to follow the diffusion in cells of various solutes with different MW. Fig. *21* shows their results in terms of the logarithm of the observed diffusion coefficients as a function of the logarithm of the molecular weight of the diffusing species. A *distinct* inflection point occurs at approx. 2500 Da.-- just about the molecular weight range where it is proposed that macromolecules in aqueous solution become vicinal hydrated. This tendency is even more obvious in Fig. *22* where the product of the observed diffusion constant and the viscosity of the aqueous medium is plotted versus the log[MW]: an unmistakable change in slope occurs just about 1 kDa. -- as would be expected if this MW range indeed represents the lower limit for the onset of vicinal hydration.
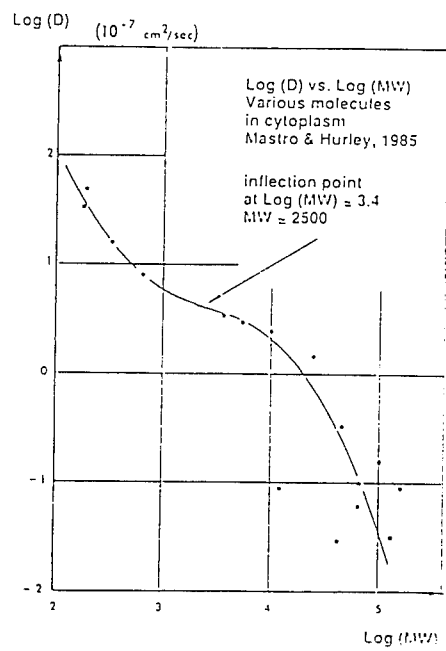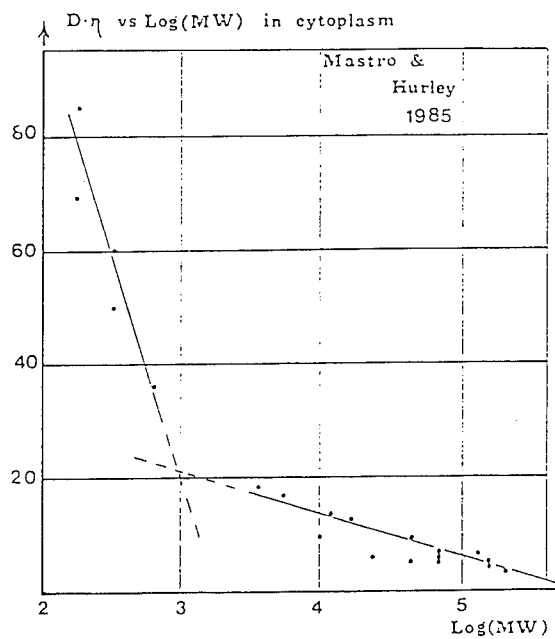
FIG. 21

FIG. 22

As discussed elsewhere in this report, the vicinal water -- or at least a significant fraction of the vicinal water -- is extremely sensitive to its past thermal and mechanical history. Thus heating the vicinal water past one of its transition temperatures will apparently destroy the stable structure below that T_k and upon cooling the sample down below this point the original vw structure reforms only slowly. Similarly, shearing the vicinal water appears to break down the prevailing vw structure. This was for instance reported by Peschel and Adlfinger who observed that with increasing rate of expelling the water layers [i.e. increasing shear-rate] between the quartz plates of their force-balance instrument, the apparent viscosity of the intervening water layers decreased from a rather high value (of the order of ten times the bulk value) to the approximate value for bulk water. Once the vicinal water structure has been broken down -- by thermal or mechanical means -- the structure reforms only slowly. An example of the difference between data observed on heating a sample compared to cooling the sample, see for instance Fig. 'c for the amount of "bound water" in 30 % PEO solutions.

It should be noted that much of the evidence for a change in solute behaviour of polymers near a MW of 1 kDalton, has come from studies on PEO, both those described in this report as well as some derived from the literature. However, it is unlikely that the change in solute properties merely reflect some peculiarity of the PEO polymers. Consider for instance the rather abrupt change in d[diff.coeff.]/d[MW] near approx. 1 kD reported by Stein and Nir; this study was based on diffusion data from about 31 different solutes, ranging from He to very large proteins. Note also, that remarkably sharp changes in solute behaviour (especially ultrasonic properties) near 1 kD were observed by _____ and _____ in solutions of Dextrans. This observation is likely of considerable importance because of the suspected widely differing nature of the hydration between PEO and Dextrans. (Recall for instance that two mutually *immiscible* liquid phases exist at room temperature between aqueous solutions of PEO and Dextrans -- even though each may be 90 % water.)

EXPERIMENTAL. PART B: PHOTON CORRELATION
SPECTROMETRY (PCS) (for particle sizing.)

The quantitative treatment of hindered settling -- such as observed in the
sedimentation of erythrocytes in whole, anti-coagulated blood -- is
generally based on the Stokes law for the sedimentation of a single
(spherical) particle. So far, only approximate theories have been developed
and only for low concentrations, usually less than one percent solids; no
rigorous theory presently exists to account for the settling of concentrated
suspensions of non-spherical [let alone non-rigid] particles in non-
newtonian fluids. Nontheless, it appears likely that any ultimate theory of
hindered settling must somehow take into account the "effective" diameter
of the settling particles -- including the red cells in the case of hindered
settling of whole blood. It is proposed that one factor which may influence
the overall, apparent "diameter" of particles (including the erythrocytes) is
the possible existence of extensive, vicinal surface hydration. This idea is
hardly new and over the years it has been severely critized by many
authors; indeed, the evidence for such surface hydration is weak but not
entirely without merrit. As discussed in the present report - based on our
measurements in connection with the AF Grant - and in part based on the
viscosity studies carried out during the author's AF Summer Research
Programs - vicinal surface hydration effects are real but may be rather
"delicate" in the sense of being highly shear rate dependent. Thus, the
vicinal hydration structures envisioned in this study are notably different
from the classically assumed, essentially high-energy hydration of surface
charges or strongly polar surface molecules. Also, as discussed elsewhere
in considerable detail, the vicinal water structures are believed to differ
only slightly from the bulk structures and the difference in the energetics of
the two forms of water is likely small, say ten to a few hundred cal/mole,
-- in other words less (or far less) that kT at room temperature. This may
in part explain why many previous investigators have failed to observe the
vicinal water structures. Finally, recall the proposition stated earlier in this
report: vicinal water undergoes more or less abrupt changes with
temperature at a number of critical temperatures ranges, T_k (for instance

near 14 - 16, 29 - 32 and 44 - 46 °C). Conversely, if anomalies are observed at any one of these temperatures (or especially at two or more of these critical temperature ranges) it suggests that vicinal water is indeed present and influences the overall properties of the system.

Author's question to readers with exceptionally good eyesight: does anyone ever read these reports? or are we just spinning our wheels? Please advise me if you are reading this report, - especially if you might have an interest in our work..

We have carried out some particles size measurements on some well-defined, rigid spherical particles by means of a Coulter Counter particle size analyzer based on a Photon Correlation Spectrometric (PCS) method. The particles were submicron-sized polystyrene (PS) spheres in pure water and measurements were made of the apparent particle sizes as a function of temperature.

Suspensions were prepared from PS sphere suspensions as obtained from Bangs Laboratories, Inc.   Nominal diameters for these particles were 0.170 and 0.50 microns. Suspensions of approx. 10^{-3} % were prepared and placed in plastic cuvettes (1 cm path length) and the cuvettes placed in the Coulter Co. Particle Size Analyzer (Model CN4 SD). A scan was made and the temperature of the sample holder increased to the next higher temperature wanted;   a period of 2 min was allowed to elapse after reaching the new temperature before a subsequent run was initiated (to insure thermal equilibrium.) Note that in all of these runs measurements were made only with increasing temperatures. Note also, the samples were NOT stirred (or otherwise "disturbed" mechanically) during the whole measuring sequence.

Some typical results are shown in Figs. *13* -- *16*.

FILE: APRBP.2

APPARENT DIAMETER. IN NM. OF PS-SPHERES
IN AQUEOUS SUSPENSION. NOMINAL DIAMETER:
500 nm.. DATA: DROST-HANSEN & SHAHMOHAMADY
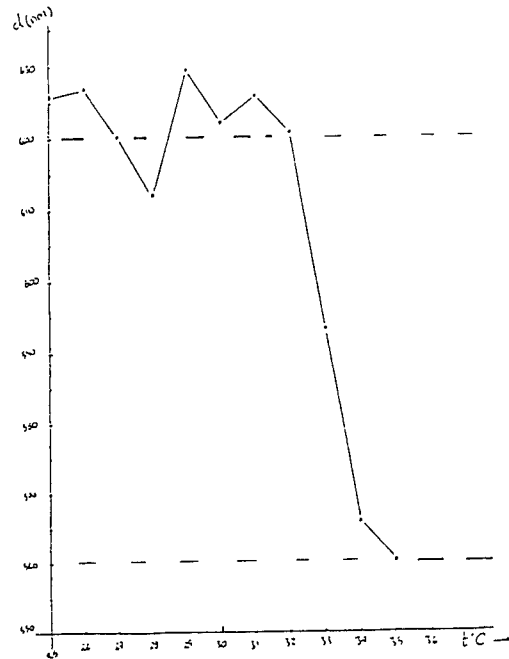UNPUBL. 1992 [SER. 2]

FIG. 23

APPARENT DIAMETER, IN NM, OF PS-SPHERES
IN AQUEOUS SUSPENSION. NOMINAL DIAMETER:
500 nm.. DATA: DROST-HANSEN & SHAHMOHAMADY
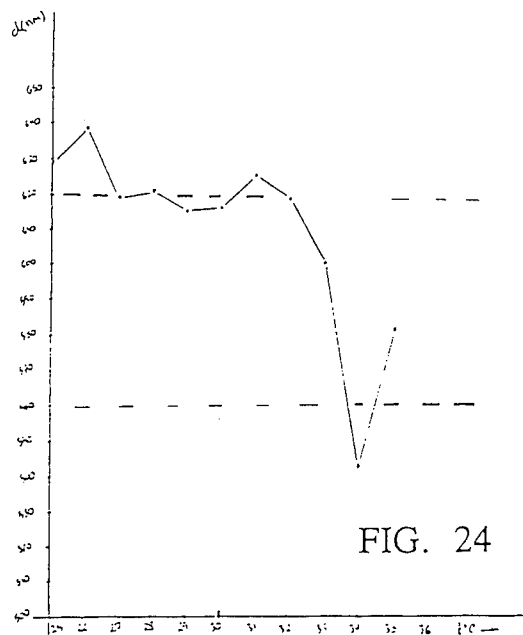UNPUBL. 1992 [SER. 4]

FIG. 24

The data for the apparent particle diameters are highly unusual and likely very significant. The measured particle diameters, for temperatures below about 30° - 32 ^oC, are about 30 % larger than the nominal, solid diameters. Above the transition temperature the apparent diameters decrease abruptly by about 60 nm (or 600 A). We propose that the observed sizes reflect the actual "effective" diameters as determined by the hydrodynamics of the vicinally hydrated particles in view of the fact that the photon correlation spectroscopy actually measures the diffusion coefficient (from which in turn the apparent diameter is calculated.) The sharp drop at 30 ^{o} - 32^oC represents the structural transition in the vicinal hydration hull from the vicinal water structure stable below T_k to the vw structure stable above this thermal transition. The difference between the two values then leads to a minimum estimate of the thickness of the vicinal hydration hull, namely 0.5 x 60 nm = 30 nm = 300 A = approx. 100 $d[H_2O]$ in good agreement with many other independent estimates for the thickness of the vicinal water structures. Note that these measurements were carrried out with as little mechanical disturbance as possible of the particle suspensions. In a subsequent study (a continuation of the original project) we have repeated similar measurements but stirring the contents of the cuvettes with a small magnetic stirrer between each measurement (and allowing only a few minutes between consecutive scans.) In these measurements we find a distinct but less pronounced, more or less uniform decrease in apparent particle size as a function of temperature -- i.e. without an abrut drop in the apparent diameter at T_k.

It appears from these and a considerable number of other studies in the authors Laboratory that vicinal water exhibits hysteresis: it is indeed sensitive to the past thermal as well as mechanical history of the samples. Allowed sufficiently long times the vicinal water structures do regenerate. The time for the vicinal water to regenerate appears to depend somewhat on the specific nature of the systems studied; times of the order of hours to a day have been encountered. However, vicinal water is indeed the thermodynamically stable form of interfacial water. In view of the hysteresis mentioned above it is hardly surprising that many investigators have failed to observe any consistent behaviour of vicinal water.

SUMMARY AND CONCLUSIONS.

The viscosity measurement on aqueous polymer solutions have shown that:

A)   Anomalies occur in the viscosity of aqueous polymer solutions at the thermal anomaly temperatures (T_k) of vicinal water.   This has been observed with both PEO and Polyvinyl pyrrolidone solutions, at least for polymers above a certain critical Molecular Weight (about 1000 Dalton.) This suggests that polymers in aqueous solution are vicinally hydrated, akin to the vicinal hydration structures at the solid/water interface.

The above conclusions agree with thermal anomalies previously reported in the literature from rheological data on both aqueous solutions and polymer gels (for instance gels made of fish meal, etc., i.e. primarily concentrated protein systems.)

B)   Measurments of the temperature dependence of viscous flow of PEO solutions have yielded apparent Energies of Activation ($\Delta E^{\neq}$) for viscous flow of these solutions.   When plotted against the MW of the polymer, $\Delta E^{\neq}$ is found to change rather abruptly for MW of the order of 1000 Dalton -- in agreement with our earlier expectations based on published data in the literature.

C)   Based on the above observations, together with various reports in the literature, we are lead to the conclusion that most (or all) macro-molecules in aqueous solutions are vicinally hydrated.   Such vicinal hydration must significantly influence the intracellular phase of all living cells, and -- in the context of the present study -- affect the volume, and shape (as well as the tendency to aggregate) of all erythrocytes.   Thus the ESR must be expected to reflect the structure and properties of vicinal water -- as we have indeed observed in our in-vitro studies of the hindered settling of red cells in whole blood.

Our measurements of particles sizes have shown that:

D)   Well-defined, solid Polystyrene spheres have apparent radii far larger the nominal, solid-sphere diameters of the particles, *when measured with a Photon Correlation Spectrometer* (Coulter Co., Model CN4 SD). We believe these larger, apparent diameters reflect the vicinal hydration hulls of the particles. It is hard to overestimate the significance of this finding: if vicinal hydration occurs to such an extent, then rates of diffusion of the particles must be notably affected and "classical" estimates of diffusion coefficients/particle sizes will likely be in error!

E)   The apparent, enhanced particle diameters are highly temperature sensitive. Thus upon heating, for instance, from 25 ^{o}C to 37 ^{o}C, the observed, apparent particle diameters appear to decrease abruptly near 30 - 32°C, suggesting that the observed diameters are indeed those determined by the vicinal hydration hulls of the PS spheres. We propose, if only tentatively, that *erythrocytes may likewise be vicinally hydrated.*

F)   At higher temperatures, say from 40 ^{o} to 50 ^{o}C the behaviour of the PS spheres are more complicated. In these cases, *increases* in the apparent diameters are usually observed but NOT necessarily right at T_k for the third, vicinal water transition (44 - 46°C.)

G)   If one accepts as real the apparent, observed effective diameters of the PS shperes, the change in the effective thickness of the vicinal hydration hull around 30°-32 ^{o}C amounts to about 0.5 x 60 nm or 300 Å. Such a distance is indeed in good agreement with the order of magnitude estimates for the effective thickness of vicinal water obtained by a variety of other methods.

In Summary: all our results continue to support the idea that interfacial water is restructured at solid interfaces and that the depth of the "vicinal" layers [of the order of hundreds of Angstrom] far exceeds more classical estimates (of only one or a few molecular layers of water.) In addition to finding vicinal water at the solid/water interface we now also observe vicinal hydration of macromolecules in solution, at least for sufficiently large polymers. Our results suggest that the critical minimum size above which vicinal hydration occurs is about 1 kDalton.

The findings summarized above have a direct bearing on the ultimate objective of our research, namely providing a molecular basis for hemorheology [and, in turn, hemodynamics.] The vicinal hydration of "solid" surfaces must affect the multitude of internal membrane surfaces of the erythrocytes; in addition, all the larger macromolecules present in the erythrocyte -- as well as in the plasma -- now also appear to be vicinally hydrated. No wonder then that red cell volumes reflect the presence of vicnal water, for instance by abrupt changes at 30 ^{o} and 45 ^{o}C. Furthermore, the surfaces of erythrocytes are likely vicinally hydrated and this must affect such processes as diffusion rates of the cells; extent and dynamics of surface adsorption of proteins and tendency to rouleaux formation. Finally, if indeed all polymers in aqueous solution are vicinally hydrated, then one must expect the macromolecules in the plasma (and serum) to be similarly hydrated and in turn influence the rheological behavior. Strong evidence for this has been obtained independently in our viscosity data on both plasma and serum.

FILE: APRBP93Q

10-57